The cardiac L-type calcium current: existing models and methods of improvement

Aditi Agrawal

St Catherine's College

Computational Biology Group

Department of Computer Science

University of Oxford

A thesis presented for the degree of

Doctor of Philosophy

Trinity 2022

Supervisors:

Prof. David J. Gavaghan

Prof. Gary R. Mirams

Dr. Michael Clerx

Industrial supervisors:

Dr. Liudmila Polonchuk

Dr. Ken Wang

Acknowledgements

This thesis would not have been possible without my supervisors: Gary, Michael, and David. A few words are not enough to thank them for the time they've put into my projects over the course of my DPhil. Their patience, insight, and enthusiasm were pivotal to all research presented in this thesis. I would also like to thank Liudmila and Ken at Roche for their help with experimental data and meaningful discussions.

I acknowledge the contribution of Evgenia at Roche who performed the patch-clamp experiments used in Chapters 5 and 7, as I was unable to travel due to the pandemic. I would also like to thank all members of the research group. In particular, Maurice for developing the story feature of Web Lab which allows the results of Chapter 4 to be presented in an interactive manner, Chon for giving advice on several occasions, and Alejandra for providing motivation during the writing-up phase of the DPhil.

I am grateful to St Catz for providing me with a place to stay, money to live, and giving me a sense of belonging to a community.

I feel blessed to have had the continued support of Mum, Dad, and Sushant. In the past few years they've found a way to bring home to me despite thousands of miles between us.

Finally, I would like to mention both old and new friends for providing fun-filled moments with game nights, impromptu trips, and lots of good food. A special mention to Aditya, Mayur, and Varnika who've been an invaluable part of my DPhil journey.

Abstract

The heart plays a crucial role in the circulatory system, pumping blood to and from the body. The pumping action is due to the rhythmic contraction of the muscle cells of the heart (cardiomyocytes). This 'beating' is facilitated by ionic transport across the membrane of each cardiomyocyte due to electrophysiological activity. Mathematical models that describe this electrophysiology at the organ, tissue, and cellular level are critical for the prediction of irregular beating of the heart (arrhythmia). Arrhythmias can be initiated by unintended modulations of cardiac electrophysiology by pharmaceutical drugs. Therefore, in the past decade, drug regulatory bodies have implemented the use of cardiac models for cardiac safety assessment of novel drugs. Investigating the effects of the drug on individual *ion channels* of the heart is an important aspect of such cardiotoxicity assessment initiatives. The *L-type calcium current* (I_{CaL}) is one such *ionic current*, key to cardiomyocyte contraction.

This thesis investigates if it is possible to select a model of I_{CaL} that accurately reflects its biology. This was done by first gathering 73 I_{CaL} models and identifying several choices available for individual components of the model. Next, these models were examined using identical experimental conditions thus revealing wide variability in their predictions. To understand this variability, novel experimental data was generated and a pipeline was set up to explore how data collected from a single cell using *automated patch-clamp* experiments can be used to build an I_{CaL} model. Experimental recordings of I_{CaL} were identified to be contaminated by *rundown*, which was shown, to be partly due to calcium-dependent inactivation (CDI) of I_{CaL}. A mechanistic model was then used to establish experimental conditions at which CDI-induced rundown can be minimised. Rundown-corrected data was used to develop a preliminary model of I_{CaL} characterising its voltage-dependence. Cell-specific calibrations of this model closely replicated the training data in addition to making predictions about other I_{CaL} properties. Thus, this thesis sets up a method to develop an I_{CaL} model representative of its underlying biology for a particular *context of use*.

Keywords— Cardiac modelling - L-type calcium current - mathematical modelling

Contents

1 | Introduction

1.1 Motivation

Most animals, including humans, rely on a heart to pump blood around their circulatory system. The blood carries oxygen and nutrients to all parts of the body through blood vessels while also transporting carbon dioxide and other waste products generated during metabolism to be removed from the body. The heart's ability to pump blood is due to the *contraction* and *relaxation* of the heart muscles. These mechanical changes are triggered by electrical impulses generated by the movement of several ionic species in and out of individual cardiac myocytes (muscle cells). The electric signal is carried by potassium (K^+), sodium (Na^+), calcium (Ca^{2+}), and other ions that passively flow through specific *ionic channels* or are actively moved by *ionic pumps*. Therefore, a full understanding of the mechanical function of the heart is not possible without studying the electrical activity of the heart — the field known as cardiac electrophysiology.

Mathematical modelling of cardiac electrophysiology has a history of more than 60 years, making it one of the most mature areas of systems biology. Advances in technology such as molecular cloning in the 1970s [Alberts et al., 2002] have helped to unearth increasingly detailed characteristics of individual components of a single cell. The development of the patch-clamp technique in the 1970s and 1980s was especially useful in recording ionic currents [Sakmann and Neher, 1984] (Chapter 2). While the first cardiac model ever published only had three ionic currents [Noble, 1960], the increase in knowledge of the underlying electrophysiology as well as the exponentially increasing computational power over the decades has been reflected in the development of progressively more complex mathematical models. Many of these models can be found in an online repository called the Physiome Model Repository [Yu et al., 2011] which was established to ensure a standard for sharing the models as part of the Cardiac Physiome Project [Noble et al., 2012, Hunter and Smith, 2016].

Typically, models of a single cardiac cell have been built by establishing equations or sets of equations that most closely replicate the biological features that a cell is known to have.

These equations are then empirically fitted to electrophysiological data collected from isolated cells to determine the *parameters* of the model. A single model will often have parameters determined using data collected from distinct experimental setups, cell types, and even different species. Even if all the potential sources of differences mentioned here are considered, there is also cell-to-cell variability known as *extrinsic* variability [Whittaker et al., 2020]. Many of the baseline models that have been developed use data averaged across cells so that the resultant data are not representative of any one cell/individual [Golowasch et al., 2002].

A disturbance to regular heart rhythm is called an "arrhythmia". We describe something as pro-arrhythmic if it makes arrhythmias more likely to occur or be sustained. Given the critical function of the heart in the human body, it is essential to screen novel drug compounds for pro-arrhythmic safety. In the last decade, pharmaceutical regulatory bodies such as the United States Food and Drug Administration (FDA) have begun to use cardiac models to screen novel drug compounds for proarrhythmic risk [Strauss et al., 2019]. This screening involves conducting detailed pre-clinical studies that look for unintended modulations by the drug, that may induce proarrhythmic conditions in the heart. While proarrhythmic safety clinical trials are immensely useful in establishing the safety of any new drugs released, they can take up to a year for completion and cost an average of $2 million per trial[1]. Virtual or *in silico* trials using mathematical models can be performed before *in vivo* animal and human clinical trials and thus have the potential to save thousands of individuals (both human and animal) from being exposed to possibly risky compounds in unnecessary clinical trials, as well as saving money. The use of cardiac models is one of the four pillars of the Comprehensive *in vitro* Pro-arrhythmia Assay (CiPA) initiative, which uses *in vitro* data collected from patch-clamp experiments to develop models of drug block (Chapter 2). The predictions of cardiac models incorporating these data are then compared against predictions from *in vivo* trials [Strauss et al., 2021]. Given the rich history of cardiac modelling and only a recent shift in model use from fundamental research to cardiotoxicity safety screening, there is a need to carefully re-assess the model-building process to ensure that the model developed is robust and reliable in its predictions.

[1] https://www.fda.gov/drugs/regulatory-science-action/impact-story-finding-better-test-predicting-risk-drugs-pose-heart

The *L-type calcium current* (I_{CaL}) is one of the most important ionic currents in the heart: it is responsible for increasing Ca^{2+} concentration inside the cell which leads to the contraction of the cardiac myocyte (Chapter 2). The overall aim of this thesis is to create or identify a model of I_{CaL} that can most accurately predict the behavior of I_{CaL} in the heart. Therefore, as a primary aim in this thesis, more than 70 unique models for I_{CaL} that already exist are detailed and reviewed. Interestingly, no existing study was found that explores the underlying differences between all of these models, or investigates which model should be preferred over others in a given *context of use* [Pathmanathan et al., 2017, Whittaker et al., 2020]. This thesis shows that there is a large amount of variability between the predictions made by these models, and these differences cannot be explained by physiological differences such as those of different species or cell types. However, the underlying electrophysiology of I_{CaL} can be better identified using experiments. Thus, the remainder of this thesis focuses on the process of developing an I_{CaL} model — from data-collection to model-building.

The secondary aim of this thesis is to establish a preliminary pipeline to build an I_{CaL} model using data collected from a *single* cell. First focusing on data-collection, a source of contamination in I_{CaL} when recorded using patch-clamp experiments is identified. Subsequently, the experimental conditions at which this contamination can be minimised are determined. Secondly, a methodology is established to post-process the resulting recording, which is then used to identify cell-specific parameterisations of a preliminary I_{CaL} model. The parameter sets obtained using data from different cells are then compared. A more detailed layout of the thesis is given in the next section.

1.2 Thesis outline

Chapter 2 provides the necessary background material on the underlying biology, physiology, experimental, and mathematical concepts required in this thesis.

Chapter 3 qualitatively compares almost all existing models of I_{CaL} with respect to the individual elements that make up the model for an ionic current: region of localisation of the channel within the cell, choice of gating mechanism, and the electrochemical driving term. This chapter shows that there exist many choices for each of these elements and that there is little documented evidence for the rationale or consequences of each choice.

Chapter 4 implements simulations with most of the I_{CaL} models identified in Chapter 3 and compare the model responses under various protocols at identical experimental conditions. This chapter shows that there is a large amount of variability in the predictions of the existing models. This may be due to several factors, including differences in the proposed biological mechanisms, underlying data sets, or even the different inputs that were used for the generation of the underlying data set.

The remainder of this thesis focuses on designing and optimising experimental conditions with the goal of developing an I_{CaL} model from the collected data.

Chapter 5 investigates the experimentally observed phenomenon of attenuation of I_{CaL} recordings with time — also called *rundown*. High-throughput automated patch-clamp experiments are designed and performed at varying conditions to test whether rundown can be attributed to increasing Ca^{2+} concentration inside the cell. Here the theory behind the experimental design is introduced along with an explanation of how the the recorded data is post-processed and subjected to quality control. At least part of the experimentally-observed rundown is shown to be due to Ca^{2+} accumulation at the intracellular side of the membrane.

Chapter 6 presents a mechanistic model of calcium-dependent rundown identified in the previous chapter by capturing how I_{CaL} both influences and is influenced by the Ca^{2+} concentration that changes inside a cell over the course of an experiment. The predictions of this model are used to identify the Ca^{2+}-dependent aspect of the rundown recorded in Chapter 5. This chapter also establishes the experimental conditions at which Ca^{2+}-induced rundown is minimised or eliminated.

Chapter 7 presents a pipeline to develop a preliminary model of the voltage-dependent aspect of I_{CaL}. The experimental system is optimised to avoid the rundown measured in Chapter 5 using the predictions of the model developed in Chapter 6. A novel protocol is then presented that is short enough to allow the collection of both *training* and *validation* data from the same cell. This allows all features of a model to be determined (and validated) from the same cell. The resulting cell-specific parameterisations of the model show very little variability suggesting that the variability of the I_{CaL} models presented in Chapters 3 and 4 possibly arises because of differences in the model-building process.

Chapter 8 summarises the overall findings of this thesis and discuss how each chapter contributes to the field of electrophysiology. Some limitations and possible future work that will contribute to the construction of a better I_{CaL} model is also discussed in this chapter.

2 | Background

This chapter is used to establish some essential concepts of physiology, electrophysiology, biology, physics, and mathematics that form the basis on which the research and investigations in this thesis have been undertaken. First, the anatomy of the heart is explained, highlighting the importance of the contractile cells in heart muscle (cardiomyocytes) in the functioning of the heart. Secondly, the electrophysiology of the cardiomyocyte is described which explains the mechanisms that allow the flow of free ionic species, thus facilitating the mechanical changes of a cardiomyocyte. Special emphasis is given to the role of the L-type calcium current (I_{CaL}) in a cardiomyocyte, and its underlying biological components that are responsible for its physiological features. Thirdly, I_{CaL}'s role in pathophysiology and its importance for *in silico* modelling in the CiPA paradigm is discussed. Fourthly, it is shown how the biological components of a cardiomyocytes can be represented as an electric circuit, which can subsequently be modelled using differential equations. Finally, the experimental setup for patch-clamp experiments on CHO cells that was used to collect data presented in Chapters 5 and 7 is explained.

2.1 Structure and function of the heart

The heart is a muscular organ at the centre of the cardiovascular system, pumping blood to and from different parts of the body. Essential nutrients, oxygen, hormones, and signalling molecules are sent to the various cells via blood vessels while waste products produced during metabolism are circulated to organs that remove them from the body.

Figure 2.1 (left) shows the anatomy of the heart with white arrows showing the direction of flow of the blood cells. De-oxygenated blood enters the right atrium (RA) from the superior vena cava; the RA contracts to allow the blood to be pumped through the tricuspid valve into the right ventricle (RV). The RV then contracts to pump the blood via the pulmonary valve into the pulmonary artery which carries it to the lungs to be oxygenated. Oxygenated blood then enters the heart via the pulmonary vein into the left atrium (LA), from where it is pumped into the left ventricle (LV) via the mitral valve. Finally, the LV contracts to pump the blood into the aorta which transports the blood to all parts of the body. The LA,

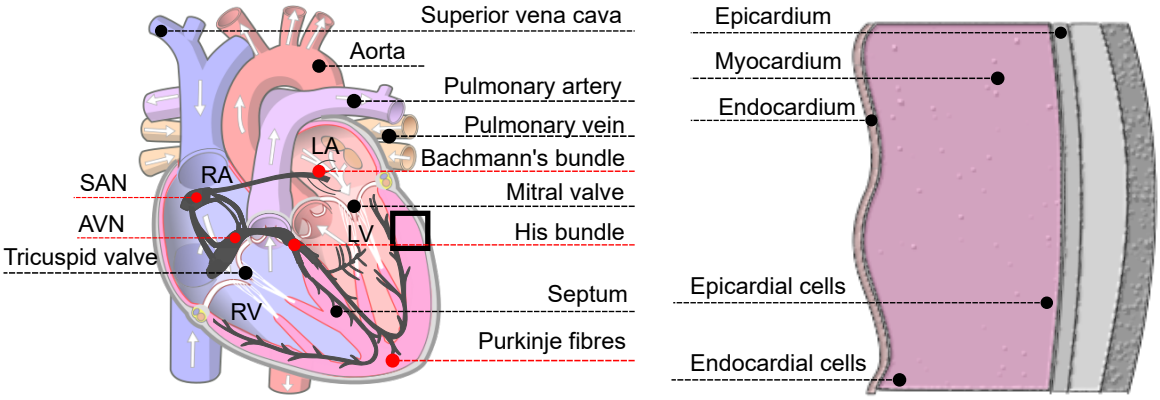

Figure 2.1: **Left**: Cross-sectional view of the heart with the white arrows showing the direction of blood flow inside the four chambers of the heart: right atrium (RA), right ventricle (RV), left ventricle (LV), and left atrium (LA). The blue colour represents the passage of de-oxygenated blood, whereas the red colour represents the passage of oxygenated blood. The electrical conduction system is shown in dark grey and is explained in the text. SAN: Sinoatrial node; AVN: atrioventricular node. An enlarged view of the boxed region is shown in the schematic on the **Right**.
The left diagram is adapted from "Diagram of the human heart" by Wapcaplet and "Shapes of the cardiac action potential in the heart" by ecgpedia, both published with a CC BY-SA licence.

LV, RA, and RV make up the four chambers of the heart, with a muscle called the septum separating the left and right sides.

The thick tissue in the muscular wall surrounding the four chambers — myocardium — allows their contraction and relaxation. The myocardium lies in the middle layer of the wall, the inner layer of the wall is lined with a thin tissue called the endocardium tissue, and the outermost layer of the wall is covered by a thin protective tissue called the epicardium (Figure 2.1, right). Cardiomyocytes or the cardiac muscle cells are found in the myocardium. Cardiomyocytes closer to the epicardium are called sub-epicardial myocytes, those nearer to the endocardium are called sub-endocardial myocytes with "sub" often dropped for convenience. The cardiomyocytes in the middle are called mid-myocardial cells, and some cells in the mid-myocardium are called M-cells, although their existence is widely debated [Sicouri and Antzelevitch, 1991, Taggart et al., 2001]. An electrical excitation ensures the coordinated contraction of the more than $\sim 5\times10^9$ [Olivetti et al., 1995] cardiomyocytes found in the muscle tissue.

A typical healthy adult human ventricular cardiomyocyte is cylindrical in shape, 100 μm to 150 μm in length and 20 μm to 35 μm in diameter [Vu and Kofidis, 2014]. It is composed of rod-like structures called the myofibrils, and each myofibril is made up of basic contractile

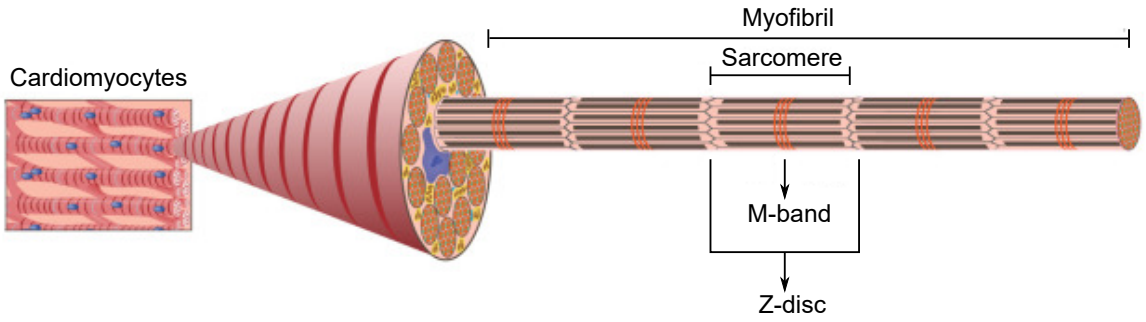

Figure 2.2: Schematic showing the bundles of myofibrils that form the muscle fibre of individual cardiomyocytes.
This figure is adapted from Ahmed et al. [2022], which was published with a CC BY licence.

units called sarcomeres. Figure 2.2 shows a sarcomere unit that further contains thick and thin myofilaments called myosin and actin respectively. These are responsible for converting chemical signals triggered by the electrical excitation into mechanical changes. When a cell is excited (*depolarised*, Section 2.2.2), Ca^{2+} enters into the cardiomyocyte, is released from internal reservoir (*calcium-induced-calcium-release*), and binds to the actin inducing a conformational change causing contraction of the cardiomyocyte [Fearnley et al., 2011]. This process is known as excitation-contraction-coupling and is the mechanism responsible for the contraction of the cardiac muscles. Excitation in one cell is transmitted to adjacent cells via *gap junctions* [Pinnell et al., 2007].

This excitation begins in specialised cardiomyocytes in the right atrium just under the superior vena cava called the sinoatrial node (SAN, shown in Figure 2.1, left) — the primary pacemaking cells of the heart. The SAN generates an electrical signal 60–100 times per minute for an average adult human. While the transmission of this excitation to the neighbouring cells continues via the gap junctions, it is transmitted to the remaining three chambers of the heart using a specialised electric conduction pathway. The excitation signal is transmitted to the left atrium via Bachmann's bundle to allow depolarisation to spread in the atria, as well as to the atrioventricular node (AVN) which delays the transmission of the signal to the ventricles. From the AVN, the signal is transmitted via the Bundle of His which separates into left and right branches for each ventricle, finally passing through the Purkinje fibres to the ventricles.

The electric conduction through various regions of the heart can be recorded using an electrocardiogram (ECG) which is a measure of voltage against time, as illustrated in Figure 2.3.

The P wave represents the excitation of the atrium, the QRS complex represents the excitation of the ventricle, and the T wave represents the loss of excitation of the ventricle [Madona et al., 2021]. The intervals between two waves of an ECG (e.g. the QT interval from wave Q to wave T) are used as indications of normal or abnormal functioning of the heart (Section 2.3).

This electrical conduction that originates from the SAN and propagates to other regions of the heart is called the sinus (or normal) rhythm. Sometimes, there are disruptions in this rhythm leading to irregular beating of the heart or arrhythmia. Arrhythmias can be broadly classified as tachycardia (irregularly fast beating) and bradycardia (irregularly slow beating). Arrhythmias can develop due to abnormal pacing of the SAN or due to triggering of other electrical signals that are out of sync from the main electrical signal, e.g. EADs (see Section 2.3). Triggered activity may also give rise to another arrhythmia mechanism which is known as re-entry where the electrical signal circles around a region of non-excitable cells in either a clockwise or anti-clockwise manner [Burashnikov and Antzelevitch, 2006, Antzelevitch and Burashnikov, 2011].

Having now described how the heart contracts and the role that the electrical conduction system plays in it, the next section describes how the electrical signal is produced.

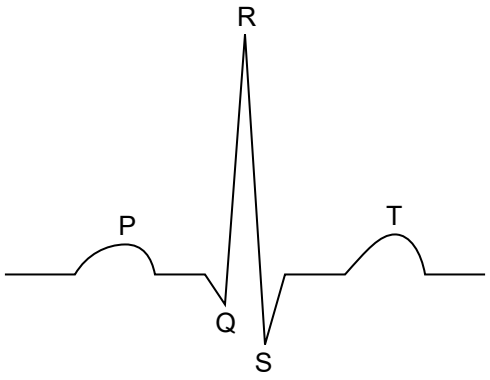

Figure 2.3: Schematic of an electrocardiogram (ECG) signal.

2.2 Electrophysiology of heart muscle cells

Cardiomyocytes can be broadly divided into two types: working and pacemaking. The SAN, AVN, Bundle of His, and the Purkinje fibres together make up the pacemaking car-

diomyocytes[1], while the atrial and ventricular cells are the working cardiomyocytes.

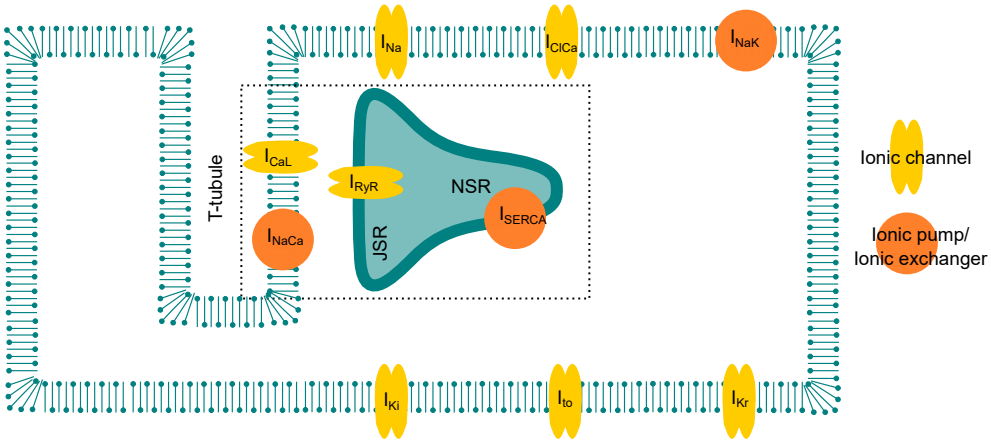

Figure 2.4: Simplified schematic of a cardiomyocyte with embedded ionic channels and pumps, discussed in the text. Boxed components are involved in calcium handling of the cell.

A simplified schematic of a working cardiomyocyte is shown in Figure 2.4. In the following subsections, the individual components of the cardiomyocyte are discussed to illustrate its underlying electrophysiology.

2.2.1 Ionic channels, pumps, and exchangers

The plasma membrane of a myocyte as shown in Figure 2.4 is called the sarcolemma. It is a lipid bilayer made up of hydrophilic heads and hydrophobic tails that prevents charged substances from diffusing across it. This bilayer thus maintains different concentrations of ionic species including sodium, potassium, calcium, and chlorine on either side of the membrane (see Table 2.1). This concentration gradient promotes the diffusion of each ionic species from a region of high concentration to a region of low concentration. This can further contribute towards the separation of charge across the sarcolemma which is maintained via *ionic pumps* (see next paragraph) giving rise to a potential difference (V_m) across the membrane. Therefore, diffusion occurs in the presence of this electric field which in turn promotes the movement of the ion toward a region of opposite charge. Thus, each ionic species experiences effects due to both the electrical and chemical gradients

[1]The pacemaking cells are also referred to as specialised cardiomyocytes, they have fewer myofibrils and T-tubules (see Figure 2.4) than typical cardiomyocytes, thus lacking contractile ability [James, 1971]. Another differentiating aspect is with respect to their size: for example, Purkinje fibres are up to 80 μm [Pappano and Gil Wier, 2013] in diameter whereas SAN cells are only approximately 8 μm [Honjo et al., 1996], and AVN cells are even smaller. Pacemaking cells are also shorter than working cardiomyocytes [Yechikov et al., 2016].

(which can be opposite to each other), together known as the electrochemical gradient. The V_m at which there is no net movement of an ionic species in either direction is called the equilibrium potential for that ion.

This section describes the biological entities that allow the permeation of ions across the sarcolemma due to selective permeability, energy, and/or ionic exchange, which together determine V_m. Ionic channels, pumps, exchangers, and cotransporters are all protein macromolecules embedded in a membrane [Hille, 2001] (shown in Figure 2.4), and many of these are selectively permeable to specific ions. The fundamental difference between the four types of transmembrane proteins is the mechanism used by each to move ions across the membrane. Ionic pumps transport ions against their electrochemical gradient using energy in the form of ATP, whereas ionic exchangers transport one type of ion down the gradient and use this energy to counter-transport another type of ion up its gradient. Cotransporters are similar to ionic exchangers, but the direction of transport of both types of ions is the same. Ionic channels, on the other hand, are pores in the lipid bilayer that allow ions to flow down their electrochemical gradient [Hille, 2001]. Ion channels in cardiac cells are often voltage-gated, though some may also be ligand-gated. Voltage-gated channels open and close in response to the changes in V_m. Conformational change induced by appropriate changes in V_m *activates* these channels from a closed state to an open state thus allowing ions to pass through. This is quickly followed by *inactivation* of the channel through a different conformational change or block of the channel's pore [Ahern et al., 2016]. Activation is reversed by *deactivation* while inactivation is reversed by *recovery from inactivation*.

Figure 2.4 shows some ionic channels, exchangers, and pumps embedded in the sarcolemma. Some of these proteins are also embedded in the membrane surrounding the sarcoplasmic reticulum (SR). The SR (similar to an endoplasmic reticulum) is a membrane-bound reservoir of Ca^{2+} inside a cardiomyocyte. It has two domains known as the junctional (JSR) and network (NSR) SR. Within the SR, a protein called calsequestrin buffers up to 40 ions of Ca^{2+} [Lu and Pu, 2020].

Ion	Extracellular concentration (mM)	Intracellular concentration (mM)	Equilibrium potential (mV)
Ca^{2+}	1.2 to 4	5×10^{-5} to 10^{-3}	94 to 150
Cl^{-}	100 to 140	10 to 20	-70 to -42
K^{+}	4 to 8	130 to 160	-100 to -74
Na^{+}	130 to 160	5 to 20	50 to 92

Table 2.1: The extracelluar and intracellular concentrations are taken from Molleman [2003] (Cl^{-} concentration has been taken from Hansen et al. [2020]). These have then been used to calculate the equilibrium potential using the Nernst equation (Equation 2.10), where T = 310 K, R = 8.314 J/mol/K, and F = 96.5 C/mmol.

2.2.2 Action potential

A change in V_m is called the *action potential* (Figure 2.5), which is the electric signal that is produced by each cardiomyocyte, initiating a heartbeat. This action potential (AP) can be divided into five phases and each phase is dominated by the movement across different ionic channels.

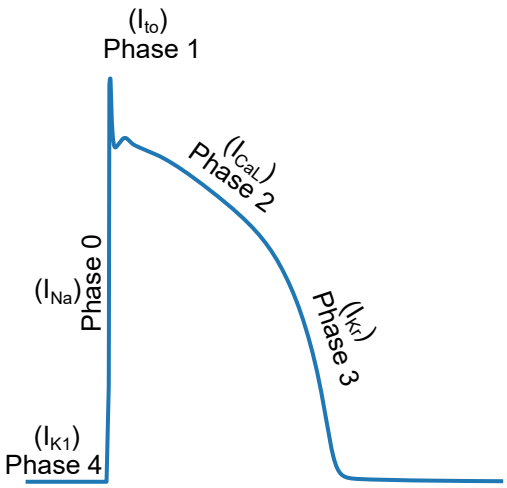

Figure 2.5: Action potential of a ventricular cardiomyocyte (epicardial) showing the change in V_m with time. The ionic current that dominates each phase is shown here and is discussed in text along with the other ionic currents. This plot was obtained by pacing the Grandi et al. [2010] model at 1 Hz.

During phase 4 of the AP, the cardiomyocyte is at the *resting membrane potential*. At this potential, there is no net movement of the ionic species across the membrane. This membrane potential is primarily maintained by the inwardly-rectifying potassium channels

(I_{K1}) [Baronas and Kurata, 2014] which bring in K^+; and further by the Na^+-K^+ pumps (I_{NaK}) which use ATP to transport $2K^+$ and $3Na^+$ against the electrochemical gradient [Fuller et al., 2013]. The resting membrane potential of cardiomyocytes is found to be near the equilibrium potential of K^+ (E_K, given in Table 2.1), around -90 mV.

Every cardiomyocyte in an adult human heart is coupled to approximately eleven adjacent cardiomyocytes [Rohr, 2004]. When the neighbouring cells are excited, ions enter the cell through gap junctions increasing V_m slightly. At this increased V_m, the 'fast sodium current' (I_{Na}) is activated, causing the rapid upstroke of V_m to positive values approaching E_{Na} (phase 0 in Figure 2.5); this is also known as depolarisation of the cell.

I_{Na} channels activate in less then 1 ms and remain open only for 2 ms to 10 ms before rapidly inactivating [Walker and Spinale, 1999]. In some cells, as the I_{Na} channels inactivate, the transient outward potassium current (I_{to}) (and, to a lesser extent, the calcium-activated chloride current, I_{ClCa}) activates to produce a rapid outward current responsible for a brief dip towards repolarisation [Grant, 2009] as shown in phase 1 of Figure 2.5.

Towards the end of the phase 1, the L-type calcium current (I_{CaL}) is activated, bringing Ca^{2+} into the cell. As phase 2 begins, the delayed rectifier potassium current (I_{Kr}) is also activated [Chen et al., 2016], which is the major outward current in this phase. These two currents balance each other out resulting in a plateau which dominates the AP [Linz and Meyer, 1998]. I_{CaL} is the major inward current responsible for maintaining the 'plateau' during phase 2 of the AP, making it an important determinant of the AP duration (APD, see Figure 2.8 in Section 2.3). Phase 2 ends as the I_{CaL} channels start to close and the net current becomes dominated by the outward I_{Kr} current (beginning of the phase 3 in Figure 2.5). The end of phase 3 is dominated by I_{K1}, resulting in repolarisation of the cell back to the resting membrane potential. The I_{Kr} channels also close as the cell enters phase 4 and the ionic charge distribution is restored across the membrane using pumps and exchangers. K^+ is pumped in while Na^+ is pumped out by I_{NaK}, Ca^{2+} is removed from the cell's cytosol by the Na^+-Ca^{2+} exchanger (I_{NaCa}) and the SR Ca^{2+}-ATPase (I_{SERCA}). The whole cycle then repeats itself.

The AP described above is that of a typical ventricular myocyte; there exist small nuances for different types of cardiomyoctyes. For example, the atrial AP has a 'triangular' AP,

as opposed to the 'spike and dome' morphology of the ventricular AP, as well as a higher resting membrane potential; these differences can be attributed to a higher density of K^+ channels that are active in phase 1 of the AP (e.g. I_{to}) [Grandi et al., 2011] and a lower density of I_{K1} channels [Bartos et al., 2015] respectively. Such differences in channel expression are also prevalent across different regions of the same cell type. For example, epicardial ventricular myocytes are 'notchier' than midmyocardial cells and endocardial ventricular cells because of a larger density of I_{to} [Furukawa et al., 1990].

Working cardiomyocytes are characteristically different from pacemaker cells, and so are their APs. While the depolarisation of a ventricular/atrial cell is determined by that of the neighbouring cells, the pacemaker cells depolarise on their own — a feature called *automaticity*. The SAN AP depolarises during phase 4 — also known as the 'pacemaker potential' [Bartos et al., 2015]. This can be attributed to several features including presence of the inward 'funny' current (I_f) carried by Na^+ and K^+, and absence of I_{K1} channels.

2.2.3 Calcium dynamics

Calcium plays a unique role in converting electrical signal to a mechanical output, as briefly mentioned in Section 2.1. Here the calcium dynamics in a typical working cardiomyocyte is elaborated.

The boxed region in Figure 2.4 encapsulates the key components involved in the calcium handling: I_{NaCa}, I_{CaL}, network SR (NSR) and junctional SR (JSR). The I_{NaCa} and I_{CaL} proteins are embedded in the T-tubule membrane which lies close to the JSR [approximately 15 nm, Hong and Shaw, 2017], in a region called the dyad. This schematic is a simplification and a typical ventricular myocyte has tens of thousands of dyads [Novotová et al., 2020]. The dyad is the site for calcium-induced-calcium-release (CICR) described below.

The $[Ca^{2+}]$ in the dyad increases during phase 2 of the AP when I_{CaL} brings Ca^{2+} into the cell. The ryanodine receptors (RyRs) on the JSR detect and release Ca^{2+} in response to this local increase in $[Ca^{2+}]$, a process called CICR. The substantial increase in $[Ca^{2+}]$ in the cytosol leads to the binding of free Ca^{2+} to the thin myofilaments and the subsequent contraction of the cardiomyocyte in a process called excitation-contraction-coupling.

The increase in $[Ca^{2+}]$ begins to inactivate the LCC (Section 2.2.4), which slows the entry

of Ca^{2+} into the cell via the sarcolemma. Excess Ca^{2+} is extruded from the cell using two mechanisms in order to restore the diastolic $[Ca^{2+}]$. Firstly, intracellular Ca^{2+} is exchanged for Na^{+} in a 1:3 ratio via I_{NaCa}, the main source of Ca^{2+} extrusion from the cell. Additionally, cytoplasmic Ca^{2+} is also taken up by the SR via I_{SERCA} on the NSR which pumps in Ca^{2+} against the concentration gradient by expending energy in the form of ATP.

The efforts of this thesis are concentrated towards the study of I_{CaL} and therefore the next section explains the electrophysiology of this current.

2.2.4 The L-type calcium channel

The L-type calcium channels (LCCs) play a critical role in calcium handling by initiating CICR which ultimately leads to the contraction of the cardiac muscle. Despite this, the first recording of an ionic current carried by Ca^{2+} was not obtained until the end of 1960s [Beeler and Reuter, 1970, Bassingthwaighte and Reuter, 1972, Dolphin, 2006] which is quite late when compared to the identification of the Na^{+} and K^{+} currents [Fozzard, 2002]. Very little was known about this current for almost 20 years thereafter so it was cautiously referred to as the 'secondary inward' or 'slow inward' current. The 'L-type' designation was born out of the characteristic *long* openings and *large* unitary conductance [Nilius et al., 1985].

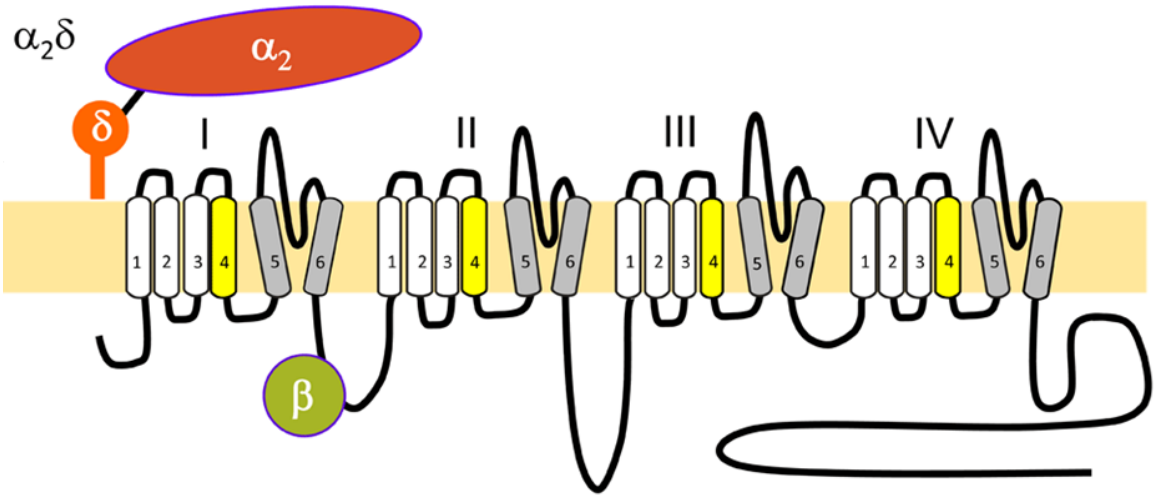

Figure 2.6: Schematic of the three subunits of the L-type calcium channel. The transmembrane subunit α_1 includes the domains marked I–IV each with six transmembrane proteins S1–S6. The remaining two subunits β and $\alpha_2\delta$ are also shown and discussed in the text.
This figure is adapted from Dolphin [2018], which was published with a CC BY licence.

The LCC is a multiprotein macromolecule complex consisting of three subunits in cardiac

cells including the principal unit α_1 and the auxiliary units β and $\alpha_2\delta$ as shown in Figure 2.6. The pore-forming subunit α_1, is responsible for the numerous functions of the LCC such as voltage sensing and ion permeation, and is the binding site for LCC antagonists such as dihydropyridines [Hofmann et al., 2014]. The major form of the α_1 subunit found in the working cardiomyocytes is $Ca_V1.2$ (encoded by the gene *CACNA1C*), whereas $Ca_V1.3$ (encoded by the gene *CACNA1D*) is predominant in pacemaker cells and neonates [Ertel et al., 2000]. The α_1 subunit of LCC is $\sim$200 kDa in weight and contains four homologous domains (I–IV), connected via cytoplasmic loops (Figure 2.6). Each domain includes six transmembrane segments (S1–S6), with a pore-forming (P) loop between S5 and S6 [Buraei and Yang, 2010, Hofmann et al., 2014]. The S1–S4 segments form the voltage sensing region, where the S4 segment specifically is positively charged and serves as the voltage sensor of the LCC. The segments S5 and S6 along with the P-loop together form the selectivity filter of the LCC for Ca^{2+}; and the four S6 helices form the activation gate [Hering et al., 2018]. Although LCCs are highly selective [up to 1000 times more than Na^+ and K^+ channels, Shorofsky and Balke, 2001] and I_{CaL} is predominantly carried by Ca^{2+}, smaller Na^+ and K^+ currents have also been measured [Hess et al., 1986] through LCCs.

The β subunit enhances the activation and inactivation of LCCs. It binds with high affinity to the α_1 subunit at a localised region in the loop connecting the homologous repeats I and II, called the α-interaction domain. Four different subfamilies of the subunit β along with several isoforms of each type are found in cardiac cells, with the predominant isoform being β_{2b} [Buraei and Yang, 2010], although some studies e.g. Weiss et al. [2015] report that β_{2a} is dominant.

The primary function of the $\alpha_2\delta$ subunit is to increase I_{CaL} by improving the trafficking of the α_1 subunit to the sarcoplasm and increasing its retention there [Dolphin, 2018]. The δ peptide anchors the larger α_2 peptide lying extracellular to the cell into place [Buraei and Yang, 2010, Klugbauer et al., 2003]. Of the four different families identified for this subunit, one of them ($\alpha_2\delta_1$) has been identified in the human heart [Dolphin, 2018].

Having described the biological components involving the LCCs, next the proposed biological mechanisms that explain the kinetics of I_{CaL} are described.

Electrophysiology of LCCs

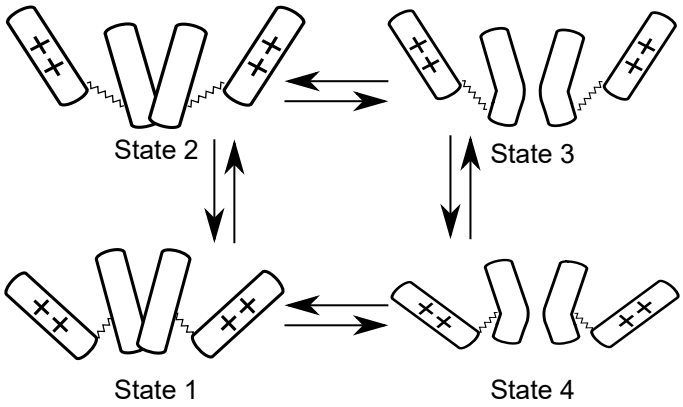

Figure 2.7: The four states involved in the activation mechanism of the L-type calcium channels as discussed in the text.

Electrically, the LCC is characterised by a fast activation occurring at sufficiently depolarised voltages (approximately $-40\,\text{mV}$), which, at the molecular level, is widely considered to be a four-state process as shown in Figure 2.7. At rest, all four voltage sensors are 'down' towards the intracellular side of the cell (state 1), and go up when the cell is depolarised (state 2), where the movement of segment S4 of domain I (and to some extent III) is considered to be the rate-limiting step [Hering et al., 2018]. This is followed by the opening of the pore so that the ions can enter the cell (state 3), and subsequent deactivation which brings back down the voltage sensor (S4) (state 4) and also closes the pore back to the resting state (state 1) [Ben-Johny et al., 2015, Flucher, 2016, Hering et al., 2018]. This activation is also shown to be modulated by the $\alpha_2\delta$ subunit [Savalli et al., 2016].

The LCCs are inactivated not just through voltage-dependent inactivation (VDI), but also via calcium-dependent inactivation (CDI). While the molecular mechanisms of both these processes have been widely studied, there is no clear indication of exactly how these inactivation work. Nevertheless, it is accepted that the inactivation gate lies in the cytoplasmic I-II linker and it is modulated using voltage-dependent and calcium-dependent processes by the β subunit at the α-interaction domain, the S6 transmembrane segments, and the C-terminal of the α_1 subunit [Findeisen and Minor Jr, 2009, Hofmann et al., 2014].

While some studies have reported that CDI is fast [20 ms to 100 ms, Kubalova, 2003, Sham et al., 1995, Stotz et al., 2004] and VDI is slow [1000 ms, Stotz et al., 2004], others have

reported both fast and slow VDI components [Lacinová, 2005]. Most experiments that have reported two different time constants of VDI have assumed current carried through a LCC by Ba^{2+} to not be inactivated by the CDI mechanisms; however, a study by Ferreira et al. [1997] showed that the fast component of the inactivation in such currents is current-dependent, implying that the CDI mechanism is not eliminated by using Ba^{2+} as a charge carrier instead of Ca^{2+}. Despite the contradictory findings, VDI is largely considered to be mediated by the movement of the I-II linker to the cytoplasmic side of the pore formed by the four S6 segments, and is modulated by the β subunit [Stotz et al., 2004] (although some studies suggest that the III-IV linker is the inactivation gate [Ames, 2021]).

CDI is considered to be dominated by the calcium-modulating protein calmodulin (CaM) which is tethered to the C-terminal of the α_1 subunit at the IQ motif (some studies also identify the I-II linker as the site of the CaM tethering [Asmara et al., 2010]). When Ca^{2+} binds to CaM, this brings about a conformational change to CaM and the resultant interactions block the channel pore via a mechanism not fully understood [Hofmann et al., 2014, Peterson et al., 1999]. The $[Ca^{2+}]$ that is hypothesised to be detected by CaM bringing about CDI is considered to be 'local' to the LCC (brief spikes in $[Ca^{2+}]$ at the channel mouth when LCC is open). Some experimental studies have also found a 'global' $[Ca^{2+}]$ (basal $[Ca^{2+}]$ between spikes dominated by diffusion from the cytosol) to affect CDI through a complex mechanism described in Tadross et al. [2008].

Having discussed the core mechanisms used to explain the kinetics of I_{CaL}, next the methods in which the kinetics of LCCs is regulated are highlighted. Ca^{2+}/calmodulin-dependent protein kinase II (CaMKII) is both regulated by $[Ca^{2+}]$, and a regulator of $[Ca^{2+}]$ via phosphorylation of both LCCs and RyRs [Maier and Bers, 2007, Winslow et al., 2016]. This co-dependence between $[Ca^{2+}]$ and CaMKII activity can create a positive feedback mechanism in which peak I_{CaL} increases when successive voltage pulses are applied, in a process called Ca^{2+}-dependent facilitation [CDF, Bers and Morotti, 2014]. In addition to CDF, following sympathetic stimulation ('fight-or-flight' response), β1-adrenergic membrane receptors are activated, which trigger intracellular processes resulting in the conversion of ATP to cyclic adenosine monophosphate (cAMP), further activating protein kinase A (PKA), which in turn phosphorylates the LCCs. This increases I_{CaL} leading to a larger Ca^{2+} influx and a larger Ca^{2+} release through CICR, which ultimately increases contractile strength [Gao

et al., 1997, van der Heyden et al., 2005]. Parasympathetic stimulation ('rest-and-digest') can reduce cAMP levels, which is known to inhibit the effects of sympathetic stimulation on I_{CaL} but appears to have little effect on the basal current [McDonald et al., 1994].

2.3 Cardiac L-type calcium current in pathophysiology

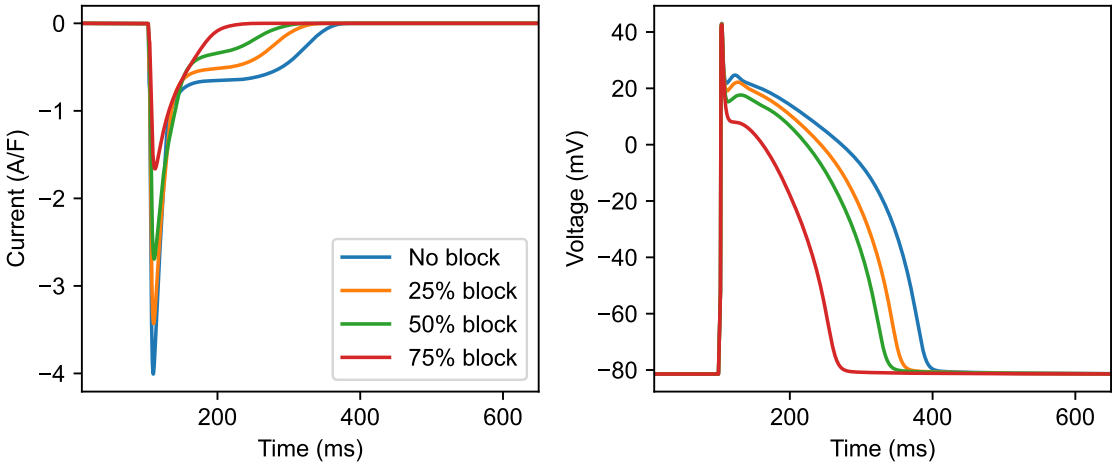

Figure 2.8: Blocking the L-type calcium current (I_{CaL}) shortens the action potential (AP) duration. **Left**: I_{CaL} and **Right**: AP during steady pacing at 1 Hz of the epicardial ventricular AP model by Grandi et al. [2010].

Given the importance of I_{CaL} in determining the AP duration (APD), as shown in Figure 2.8, it plays an important factor in both initiating, as well as treating, irregular beating of the heart (arrhythmia) [Shorofsky and Balke, 2001].

Some I_{CaL} irregularities occur congenitally. For example, in Timothy syndrome two different gain-of-function mutations on the I-II linker of $Ca_V1.2$ reduce the inactivation of the LCCs, thus enhancing APD and prolonging repolarisation [Dixon et al., 2012, Wan and Marx, 2016]. This contributes to a long QT interval which often results in mortality due to ventricular arrhythmias — in some rare cases the potentially fatal Torsade de Pointes (TdP) [Dufendach et al., 2018, Weiss et al., 2015]. On the other hand, a different congenital disease called Brugada syndrome involves a loss-of-function mutation of $Ca_V1.2$, often on the β and $\alpha_2\delta$ subunits as well. Brugada syndrome is associated with a shortened QT interval and sudden cardiac death in young adults [Sieira et al., 2016, Hofmann et al., 2014].

Abnormally high up-regulation of the channel via calcium-dependent facilitation (CDF) is also considered to be arrhythmogenic and is evidenced by observation of unusually high CaMKII levels in conditions such as heart failure [Soltis and Saucerman, 2010, Bers and Morotti, 2014].

Two important indicators of arrhythmogenesis are early-after-depolarisations (EADs) — depolarisation of the cell before it is fully repolarised (a type of triggering activity leading to abnormal impulse formation) [Charpentier et al., 1993] — and the slope of restitution curve[2] [Shattock et al., 2017]. I_{CaL} influences both of these indicators as the recovery from inactivation of I_{CaL} determines the slope of the APD restitution curve [Mahajan et al., 2008] and diminishing of the I_{CaL} 'window-current' [Hirano et al., 1992] contributes to the prevention of EAD onset [Kettlewell et al., 2019]. The reactivation of I_{CaL} within the window-current region can promote the occurrence of EADs because of the inward nature of the current [Madhvani et al., 2015, Kettlewell et al., 2019]. Thus, $Ca_V1.2$ and other subunits of the LCC have the potential of being important targets of anti-arrhythmic therapy. For example, several studies have proposed the exploration of pharmacological drugs which target I_{CaL} during its late phase so as to prevent EADs but not affect the peak I_{CaL} [Weiss et al., 2015]. Nevertheless, the use of such compounds comes with certain caveats. Their effects have to be considered not just over one ion channel, but over the entire cell because the changes in an AP are dynamically influenced by several ionic channels and pumps, and unintended pharmacological modulations of other channels can have a counter-intended effect on the overall AP [Weiss et al., 2015]. Similarly, unanticipated pharmacological regulation of I_{CaL} can lead to drug-induced arrhythmias and other adverse cardiovascular effects [it can also affect normal neuronal and endocrine function because of the prevalence of $Ca_V1.2$ in these cells in addition to cardiac cells, Striessnig et al., 2014]. Initiatives like the comprehensive *in vitro* proarrhythmia assay (CiPA) therefore take I_{CaL} into account when attempting to predict pro-arrhythmic risk [Li et al., 2019].

[2] APD typically shortens as time between APs decreases. The restitution curve is a plot of the APD against the diastolic interval [Hardy et al., 2018].

2.3.1 Comprehensive *in vitro* proarrhythmia assay

The current cardiac safety guidelines around approval of novel drugs are governed by the two regulatory guidelines established in 1990 by the International Council for Harmonisation of Technical Requirements for Pharmaceuticals for Human Use (ICH) [Vicente et al., 2018]. The ICH S7B[3] guideline recommends checking *in vitro* if the candidate drug blocks the I_{Kr} channel, and the ICH E14[4] guideline is based on investigating the QT interval. Both of the biomarkers used in the above guidelines are specific to initiation of TdP, a kind of ventricular arrhythmia. While these biomarkers are highly sensitive, they are not specific, leading to a high false positive rate which has led to the discontinuation of drugs that do not necessarily cause TdP.

The CiPA initiative was established in 2013 in response to the existing cardiac safety-assessment guidelines. The CiPA paradigm has four pillars. Firstly, it checks the effect of the candidate drug in *vitro* for multiple ion channels (e.g. I_{Kr}, I_{CaL}, I_{Na}, I_{to}). Secondly, it integrates these effects into an *in silico* cardiomyocyte model and checks for the prediction of TdP [Li et al., 2019]. Thirdly, it confirms the *in vitro* and *in silico* findings by investigating the *in vitro* effects on human induced pluripotent stem cell-derived cardiomyocytes (hiPSC-CMs[5]). Finally, it evaluates potential unanticipated effects using phase 1 ECG trials [Sager et al., 2014]. Given the crucial role of *in silico* modelling in the CiPA initiative, all ionic currents need to be modelled reliably. Modelling I_{CaL} is especially important because of the critical role it plays in the electrophysiology of the heart (see Section 2.2.4).

2.4 Mathematical modelling

Having now described the necessary biological, electrophysiological, and pathophysiological concepts needed to understand this thesis, the following sections of this chapter address the mathematical methods used in this work.

[3] https://database.ich.org/sites/default/files/S7B_Guideline.pdf
[4] https://database.ich.org/sites/default/files/E14_Guideline.pdf
[5] hiPSC-CMs have in recent years been used as a tool to model arrhythmogenic diseases. These are somatic cells which have been reprogrammed to stem cells and further differentiated into cardiomyocytes [Takahashi et al., 2007]. hiPSC-CMs have the advantage of being able to account for biological variability [Bellin et al., 2012]. However, they have certain limitations such as being representative of fetal rather than an adult cardiomyocytes [Pourrier and Fedida, 2020].

This section describes the mathematical construction of models of the action potential (AP) discussed in Section 2.2.2. Such mathematical models are critical for the *in silico* cardiac-safety assessment required for CiPA.

Individual biological entities such as the sarcolemma and ionic channels together with the ions passing through each ionic channel serve as components of an electric circuit coming together to construct the excitation signal generated by each cardiomyocyte, i.e. the AP, as shown in Figure 2.9.

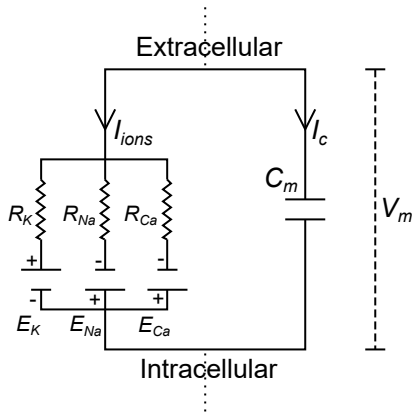

Figure 2.9: Equivalent electric circuit of a cardiomyocyte where C_m and V_m are the equivalent capacitance and voltage across the membrane respectively. The equivalent resistance and equilibrium potential across each ionic channel is given by R_X and E_X respectively. Note that for simplification this schematic only shows current through three channels.

The separation of charge across the sarcolemma gives rise to the voltage across the membrane (V_m) which serves as the energy source of the electric circuit. It is also interchangeably referred to as the *voltage difference*, *potential*, and *potential difference* and is usually measured in millivolts (mV) [Hille, 2001]. This very thin separation of the positive and negative charges causes a capacitance across the membrane (C_m), and a resulting capacitative current across the membrane (I_c). Current also flows across the membrane via the 'resistors' — ionic channels, pumps, and exchangers (transmembrane proteins).

The contribution of each individual path in the circuit (Figure 2.9) to the total V_m is given by Q_i/C_m, where Q_i is the net charge carried across the membrane. Since it is known that the total voltage across the membrane is V_m, it can be written as:

$$V_m = \frac{1}{C_m} \cdot (Q_c + Q_{ions}), \tag{2.1}$$

where Q_c and Q_{ions} are the total charge across the membrane due to capacitance and the conductance of the ionic transports/channels respectively. Next, the change in V_m with time can be calculated by differentiating Equation 2.1 with respect to time to get:

$$\frac{\mathrm{d}V_m}{\mathrm{d}t} = -\frac{1}{C_m} \cdot (I_c + I_{ions}), \tag{2.2}$$

where I_{ions} is the sum of all ionic currents flowing across the sarcolemma. Further, I_c can be neglected [but not always, Lei et al., 2020a] at no/gradual changes of V_m [Hille, 2001].

The current through each ionic channel can be written as:

$$I_X = g_X \cdot \delta, \tag{2.3}$$

where I_X is the current, g_X is the conductance (inverse of resistance) across a specific type of transmembrane protein, and δ is a 'driving term' accounting for the electrochemical forces driving the ionic movement across the channel. This force can be either linear or non-linear with respect to V_m and is modified by the electric potential that each ionic channel experiences because of the ions that pass through it. The linear driving term is Ohmic while the non-linear driving term is given by the Goldman-Hodgkin-Katz (GHK) flux equation [Goldman, 1943, Hodgkin and Katz, 1949]; the difference between the two is elaborated upon in Section 2.4.2 (as well as later in Chapter 3 in the context of I_{CaL} models).

The conductance of the ionic current given in Equation 2.3 is usually not constant, and the rates of opening/closing of the different gates in a channel change with V_m. More generally, the current for an ionic channel can be written as:

$$I_X = (\bar{g} \text{ or } \bar{P}) \cdot O \cdot \delta, \tag{2.4}$$

where the current is scaled by either the maximum possible conductance of the channel ($\bar{g}$) or a maximum permeability $\bar{P}$ with different units depending on the choice of driving force model (Chapter 3). Maximal conductance or permeability are the product of the single channel permeability and the total number of channels in the membrane [Schulz et al., 2006], which can vary over longer periods (hours to days) but are usually held constant in mathematical models. O is the fraction of open channels or the *open probability* of a

single channel that is determined by the *kinetics* of the channel and models the activation and inactivation gates which change with V_m and time. Much of the modelling effort is focused towards O, and the next section discusses the common models used to describe O.

2.4.1 Open probability

The open probability (O) of ionic channels or gating mechanism is commonly modelled using either Hodgkin-Huxley models (HHMs) or Markov models (MMs). In HHMs [Hodgkin and Huxley, 1952] the open probability is calculated as the product of several independent 'gates', e.g. one gate representing voltage-dependent activation and one representing voltage-dependent inactivation (VDI). The opening and closing of each gate is modelled using a single ordinary differential equation (ODE). If the probability of opening of a gate is d, where d can take any value between 0 and 1, then the time course of d can be represented by the ODE:

$$\frac{\mathrm{d}d}{\mathrm{d}t} = \alpha(1-d) - \beta d, \tag{2.5}$$

where t is time and α and β are rates of transition that vary with V_m. Due to the independence of gates in the HHM formulation, the total O is given by the product of all the gates of the channel.

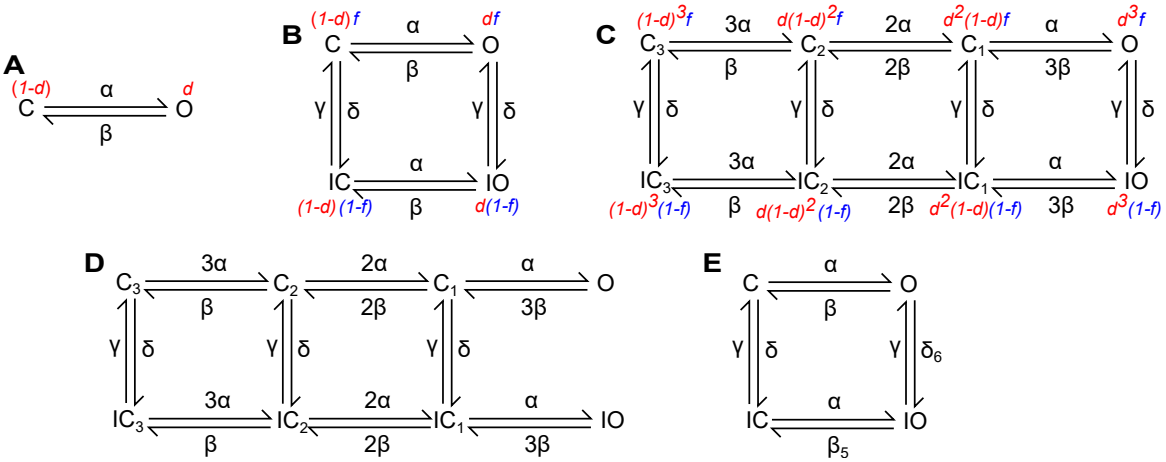

Figure 2.10: **A**, **B**, **C**, **D**, and **E** are Markov schematics. The closed — C, open — O, inactivated — I, inactivated closed — IC, and inactivated open — IO states transition from one state to the other via the voltage-dependent transition rates — α, β, γ, and δ. Equivalent Hodgkin-Huxley gates are given by d and f where applicable.

In MMs the channel is postulated to be in one of a finite number of states, and transition rates are defined between the states that can depend on V_m (as well as $[\mathrm{Ca}^{2+}]$ for LCCs). In

contrast to HHMs, where each process (activation, VDI, CDI) is independent, MMs allow a more general structure where e.g. activation and VDI are coupled [Rudy and Silva, 2006]. Therefore, all HHMs can be represented by an equivalent MM, but not all MM have a corresponding HHM.

The closed $(1-d)$ and open (d) probability of the activation gate in Equation 2.5 can be re-written as the states C and O respectively as shown in Figure 2.10A. I_{CaL} models usually have an activation (d) as well as an inactivation (f) gate, modelled using Equation 2.5. The VDI gate (f) gate additionally inactivates each state of Figure 2.10A creating an 'inactivated closed' (IC) and an 'inactivated open' (IO) state as shown in Figure 2.10B. Some ion channels may have multiple configurations in which a gate is not open. For example, there are three different closed states in Figure 2.10C. Starting from the base closed state (C_2), each transition transforms the gate to a partially open state until it is finally converted to an open state (O). In such examples, the power of each Hodgkin-Huxley gate is equal to the number of closed states for that gate (including partially open states).

Figure 2.10 shows five examples of MMs where only three schematics can be reduced to equivalent HHMs (more examples of MMS and HHMs of I_{CaL} are discussed in Chapter 3). The d and f gates can be modelled according to Equation 2.5 for A, B, and C schematics for which the total O is given by d, $d \cdot f$, and $d^3 f$ respectively. Schematics D and E on the other hand cannot be reduced to equivalent HHMs, because they have state-dependent transitions and rates.

Voltage-dependent transition rates such as α can be written as $p_1 \cdot e^{(V_m \cdot p_2)}$, where p_i are the *parameters* of the model [Beattie et al., 2018]. Previous work done in our research group has involved splitting the data collected from patch-clamp experiments (see Section 2.5.2) into *training* and *validation* data. The parameters of the proposed model can then be determined by fitting the model to the training data, and the calibrated model can then be validated by testing its predictions against data that was not used in the model fitting process — the validation data [Clerx et al., 2019a]. The optimisation algorithms used in such calibration or training processes are discussed in Appendix D (such processes are used in Chapter 7 to calibrate an I_{CaL} model).

Lastly, it is noteworthy that although CDI gates are sometimes modelled using an HHM,

they are frequently assumed to be very fast so that their ODE can be replaced by an analytic equation for their steady state [e.g. the Hill equation, Goutelle et al., 2008].

Both HHMs and MMs use ODEs which can be solved using finite difference methods described in Appendix D.

2.4.2 Driving term

The driving term (δ) is commonly modelled either via the Ohmic flux or the Goldman-Hodgkin-Katz (GHK) flux. First the GHK equation is considered.

The separation of charge across the membrane results in each chemical entity experiencing a force due to the chemical gradient as well as an electrostatic force. The net ionic flux J_X (mol $m^{-1}s^{-1}$) of any species X across a channel of length L that experiences a voltage difference V_m can be estimated from the Nernst-Planck equation:

$$J_X = -D_X \left(\frac{\partial [X]}{\partial x} + \frac{z_X F}{RT} [X] \frac{\partial \phi}{\partial x} \right), \tag{2.6}$$

where ϕ (JC^{-1}) is the electric potential, D_X (m^2s^{-1}) is the diffusion coefficient, z_X is the valency of ion X, F is Faraday's constant, R is the universal gas constant, and T is the temperature. The Nernst-Planck equation describes the motion of charged species in a fluid medium [Maex, 2013].

By assuming the electric field to be constant, $\frac{\partial \phi}{\partial x} = \frac{V_m}{L}$, Equation 2.6 can be integrated with respect to x from 0 to L to get:

$$J_X = \underbrace{\frac{D_X}{L}}_{\bar{P}_X} V_m \frac{z_X F}{RT} \left(\frac{1 - [X]_o \exp\left(-z_X V_m F / RT\right)}{1 - \exp\left(-z_X V_m F / RT\right)} \right), \tag{2.7}$$

where $[X]_o$ and $[X]_i$ are assumed to be the concentrations of X at $x = L$ and $x = 0$ respectively [Keener and Sneyd, 1998]. By re-writing D_X/L as the permeability ($\bar{P}_X$) and multiplying the above equation with $z_X F$ on both sides, J_X can be re-written as a current density I_X (Am^{-2}):

$$I_X = \bar{P}_X V_m \frac{z_X^2 F^2}{RT} \left(\frac{[X]_i - [X]_o \exp\left(-z_X V_m F / RT\right)}{1 - \exp\left(-z_X V_m F / RT\right)} \right), \tag{2.8}$$

The resulting equation (Equation 2.8) shows a non-linear dependence on voltage. Further, to account for the deviation of ionic species from ideal behaviour, the activity coefficient γ is often introduced [Hemond and Fechner, 2014]; and $[X]$ is replaced with $\gamma[X]$, to get:

$$I_X = \bar{P}_X \underbrace{V_m \frac{z_X^2 F^2}{RT} \left(\frac{\gamma_i [X]_i - \gamma_o [X]_o \exp\left(-z_X V_m F/RT\right)}{1 - \exp\left(-z_X V_m F/RT\right)} \right)}_{\delta_{\text{GHK}_X}}, \tag{2.9}$$

where δ_{GHK_X} is the GHK equation.

Interestingly, for the condition of no current in δ_{GHK_X}, the equivalent equilibrium voltage (E_X) is given by:

$$E_X = \frac{RT}{z_X F} \ln \frac{\gamma_o [X]_o}{\gamma_i [X]_i}, \tag{2.10}$$

where E_X is the V_m at which there is no net movement of the charged entity X because of balanced chemical and electrostatic forces. Equation 2.10 is the same as the Nernst equation (γ_i and γ_o are usually considered to be equal when using this equation).

The Ohmic equation ($\delta_{\text{Ohmic}} = V_m - E_X$) assumes that the driving term for any ion X is given by the difference in the membrane voltage and the equilibrium voltage of that species. Therefore, when using δ_{Ohmic}, the current varies linearly with V_m.

The use of both types of driving terms is discussed in Chapter 3 in the context of I_{CaL} models.

2.5 Experimental setup

This section describes the techniques used to measure current in the work presented in this thesis and explain the physical background of the methods adopted.

2.5.1 Experimental system: Chinese hamster ovary cells

Since the focus of this thesis is towards the modelling of I_{CaL}, in the experimental work described in Chapters 5 and 7, whole-cell patch-clamp techniques (see Section 2.5.2) are adopted to record the isolated I_{CaL}. The isolation of single proteins has been made possible because of advances in molecular cloning of genes and cell culture technology. The

isolated $Ca_V1.2$ subunit (along with auxiliary units β and $\alpha_2\delta$) from a cardiomyocyte is overexpressed in the epithelial-like Chinese hamster ovary (CHO) cells.

Morphologically, CHO cells are different from cardiomyocytes, with the prominent differences being that CHO cells are spherical [6–18 μm in diameter, Han et al., 2006] rather than cylindrical in shape, they lack the myofibrils and myofilaments that are typical of myocytes, and finally they do not have an explicit CICR mechanism via the endoplasmic reticulum. Nevertheless, some Ca^{2+}-activated Ca^{2+} release from other internal reserves of Ca^{2+} have been reported, albeit to a much lesser degree than that enacted by the sarcoplasmic reticulum [Iredale and Hill, 1993, Gamper et al., 2005].

CHO cells have been widely used as an expression system for proteins since the 1950s because they are easy to transfect with the target gene [Gamper et al., 2005]. Additionally, it is a mammalian expression system and therefore the post-translational modification of the proteins resembles humans more closely than other cell lines [Sharker and Rahman, 2021]. This is especially useful for the LCC because its $\alpha_2\delta$ units are heavily glycosylated [Hofmann et al., 2014]. Finally, CHO cells are well-suited for electrophysiological experiments because they have been reported to have very few currents endogenous to the cell and 'patch' (see Section 2.5.2) easily [Gamper et al., 2005].

For the reasons listed above, heterologous expression systems like CHO cells are useful for ion channel gating studies. However, they are ultimately different from the actual cell in which the ion channel is normally expressed (i.e. cardiomyocytes). Therefore, there may be differences in the perceived gating of an ion channel in a CHO cell as compared to a cardiomyocyte. This is especially important in the context of LCCs (overexpressed in CHO cells in Chapters 5 and 7) which are heavily modulated and regulated by proteins and kinases (see "Electrophysiology of LCCs" in Section 2.2.4).

2.5.2 Patch-clamp experiments

Electrophysiological measurements can be made from a cell using patch-clamp techniques. The voltage-clamp is a type of patch-clamp in which the voltage is fixed across the cell membrane as desired by the experimenter so that the corresponding membrane current can be recorded. This principle is depicted in the schematic in Figure 2.11 (left and centre).

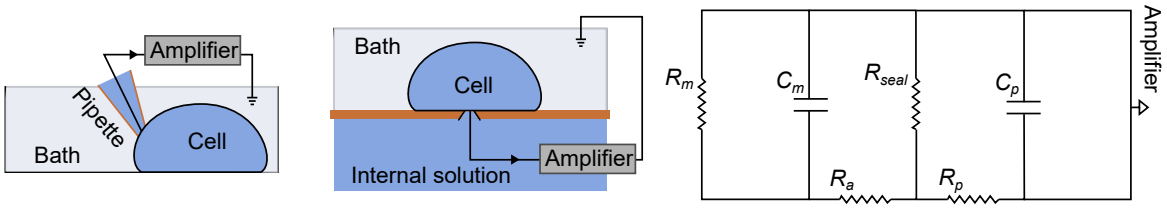

Figure 2.11: **Left**: Whole-cell patch-clamp configuration using a glass pipette. **Centre**: Whole-cell patch-clamp configuration using a planar patch. **Right**: Equivalent electric circuit for the whole-cell patch-clamp configuration where R_a, R_{seal}, and R_p are the access, seal, and pipette resistance respectively. C_p is the pipette capacitance.

The schematic in Figure 2.11 (left) represents a traditional setup where a glass pipette with a small hole of 0.5–2 μm diameter [Priel et al., 2007] is placed next to the cell membrane. A tight seal is formed between the pipette and the cell by the application of suction. After the formation of the seal, a short burst of suction (or in some cases current) is used to rupture the patch of the membrane caught within the pipette hole to create a whole-cell patch-clamp configuration. This contact of the pipette to the intracellular components of the cell along with its much larger volume allows the experimenter to control the internal composition of the cell including organic and inorganic salts; however there is a risk of 'washout' of the cytosolic factors from the pipette hole [Molleman, 2003].

The schematic in Figure 2.11 (centre) represents a planar patch which differs from the traditional setup such that the pipette is replaced by a hole on a plane from which the intracellular solution enters the cell. The initial seal between the cell and the *patch hole* is formed due to gravity. Although some cells may rupture as soon as they come in contact with the patch, all cells rupture to form the whole-cell patch-clamp configuration after the application of suction.

A low-resistance electrode within the pipette (or the patch-hole, R_p) comes in direct electrical contact with the cytoplasm of the cell while the other electrode is in the extracellular solution (commonly referred to as the bath solution). This completes an electric circuit between the intracellular and extracellular sides of the cell with the potential difference measured between them directly reflecting the membrane potential. This recorded voltage is compared against the voltage set by the experimenter using the command voltage. The difference in voltage is corrected by a compensatory current injection by the amplifier into the cell via the pipette electrode; this compensatory current is equal in magnitude to the

current passing through the membrane, but opposite in sign. The whole-cell configuration allows measurement of the total current across the membrane.

This patch-clamp setup can be represented by an equivalent electric circuit as shown in Figure 2.11 (right). The pipette entry to the cytoplasm creates a small resistance called the access resistance (R_a); this is in series with R_p, and together they are measured as the series resistance (R_s, where $R_s = R_a + R_p$). The pipette seal also creates a seal resistance (R_{seal}) in parallel to the total membrane resistance (R_m). R_{seal} should be very large to prevent the *leak* of the intracellular composition of the cell outside, as well as to prevent shorting of the electrical circuit. The total membrane potential recorded across the electrodes is distributed over the amplifier and R_s. According to Khirchhoff's voltage law, the proportion of the voltage drop across each resistance in a series circuit is directly proportional to its magnitude. Therefore, in order to ensure that the voltage drop across the membrane is accurately measured, the resistance across the amplifier probe is often more than 1000 times the pipette resistance (R_p). Nevertheless, R_p should be as small as possible to ensure the quality of the recordings. The thin glass pipette (or the patch hole) also has a separation of charge across the intracellular and extracellular solutions, thus creating a capacitance (C_p). This C_p can contribute to a delay in voltage change and is often corrected by the introduction of a 'negative' capacitor by an amplifier. Similarly, the capacitance across the membrane (C_m) also creates a delay in the voltage change determined by the time constant — R_sC_m. These can be measured by injecting a small current into the cell through the pipette and measuring the voltage deflection [Molleman, 2003].

Although the patch-clamping technique described here is performed manually, in the last few decades, automated patch-clamp machines have started replacing manual patch-clamps for electrophysiolgical recordings. In the automated setting, recordings from hundreds of cells can be taken at the same time using chip plates with multiple 'wells' using a planar patch setup. High resistance seals of the cell form holes at the bottom of each well, from where the intracellular solution enters the cell. One such high-throughput automated machine — Syncropatch 384PE platform (Nanion Technologies) — is used to make simultaneous recordings from 384 cells in a planar patch whole-cell configuration (patch-clamp recordings of Chapters 5 and 7 have been made using this machine). Each experiment uses a "chip" containing wells arranged into 16 rows (labelled from A–P) and 24 columns (la-

belled from 1–24). Each well contains a cell during the experiment and is kept in place via application of a suction which allows the intracellular solution (containing BAPTA, the Ca^{2+}-chelating buffer) to enter the cell as shown in Figure 2.11 (centre). After some time t_0 has passed since the rupturing of the cell, the voltage-clamp is applied and the Syncropatch records the current from this time onward.

2.6 Summary

The biological, electrophysiological, physical, and mathematical concepts of the heart required to understand this thesis were introduced in this chapter with an emphasis on mathematical models and patch-clamp techniques relevant for Chapters 3–7. The significance of cardiac models was highlighted in light of their importance in the safety paradigms for novel pharmaceutical compounds. While the concepts described here are in the context of the heart, many of them are directly applicable to other fields. For example, the generation of action potentials works similarly in neurons, skeletal, smooth, and other muscle cells.

This thesis focuses on the L-type calcium channel (LCC). Therefore, in this chapter, the underlying biological mechanisms of LCCs' electrophysiology were described along with their importance in the pathophysiology of the heart. In the next chapter, the different types of LCC models that have been developed over the years have been introduced and analysed.

3 | Qualitative comparison of the models of L-type calcium current

This chapter is adapted from Agrawal et al. [2022], a paper on which I am first author entitled: "Models of the cardiac L-type calcium current: a quantitative review", available at https://doi.org/10.1101/2021.10.04.462988. I led the research of this paper by screening and collecting I_{CaL} models to be included in the study, analysing individual components of the models, and subsequently designing and performing identical experiments on the models.

3.1 Introduction

In the previous chapter the importance of the L-type calcium current (I_{CaL}) in a cardiac action potential (AP) was established. Its critical role in cardiac cellular electrophysiology has led to extensive modelling efforts, and a large number of models of cardiac I_{CaL} electrophysiology have been published since the 1970s. When incorporated into models of the cardiac action potential (AP), I_{CaL} models have a long and successful history of application in fundamental electrophysiology research [Noble and Rudy, 2001]. More recently, they have been used or proposed for use in drug safety assessment [Mirams et al., 2012] and risk stratification in cohorts with ion channel mutations as part of the second pillar of the CiPA paradigm [Hoefen et al., 2012]. Choosing an I_{CaL} model for such safety-critical applications is not an easy task, as several models can be found in the literature, which vary widely in their structure and assumptions. On a more fundamental level, each model of I_{CaL} represents a testable theory of its physiology, and the existence of so many competing theories reveals both gaps in our knowledge and a need for their comparison and synthesis. This chapter represents the first major steps to facilitate a critical reassessment by the community, by collecting I_{CaL} models and analysing their qualitative differences. The next chapter provides a quantitative comparisons of the models collected in this chapter based on simulations. To begin, the common structure of the I_{CaL} models is described briefly.

The first published models of a cardiac calcium current appeared in the 1970s [Bassingth-

waighte and Reuter, 1972, McAllister et al., 1975], only a few years after the first calcium current recordings in cardiac preparations. All models assessed in this chapter can be expressed in a common form:

$$I_{CaL} = (\bar{g} \text{ or } \bar{P}) \cdot O(V_m, [Ca^{2+}], t) \cdot \delta(V_m, [Ca^{2+}]). \tag{3.1}$$

A variety of approaches taken to modelling O and δ, as well as factors not included in Equation 3.1 such as channel localisation and regulation by other variables are discussed. A reductionist approach is taken and components affecting I_{CaL} (e.g. local calcium dynamics, CaMKII signalling or β-adrenergic stimulation) are regarded as separate entities. Examples of the full equations for early [McAllister et al., 1975] and more recent models [Faber and Rudy, 2000] are given in Appendix A.1.

In this chapter (and the next) the models that have been used to describe cardiac mammalian I_{CaL} to date are identified and discussed. The process by which the models included in this chapter have been been identified is discussed followed by classifying the 73 models by their origins, the assumptions made by their authors about L-type calcium channel (LCC) localisation and the variables that regulate I_{CaL}, and the equations used for I_{CaL} gating and driving force.

3.2 Literature survey

Models of I_{CaL} were identified by searching on PubMed (in March 2021) for publications containing the term "L-type calcium channel". Since many I_{CaL} models are presented as part of a larger modelling effort, the term "cardiac cell model" was also included and lists of models such as those given in Noble et al. [2012] and Heijman [2012] were scanned. To constrain the study, only included I_{CaL} models that were presented by the authors as representing I_{CaL} from healthy human or mammalian cells were included in the study. Similarly, the focus was towards selecting basal (versus adrenergically stimulated) I_{CaL} models.

Older models of 'calcium current' and 'slow' or 'second inward' current were included if they modelled atrial, ventricular, or Purkinje cells, in which L-type is the dominant calcium current [Gaborit et al., 2007]. The models included this way were by Bassingthwaighte and

Reuter [1972], McAllister et al. [1975], Beeler and Reuter [1977], DiFrancesco and Noble [1985], Hilgemann and Noble [1987], and Noble et al. [1991]. Some older models were excluded if they modelled the sino-atrial node, in which the dominant calcium current is of the T-type [Mesirca et al., 2014]. Next, modern models were selected where the authors explicitly included an L-type calcium current.

Some studies included several model variants. The models by Pandit et al. [2001], Ten Tusscher et al. [2004], Ten Tusscher and Panfilov [2006], O'Hara et al. [2011], and Tomek et al. [2019] have epi-, endo-, or M-cell variants but the I_{CaL} kinetics are the same. In simulations where a whole-cell model was used (Chapter 4), the epicardial variant of these models was used. Similarly, the apical cell model (representing cells at the apex/tip of the ventricles) was chosen for Bondarenko et al. [2004]. The I_{CaL} kinetics varies among the different versions presented for Inada et al. [2009], Paci et al. [2013], and Varela et al. [2016], for which the atrio-nodal (a transitional region between atrium and atrioventricular node), atrial-like, and right-atrial model versions were chosen respectively.

The next selection was based on the model equations. Models were excluded from our overview if they only changed the value of conductance or permeability parameter from a previous model; models were included if they introduced new equations, made changes to equations, or changed rate or driving force parameter values. Models for which the equations were not fully given in the publication or an online addendum were also excluded in this step (9 models in total), as were models for which the equations were suspected to contain typesetting errors (1 model). Due to its historic importance, an exception was made for Bassingthwaighte and Reuter [1972] for which the published equations did not match the accompanying figures.

Applying these criteria a total of 73 distinct I_{CaL} models were found spanning over five decades of research.

3.3 Model provenance

Models are not created in isolation, but inherit ideas, equations, and parameter values from previous models. Figure 3.1 presents a tentative 'phylogeny' of I_{CaL} models, showing how

the models that are in use today were derived from one another over time. To establish these relationships, the model publications were scanned for explicit references to parent models. In some cases [e.g. Rasmusson et al., 1990] the parent models did not meet the selection criteria used in this study, which is indicated in the figure by a dashed line. In other cases [e.g. Lindblad et al., 1996, Demir et al., 1999, Bondarenko et al., 2004] the parent model was not mentioned explicitly but could be inferred from the equations.

In constructing the figure, each model was attempted to limit to a single parent. This is a simplification, and the figure should not be read as a statement on originality. For the models up to around 1995 it is likely that each model 'inherited' in some way from all other models published up to that time.

The phylogeny shows that many models have encountered species switches over the course of their development. For example, Grandi et al. [2010] (human) inherits from Shannon 2004 (rabbit), Luo-Rudy 1994 (guinea pig), and Rasmusson 1990 (bullfrog). Similarly, the histories of the O'Hara et al. [2011] and Paci et al. [2013] models also contain several species switches. Note that this does not necessarily suggest re-use of data, as models are frequently re-parameterised to new data sets. However, inheritance of parameter values (and thereby indirectly of data sources) is also very common in electrophysiology models [Niederer et al., 2009].

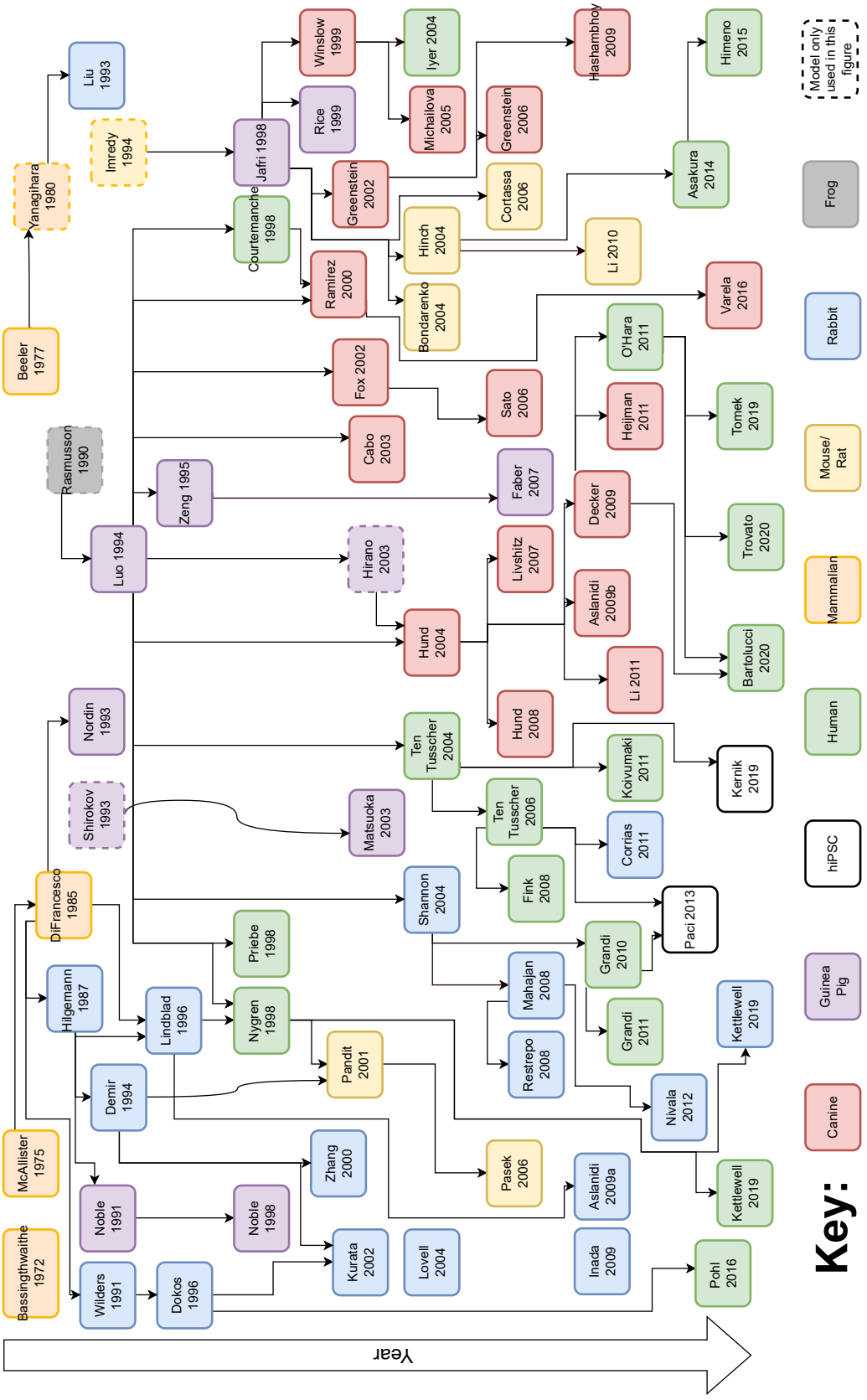

Figure 3.1: A schematic (and simplified) representation of human and mammalian I_{CaL} model development from 1972 to present. The key describes the species associated with each model.

3.4 Local calcium concentration and spatial organisation

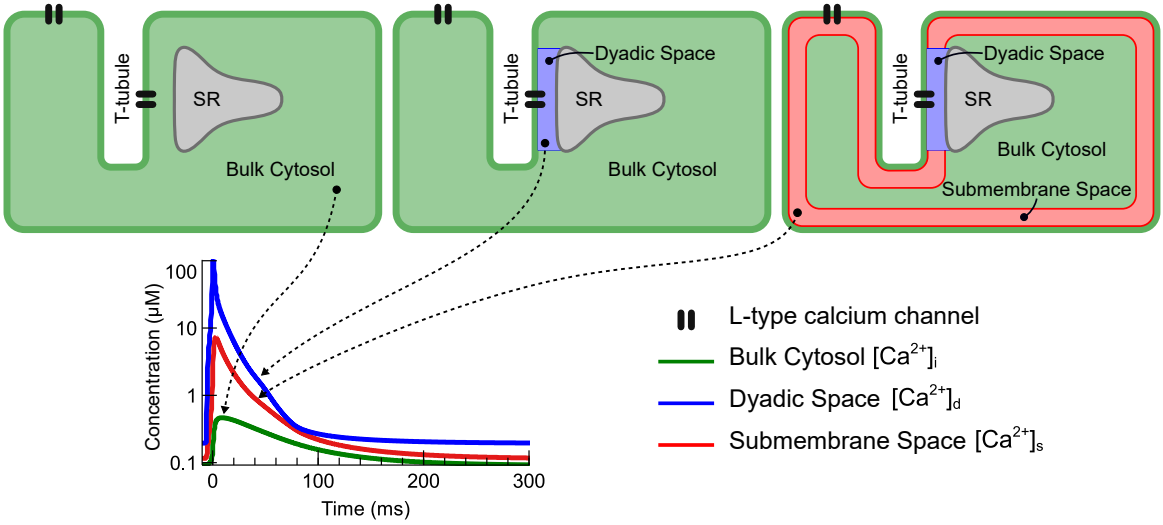

Figure 3.2: Schematic representations of a cardiomyocyte illustrating three common models of subcellular subspaces and LCC localisation. In small subspaces $[Ca^{2+}]$ can differ from the bulk cytosolic concentration by orders of magnitude, as illustrated in the lower panel which shows calcium transients from the Grandi et al. [2010] AP model stimulated at 1 Hz (note the logarithmic scale on the y-axis).

As discussed in Chapter 2, the $[Ca^{2+}]$ local to the LCC causes inactivation of the channel. $[Ca^{2+}]$ also plays an important role in calcium-induced-calcium-release (CICR) and other regulation of I_{CaL}. Therefore, several studies, both experimental and mathematical, have argued that I_{CaL}, CICR, and I_{CaL}-regulation cannot be understood without treating the Ca^{2+} concentration at the intracellular channel mouth as a separate entity from the 'global' or 'bulk' cytosolic concentration. Modellers of the cardiac AP have therefore divided the cell into smaller-volume 'subspaces' in which calcium ions, carried in by I_{CaL} or released from the SR, can cause $[Ca^{2+}]$ to transiently rise to much higher levels than those seen in the bulk cytosolic space [Colman et al., 2022]. Figure 3.2 shows three commonly used subspace configurations. In the simplest type of AP model, shown on the left, there are no subspaces and I_{CaL} flows directly into the bulk cytosol (e.g. DiFrancesco and Noble [1985]). The second type of cardiac model adds a dyadic space (Chapter 2), sometimes also called the 'junctional' or 'cleft' space. The illustration also shows LCCs connected directly to the bulk cytosol, as some cardiac models have a fraction ($\sim$10%) of I_{CaL} flowing directly into the cytosol [e.g. Tomek et al., 2019]. The third type of subspace model retains the dyadic space, but adds a 'submembrane' or 'subsarcolemmal' space just below the remainder of the cell

membrane, so that I_{CaL} flows either into the dyadic or the submembrane space. An example of this configuration, including compartment sizes and experimental references, is given in Shannon et al. [2004]. Note that there are no hard boundaries between the subspaces: calcium can diffuse freely between them, but it is assumed that the rate of diffusion is slow enough for subspace $[Ca^{2+}]$ elevations to arise. In this chapter, $[Ca^{2+}]_i$ is used to denote the bulk cytosolic concentration, $[Ca^{2+}]_s$ for the submembrane space concentration, and $[Ca^{2+}]_d$ for the dyadic space concentration.

In Figure 3.2, and in the models it represents, a single t-tubule is used to represent a vast t-tubular network, and a single dyadic space represents all (thousands of) dyads. To allow further spatial heterogeneity, some studies (particularly those interested in calcium 'sparks' arising locally within a myocyte) have gone further and discretised the cell into a 3d network of 'functional release units[1]', each with their own calcium concentration [see e.g. Rice et al., 1999, Nivala et al., 2012]. Alternative, less computationally intense, approaches have been used by e.g. Nordin [1993], who define a 'superficial, middle, and deep myoplasm', and Koivumäki et al. [2011], who modelled the myocyte as a series of concentric shells.

These different models of cell geometry and $[Ca^{2+}]$ concentrations complicate the task of comparing I_{CaL} models in an AP model. Different assumptions about channel localisation in an AP model will lead to LCCs experiencing different intracellular calcium concentrations. I_{CaL} models subsequently have different assumptions about CDI and driving force. Furthermore, since I_{CaL} gating models are often calibrated in the context of an AP model, several more parameters in the I_{CaL} model will be sensitive to the chosen localisation.

To gain an overview of how the spatial model affects the model of I_{CaL} electrophysiology, the 73 I_{CaL} models were grouped by the calcium concentrations assumed to affect I_{CaL} gating (O) and driving force (δ), leading to the twelve categories shown in Table 3.1. Note that not all models shown in this table fit neatly into the three subspace configurations shown in Figure 3.2: the studies by Asakura et al. [2014] and Himeno et al. [2015] both define an extra intermediate subspace, between dyadic and bulk cytosolic; the model by Heijman et al. [2011] has a very small subspace *within the dyadic space*, into which only I_{CaL} flows; and the models by Noble et al. [1998], Mahajan et al. [2008], and Restrepo et al. [2008]

[1] Primarily consists of the L-type calcium channels and the ryanodine receptors.

use different concentrations for the gating and driving force, which means they cannot be neatly assigned a position in Figure 3.2.

Interestingly, only the six models in rows 9 and 10 of Table 3.1 show a dependency on more than one $[Ca^{2+}]$, and in all six this arises from the assumption that there are two distinct populations of LCCs, located in separate subspaces. The models in rows 11 and 12 assume that gating depends on the $[Ca^{2+}]$ in the dyadic nanodomain near the LCCs, but that the driving force is determined by the larger space surrounding it, which is the bulk cytosol in [Noble et al., 1998] and the subsarcolemmal space in Mahajan et al. [2008] and Restrepo et al. [2008]. None of the models surveyed had the local and global components of CDI suggested by Tadross et al. [2008] in their O term.

The naming of spaces varies between studies, and sometimes overlaps or conflicts. In preparing Table 3.1 (and Figure 3.3), a subspace was classified as 'dyadic' if its primary role was in calcium handling (e.g. if it contained LCCs and connected to the SR) while the term 'submembrane' space was used only if several ion species flowed in and out of it, and it covered all or most of the (outer and t-tubular) membrane. An example where this conflicts is Sato et al. [2006], a subspace termed 'submembrane' by the authors was classified as a 'dyadic' a subspace.

3.5 Regulating variables

In addition to the membrane potential (V_m) and (local) intracellular $[Ca^{2+}]$, I_{CaL} models have been developed that are sensitive to several other variables. The most common of these is the CaMKII concentration, which is tracked in the model by Hund and Rudy [2004] and its descendants, and is used to estimate the fraction of CaMKII-phosphorylated channels in order to model CDF. The models by Matsuoka et al. [2003], Asakura et al. [2014], and Himeno et al. [2015] multiplied O by a term depending on the intracellular ATP concentration, to reproduce an effect observed by Noma and Shibasaki [1985], while the model by Michailova et al. [2005] based itself on experimental work by O'Rourke et al. [1992] showing that these effects were due to [MgATP] rather than the free ATP concentration. Parasympathetic (ACh) inhibition of I_{CaL} was included in the model by Pohl et al. [2016]. Finally, the work by Hinch et al. [2004] uses a single model to describe the L-type calcium

No.	Models	O	δ
1	Bassingthwaighte and Reuter [1972], McAllister et al. [1975], Liu et al. [1993], Demir et al. [1994], Lindblad et al. [1996], Zhang et al. [2000], Aslanidi et al. [2009a], Inada et al. [2009], and Kettlewell et al. [2019]	-	-
2	Beeler and Reuter [1977], Noble et al. [1991], and Wilders et al. [1991]	-	$[Ca^{2+}]_i$
3	Courtemanche et al. [1998], Ramirez et al. [2000], Lovell et al. [2004], and Varela et al. [2016]	$[Ca^{2+}]_i$	-
4	Kurata et al. [2002]	$[Ca^{2+}]_s$	-
5	Jafri et al. [1998], Rice et al. [1999], Nygren et al. [1998], Winslow et al. [1999], Pandit et al. [2001], Bondarenko et al. [2004], Iyer et al. [2004], Michailova et al. [2005], Cortassa et al. [2006], Pásek et al. [2006], and Koivumäki et al. [2011]	$[Ca^{2+}]_d$	-
6	DiFrancesco and Noble [1985], Hilgemann and Noble [1987], Luo and Rudy [1994a], Zeng et al. [1995], Dokos et al. [1996], Priebe and Beuckelmann [1998], Fox et al. [2002], Cabo and Boyden [2003], Matsuoka et al. [2003], Ten Tusscher et al. [2004], Paci et al. [2013], Pohl et al. [2016], and Kernik et al. [2019]	$[Ca^{2+}]_i$	$[Ca^{2+}]_i$
7	Nordin [1993], Sato et al. [2006], and Corrias et al. [2011]	$[Ca^{2+}]_s$	$[Ca^{2+}]_s$
8	Hinch et al. [2004], Hund and Rudy [2004], Greenstein and Winslow [2002], Greenstein et al. [2006], Ten Tusscher and Panfilov [2006], Faber et al. [2007], Livshitz and Rudy [2007], Fink et al. [2008], Hund et al. [2008], Aslanidi et al. [2009b], Decker et al. [2009], Hashambhoy et al. [2009], Li et al. [2010], Rovetti et al. [2010], Heijman et al. [2011], O'Hara et al. [2011], Li and Rudy [2011], Nivala et al. [2012], Bartolucci et al. [2020], and Trovato et al. [2020]	$[Ca^{2+}]_d$	$[Ca^{2+}]_d$
9	Tomek et al. [2019], Asakura et al. [2014], and Himeno et al. [2015]	$[Ca^{2+}]_i$, $[Ca^{2+}]_d$	$[Ca^{2+}]_i$, $[Ca^{2+}]_d$
10	Shannon et al. [2004], Grandi et al. [2010], and Grandi et al. [2011]	$[Ca^{2+}]_s$, $[Ca^{2+}]_d$	$[Ca^{2+}]_s$, $[Ca^{2+}]_d$
11	Noble et al. [1998]	$[Ca^{2+}]_d$	$[Ca^{2+}]_i$
12	Mahajan et al. [2008] and Restrepo et al. [2008]	$[Ca^{2+}]_d$	$[Ca^{2+}]_s$

Table 3.1: I_{CaL} models grouped according to the $[Ca^{2+}]$ they are assumed to depend on in their open probability (O) and driving force (δ). For a graphical overview, see Figure 3.3.

channels and ryanodine receptors, leading to a dependency on the state of the SR (interestingly, this model uses the $[Ca^{2+}]_i$ to estimate the concentration in the dyadic space).

Not many models surveyed in this chapter include effects of β-adrenergic stimulation on I_{CaL}, but this is partly due to our selection criteria (see Section 3.2). An overview of studies focusing specifically on β-adrenergic stimulation (which almost always included effects on I_{CaL}) is given in the supplement to Heijman et al. [2011].

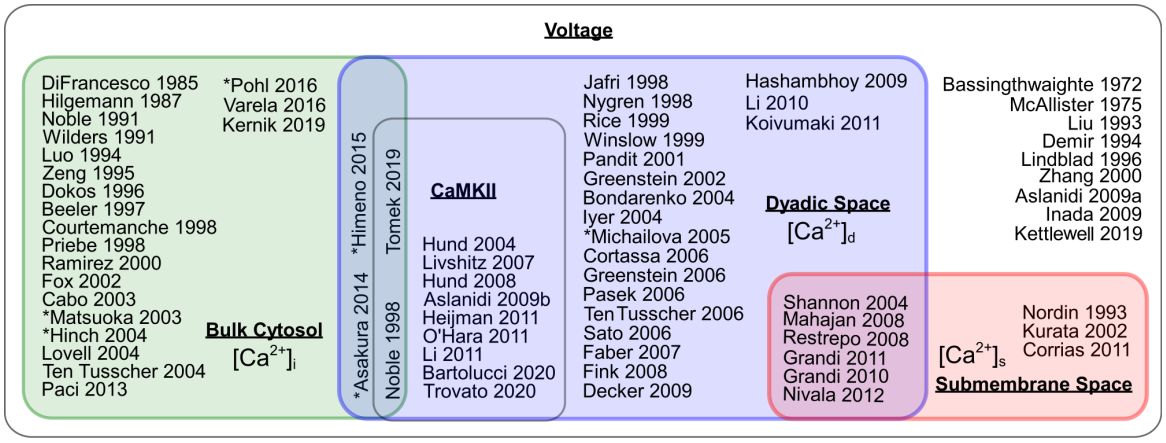

Figure 3.3: A Venn diagram showing the dependency of I_{CaL} gating and/or driving force on $[Ca^{2+}]$ and [CaMKII]. All models shown here depend on voltage. I_{CaL} models inside the green, blue, and red boxes depend on bulk cytosolic calcium, dyadic space calcium, and submembrane space calcium respectively, and models inside the black-edged central box also depend on the concentration of CaMKII. Models marked with an asterisk depend on additional variables (as described in the main text).

An overview of the dependencies of each I_{CaL} model in this study is provided in Figure 3.3.

3.6 Gating mechanisms

The feature that varies most between I_{CaL} models is the set of equations used to describe the fraction of open channels, O. This part of the model determines how the current changes over time, i.e. it describes the current kinetics or gating. This section presents a classification of I_{CaL} models into 15 distinct groups based on their gating equations.

As discussed in Chapter 2, I_{CaL} gating is commonly modelled using Hodgkin-Huxley models (HHMs), Markov models (MMs), or even the Hill equation for $[Ca^{2+}]$-dependent inactivation (CDI) gates. In the original and most common formulation, where the open probability (O) of an HHM is the product of a number of independent gates, an equivalent MM can be written for each HHM [Keener and Sneyd, 1998]. However, many I_{CaL} models use extensions to the classical Hodgkin-Huxley (HH) scheme, e.g. they introduce a non-inactivating fraction of channels [McAllister et al., 1975, see B in Figure 3.4], or model the current as if arising from two separate channel families [Nygren et al., 1998]. Such models have no obvious single MM equivalent. For examples of MM with and without an HHM counterpart and a graphical explanation of how to convert between the formalisms, see

Figure 2.10 in Chapter 2 [Rudy and Silva, 2006]. Taking these equivalences into account, 15 distinct gating models were identified, as shown schematically in Figure 3.4. Where possible, models are shown in an MM representation.

Each gating type is described briefly below. Some models define more than one copy of the same gating model but with changes in parameters or $[Ca^{2+}]$ to account for LCC localisation or phosphorylation; changes in such properties is not shown in this section, only the changes in the gating model structure.

Type A is the earliest and most straightforward gating mechanism, consisting of voltage-dependent activation (d) and inactivation (f), modelled as independent gates that are not affected by $[Ca^{2+}]$ [Bassingthwaighte and Reuter, 1972]. Wilders et al. [1991] is a unique model within this group because its time constant of inactivation is not voltage-dependent but rather depends on the fraction of inactivation f. **Type B** extends type A by adding a non-inactivating fraction of channels d', leading to an open probability $O = d \cdot f + d'$ [McAllister et al., 1975].

The **type C** gating mechanism extends type A by adding a CDI gate, usually written as f_{Ca}. In **type C1** this is modelled as an instantaneous process, so that the fraction of open f_{Ca} gates is given by a Hill equation with Hill coefficient 2 in Luo and Rudy [1994a] but 1 in the other C1-type models. **Types C2** and **C3** use an ODE to model the evolution of f_{Ca}. C2 has calcium-dependent inactivation but calcium-*in*dependent recovery [DiFrancesco and Noble, 1985], while both inactivation and recovery are calcium-dependent in C3. **Type C4** has an instantaneous f_{Ca} gate, but also incorporates calcium-sensitivity in its gate for VDI, making it a dual voltage-calcium-dependent inactivation gate.

Gating **type D** is similar to type C in its HH form, except that the activation gate d is cubed [Nordin, 1993]. In the MM structure, this equates to adding several closed states, as shown in Figure 3.4D.

An even larger Markov scheme is used by models of **type E1**, in which five steps are required to fully activate (similar to a fifth power in HH terms). In the original implementation, this model was written as a combination between an HHM (for VDI) and an MM for activation and CDI [Jafri et al., 1998]. The mechanism for CDI in this model is a switch to a 'mode Ca' in which transitions to the open state are extremely slow [Imredy and Yue,

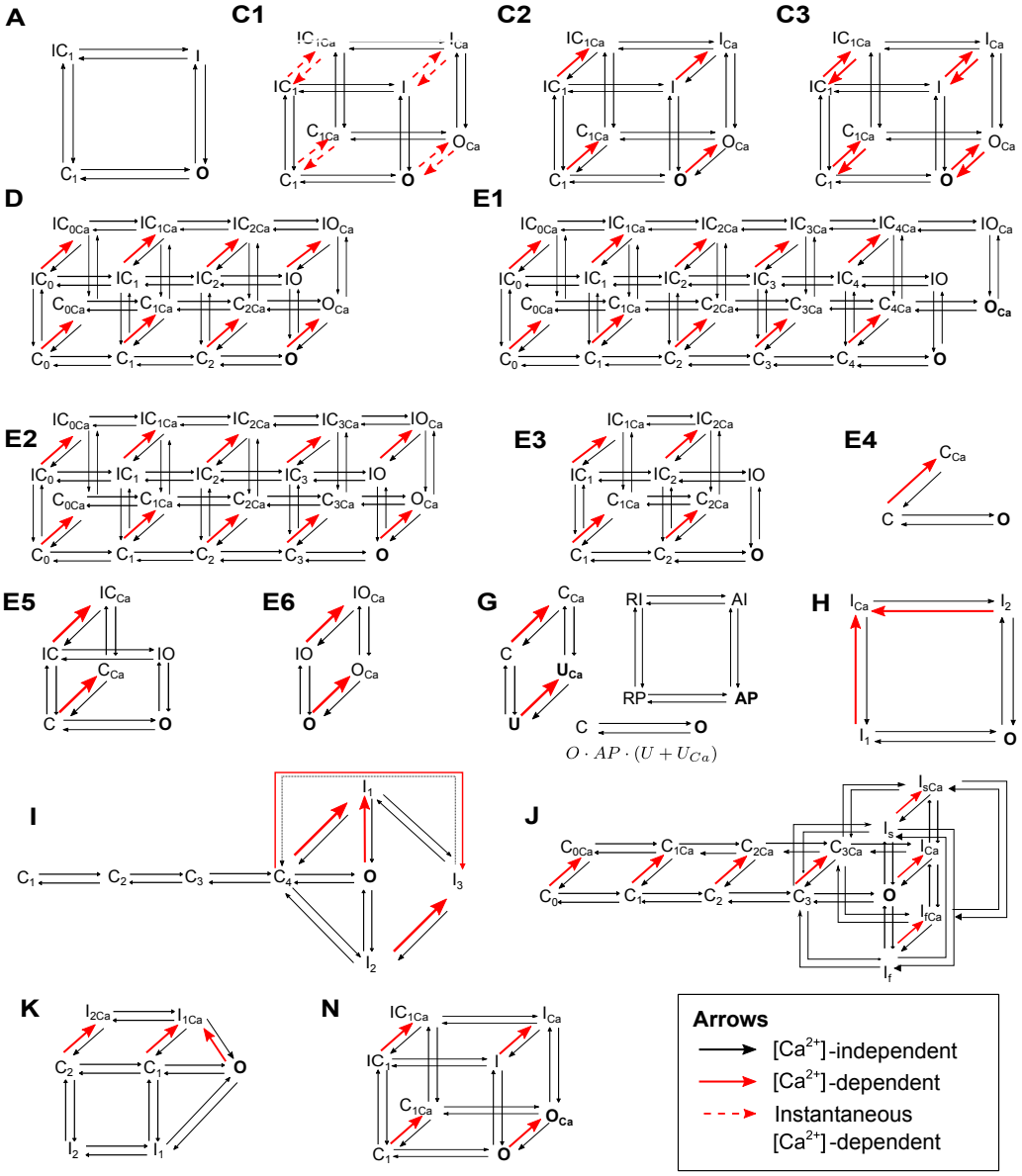

B $d \cdot f + d'$

C4 $d \cdot f(V, Ca) \cdot f_{Ca_\infty}$

F1 $d \cdot (x_{Ca,\infty} \cdot f_f + (1 - x_{Ca,\infty}) \cdot f_s)$

F2 $d \cdot (x_{Ca} \cdot f_f + (1 - x_{Ca}) \cdot f_s)$

F3 $d \cdot (x \cdot f_f + (1 - x) \cdot f_s) \cdot f_{Ca}$

F4 $d \cdot (f_f + f_s)$

L1 $d^n \cdot f_f \cdot f_s \cdot f_{Ca_f} \cdot f_{Ca_s}$

L2 $d \cdot f_f \cdot f_s \cdot f_{Ca_f} \cdot f_{Ca_s}$

L3 $d \cdot f \cdot f_{Ca_f} \cdot f_{Ca_s}$

M $d \cdot f_f \cdot f_s \cdot f_{Ca}$

O $d \cdot (1 - f_{Ca}) \cdot (x \cdot f_{1f} + (1 - x) \cdot f_{1s}) + d \cdot f_{Ca} \cdot r \cdot (y \cdot f_{2f} + (1 - y) \cdot f_{2s})$

Figure 3.4: **Models of I_{CaL} gating.** Each label in this figure (A, C1, C2, ...) indicates a distinct gating mechanism, as described in detail in the text. Where possible, models are shown in an MM representation. MM state labels include *C*losed, *I*nactivated, *O*pen, *A*ctivated, *U*ncovered, *R*esting, and *P*rimed. Subscripts *s* and *f* are used to indicate states involved in 'slow' and 'fast' transitions, while the *Ca* subscripts indicate states involved in calcium-dependent transitions. The conducting states in each Markov structure are shown in bold. Where models have more than one conducting state, the total open fraction is found by adding the occupancy of all conducting states together. The open probability equation for G is shown within the figure. In the HH equations, d and f denote activation and inactivation gates respectively, and f_{Ca} gates are calcium-dependent.

1994]. A slight variation, which is still classified as E1, is given by Iyer et al. [2004] who removed the O_{Ca} and OI_{Ca} states. Several simplifications of the E1 scheme have been proposed, reducing it from 24 to 20 states [**type E2**, Michailova et al., 2005], 10 states [**type E3**, Greenstein and Winslow, 2002], and even 3 states [**type E4**, Hinch et al., 2004]. Note that, to arrive at the representation of the E2 type shown here, the model by Michailova et al. [2005] was reinterpreted as an MM and the terms accounting for [MgATP] effects and a constant factor x were omitted. The study by Li et al. [2010] extended the E4 type by re-adding VDI, creating the 6-state **type E5**. Similarly, Asakura et al. [2014] extended E4 with a fourth state to create **type E6**.

Type F gating mechanisms again assume that I_{CaL} has fast and slow modes [citing evidence from Imredy and Yue, 1994, You et al., 1995]. In **type F1**, the fraction of channels in slow mode is determined by an instantaneous calcium binding process [Nygren et al., 1998] or fixed to a constant [Kettlewell et al., 2019], while in **type F2** this process is modelled with an ODE [Pandit et al., 2001]. Type F3 separates fast and slow kinetics from calcium by fixing the fraction of channels with fast VDI to 73% and introducing a separate CDI process [Pohl et al., 2016]. A similar two-component model but without CDI was introduced by Inada et al. [2009], which was labelled as **type F4**.

The **type G** gating mechanism [based on earlier work by Shirokov et al., 1993, for which the full equations could not be found] consists of three independent MMs for activation, VDI, and CDI [Matsuoka et al., 2003]. In the MM for CDI, the binding of a Ca^{2+} ion brings the system into a state where recovery from inactivation is much slower.

A new **type H** gating mechanism was introduced by Lovell et al. [2004], consisting of a four state MM with activation, VDI and CDI. In this model, CDI can only occur when the channel is already in a non-conducting state. More complex MMs were introduced by Bondarenko et al. [2004], Faber et al. [2007], and Mahajan et al. [2008] to create **types I**, **J**, and **K** respectively. The scheme in type I was inspired by structure-function relationships in a homology model based on *Shaker B* voltage-gated K^+ models. Type J includes a fast and a slow VDI , to reflect gating current experiments by Ferreira et al. [2003]. The type K model incorporates ideas from Soldatov [2003] and Cens et al. [2006], who argued that CDI is a voltage-dependent process that is greatly accelerated when Ca^{2+} binds to the channel

[see also Pitt et al., 2001]. Its Markov scheme is reduced by combining two open states into one, and reducing the five-state activation to a three-state process [Rose et al., 1992].

The **type L1** gating mechanism by Hund and Rudy [2004] consists of activation, fast and slow VDI, and fast and slow CDI. In this model, CDI depends on $[Ca^{2+}]_d$ but also has an I_{CaL}-dependence, to approximate the raised $[Ca^{2+}]$ at the cytosolic channel mouth [this was based on the model by Hirano and Hiraoka, 2003, for which the full equations could not be found]. The activation variable is raised to a time- and voltage-dependent power n (modelled as an ODE) which accounts for a 'fast voltage-dependent facilitation' described by Kamp et al. [2000]. In **type L2** this is simplified to use a constant $n = 1$ [Aslanidi et al., 2009b], and **type L3** simplifies this further by combining fast and slow VDI into a single gate [Hund et al., 2008]. All type L models have a fast CDI gate (f_{Ca_f}) that accounts for CDF by CaMKII-dependent phosphorylation.

The study by Ten Tusscher and Panfilov [2006] extended their previous C3 type model with an extra gate, leading to **type M**. Note that this can also be seen as a simplification of type L2.

The MM scheme for **Type N** is somewhat similar to C2, but with the important difference that it has two conducting states (so that this MM can no longer be reduced to an equivalent HHM). Like type K, this gating model is based on the idea that Ca^{2+} binding in CDI 'removes a brake' on a voltage-dependent process [Pitt et al., 2001]. This is very similar to the 'mode-switching' idea underlying E1. Heijman et al. [2011] uses a variation of this scheme, in which the rates of CDI and VDI are modulated by [CaMKII]. In addition, this model uses a second copy of the same MM structure but with modified rates to represent PKA-phosphorylated (β-adrenergically stimulated) LCCs. Another variation is used by Bartolucci et al. [2020], who borrow two state variables from the model by O'Hara et al. (called n and j in the publication, but shown as f_{Ca} and r respectively in Figure 3.4O) which are used to determine the transition rate into the 'Ca' states. As in the model by Heijman et al., two copies of the same model are maintained, but this time the phosphorylated population is CaMKII- rather than PKA-phosphorylated.

Type O gating, introduced in [O'Hara et al., 2011], splits the channels into several fractions. First, a $[Ca^{2+}]$ dependent variable (called the 'n-gate' in the original publication but f_{Ca} in

our notation) splits the channels into a fraction in 'VDI mode' and a fraction in 'CDI mode'. As in types K and N, the underlying assumption is that Ca^{2+} binding (modelled by the 'n-gate') brings the LCCs into a state where a voltage-dependent 'CDI' process can occur [Pitt et al., 2001, Kim et al., 2004]. In turn, each fraction (VDI mode and CDI mode) is split into a fast and slow fraction, with a fixed ratio (x in Figure 3.4) between fast and slow 'VDI-mode inactivation' and a voltage-dependent ratio (y in Figure 3.4) between fast and slow CDI-mode inactivation. All three type O models in this chapter include CaMKII-phosphorylation via a second copy of the model with altered rate equations.

Table 3.2 shows how each model fits into this classification. In addition to the gating type, it lists each model's cell type, species, and the simulated temperature (where stated). The final column provides an indication of the major data sources used in the model's construction. For the earlier generation of models, this data source is often hard to establish, as parameters were commonly set by hand to create a model that was acceptably close to a wide range of observations (typically measured in tissue preparations, and sometimes spanning several species). The details on how to access the full list of data sources is given in Table A.1 in Appendix A.

Table 3.2: Models classified by their gating type, with additional information of cell type, species, temperature (T) and the major data sources used in each model's construction. The equivalent MM schematic/equation for each gating class is shown in Figure 3.4. Minor variants within each class are indicated with (*) and explained in the text.

	Models	**Cell**	**Species**	**T**	**Major data sources**
A	Bassingthwaighte and Reuter [1972]	Ventricle	Mammalian		Beeler and Reuter [1970]
	Beeler and Reuter [1977]	Ventricle	Mammalian		Beeler and Reuter [1970], Reuter [1973,9], Gettes and Reuter [1974]
	Noble et al. [1991]	Ventricle	Guinea Pig	37	-
	*Wilders et al. [1991]	SAN	Rabbit	37.5	Nakayama et al. [1984], Hagiwara et al. [1988]
	Liu et al. [1993]	AVN	Rabbit	35	Liu et al. [1993]
B	McAllister et al. [1975]	Purkinje	Mammalian		Reuter [1968], Vitek and Trautwein [1971]
	Demir et al. [1994]	SAN	Rabbit	37	Nilius [1986], Hagiwara et al. [1988], Fermini and Nathan [1991]
	Lindblad et al. [1996]	Atrium	Rabbit	35	Nilius [1986], Hagiwara et al. [1988], Kawano and Hiraoka [1991]
	Zhang et al. [2000]	SAN	Rabbit	37	Nilius [1986], Hagiwara et al. [1988], Fermini and Nathan [1991], Demir et al. [1994]
	Aslanidi et al. [2009a]	Atrium	Rabbit	35	Ko et al. [2006]
C1	*Luo and Rudy [1994a]	Ventricle	Guinea Pig	37	-
	Zeng et al. [1995]	Ventricle	Guinea Pig	37	-
	Priebe and Beuckelmann [1998]	Ventricle	Human	37	Beuckelmann et al. [1991,9]
	Cabo and Boyden [2003]	Ventricle	Canine	37	Aggarwal and Boyden [1995,9]

Table 3.2 continued from previous page

	Models	Cell	Species	T	Major data Sources
C2	DiFrancesco and Noble [1985]	Purkinje	Mammalian	37	-
	Dokos et al. [1996]	SAN	Rabbit	37	Nakayama et al. [1984], Hagiwara et al. [1988], Habuchi et al. [1990], Satoh [1994]
	Shannon et al. [2004]	Ventricle	Rabbit	37	-
	Grandi et al. [2010]	Ventricle	Human	37	Pelzmann et al. [1998], Li et al. [1999], Magyar et al. [2002]
	Grandi et al. [2011]	Atrium	Human	37	Li and Nattel [1997], Shannon et al. [2005]
C3	Courtemanche et al. [1998]	Atrium	Human	37	Friedman et al. [1996], Li and Nattel [1997], Sun et al. [1997]
	Noble et al. [1998]	Ventricle	Guinea Pig	37	Linz and Meyer [1997]
	Ramirez et al. [2000]	Atrium	Canine	37	Yue et al. [1997]
	Fox et al. [2002]	Ventricle	Canine	37	-
	Kurata et al. [2002]	SAN	Rabbit	37	Nakayama et al. [1984], Hagiwara et al. [1988], Kawano and Hiraoka [1991], Fermini and Nathan [1991]
	Ten Tusscher et al. [2004]	Ventricle	Human	37	Beuckelmann et al. [1991], Bénitah et al. [1992], Mewes and Ravens [1994], Li and Nattel [1997], Sun et al. [1997], Pelzmann et al. [1998], Magyar et al. [2002]
	Sato et al. [2006]	Ventricle	Canine	35	Puglisi et al. [1999]
	Corrias et al. [2011]	Purkinje	Rabbit	37	Kass and Sanguinetti [1984], Hirano et al. [1989]
	Varela et al. [2016]	Atrium	Canine	37	Ehrlich et al. [2003]

Table 3.2 continued from previous page

	Models	Cell	Species	T	Major data Sources
	Kernik et al. [2019]		iPSC-CM	37	Ma et al. [2011], Veerman et al. [2016], Li et al. [2017]
C4	Hilgemann and Noble [1987]	Atrium	Rabbit	37	-
D	Nordin [1993]	Ventricle	Guinea Pig	37	Taniguchi et al. [1983], Egan et al. [1989], Nordin et al. [1989]
E1	Jafri et al. [1998]	Ventricle	Guinea Pig	37	McDonald et al. [1986], Hadley and Lederer [1991], Shirokov et al. [1993], Imredy and Yue [1994]
	Rice et al. [1999]	Ventricle	Guinea Pig	37	-
	Winslow et al. [1999]	Ventricle	Canine	37	Tseng et al. [1987], Kääb et al. [1996]
	Greenstein and Winslow [2002]	Ventricle	Canine	37	Tseng et al. [1987], Rose et al. [1992], Kääb et al. [1996]
	*Iyer et al. [2004]	Ventricle	Human	37	Li et al. [1999], Magyar et al. [2002]
	Cortassa et al. [2006]	Ventricle	Rat	37	-
	Hashambhoy et al. [2009]	Ventricle	Canine	37	
E2	Michailova et al. [2005]	Ventricle	Canine	37	-
E3	Greenstein et al. [2006]	Ventricle	Canine	37	-
E4	Hinch et al. [2004]	Ventricle	Rat	25	Zahradníková et al. [2004]
E5	Li et al. [2010]	Ventricle	Mouse	35	Li et al. [2010]
E6	Asakura et al. [2014]	Ventricle	Human	37	Beuckelmann et al. [1991], Mewes and Ravens [1994], Pelzmann et al. [1998], Li et al. [1999], Magyar et al. [2002]

Table 3.2 continued from previous page

	Models	Cell	Species	T	Major data Sources
	Himeno et al. [2015]	Ventricle	Human	37	Mewes and Ravens [1994], Pelzmann et al. [1998], Magyar et al. [2002]
F1	Nygren et al. [1998]	Atrium	Human	33	Escande et al. [1986], Le Grand et al. [1991], Bénitah et al. [1992], Le Grand et al. [1994], Mewes and Ravens [1994], Li and Nattel [1997]
	Kettlewell et al. [2019]	Atrium	Human	36	Kettlewell et al. [2019]
	Kettlewell et al. [2019]	Atrium	Rabbit	36	Kettlewell et al. [2019]
F2	Pandit et al. [2001]	Ventricle	Rat	22	Sun et al. [2000]
	Pásek et al. [2006]	Ventricle	Rat	22	Katsube et al. [1998]
F3	Pohl et al. [2016]	SAN	Human	37	Li and Nattel [1997]
F4	Inada et al. [2009]	AVN	Rabbit	37	-
G	Matsuoka et al. [2003]	Ventricle	Guinea Pig	37	Noma and Shibasaki [1985], Hagiwara et al. [1988], Boyett et al. [1994], Takagi et al. [1998]
H	Lovell et al. [2004]	SAN	Rabbit	37	Kodama et al. [1999]
I	Bondarenko et al. [2004]	Ventricle	Mouse	25	Bondarenko et al. [2004]
J	Faber et al. [2007]	Ventricle	Guinea Pig	37	Cavalié et al. [1986], Rose et al. [1992], Höfer et al. [1997], Vornanen and Shepherd [1997], Findlay [2002,0]
K	Mahajan et al. [2008]	Ventricle	Rabbit	35	Mahajan et al. [2008]
	Restrepo et al. [2008]	Ventricle	Rabbit	35	-
	Nivala et al. [2012]	Ventricle	Rabbit	37	-
L1	Hund and Rudy [2004]	Ventricle	Canine	37	Sun et al. [1997], Rubart et al. [2000], Kamp et al. [2000], Miyoshi et al. [2003]

Table 3.2 continued from previous page

	Models	Cell	Species	T	Major data Sources
	Livshitz and Rudy [2007]	Ventricle	Canine	37	-
L2	Aslanidi et al. [2009b]	Purkinje	Canine	35	Han et al. [2001]
	Li and Rudy [2011]	Purkinje	Canine	37	Han et al. [2001]
L3	Hund et al. [2008]	Ventricle	Canine	37	-
M	Ten Tusscher and Panfilov [2006]	Ventricle	Human	37	Magyar et al. [2002]
	Fink et al. [2008]	Ventricle	Human	37	-
	Koivumäki et al. [2011]	Atrium	Human	33	Li and Nattel [1997]
	Paci et al. [2013]	Atrium	iPSC-CM	37	Ma et al. [2011]
N	Decker et al. [2009]	Ventricle	Canine	37	Tseng [1988], Aggarwal and Boyden [1995], Rubart et al. [2000], Szabó et al. [2005]
	Heijman et al. [2011]	Ventricle	Canine	37	-
	Bartolucci et al. [2020]	Ventricle	Human	37	Magyar et al. [2002], Fülöp et al. [2004], O'Hara et al. [2011]
O	O'Hara et al. [2011]	Ventricle	Human	37	Magyar et al. [2002], Fülöp et al. [2004], O'Hara et al. [2011]
	Tomek et al. [2019]	Ventricle	Human	37	Magyar et al. [2002]
	Trovato et al. [2020]	Purkinje	Human	37	-

3.7 Driving force

Two types of driving force are common in I_{CaL} models. An Ohmic driving force for a current carried by a single species takes the form:

$$\delta_{\text{Ohmic}} = (V_m - E_{\text{rev}}), \tag{3.2}$$

where E_{rev} is the *reversal potential*, at which the current reverses direction (Section 2.4.2). For currents carried by a single species, the reversal potential can be calculated using the

Nernst equation (Equation 2.10). The units of the gas constant are frequently chosen as mJ/K/mol to yield a reversal potential in mV. A model with an Ohmic driving term is written $I = \bar{g} \cdot O \cdot (V - E_{\text{rev}})$, where $\bar{g}$ is in nano Siemens (nS) for a current in pico Amperes (pA).

A more complex model of the electrochemical driving force is given by the Goldman-Hodgkin-Katz (GHK) flux equation [Goldman, 1943, Hodgkin and Katz, 1949]:

$$\delta_{\text{GHK}} = V_m \frac{z_X^2 F^2}{RT} \left(\frac{\gamma_i [X]_i - \gamma_o [X]_o e^{-z_X V_m F/(RT)}}{1 - e^{-z_X V_m F/(RT)}} \right). \tag{3.3}$$

The GHK equation is derived from the Nernst-Planck equation and involves assuming a constant electrical field throughout the channel, therefore, the GHK equation and its derivatives are also known as 'constant field theory' [Section 2.4.2, Keener and Sneyd, 1998]. Assuming concentrations in mM $=$ mol/m^3 and using matching units for V_m and RT/F, a model with a GHK driving term is written as $I = \bar{P} \cdot O \cdot \delta_{\text{GHK}}$, where $\bar{P}$ is in L/ms ($=$ m^3/s) for a current in A, in L/(F $\cdot$ ms) for a current in A/F, or in cm/s for a current in μA/cm^2.

A number of early studies used a modified GHK equation, which accounts for the (hypothesised) presence of a charged particle near the channel mouth, causing a change, V_0, in the voltage across the channel [Frankenhaeuser, 1960]:

$$\delta_{\text{GHK'}} = (V_m - V_0) \frac{z_X^2 F^2}{RT} \left(\frac{\gamma_i [X]_i e^{V_0 \frac{z_X F}{RT}} - \gamma_o [X]_o e^{(V_m - V_0) \frac{-z_X F}{RT}}}{1 - e^{(V_m - V_0) \frac{-z_X F}{RT}}} \right). \tag{3.4}$$

So far, the current has been assumed to exclusively carried by Ca^{2+}, i.e. a perfectly selective channel. For this situation, δ_{Ohmic}, δ_{GHK}, and $\delta_{\text{GHK'}}$ all predict a current that reverses at the potential given by the Nernst equation. For typical concentrations, this would lead to a current that reverses in the range 50–150 mV, which is significantly higher than experimental estimates of 40–70 mV. If, however, the channel is assumed to be even very slightly permeable to Na^+ and K^+, then the much higher internal concentrations of those ions compared to $[Ca^{2+}]$ has a significant effect on the reversal potential.

A simple model for currents with multiple carriers can be made by assuming that each species travels through the channel without affecting the others, so that the total current is

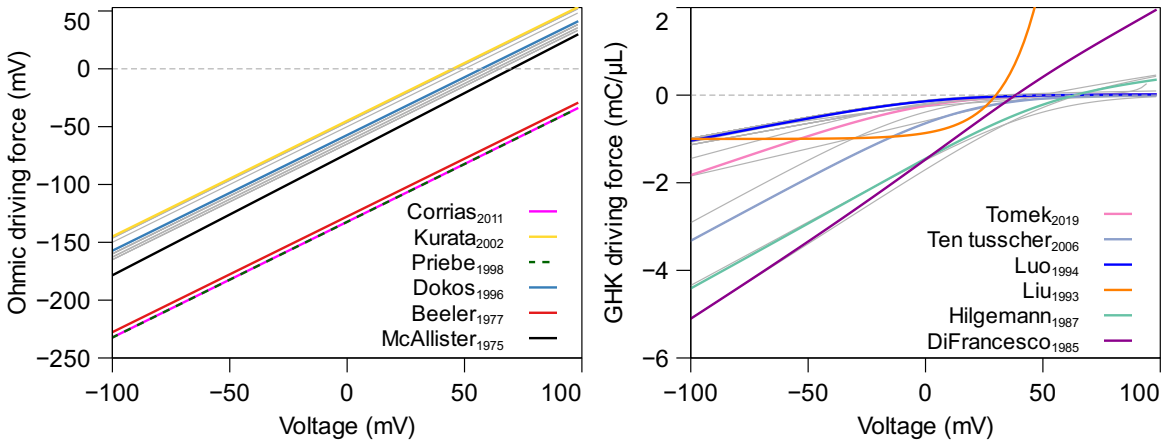

Figure 3.5: Driving term as a function of voltage for models with an Ohmic driving term (**Left**) and a (normal or modified) GHK driving term (**Right**). In the left panel, the majority of models are plotted in grey and are shown to form a tight cluster, reversing at around 60 mV. The lower and upper bounds for this cluster are marked by McAllister et al. [1975] and Kurata et al. [2002], which are indicated in colour, along with three outliers [Beeler and Reuter, 1977, Priebe and Beuckelmann, 1998, Corrias et al., 2011] that do not show a reversal potential within the physiological range. In the right panel, most currents are again shown in grey, but a selection of models are shown in colour to show the range of behaviours observable by varying the activity coefficients and voltage offset V_0 [DiFrancesco and Noble, 1985, Hilgemann and Noble, 1987, Luo and Rudy, 1994a, Hund and Rudy, 2004, Ten Tusscher and Panfilov, 2006, Tomek et al., 2019].

simply a sum of single-species currents (independent flux assumption). Equations for E_{rev} can still be derived with this assumption [see e.g. Campbell et al., 1988, Keener and Sneyd, 1998], but the predicted reversal potentials from Ohmic and GHK models are no longer the same. In both equations, the reversal potential of a multi-species current depends strongly on the ratio between the species' permeabilities $\bar{P}_X$ (or, if an Ohmic term is used, their conductances $\bar{g}_X$). A study by Campbell et al. [1988] measured the reversal potential of I_{CaL} in bull-frog atrial myocytes, and compared this to predictions using different ratios of $\bar{P}_{\text{K}} : \bar{P}_{\text{Ca}}$. They found that good agreement with experiment could be found using a GHK equation (Equation 3.3), provided the channel was highly selective to $[\text{Ca}^{2+}]$ (>95% of the I_{CaL} is carried by $[\text{Ca}^{2+}]$ at 0 mV).

To compare different models' driving terms, the internal and external concentrations were set to fixed levels, and the driving terms were plotted as a function of voltage in Figure 3.5. The concentrations used were: $[\text{Na}^+]_\text{o} = 140$ mM, $[\text{Na}^+]_\text{i} = 10$ mM, $[\text{K}^+]_\text{o} = 5$ mM, $[\text{K}^+]_\text{i} = 140$ mM, $[\text{Cl}^-]_\text{o} = 150$ mM, $[\text{Cl}^-]_\text{i} = 24$ mM, $[\text{Ca}^{2+}]_\text{o} = 2$ mM and $[\text{Ca}^{2+}]_\text{s} = [\text{Ca}^{2+}]_\text{i} = [\text{Ca}^{2+}]_\text{d} = 10^{-4}$ mM. (Note that these values may differ from the concentrations

that the models were designed for, the concentrations used in the experiments they were calibrated with, or the physiological concentrations in real cells.) In models where I_{CaL} is carried by multiple species, the 'net driving term' was calculated by summing up the contributions of each component, and weighting by the component's permeability relative to the calcium component (e.g. the calcium component has weight $\bar{P}_{Ca}/\bar{P}_{Ca} = 1$, the potassium component has weight $\bar{P}_{K}/\bar{P}_{Ca}$, etc.).

The left panel of Figure 3.5 shows δ for the models in this study that used an Ohmic driving term (models for which the full equations were not found are omitted). Rather than using the Nernst equation, most of these models set a constant reversal potential in the range of 45–70 mV. As expected, models that do use the single-species Nernst equation (without any modifications) [Priebe and Beuckelmann, 1998, Corrias et al., 2011] show a reversal potential well outside of the physiological range. The right panel in Figure 3.5 shows δ for models with a GHK (or GHK') driving term. Most of these models do not show a true reversal of current, with the driving force approaching zero for high voltages. Only models with a high permeability for sodium and potassium ions [DiFrancesco and Noble, 1985, Hilgemann and Noble, 1987] show a positive driving force for high voltages. Finally, the model by Liu et al. [1993] uses neither an Ohmic nor a GHK driving term, but an exponentially increasing flux and is shown in the right panel.

A list of models with Ohmic driving terms is given in Table 3.3. For models using a fixed E_{rev}, the numerical value is shown, while the equation used for E_{rev} is shown for the remainder. None of the models with Ohmic driving terms in this study explicitly modelled potassium or sodium components of I_{CaL} (although their existence may be implicitly acknowledged in the models with a fixed reversal potential).

A similar list for models with GHK (and GHK') driving is given in Table 3.4, along with the offset V_0 (if used), the activity coefficients for internal and external calcium, and the ratio between the permeability coefficients of potassium and sodium with respect to calcium.

The earliest studies in this table all use a voltage shift parameter $V_0 = 50$ mV, but this form is rarely seen in later models. Models with a large V_0 also assume a large contribution of sodium and potassium ions, consistent with the analysis by Campbell et al. [1988].

The model by Luo and Rudy [1994a] abandons the use of V_0 and introduces the values

$\gamma_i = 1$ and $\gamma_o = 0.341$ for the activity coefficients of internal and external calcium. These values can be calculated using the Pitzer equations [Pitzer and Mayorga, 1973], while the frequently used value $\gamma_i = 1$ appears to arise from assuming that low internal $[Ca^{2+}]$ leads to near-ideal behaviour. Instead of using constant values, the model by Tomek et al. [2019] calculates the activity coefficients using the Davies equation [Davies and Malpass, 1964], which is a precursor to Pitzer's work (although the first version of this model erroneously used a natural logarithm instead of a base-10 logarithm for the calculation, see https://bit.ly/3tqD4gP). Activity coefficients for sodium and potassium are usually taken to be 0.75 internally and externally, and are not shown in the table.

Although there is a common consensus that I_{CaL} is carried by multiple ion species, the ratio of permeabilities between the different species varies greatly between models, and several studies have cited the low permeability to potassium and sodium as a reason to omit these components from the model altogether (avoiding their impact on the reversal potential by using a fixed rather than a calculated value). Estimates of LCC selectivity have gone up over time: in general, older models assume larger contributions from sodium and potassium, while more recent models assume a much more selective channel. The high selectivity of LCCs is especially evident when comparing values from Table 3.4 to estimated selectivity ratios of other channels, e.g. $\bar{P}_{Na} : \bar{P}_K \approx 1{:}140$ for I_{Kr} [Sanguinetti et al., 1995], while $\bar{P}_K : \bar{P}_{Na}$ has been estimated as 1:10 for I_{Na} [Amin et al., 2005].

Modellers starting with Jafri et al. [1998] have attempted to incorporate evidence that monovalent permeation goes down when there is a significant Ca^{2+} influx — i.e. that the independent flux assumption does not hold. In these models, which consider only a calcium and a potassium component, the permeability to potassium is a function of the calcium driving force, so that $\bar{P}_K$ goes down when $\bar{P}_{Ca}$ is high [Jafri et al., 1998, Winslow et al., 1999, Fox et al., 2002, Iyer et al., 2004, Cortassa et al., 2006]. This is indicated with $f(V_m, \mathrm{Ca})$ in Table 3.4. Ca^{2+} influx, on the other hand, seems able to continue even when net I_{CaL} is outward [Zhou and Bers, 2000].

Finally, some of the models in Table 3.4 use a slight variation of the (normal or modified) GHK equation. The model by Jafri et al. [1998] and many of its descendants, [Rice et al., 1999, Winslow et al., 1999, Iyer et al., 2004, Michailova et al., 2005, Cortassa et al., 2006]

use a constant internal calcium activity $\gamma_i[Ca^{2+}]_i = 0.001\,\text{mM}$ [Smith, 1996]. The model by Ten Tusscher and Panfilov [2006] uses a GHK equation in which V_m is offset by $15\,\text{mV}$, but without the extra term $\left(\exp\left(V_o \frac{z_X F}{RT}\right)\right)$ used in Equation 3.4.

While some models published as recently as 2019 have assigned an Ohmic flux to I_{CaL} models, their is strong support for the GHK flux. Firstly, experiments have found evidence of rectification of I_{CaL}, implying it is much stronger in one direction than the other. In fact, even though theoretical calculations for high internal $[Ca^{2+}]$ achieved in the dyads predict a reversal of the flux carried by Ca^{2+}, this has not been observed in experiments. Secondly, the $\sim 10^5$ times concentration difference of $[Ca^{2+}]$ across the membrane, coupled with the small permeability to Na^+ and K^+ favour the use of the GHK flux equation [Hille, 2001].

Table 3.3: Reversal potentials for models using an Ohmic driving force (Equation 3.2). The final two columns provide representative E_{rev} values during the AP ('systole') and in the refractory phase ('diastole'), for models in which E_{rev} is given by an equation and for which a full AP model was available.

Models	**E_{rev} (mV)**	Sys. (mV)	Dia. (mV)
Bassingthwaighte and Reuter [1972]	42		
McAllister et al. [1975]	70		
Beeler and Reuter [1977]	$-82.3 - 13.0287 \ln \frac{[Ca^{2+}]_i}{1000\,mM}$	72	120
Demir et al. [1994]	46.4		
Lindblad et al. [1996]	60		
Dokos et al. [1996]	$-75 + \frac{RT}{2F} \ln \frac{[Ca^{2+}]_o}{[Ca^{2+}]_i}$		
Courtemanche et al. [1998]	65		
Nygren et al. [1998]	60		
Priebe and Beuckelmann [1998]	$\frac{RT}{2F} \ln \frac{[Ca^{2+}]_o}{[Ca^{2+}]_i}$	106	127
Ramirez et al. [2000]	65		
Zhang et al. [2000]	46.4		
Pandit et al. [2001]	65		
Kurata et al. [2002]	45		
Bondarenko et al. [2004]	63		
Lovell et al. [2004]	49.72		
Aslanidi et al. [2009a]	50		
Inada et al. [2009]	62.5		
Corrias et al. [2011]	$\frac{RT}{2F} \ln \frac{[Ca^{2+}]_o}{[Ca^{2+}]_i}$	86	166
Koivumäki et al. [2011]	60		
Pohl et al. [2016]	$-75 + \frac{RT}{2F} \ln \frac{[Ca^{2+}]_o}{[Ca^{2+}]_i}$		
Varela et al. [2016]	60		
Kettlewell et al. [2019] (human)	38.4		
Kettlewell et al. [2019] (rabbit)	49.5		

Table 3.4: GHK and GHK' parameters in models using GHK driving terms (Equation 3.4). Models marked with a (*) use variations of the GHK equation (as discussed in the main text).

Models	**V_o** (mV)	γ_i	γ_o	$\bar{P}_K : \bar{P}_{Ca}$	$\bar{P}_{Na} : \bar{P}_{Ca}$
DiFrancesco and Noble [1985]	50	1	1	1:100	1:100
Hilgemann and Noble [1987]	50	1	1	1:500	1:100
Noble et al. [1991]	50	1	1	1:500	1:100
Wilders et al. [1991]	50	1	1	1:100	1:100
Nordin [1993]	50.1	1	1	1:197.3	-
Luo and Rudy [1994a]	0	1	0.341	1:2798	1:800

Models	$\mathbf{V_o}$ (mV)	γ_i	γ_o	$\bar{P}_{\mathrm{K}} : \bar{P}_{\mathrm{Ca}}$	$\bar{P}_{\mathrm{Na}} : \bar{P}_{\mathrm{Ca}}$
Zeng et al. [1995]	0	1	0.341	1:2798	1:800
*Jafri et al. [1998]	0	1	0.341	$f(V, Ca)$	-
Noble et al. [1998]	50	1	1	1:500	1:500
*Rice et al. [1999]	0	1	0.341	-	-
*Winslow et al. [1999]	0	1	0.341	$f(V, Ca)$	-
Fox et al. [2002]	0	1	0.341	$f(V, Ca)$	-
Greenstein and Winslow [2002]	0	1	0.341	-	-
Cabo and Boyden [2003]	0	1	0.341	1:1554	1:444
Matsuoka et al. [2003]	0	1	1	1:2730	1:54054
Hinch et al. [2004]	0	1	1	-	-
Hund and Rudy [2004]	15	1	0.341	-	-
*Iyer et al. [2004]	0	1	0.341	$f(V, Ca)$	-
Shannon et al. [2004]	0	0.341	0.341	1:2000	1:36000
Ten Tusscher et al. [2004]	0	1	0.341	-	-
*Michailova et al. [2005]	0	1	0.341	1:540	-
*Cortassa et al. [2006]	0	1	1	$f(V, Ca)$	-
Greenstein et al. [2006]	0	1	0.341	-	-
Sato et al. [2006]	0	1	0.341	-	-
Pásek et al. [2006]	0	1	0.341	-	-
*Ten Tusscher and Panfilov [2006]	15	0.25	1	-	-
Faber et al. [2007]	0	0.01	0.341	1:2780	1:800
Livshitz and Rudy [2007]	15	0.341	0.341	-	-
*Fink et al. [2008]	15	0.25	1	-	-
Hund et al. [2008]	0	1	0.341	-	-
Mahajan et al. [2008]	0	1	0.341	-	-
Restrepo et al. [2008]	0	0.341	0.341	-	-
Aslanidi et al. [2009b]	15	1	0.341	-	-
Decker et al. [2009]	0	1	0.341	-	-
Hashambhoy et al. [2009]	0	1	0.341	-	-
Grandi et al. [2010]	0	0.341	0.341	1:2022	1:36000
Li et al. [2010]	0	1	1	-	-
Grandi et al. [2011]	0	0.341	0.341	1:2000	1:36000

Models	$\mathbf{V_o}$ (mV)	γ_i	γ_o	$\bar{P}_{\mathrm{K}} : \bar{P}_{\mathrm{Ca}}$	$\bar{P}_{\mathrm{Na}} : \bar{P}_{\mathrm{Ca}}$
Heijman et al. [2011]	0	1	0.341	-	-
Li and Rudy [2011]	15	1	0.341	-	-
O'Hara et al. [2011]	0	1	0.341	1:2798	1:800
Nivala et al. [2012]	0	1	0.341	-	-
Paci et al. [2013]	0	1	0.341	-	-
Asakura et al. [2014]	0	1	1	1:682	1:54054
Himeno et al. [2015]	0	1	1	1:2730	1:54054
Kernik et al. [2019]	0	0.341	0.341	1:2000	1:36000
Tomek et al. [2019]	0	f	f	1:2798	1:800
Bartolucci et al. [2020]	0	1.2	0.341	1:2801	1:800
Trovato et al. [2020]	0	1	0.341	1:2798	1:800

3.8 Summary

In this chapter, 73 models of mammalian I_{CaL} were collected and qualitatively compared according to several factors. These models were then classified into fifteen major gating mechanisms with a further thirteen subtypes. Similarly, the flux of the current was identified to have been modelled using different variations of the driving term — Ohmic, GHK, and modified GHK equation. This massive variation in the model components is surprising since all models are meant to represent the same biological entity. While it is possible that LCCs from different regions of the heart or from distinct species may contribute to minor differences in parameter values in the model, it is unlikely that such differences contribute to changes in the number of gating variables which implies different biological mechanisms.

Secondary factors that determine a model's behaviour, including regulating variables and assumptions about the localisation of the channel within a cell were also compared in this chapter. It was found that nearly all recently published models treat the LCC as localised in the dyadic subspace. Finally, the ancestry of I_{CaL} models was also identified.

The discrepancies in the volume of localisation and driving force were found to be small enough to be explained by the reflection of increase in biological knowledge due to advancements in experimental techniques over the years. However, the much higher variation

in the modelling of the open probability of I_{CaL} was surprising. Even models that represent the same species and region of the heart were found to have astonishing variations in how its gating mechanism works. It is unlikely that such different underlying biological mechanisms exist from one cell to another in a population (of both cells and individuals).

In the next chapter, the predictions of the I_{CaL} models collected in this chapter are compared by running simulations with conventional voltage-clamp protocols, and with protocols designed to highlight physiologically relevant I_{CaL} characteristics.

4 | Simulated comparison of models of the L-type calcium current

This chapter is adapted from Agrawal et al. [2022], a paper on which I am first author entitled: "Models of the cardiac L-type calcium current: a quantitative review", available at https://doi.org/10.1101/2021.10.04.462988. I led the research of this paper by screening and collecting I_{CaL} models to be included in the study, analysing individual components of the models, and subsequently designing and performing identical experiments on the models.

4.1 Introduction

The previous chapter provided a quantitative comparison of 73 models. Here a subset of 60 models was compared *quantitatively*, by simulating the application of several experimental protocols and comparing the *functional* differences [Cooper et al., 2011]. This is especially necessary because often new models are published in a paper format which does not allow an easy quantitative comparison with other models.

The models identified in the previous chapter but not included in this chapter for the quantitative study were excluded on two criteria. Firstly, studies that calculated the current by considering the sum of all individual LCCs stochastically were not simulated here, to ensure reproducibility of the results. These included the studies by Greenstein and Winslow [2002], Restrepo et al. [2008], Hashambhoy et al. [2009], and Nivala et al. [2012]. Secondly, models for which the gating of the I_{CaL} model was linked to the ryanodine receptors were also excluded from simulations in this chapter to study I_{CaL} in isolation. These included the studies by Hinch et al. [2004], Greenstein et al. [2006], Asakura et al. [2014], and Himeno et al. [2015].

Simulations were run using voltage-clamp protocols for activation, voltage-dependent inactivation (VDI), recovery from VDI, as well as calcium-dependent inactivation (CDI). To compare the predicted I_{CaL} during an action potential (AP), simulations were performed where either the AP (AP-clamp) or both the AP and calcium transient (CaT) (AP-CaT-

clamp) are 'clamped' to a predetermined time-course. The models were grouped according to the qualitative aspects identified earlier to test if the variability in the predictions can be reduced.

4.2 Methods

4.2.1 Ionic concentrations

Extracellular concentrations were set to $[Na^+] = 140\,\text{mM}$, $[K^+] = 5\,\text{mM}$, $[Cl^-] = 150\,\text{mM}$, and $[Ca^{2+}] = 2\,\text{mM}$, and kept constant at these values. Similarly, intracellular concentrations were fixed to $[Na^+] = 10\,\text{mM}$, $[K^+] = 140\,\text{mM}$, and $[Cl^-] = 24\,\text{mM}$ in all compartments. This corresponds to a patch-clamp setting where these concentrations are well buffered by the bath and pipette solutions. Except where stated otherwise, the intracellular Ca^{2+} concentrations ($[Ca^{2+}]_i$, $[Ca^{2+}]_d$, and $[Ca^{2+}]_s$) were fixed to 0.1 µM. These fixed concentrations allow the current kinetics to be compared in the absence of channel localisation effects (but may vary from the values for which individual models were designed); the impact of this choice will be revisited later. Variables representing $[Ca^{2+}]$ in the SR and [CaMKII] were left to vary as dictated by the model equations. However, these variables remain constant (or close to constant) when all internal $[Ca^{2+}]$ are fixed.

4.2.2 Simulation methods

As the basis for our simulations, CellML 1.0 or 1.1 files [Hedley et al., 2001] were used which contained either a single I_{CaL} model, or an I_{CaL} model embedded into a larger model of the AP. When simulating basic voltage-clamp protocols (activation, VDI, recovery, CDI) AP models were reduced to I_{CaL}-only models by fixing the values of V_m and all external and internal ionic concentrations to predetermined levels (see Sections 4.2.2 and 4.2.1). In the AP- and AP-CaT-clamp simulations, some non-I_{CaL} model features are preserved (e.g. the internal calcium and CaMKII dynamics), so that these simulations require a full AP model (see Section 4.3.4).

Where possible, model implementations were obtained from the Physiome Model Repository [PMR, Yu et al., 2011]. Thirty-five models obtained this way could be used directly,

while a further thirteen needed corrections to either units or equations. To limit the scope of this correction work, five models were reduced to I_{CaL}-only models in the process. Eight models were corrected in AP form, after which the new versions were uploaded to the PMR. A file for the model by Pásek et al. [2006] was also obtained from the PMR. This model has a separate variable for the voltage across the T-tubular membrane, distinct from the 'main' transmembrane potential. To compare the channel kinetics consistently, this model was modified manually to set this secondary voltage equal to V_m.

For eleven models no CellML files were available so new implementations were created based on published equations or code. An AP model implementation was created for Heijman et al. [2011], while CellML models containing only I_{CaL} were created for Wilders et al. [1991], Liu et al. [1993], Nordin [1993], Cabo and Boyden [2003], Cortassa et al. [2006], Sato et al. [2006], Faber et al. [2007], Hund et al. [2008], Li and Rudy [2011], Kernik et al. [2019].

This resulted in a set of 60 model files that could be used to simulate I_{CaL} in isolation, and a subset of 44 files that provided a full model of the AP.

Software

Simulations were run using the Cardiac Electrophysiology Web Lab [Cooper et al., 2016, Daly et al., 2018]. This is a resource developed to allow the characterisation and comparison of cardiac electrophysiology models in a wide range of experimental scenarios. It uses a novel protocol language that allows the user to separate the details of the mathematical model from the experimental protocol being simulated. Simulations were also performed for calcium sensitivity (see Section 4.3.3) by solving the model equations using CVODE version 3.1.2 (Appendix D) as incorporated in Myokit [Clerx et al., 2016] version 1.28.4, using Python version 3.7.3.

Model annotations and modifications

To run simulations in the Web Lab, models are encoded in CellML format and annotated with metadata terms. These terms allow variables in different models with the same physiological meaning to be identified, read out in units of choice, and manipulated. This is a useful feature for this study as the 60 models do not use consistent naming.

The following variables were annotated in all models: time, membrane potential (V_m), the total I_{CaL}, driving term (δ), and the open probability (O). When annotating driving term variables, distinct metadata terms were used for Ohmic and GHK formulations. When annotating I_{CaL} in models that split the current into multiple components (by ionic species, phosphorylated/non-phosphorylated fraction, or biological subcompartment), the variable that represents the sum over all these aspects was selected. For this purpose, a new variable was often introduced in the CellML files. Similarly, O is sometimes split into components with or without phosphorylation, δ can be split by ionic species, and both O and δ are occasionally split by the biological compartment. For all such cases, new variables O and δ were introduced and annotated as the weighted average over all these components. This weighting was made based on the fraction of phosphorylated channels, the relative permeability of each ionic species with respect to calcium, and/or the fraction of channels in each biological compartment. For example, where I_{CaL} was calculated as a linear combination of a calcium, potassium, and sodium component

$$I_{CaL} = \left(\bar{P}_{Ca}\delta_{GHK_{Ca}} + \bar{P}_{K}\delta_{GHK_{K}} + \bar{P}_{Na}\delta_{GHK_{Na}}\right) O,$$

a weighted term for a GHK driving force and current carried by three ion species was calculated as:

$$\delta_{weighted} = \delta_{GHK_{Ca}} + \frac{\bar{P}_{K}}{\bar{P}_{Ca}} \cdot \delta_{GHK_{k}} + \frac{\bar{P}_{Na}}{\bar{P}_{Ca}} \cdot \delta_{GHK_{Na}},$$

where $\delta_{GHK_{Ca}}$, $\delta_{GHK_{K}}$, and $\delta_{GHK_{Na}}$ are the driving force terms calculated for each species separately.

Finally, the variables representing intra- and extra-cellular concentrations of Ca^{2+}, Na^{+}, K^{+}, and Cl^{-} were annotated. For external concentrations, most models use a single constant-parameter but some make a distinction between a constant 'bath concentration' and a time-varying 'cleft concentration' near the cell. All three types of external concentration ('bath', 'cleft', or simply 'external') were annotated and manipulated by the Web Lab during simulation. Similarly, intracellular concentrations for bulk cytosol, submembrane space, and dyadic space concentration were annotated (and later manipulated)

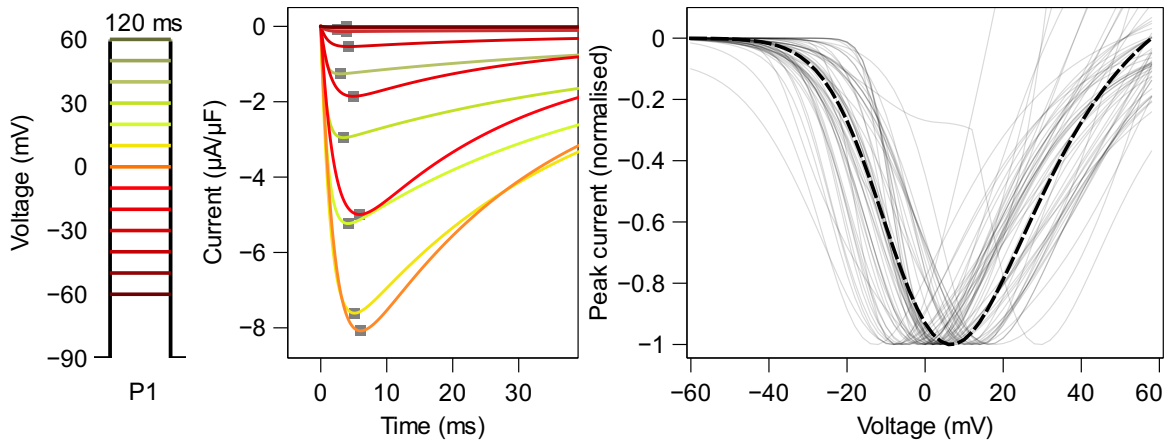

Figure 4.1: **Left**: Voltage-clamp protocol used to characterise activation (see main text for details). **Centre**: The current predicted by the Grandi et al. [2010] model, simulated with fixed internal and external concentrations and a constant level of CDI. Traces from successive sweeps are overlaid and colour-coded to match the P1 steps in the first panel. The peak I_{CaL} at each voltage step is marked with a grey square. These values are used to construct the I-V curves on the right, as shown in the animation online (see Table A.1). **Right**: Normalised peak I_{CaL} versus step voltage for 56 (out of 60) models (the direction of the current was preserved during normalisation). The black dashed line shows the I-V curve from Faber et al. [2007], which is close to the median response. The models by McAllister et al. [1975], Beeler and Reuter [1970], Liu et al. [1993], and Corrias et al. [2011] showed outlier responses, and are plotted separately in Figure 4.2.

4.3 Results

4.3.1 Voltage-dependence of activation

To show model predictions of voltage-dependence of activation, a voltage-clamp protocol was adapted from O'Hara et al. [2011]. This is a typical example of the type of protocol commonly used to study I_{CaL} activation experimentally, but there are some notable differences between these experiments and our simulation. First, the simulated voltage is set *exactly* to the values dictated by the protocol [corresponding to an ideal rather than a realistic voltage clamp, see Lei et al., 2020a]. Secondly, internal and external concentrations are held constant during the simulation (see Section 4.2.1), so that CDI is kept at a fixed (but model-dependent) level. When using AP models, this 'clamping' of voltage and concentrations also serves to remove all interaction with other ionic currents, so that this is a simulation of I_{CaL} in isolation.

The activation protocol consists of repeating units called *sweeps*. Each sweep starts with a

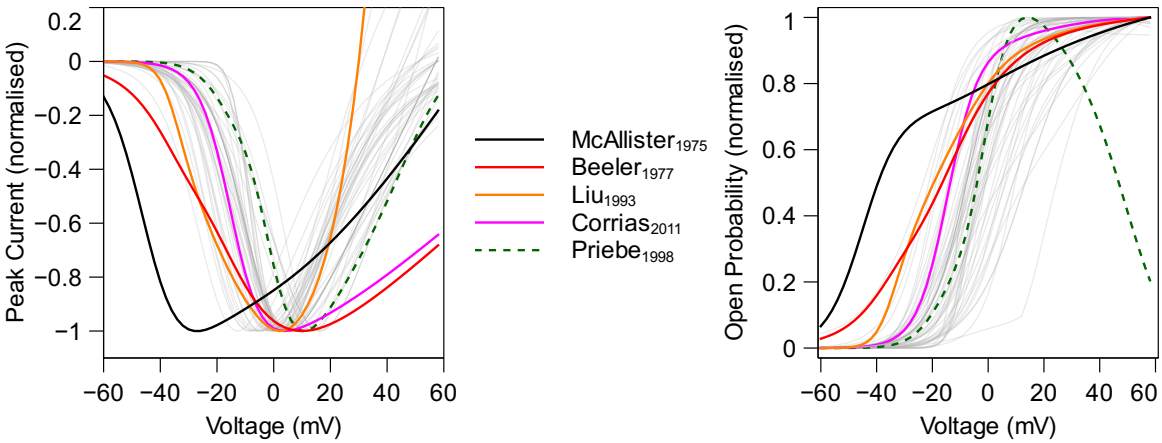

Figure 4.2: **Left**: I-V curve and **Right**: Normalised peak open probability plotted against test potential for all 60 models. The 4 outliers and the model by Priebe and Beuckelmann [1998] are highlighted in colour and discussed in the main text; the others are shown in grey.

20 s segment where V_m is kept at the *holding potential* of -90 mV, followed by a 120 ms step to the *test potential*, denoted by P1 in Figure 4.1 (left). The test potential P1 is -60 mV for the first sweep and increases by 2 mV per sweep up to $+60$ mV in the final sweep (for clarity, only a subset of these fine-increment sweeps is shown in the figure). In our simulations, current was recorded during P1 to measure the peak I_{CaL} (denoted I) at each sweep (Figure 4.1, centre) which was then normalised as $\bar{I} = I/|\min I|$. Next, the normalised peak current, $\bar{I}$, was plotted against the test potential for all models, leading to the normalised I-V curves shown in Figure 4.1 (right). The midpoint of activation ($V_{0.5}$) for each model was also calculated by finding the point where the normalised I-V curve first crosses -0.5.

Most I_{CaL} models predict that channels begin to activate at membrane voltages around -40 mV and that I_{CaL} reaches its maximum magnitude between -20 to $+20$ mV. The $V_{0.5}$ varies between -48 to $+15.3$ mV for the models in this study while the median $V_{0.5}$ is -13.5 mV. By comparison, examples from the experimental (patch-clamp) literature show that LCCs start to activate at around -40 mV, that peak I_{CaL} is observed between about -5 to 10 mV, and that $V_{0.5}$ lies between -25 to -10 mV [Pelzmann et al., 1998, Van Wagoner et al., 1999, Magyar et al., 2000].

Figure 4.2 shows a closer view of the outlier models not included in Figure 4.1. The left panel shows the I-V curve for all 60 models, including outliers which are highlighted in colour. This includes the two oldest models in our quantitative review [McAllister et al.,

1975, Beeler and Reuter, 1977], both of which are based on tissue rather than isolated-cell measurements and so a difference in their activation kinetics is not surprising. However, some more interesting effects are observed when the currents are dissected into open probability and driving force, as is done in the right panel which shows *normalised* open probability versus voltage (defined as $\bar{\mathrm{O}} = \mathrm{O}/|\max \mathrm{O}|$). Of the 4 outliers, only the McAllister et al. [1975] model has an unusual O-V curve, causing peak $\mathrm{I_{CaL}}$ to be reached at a lower voltage than other models. The models by Beeler and Reuter [1977], and Corrias et al. [2011] have more typical O-V curves, but exhibit unusually large currents at higher voltages (left panel) due to their unusually large driving force (see Figure 3.5 and Table 3.3). Interestingly, the model by Priebe and Beuckelmann [1998] has a similar driving term (Figure 3.5), but this is compensated by an outlier O-V curve, leading to a regular I-V curve (Figure 4.2, but see also Figure 4.11). Finally, the model by Liu et al. [1993] has an unusual I-V curve not due to its O-V curve but due to its exponentially increasing driving term. This dissection of $\mathrm{I_{CaL}}$ into O and δ shows how irregularities in one aspect of a model (e.g. O) can sometimes be compensated by irregularities in another (e.g. δ).

4.3.2 Voltage-dependent inactivation

Next, voltage-dependent inactivation (VDI) is illustrated using simulations with a protocol adapted from Magyar et al. [2000], shown in Figure 4.3 (left). As with activation, predictions are shown for ideal voltage clamp and perfectly buffered ionic concentrations leading to a fixed but model-dependent level of CDI, so that there are important caveats when comparing these simulations to experimental data. Each sweep in the protocol starts with 20 s at a holding potential of -90 mV, followed by a 500 ms step (P1) to a variable *conditioning potential* and a 120 ms step (P2) to a fixed *test potential* of 0 mV. The conditioning potential at P1 is -90 mV for the first sweep and increases by 2 mV per sweep up to 30 mV for the final sweep (a subset of which is shown in the figure). Current was recorded during P2 to measure peak current (I, Figure 4.3, centre), which was normalised ($\bar{\mathrm{I}} = \mathrm{I}/\min \mathrm{I}$) and plotted against conditioning potential to construct the I-V curves shown in Figure 4.3 (right).

This figure shows that most models predict inactivation to set in at around -60 mV or greater. The conditioning potential after which the peak $\mathrm{I_{CaL}}$ is halved ($\mathrm{V_{0.5}}$) varied be-

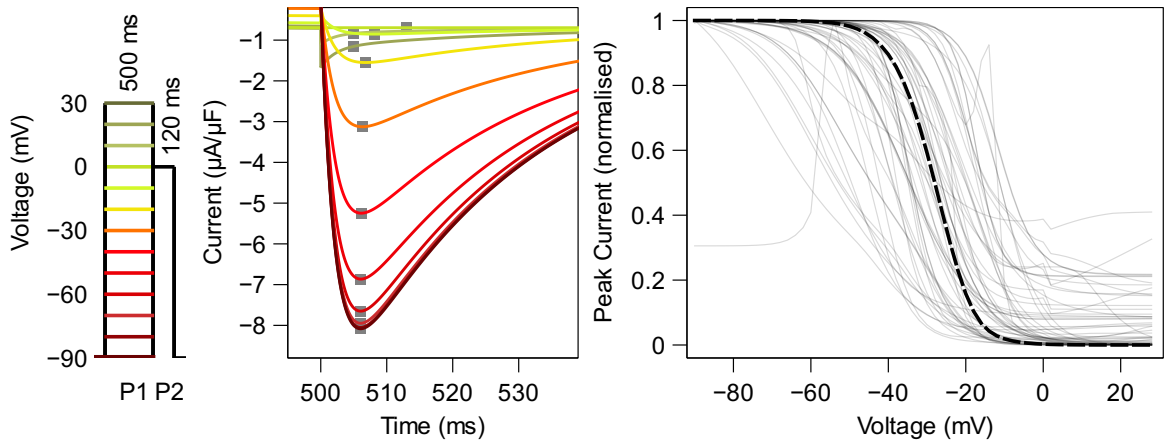

Figure 4.3: **Left**: Voltage-clamp protocol used to characterise voltage-dependent inactivation (see main text for details). **Centre**: Current response during P2 as predicted by the Grandi et al. [2010] model, with constant ionic concentrations and a fixed level of CDI. Traces from successive sweeps are overlaid and colour-coded to match the P1 steps in the left panel. The peak I_{CaL} at each voltage step (marked with grey squares) is used to construct the I-V curves on the right, as shown in an animation (see Table A.1). **Right**: Normalised peak I_{CaL} versus step voltage curve for 60 models. The I-V curve from Kurata et al. [2002], which is close to the median response over all models, is highlighted with a black dashed line.

tween -59.3 to $+10$ mV for the models in this study while the median $V_{0.5}$ was -29.9 mV. By comparison, examples from ventricular cells at physiological temperature show LCCs beginning to inactivate after a conditioning voltage of around -60 mV, with $V_{0.5}$ lying between -30 and -24 mV [Li et al., 1999, Kim et al., 2016].

Time-course of recovery

Model predictions of the time I_{CaL} takes to recover from inactivation are shown using a protocol adapted from Fülöp et al. [2004] (Figure 4.4, left). Each sweep in this protocol starts with 10 s at a holding potential of -90 mV, followed by a 500 ms step (P1) to a conditioning potential of 0 mV. The potential is then set back to -90 mV for a duration that varies from sweep to sweep, followed by a 120 ms second step (P2) to 0 mV. The interval duration is 10 ms for the first sweep and increases by 10 ms per sweep up to 50 ms, after which it increases by 25 ms per sweep up to 1000 ms (a subset of which are shown in the figure).

Peak I_{CaL} was recorded during P1 ($I_{conditioning}$) and P2 (I_{test}) for all sweeps (Figure 4.4, centre). This was normalised as $\bar{I} = I_{conditioning}/I_{test}$ and the normalised peak I_{CaL} ($\bar{I}$) was

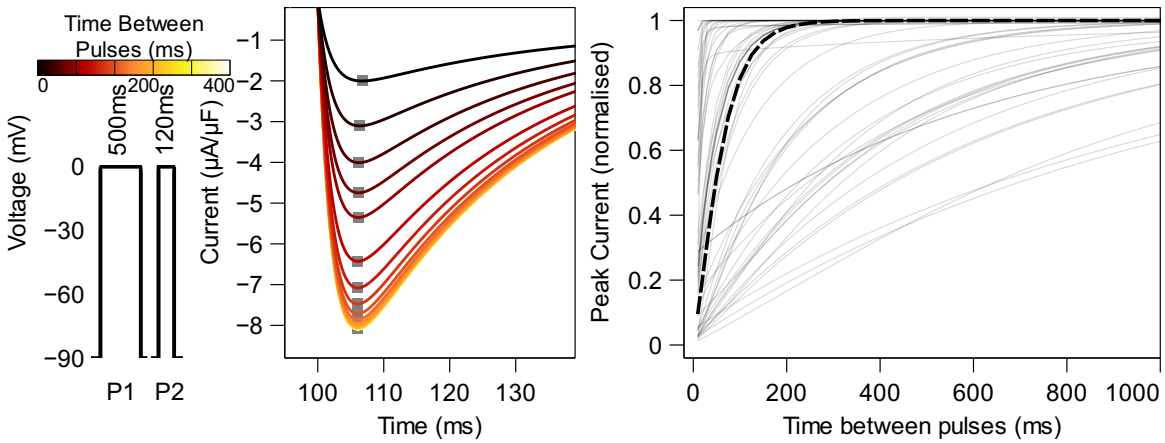

Figure 4.4: **Left**: Voltage-clamp protocol to characterise recovery from inactivation, with a variable time interval between P1 and P2 of 10, 20, 30, 40, 50 ms and increment steps of 25 ms thereafter until 1000 ms (see main text for details). **Centre**: Example of I_{CaL} predictions (constant $[Ca^{2+}]$) during P2, from the model by Grandi et al. [2010]. The colours of each line match the colour shown above the interval length in the left panel. Traces from successive sweeps are overlaid and the peak I_{CaL} is marked at each sweep. This is then used to construct the curves on the right, as shown in an animation (see Table A.1). **Right**: Normalised peak I_{CaL} versus time curves for all 60 models. The prediction from Fink et al. [2008] is close to the median response across all models and is highlighted with a black dashed line.

plotted against interval length to construct the current-time curves shown in Figure 4.4 (right).

An exponential function $1 - \exp(-t/\tau)$ was fitted to each model's current-time curve to yield the time constant of recovery from inactivation τ. This τ varies between 1.4 to 995.7 ms for the models in this study while the median τ is 49.2 ms. This is much faster than examples from ventricular cells at physiological temperature, in which τ ranged from 50 to 700 ms [Li et al., 1999, Kim et al., 2016].

4.3.3 Calcium-dependent inactivation

To study the effects of calcium-dependent inactivation (CDI), the inactivation protocol of Figure 4.3 was repeated at constant internal (bulk, dyadic, and submembrane) $[Ca^{2+}]$ of 1 pM 0.1 μM, and 300 μM. The lowest value represents a situation with near to no $[Ca^{2+}]$, while the other two values represent the normal range of calcium concentrations in the dyadic space during an AP [Fearnley et al., 2011]. Post-processing proceeded similarly to before: peak I_{CaL} was identified at each sweep, but normalisation was performed using the

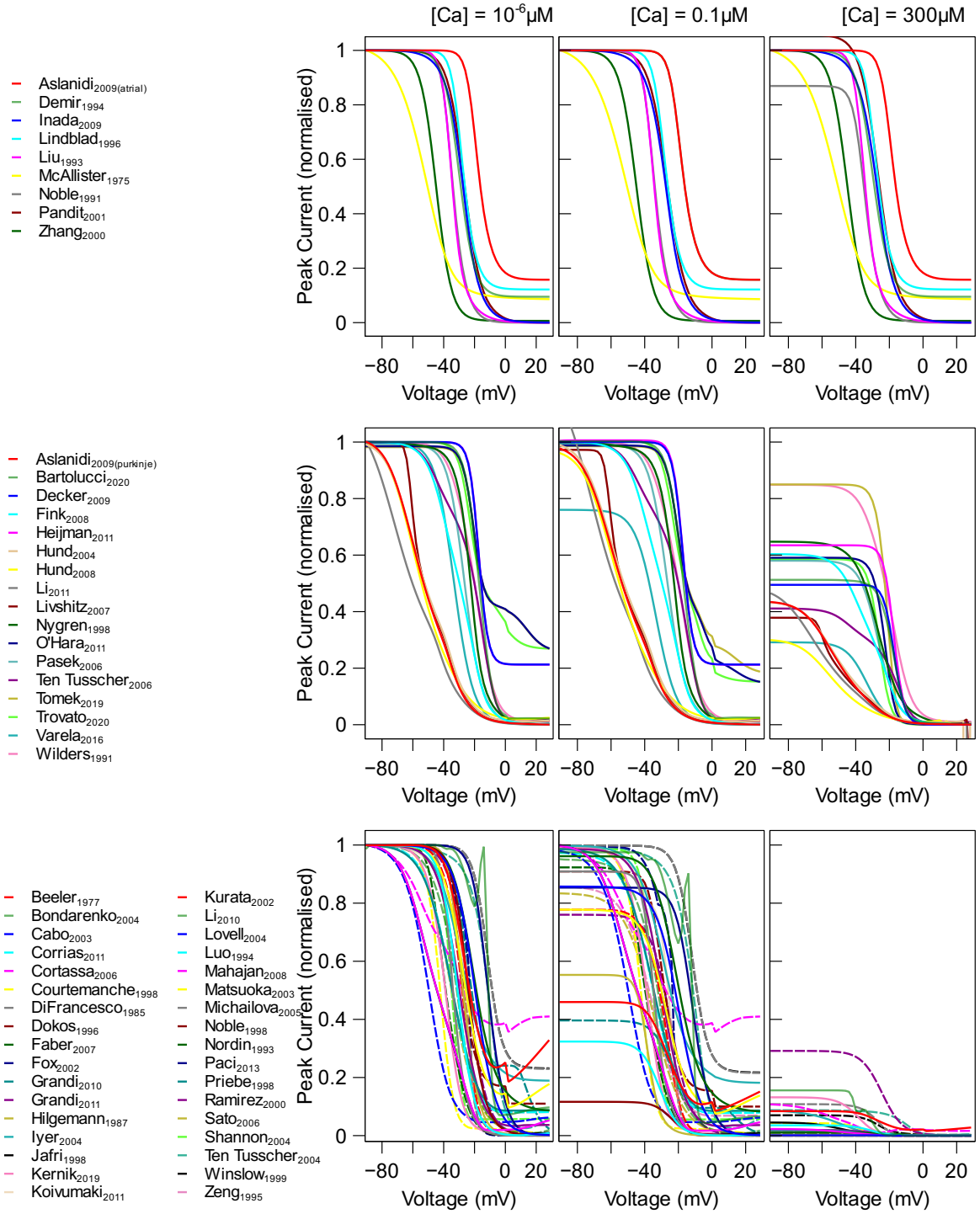

Figure 4.5: The inactivation protocol of Figure 4.3, for an internal $[Ca^{2+}]$ of 1 pM (**Left**), 0.1 µM (**Centre**), and 300 µM (**Right**). Results are grouped into three categories based on their sensitivity to $[Ca^{2+}]$: insensitive or weakly sensitive (**Top**, 9 models); mildly sensitive (**Middle**, 17 models); and strongly sensitive (**Bottom**, 34 models).

maximum peak I_{CaL} measured at 1 pM, so that the magnitude of the low, moderate, and high $[Ca^{2+}]$ curves can be compared.

Figure 4.5 shows the resulting I-V curves for the three experimental conditions. For ease of presentation, results have been split into three categories: insensitive or weakly sensitive to $[Ca^{2+}]$; mildly sensitive; and strongly sensitive to $[Ca^{2+}]$. To assign a model to a sensitivity class, a 'root mean squared difference' measure was defined between the I-V curves for extreme concentrations as:

$$\text{RMSD} = \sqrt{\frac{1}{n}\sum_{i=1}^{n}\left(\bar{I}_{\text{high Ca}_i} - \bar{I}_{\text{low Ca}_i}\right)^2}, \tag{4.1}$$

where n is the number of points in each I-V curve. A model was classified as weakly sensitive if RMSD < 0.1 (9 models), mildly sensitive if $0.1 \leq$ RMSD ≤ 0.5 (17 models), and strongly sensitive if RMSD > 0.5 (34 models). Of the 9 models in the lowest sensitivity category, only Noble et al. [1991] and Pandit et al. [2001] account for $[Ca^{2+}]$ in their equations at all; the remaining 7 have no $[Ca^{2+}]$ terms in either O or δ (see Table 3.1, Row 1).

$[Ca^{2+}]$ sensitivity and localisation

To further investigate the differences in predicted sensitivity to $[Ca^{2+}]$ a simple protocol was used which consisted of a -90 mV holding potential and a single brief step to 0 mV (i.e. the first sweep shown in Figure 4.3). Starting from an internal (bulk, dyadic, and submembrane) $[Ca^{2+}]$ of 1 pM (i.e. almost no Ca^{2+}), the experiments were repeated with increasing concentrations until a 50% drop in the peak I_{CaL} was observed. Note that each repeat was started from the same initial conditions: no build-up of CDI (or CDF) occurred between repeats. The resulting concentration was termed the CDI_{50} $[Ca^{2+}]$.

Using this procedure, the CDI_{50} $[Ca^{2+}]$ was obtained for 49 out of the 51 mildly and strongly $[Ca^{2+}]$ sensitive models, as shown in Figure 4.6. The models by Wilders et al. [1991] and Nygren et al. [1998] did not produce a 50% drop at any of the tested levels. The calculated CDI_{50} is shown in Figure 4.6 (left) and varies across different models from 0.16 µM (10^{th} percentile) to 338 µM (90^{th} percentile) while the median CDI_{50} is 83.6 µM.

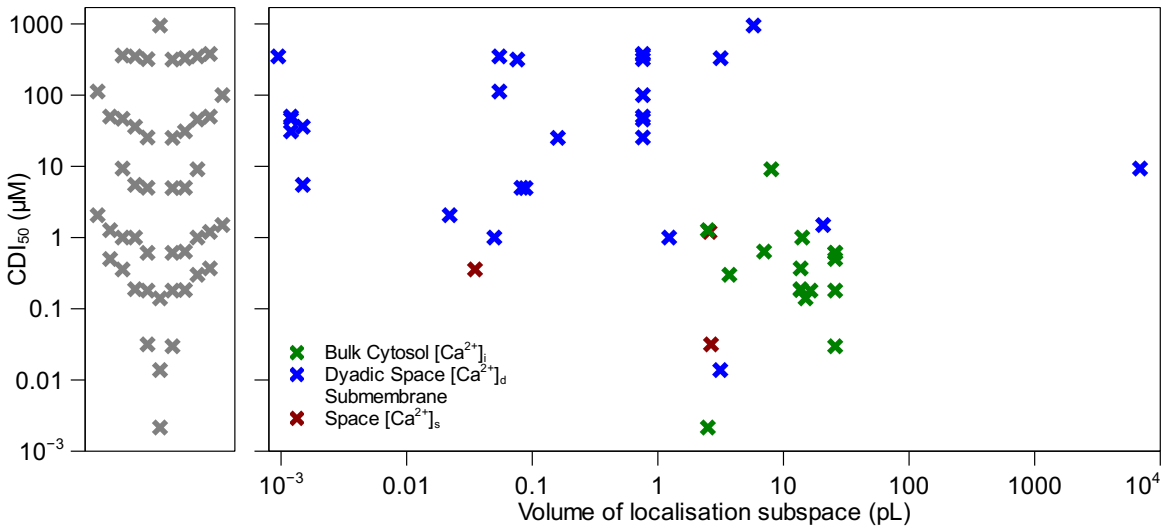

Figure 4.6: **Left**: CDI_{50} for 47 out of the 49 mildly or strongly $[Ca^{2+}]$ sensitive models (see main text for details). **Right**: CDI_{50} plotted against the volume of the subspace assumed to contain the LCCs, for the 47 models. Colours indicate the subspace containing the channels, or the subspace containing the majority of channels in situations where LCCs are assigned to multiple spaces.

In a more realistic situation, where $[Ca^{2+}]$ is not held constant throughout the cell, Ca^{2+} flowing into a subspace will induce a change in local $[Ca^{2+}]$ with a rate that depends inversely on the subspace volume V_{local} (assuming there is no buffering or diffusion of Ca^{2+}). Therefore models in which I_{CaL} flows into large subspaces may expect to compensate for the slower local $[Ca^{2+}]$-change with a more sensitive CDI, and vice versa. This is explored in Figure 4.6 (right), in which the CDI_{50} concentration is plotted against V_{local}. For models in which LCCs are present in multiple biological subspaces, the volume was calculated as a weighted average: For example, 80% of the LCCs in the model by Tomek et al. [2019] lie in the dyadic space, whereas only 20% lie in the submembrane space, leading to a weighted average volume $V_{\text{local}} = 0.8V_d + 0.2V_s$. The models by Beeler and Reuter [1977] and Mahajan et al. [2008] were omitted as the volume of their localisation space could not be determined from the manuscripts.

Figure 4.6 (right) shows a weak correlation between the predicted CDI_{50} and the corresponding V_{local}, suggesting that modelled CDI is to some limited extent influenced by the size of the compartment that I_{CaL} flows into. This is another example where one aspect of the model compensates for another.

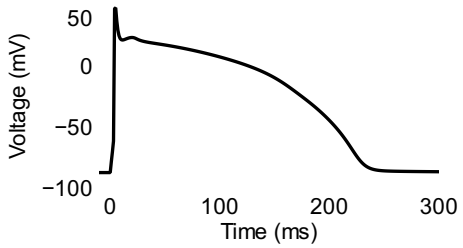

Figure 4.7: The AP waveform used in AP- and AP-CaT-clamp simulations in Figures 4.8–4.10. This action potential was derived from a 1 Hz simulation of the model by Grandi et al. [2010].

4.3.4 AP and AP-CaT clamp predictions

The experiments simulated so far use voltage-step protocols which bring out a wide range of I_{CaL} kinetics but are very different from the voltage signals experienced by LCCs *in situ*. The final aspect reviewed is the models' prediction of the I_{CaL} current elicited by a predefined AP. As before, an idealised voltage-clamp was simulated, but this time the internal $[Ca^{2+}]$ was allowed to vary. Because models including CDI differ in their geometrical layout, there is no obvious 'best' way to do this. Assumptions about internal calcium dynamics will impact the (estimated or calibrated) parameters governing I_{CaL} kinetics, and to bring these to the foreground the internal calcium concentrations in these simulations may be chosen to vary as defined by the model equations. If, however, only the models' I_{CaL} equations are of interest, it is preferable to force an identical CaT at the internal channel mouth in each simulation.

To address these conflicting aims, a series of three complementary simulations were performed. First, an AP-clamp was simulated in which the internal calcium concentration(s) was allowed to vary according to model equations (**AP clamp 1**). Secondly, a dual AP-CaT-clamp was performed, in which all internal $[Ca^{2+}]$ (including the subspaces) were clamped to the same pre-calculated bulk cytosolic CaT (**AP clamp 2**). Thirdly, a combined AP-CaT-clamp was performed in which bulk cytosol, submembrane space, and dyadic space $[Ca^{2+}]$ were clamped to pre-calculated transients appropriate to the subspace (**AP clamp 3**). The AP and CaT measurements were chosen from the Grandi et al. [2010] human ventricle model during 1 Hz at steady pacing of the model (Figure 4.7, 3.2), as this is the earliest human model in which all three subspaces are defined (note that unlike other human AP models, there is a slight delay between the AP and CaT waveforms of the model by Grandi

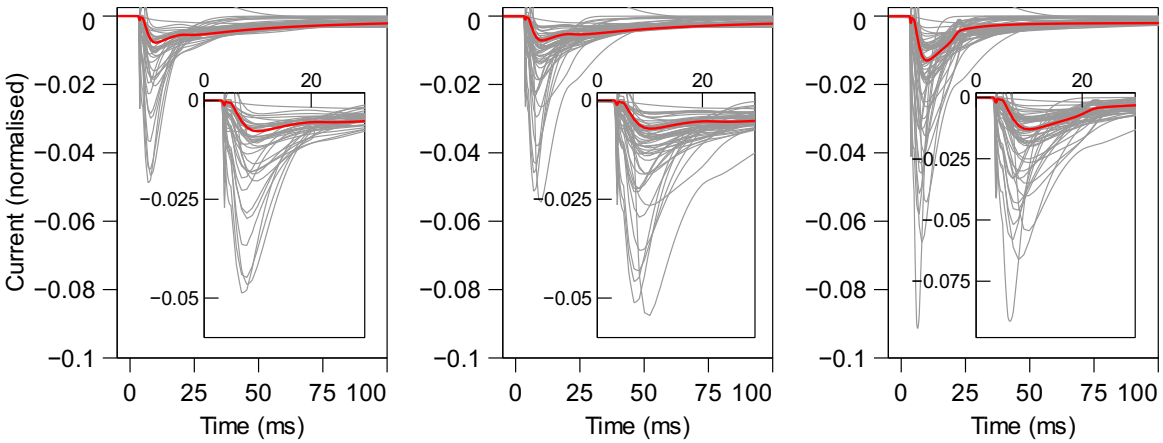

Figure 4.8: Variation in the I_{CaL} predictions in response to AP and AP-CaT clamp. Currents are shown normalised to the total charge carried (see text). **Left**: Simulated response to AP clamp 1, in which internal $[Ca^{2+}]$ are determined by each model's equations. **Centre**: Simulated response to AP clamp 2, in which all internal $[Ca^{2+}]$ are clamped to an identical predetermined bulk-cytosolic CaT. **Right**: Simulated response to AP clamp 3, in which $[Ca^{2+}]_i$, $[Ca^{2+}]_s$, and $[Ca^{2+}]_d$ are clamped to the bulk cytosolic, submembrane, and dyadic CaT from the model by Grandi et al. [2010]. Results for AP clamp 1 are limited to 44 cases where an AP model CellML file was available, whereas all 60 models are shown for the remaining AP clamps. Predictions from Grandi et al. [2010] are highlighted in red.

et al. [2010], so the choice of this CaT is not representative of the underlying calcium dynamics of other models). Because AP clamp 1 requires an AP model, this simulation was only performed for the 44 models for which a CellML file for the full AP model was available. For AP models with epi-, endo-, and mid-myocardial variants, the epicardial version was used. AP clamp 2 and 3 were performed for all 60 models. In all three simulations, I_{CaL} was normalised with respect to the total charge carried: $\bar{I}(t) = I(t)/|\int_t I(t)dt|$. The resulting normalised currents are shown in Figure 4.8.

Variation in gating across models is not easily explained

All three AP clamps in Figure 4.8 show considerable variation in predicted (normalised) I_{CaL} between models. Some of this variation may be explained as a result of differences in e.g. species and cell-type, or more mundane factors such as the year of publication. To test this assumption, the 60 models were divided into groups according to several criteria and investigated whether this resulted in groups with reduced variation. The 'compromise' protocol AP Clamp 3 was chosen for this purpose. To remove effects of varying driving terms and maximal conductances, the predicted open probability (O) was compared rather

than I_{CaL}. To give an indication of the variation within a group, the 'normalised root mean square difference' (NRMSD) of the observed open probabilities of all models in the group was used, which was defined as:

$$\text{NRMSD}_{\text{group}} = \sqrt{\frac{1}{m \cdot n} \sum_{i=1}^{m} \sum_{j=1}^{n} \left(O_{ij} - \hat{O}_i \right)^2} \tag{4.2}$$

$$\hat{O}_i = \frac{1}{n} \sum_{j=1}^{n} O_{ij}. \tag{4.3}$$

Here, O_{ij} represents the open probability measured in response to the 'AP-CaT clamp 3' protocol at the i^{th} time step for the j^{th} model, m is the total number of time points, and n is the total number of models within the group.

If grouping by a particular category reduced variability, the NRMSD within each group would be expected to be lower than the NRMSD of the original group-of-all-models ($\text{NRMSD}_{\text{total}} = 0.139$). This can be quantified by defining a relative measure $\text{NRMSD}_{\text{relative}} = \text{NRMSD}_{\text{group}}/\text{NRMSD}_{\text{total}}$. A grouping can be considered to be better than baseline if its $\text{NRMSD}_{\text{relative}}$ is less than one.

First, the effects of grouping models chronologically was investigated by grouping each model into one of four categories depending on the year of publication. This is shown in Figure 4.9, where some convergence can be observed in model predictions over time, indicated by a decreasing $\text{NRMSD}_{\text{relative}}$. Although this is encouraging, some degree of convergence should be expected as more recent models are often refinements of previous models in the same age category. Large variability should also expected from the models published before the 1990s, which depend on data obtained from a wider range of experimental techniques.

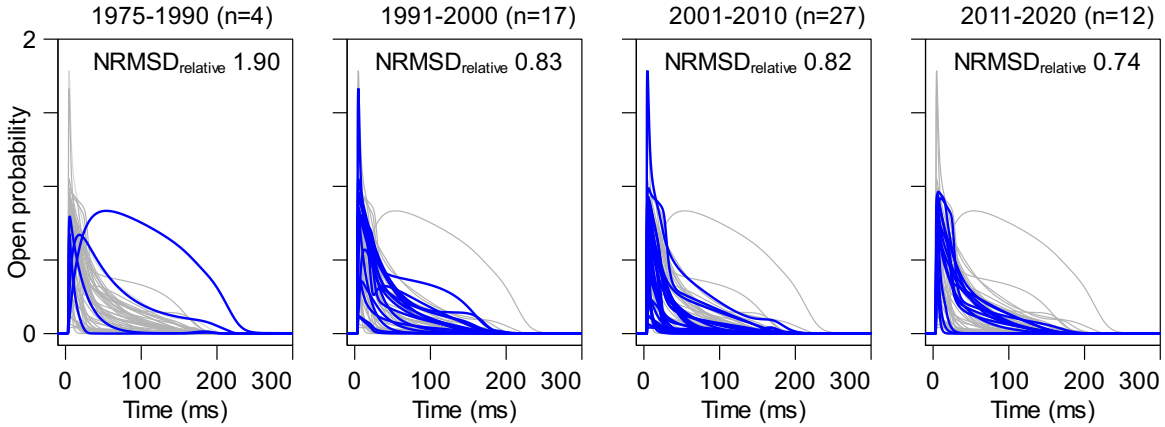

Figure 4.9: Open probability in response to AP clamp 3, grouped according to date of publication, shows a degree of convergence over time. Blue curves in each panel correspond to I_{CaL} predictions of models within the corresponding period, while the remaining predictions are shown in grey. (Note how some models allow O to be greater than 1, so that it is not strictly a probability in these models.)

Next, models were grouped according to the approach used to account for how the calcium concentrations affect the open probability, depicted by the rows in Table 3.1. On this basis, Figure 4.10 shows the models grouped into 6 classes: no $[Ca^{2+}]$ (row 1, 2), $[Ca^{2+}]_i$ (row 3, 6), $[Ca^{2+}]_s$ (row 4, 7), $[Ca^{2+}]_d$ (row 5, 8, 11, 12), $[Ca^{2+}]_i$ and $[Ca^{2+}]_d$ (row 9), and $[Ca^{2+}]_s$ and $[Ca^{2+}]_d$ (row 10). It shows that that most groups formed on the basis of the local $[Ca^{2+}]$ near the LCC have at least $\sim$20% less disagreement amongst the predictions across models than the baseline. This indicates that the modelled localisation of the LCCs plays an important role in determining model predictions. Note that class 5 contains only a single model [Tomek et al., 2019] so that no $NRMSD_{relative}$ can be calculated. Similarly, all three models in class 6 [Shannon et al., 2004, Grandi et al., 2010,0] were developed by the same research group, which explains the very low NRMSD in this group.

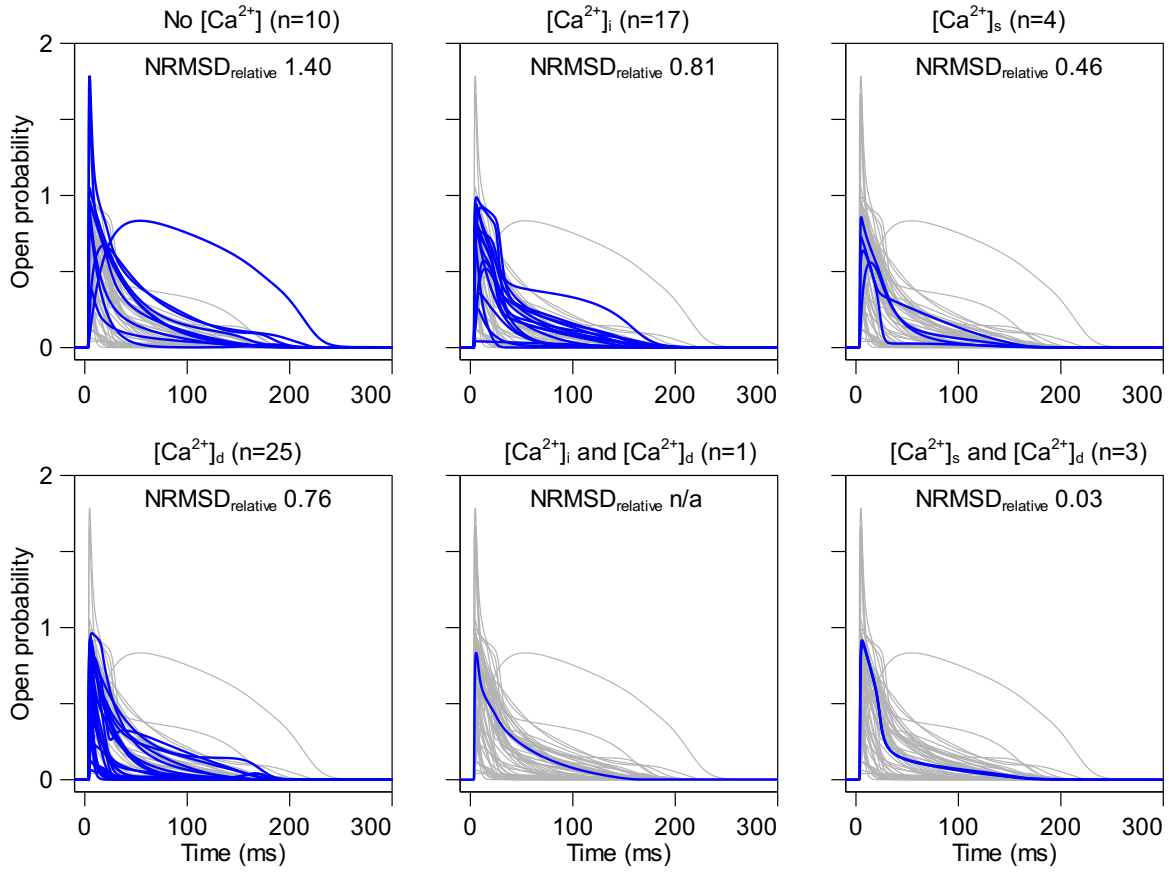

Figure 4.10: Open probability (O) in response to AP Clamp 3, grouped by local $[Ca^{2+}]$ as shown by the rows in Table 3.1 where each row represents an O or driving term dependence on different local $[Ca^{2+}]$. The first panel 'No $[Ca^{2+}]$' shows the models from rows 1 and 2, followed by 'Bulk cytosol $[Ca^{2+}]$' (rows 3 and 6); 'Submembrane space $[Ca^{2+}]$' (rows 4 and 7); 'Dyadic space $[Ca^{2+}]$' (rows 5, 8, 11, and 12); '$[Ca^{2+}]_i$ and $[Ca^{2+}]_d$' (row 9); and '$[Ca^{2+}]_s$ and $[Ca^{2+}]_d$' (row 10). In each panel, blue curves show I_{CaL} predictions from models within the corresponding group, while the remaining predictions are shown in grey.

Finally, grouping the models by species and cell types were investigated. $NRMSD_{relative}$ were obtained for groups of human (0.82, n=14), canine (0.62, n=14), rabbit (0.9, n=14), and guinea pig (0.83, n=8) models. When grouping by cell type the $NRMSD_{relative}$ was calculated for atrial (0.94, n=10), ventricular (1.05, n=35), sino-atrial (0.87, n=6), and Purkinje cells (0.83, n=6) (see Appendix A.2). (Examples of I_{CaL} in response to AP waveforms from an epicardial ventricular, endocardial ventricular, and atrial model are shown in a live interactive story[1]). Most groupings showed a small improvement on the baseline, but the only major reduction in $NMRSD_{relative}$ was seen in the group of canine models.

Of all tested criteria, grouping by local $[Ca^{2+}]$ near the LCCs exhibited the most consistent

[1] https://scrambler.cs.ox.ac.uk/stories/14

predictions.

4.4 Discussion

In this chapter, the predicted I_{CaL} from 60 models was examined using three common voltage-clamp protocols, as well as more complex AP and AP-CaT-clamp protocols. Great variability was observed between model predictions, which was somewhat diminished when grouping the models by their assumptions about LCC localisation, but no grouping could be found that significantly reduced (or explained) this variability. On several occasions, different parts of an I_{CaL} model were observed to compensate for each other: unusual driving terms can be cancelled out by unusual gating, and modelled calcium-sensitivity in CDI weakly correlated with the volume of the subspace LCCs were assumed to occupy.

These sixty models and the thirteen further models examined qualitatively in the previous chapter, along with the further models not covered here, represent a huge effort and a great achievement by the cell electrophysiology community. It is perhaps surprising, however, that no consensus or even 'gold-standard' model has emerged for I_{CaL}, or even subcomponents δ and O. This situation presents a challenge for future modellers who need to choose an I_{CaL} model for their studies, or may even wish to add a 74^{th} model. This section will focus on the open problem: What new experimental or analytical work is needed to help us choose between different models of the electrochemical driving force and (voltage and calcium-dependent) gating?

A major difficulty when comparing I_{CaL} models is that, although they share a common structure, their driving term (δ), voltage-dependent kinetics, and calcium sensitivity interact in ways that allow irregularities in one aspect to be compensated in another. For example, the unusual open probability (O) of the model by Priebe and Beuckelmann [1998] (Figure 4.2) was shown to be compensated by a large reversal potential in its driving term (Figure 3.5) to give a typical I_{CaL}. Such compensation allows the model to predict a current similar to other models for some protocols (Figure 4.11, middle) but different current at other protocols (Figure 4.11, right). Similarly, the models by Demir et al. [1994], Lindblad et al. [1996], and Aslanidi et al. [2009a] allow O to be greater than one (so that the usual interpretation of open probability does not apply), which can be compensated for in either δ or a reduced

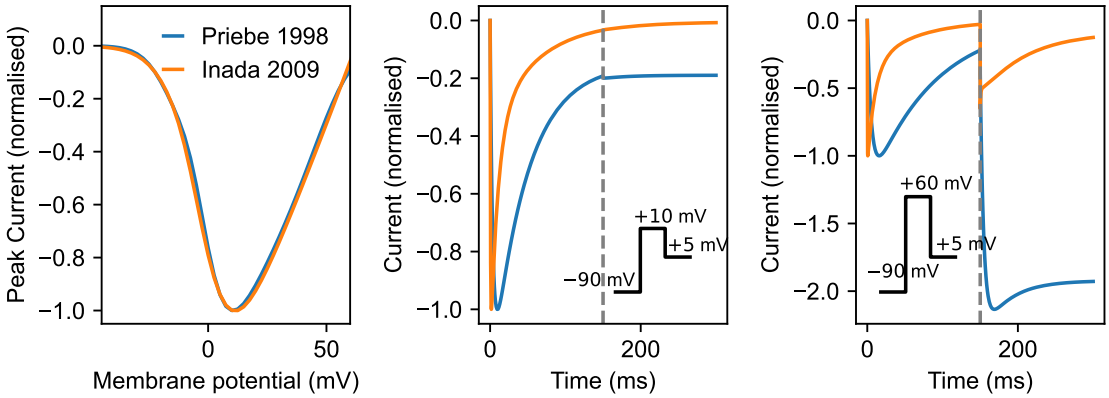

Figure 4.11: Compensation can hide model differences. **Left**: The IV curves for Inada et al. [2009] and Priebe and Beuckelmann [1998], normalised to the peak I_{CaL}. These models were chosen because their IV curves almost overlap, suggesting similar activation characteristics. However, the model by Priebe & Beuckelmann is known to have an unusually low open probability at higher voltages (Figure 4.2) which is compensated by a stronger driving term (Figure 3.5). **Middle**: A step protocol showing quantitative, but not qualitative model differences. The membrane potential is held at -90 mV (not shown), then stepped up to 10 mV (0 to 150 ms), and then down to 5 mV. Currents are shown using the same normalisation as before. In both models the step to 10 mV elicits the maximal response, followed by inactivation, which continues after the step to 5 mV. **Right**: A step to 60 mV elicits a much weaker response in both models (notice the scale on the y-axes). At this potential, the models are expected to fully activate and inactivate. However, the subsequent step to 5 mV reveals further activation in the model by Priebe & Beuckelmann, leading to an unexpected biphasic response, and a qualitative difference between the models' activation characteristics.

maximal conductance. The model by Beeler and Reuter [1970] has a strong sensitivity to $[Ca^{2+}]$ (Figure 4.5) but does not include CDI, deriving its $[Ca^{2+}]$-dependence from an unusually strong driving force (Figure 3.5) instead.

Compensation also comes into play when creating or modifying AP models, which often require calibration of the sub-models (e.g. the I_{CaL} model) to cell-level observations [Whittaker et al., 2020]. For example, Figure 4.6 shows how a high sensitivity to calcium can be compensated by postulating a bigger subspace near the LCCs, leading to a lower local $[Ca^{2+}]$. More generally, an I_{CaL} model's CDI gating may have to be tuned to the specific CaT in the AP model it was designed for (which suggests that some of the variability observed in Section 4.3.4 may be attributed to compensation for differences in CaT). Similarly, irregularities in an I_{CaL} model can, to a degree, be compensated by irregularities in the outward K^+ currents and in the other components involved in CICR.

A model with subtly compensated defects may reproduce many electrophysiological phenomena seen in the experimental data, but through mechanisms that do not reflect those in the real cell. As a result, its predictions are likely to be unreliable when extrapolating to new, e.g. pathophysiological, situations. In this section, an I_{CaL} model is once again broken into its constituent parts, and possible experiments are discussed that could allow the study of each component in isolation.

Driving term

The study of the electrochemical force driving I_{CaL} flux through the open channels is complicated by the wide range of calcium concentrations in a myocyte and the much higher concentrations of Na^+ and K^+ ions near the LCCs. Different models have been proposed as a result, starting with the Ohmic and GHK forms discussed in this review, but quickly moving on to more elaborate equations [Hess and Tsien, 1984, Roux et al., 2004] that (perhaps due to their computational cost) were never incorporated into AP models. This has left the question of how best to *approximate* δ in a computationally tractable I_{CaL} model unanswered, and none of the studies surveyed here showed a comparison of different driving-term models to motivate their choice.

To decide between driving force models, specialised experiments may be required that can separate driving force from kinetics and CDI. Single-channel 'excised-patch' experiments have shown promise in this respect [Hess et al., 1986, Greenstein and Winslow, 2002], and have the potential to allow rapid variation of internal (inside-out) or external calcium concentrations (outside-out), to levels that a whole cell may not tolerate, and in removing obfuscating effects from intracellular buffers and transporters [Gradogna et al., 2009]. Single-channel results could then be scaled up to whole-cell level, with stochastic channel simulations used to check if a simple scaling approximation holds well enough when only small numbers of channels are open, or if a more complex method is needed.

Another interesting approach could be to fit Ohmic and/or GHK models to predictions from more sophisticated models of ionic permeation [Roux et al., 2004].

The same approaches could be used to try and resolve differences in relative permeability to different ionic species (Table 3.4). In the models reviewed in this study, the activity

coefficients were found to be highly similar between models. It is interesting to note that their values depend on experimental conditions and so could be calculated as part of the model (although within physiological ranges of temperature and ionic concentrations they change by less than 0.1% during an action potential at 1 Hz pacing).

CDI and calcium dynamics

Calcium-dependent inactivation (CDI) is one of the most challenging aspects of modelling I_{CaL} and the degree of CDI predicted by different models varies widely (Figure 4.5). CDI depends on the (fluctuating) calcium concentration at the intracellular channel side, and so model assumptions about channel localisation and cell geometry have a strong impact on modelled CDI, as evidenced by the relationship between subspace volume and CDI_{50} in Figure 4.6 and by the reduction in variability between models when grouping by channel localisation.

Experimentally, CDI can be separated from voltage-dependent kinetics and driving term to some degree by using voltage protocols with a single repeating step, so that voltage effects are consistent — if still unknown. This approach has been used in Chapter 5 to investigate CDI in I_{CaL}. However, the local calcium concentration is difficult to control, as the very low $[Ca^{2+}]$ maintained in living cells means the calcium influx through I_{CaL} causes a significant change. In myocytes, a bewildering array of processes affect and are affected by local $[Ca^{2+}]$ [Bers, 2008]. In heterologous expression systems, calcium-buffers are required to keep $[Ca^{2+}]$ at levels the cells can tolerate [You et al., 1997]. Bulk cytosolic $[Ca^{2+}]$ can be measured optically using fluorescent dyes [Herron et al., 2012] but measuring local calcium elevations in subspaces (or 'microdomains') is technically challenging [Acsai et al., 2011]. As a result, there is no simple set-up in which CDI can be studied, and analysing data from experiments targeting CDI requires consideration of intracellular $[Ca^{2+}]$ gradients, diffusion, and buffering. Although analytical solutions exist for simplified scenarios [Smith, 1996], it is likely that numerical simulations [e.g. Rice et al., 1999, Greenstein and Winslow, 2002, Koivumäki et al., 2011, Nivala et al., 2012] will be required for this purpose. A combination of analytical solution and numerical simulations have been used in Chapter 6 to model CDI.

Voltage-dependent kinetics

The equations for O vary more from model to model than those for any other aspect of I_{CaL} (Figure 3.4), and large variability was found in the predicted response to voltage-clamp protocols, which cannot be easily reduced by grouping models by e.g. cell type. While most studies of I_{CaL} kinetics have used conventional voltage-step protocols (such as shown in Figures 4.1, 4.3, and 4.4), recent advances in protocol design for I_{Kr} [Beattie et al., 2018, Clerx et al., 2019a] may be translatable to I_{CaL}. Application of such protocols in high-throughput settings [Lei et al., 2019] with careful consideration of experimental artefacts [Lei et al., 2020a,0] may help produce rich data sets that will allow us to distinguish between the different proposed gating mechanisms and study (biological or experimental) variability. Such an approach, however, would require that voltage and calcium effects are independent (or at least can be studied independently) and may rely on accurate CDI and driving term models already being available. Alternatively, it may be possible to derive gating models as simplifications of more detailed molecular dynamics models [Silva, 2018, Ramasubramanian and Rudy, 2018]. In either case, care must be taken to create independent training and validation data sets, so that the most crucial part of the gating model, its predictive power, can be assessed [Whittaker et al., 2020]. Training and validation data sets are created in Chapter 7 using advanced protocols in high-throughput patch-clamp settings to pin down the voltage-dependent kinetics of I_{CaL}.

4.5 Summary

In this chapter, simulations were run on sixty models of I_{CaL} using conventional as well as physiological voltage-clamp protocols. The resulting predictions showed a wide variability that could not be explained by trivial differences such as species or cell types. Nevertheless, some consensus emerged when considering factors such as the localisation of the channel. A possible reason for this consensus could be that irregularities across different models of the LCC are compensated by the corresponding volumes of localisation to give similar APs. Such compensation of different modelling aspects by each other was also a larger theme identified by different examples in this chapter.

Much of the variability in predictions can also be explained by the assumption of several

types of gating mechanisms across models. Indeed, some of the variability can be reduced by eliminating some of the models that replicate outdated or incomplete biological concepts in light of the latest knowledge about the electrophysiology of LCCs.

In order to understand the underlying biology of I_{CaL} and to identify a model that best represents it, one approach could be to match models to a particular data set. A straightforward method to do this could be to simply try fitting each gating scheme and each driving term model, choosing the simplest combination that fits, and then verifying its predictive power on a separate data set (which should also tell us something about the limitations of the model). Therefore, the subsequent chapters in this thesis lay out suggested steps on how to collect and post-process data and then fit an I_{CaL} model to it. In the following chapter, the practical difficulties associated with creating a good quality data set for I_{CaL} modelling are investigated.

5 | Patch-clamp experiments to investigate rundown in L-type calcium current recordings

Due to COVID-19 travel restrictions, the patch-clamp experiments in this chapter were performed in Basel, by collaborators at Roche, but I helped to design them and performed all the data analysis, drew conclusions, and interpretations.

5.1 Introduction

The previous chapter showed that there is a vast variability in the predictions of the existing L-type calcium current (I_{CaL}) models. There is therefore a need to critically compare these against experimental data. I_{CaL} can be recorded using patch-clamp techniques, as discussed in Section 2.5.2. Although some amount of rundown is often reported for many ionic channels, it is exceptionally pronounced for the L and N-type calcium currents [Kameyama et al., 1989]. Given the importance of obtaining reliable data recordings to study any current, this chapter and the next focus on investigating the factors influencing rundown.

Figure 5.1 shows an example of rundown observed in whole-cell automated planar patch, voltage-clamp experiments. This rundown is shown during successive channel opening steps where the membrane voltage (V_m) was clamped at 0 mV for 150 ms interspersed by a holding potential duration (t_{hold}) of 10 s at -90 mV.

In whole-cell patch-clamp experiments, rundown is attributed to several factors including 'washing away' of phosphorylating agents (e.g. ATP) which are essential in increasing the activity of the L-type calcium channels (LCCs) [Belles et al., 1988], as discussed in Section 2.2.4. A further reason for rundown is considered to be loss of LCCs with time due to activation of Ca^{2+}-dependent enzymes that can cause its proteolytic degradation [Belles et al., 1988, Sarantopoulos et al., 2004].

Previous studies have also found that use of buffers with a high chelating activity for calcium are associated with less rundown [Belles et al., 1988, Sarantopoulos et al., 2004]. This suggests that an accumulation of Ca^{2+} inside the cell, near the membrane could contribute to rundown. This hypothesis is further supported by the experimental observation of

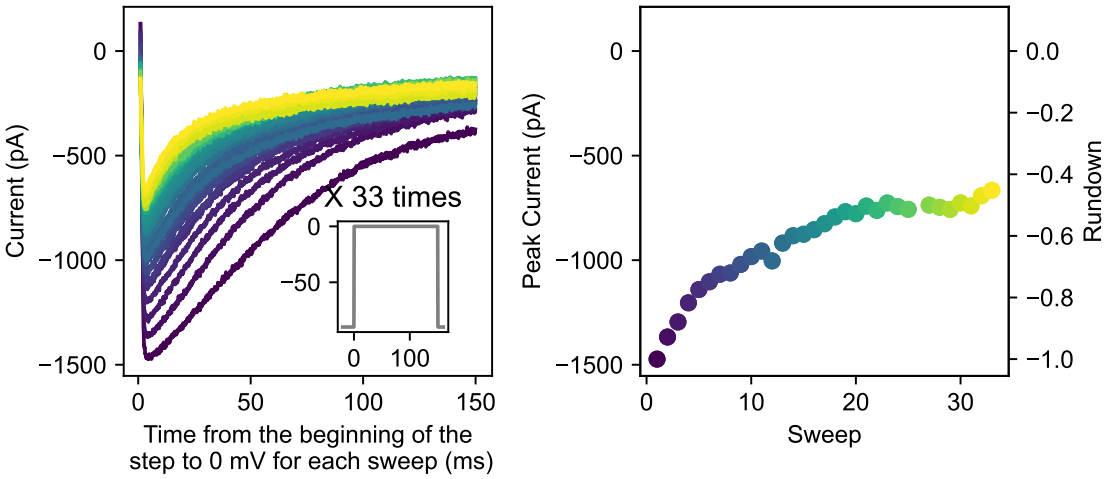

Figure 5.1: **Left**: I_{CaL} recorded at successive channel opening steps overlaid with first and last step to 0 mV shown in indigo and yellow recordings respectively. **Inset**: Voltage-clamp protocol during which current is recorded, interspersed by a holding potential at −90 mV for 10 s. **Right**: Peak I_{CaL} recorded at each successive step (sweep) on the left axis, and rundown on the right axis.

prominent rundown in ionic channels that are known to be inactivated by local $[Ca^{2+}]$ [McNaughton et al., 1998]. In accordance with these literature findings, to reduce free Ca^{2+} in the cell, the intracellular solution in the experiment shown in Figure 5.1 included a calcium chelating buffer (BATPA). Similar experiments performed in the absence of any calcium chelating buffer result in almost no recording of current.

This chapter investigates whether the accumulation of Ca^{2+} close to the intracellular side of the channel and subsequent calcium-dependent inactivation (CDI) of LCCs, explains the observed rundown. To test this hypothesis, an automated patch-clamp machine was used to measure current in CHO cells transfected with and overexpressing $Ca_V1.2$. The experimental conditions were varied with the aim of increasing or decreasing the concentration of intracellular Ca^{2+} ($[Ca^{2+}]_i$) and comparing the amount of rundown. These conditions include a higher temperature, block of the sodium-calcium exchanger (I_{NaCa}), and varying t_{hold} in the voltage-clamp protocol shown inset in Figure 5.1. Increases in temperature alter channel gating to increase the amount of I_{CaL} flowing into the cell, which in turn increases $[Ca^{2+}]_i$. The block of I_{NaCa} will cause less extrusion of Ca^{2+} from inside the membrane to outside the cell, resulting in more buildup of local $[Ca^{2+}]$ near the LCCs. Finally, decreasing t_{hold} will increase the frequency of LCC opening and Ca^{2+} entry to the cell, and provide less

time for Ca^{2+} to diffuse away from the LCCs it enters through. Increased rundown was observed in all these experimental conditions that should promote $[Ca^{2+}]_i$ accumulation. This chapter provides experimental evidence that, at least in part, rundown can be explained by CDI increasing over the course of a patch-clamp experiment.

5.2 Methods

5.2.1 Patch-clamp experiments

Whole-cell patch-clamp voltage-clamp experiments were performed on ready-to-use[1] CHO cells at passage 9[2], stably transfected[3] with $Ca_V1.2$ using the Syncropatch 384PE platform (Nanion Technologies). This is a high-throughput automated patch-clamp system that allows simultaneous recordings from 384 wells (arranged into 16 rows and 24 columns). Previously described in Section 2.5.2, it has a planar patch setup (Figure 2.11, centre) where the intracellular solution enters the cell from a *patch hole*, and this solution dominates the concentrations in the cytosol. Composition of both 'bath' (extracellular) and intracellular solutions used in this study are given in Table 5.1. After a user-defined time (t_0) passed that allowed the intracellular solution to diffuse into the cell, a voltage-clamp protocol (see Section 5.2.2) was applied and the syncropatch recorded the current from this time onwards. At 325 s, 10 μM of the LCC blocker *nifedipine* (which should selectively block I_{CaL} by at least 90% [Shen et al., 2000]) was added and the experiment was run for a total of 561 s. At each sweep of the protocol (Section 5.2.2), in addition to recording the current at a frequency of 10 kHz, the machine also estimated the membrane capacitance (C_m), seal resistance (R_{seal}), and series resistance (R_s).

To reduce I_{NaCa}, cells in columns 1–12 were treated with 10 μM of the I_{NaCa} blocker ORM-10103 (causing >90% block [Jost et al., 2013]) while cells in columns 13–24 were treated with the control DMSO. Finally, the experiment was performed at two temperatures: 298 K

[1] Cell preparations that are stored as a bank of uniform aliquots ready for immediate use, usually after thawing of the cells from a cryopreserved state [Gazzano-Santoro et al., 2014].

[2] The passage number of a cell culture is a record of the number of times the culture has been subcultured (harvested and reseeded). This technique allows the cells to be kept alive and growing under cultured conditions for extended periods of time [Mather and Roberts, 1998].

[3] Transfection is a laboratory cell culture technique that introduces foreign nucleic acids into cells. It can be stable or transient in nature. Stable transfection integrates foreign DNA into the host nuclear genome in order to sustain long-term expression [Fus-Kujawa et al., 2021].

and 310 K, for each of the three voltage-clamp protocols (see Section 5.2.2) equating to six chips (see Figure 5.2).

Solution titrated with **Compound**	**Intracellular** *1M KOH* mM	**Fill chip** *1M NaOH* mM	**Seal enhancer** *1M HCL* mM	**Reference** *1M HCL* mM	**Extracellular** mM
KCl	10	4	-	4	3.5
KF	100	-	-	-	-
NaCl	5	150	-	80	78.75
Na-ATP	4	-	-	-	-
Na-GTP	0.1	-	-	-	-
CaCl2	-	1.2	10	1	2.15
MgCl2	-	1	1	1	1
CsCl	-	-	4	-	0.5
HEPES	10	10	10	10	10
BAPTA	10	-	-	-	-

Table 5.1: Electrophysiology solutions for the $Ca_V1.2$ assay on the automated patch machine. The extracellular solution shows the resulting concentrations after sequential addition of half bath volume of "fill chip", "seal enhancer", and "reference" (twice) solutions. Each time the bath is full, the volume is halved so that the same volume of the next solution can be added, until there is a 1:1:6 proportion of the net extracellular solution. Therefore, the extracellular solution = 0.125×Fill chip + 0.125×Seal enhancer + (0.25 + 0.5)×Reference. The pH of the intracellular solution is 7.2, while that of the bath solutions varies from 7.2–7.4.

5.2.2 Voltage-clamp protocol

Each of the three voltage-clamp protocol consist of identical sweeps. A single sweep is 1.02 s shown inset in Figure 5.3C: a 10 ms step to −90 mV is followed by a 100 ms step to −120 mV, a 400 ms ramp from −120 mV to −90 mV, a 350 ms step to −90 mV, a 150 ms step to 0 mV, and finally a 10 ms step to −90 mV. The step to −120 mV ensures that the L-type calcium channels (LCCs) are completely closed, while the ramp from −120 to −90 mV is useful in the calculation of the linear leak current (I_{leak}, described in the next section). Finally, the step to 0 mV opens the channel for the flow of I_{CaL}. When comparing any two sweeps in these protocols, voltage-dependent kinetics of I_{CaL} remain the same, thus allowing the observation of changes due to calcium-dependent kinetics (or other experimental factors). The three voltage-clamp protocols differ from each other with respect to the time of the holding potential between two steps to 0 mV or t_{hold} — chosen to be 10 s, 20 s, or 40 s. This equates to 33, 17, and 9 sweeps for each protocol before the addition of

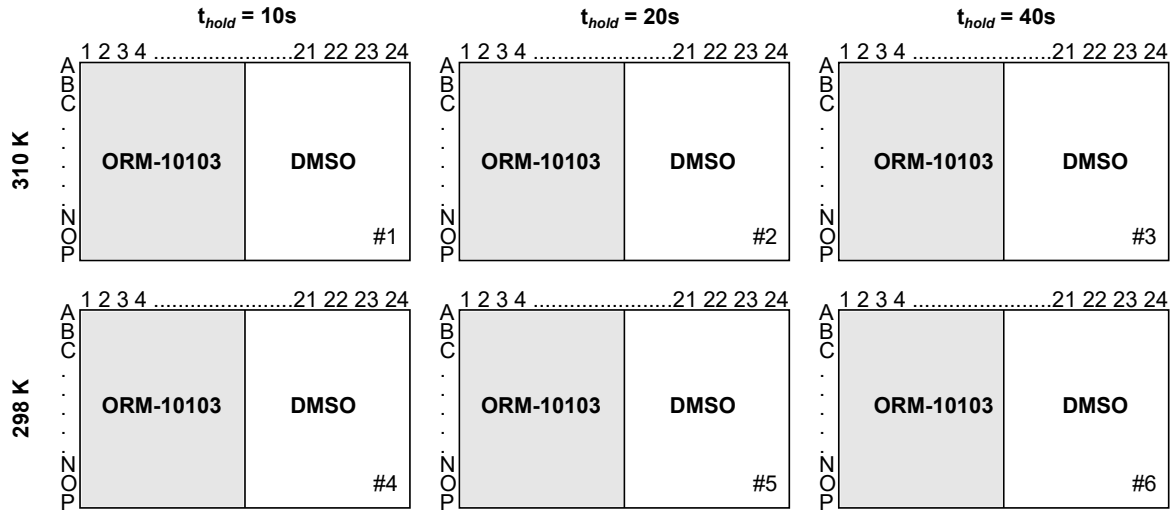

Figure 5.2: Two temperatures and three protocols equate to 6 chips. Two conditions per chip (block or no block of I_{NaCa}) equate to twelve conditions. This results in $12 \times 16 = 192$ wells per condition.

nifedipine, and 23, 11, and 5 sweeps after.

5.2.3 Post-processing

Currents measured were post-processed to reduce the effects of capacitance, linear leak, and any endogenous currents. At the point of step-wise change in the membrane voltage (V_m), the current recorded is the sum of both capacitative and ionic current [Armstrong and Bezanilla, 1974, Hille, 2001], as also shown in Equation 2.2. To remove the capacitative effect from the currents at each sweep i (I_i), recordings for 1 ms after the step-wise V_m changes (steps to -120 mV, 0 mV, and -90 mV in the voltage-clamp protocol, Section 5.2.2) were removed from the analysis. The resultant current is shown in Figure 5.3A–B for two sweeps.

To extract I_{CaL_i} from I_i, each recording was first corrected for leak current to obtain $\hat{I}_i$ (Equation 5.1), and subsequently the recording from the second sweep after the addition of drug (n_2) was used to remove the effect of endogenous current (Equation 5.3). The equation for leak subtraction at each sweep (i) is given by:

$$\hat{I}_i = I_i - I_{leak_i}, \tag{5.1}$$

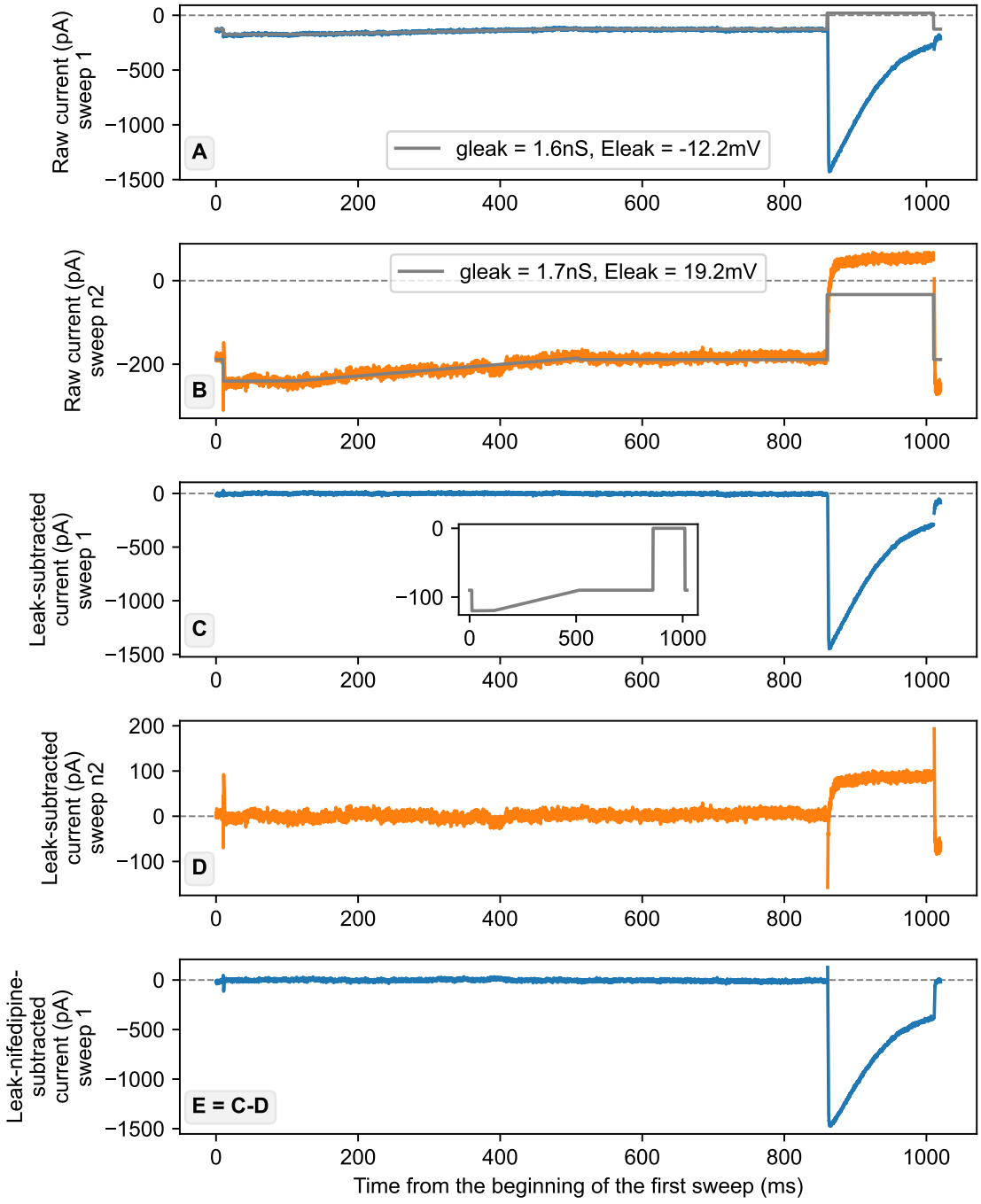

Figure 5.3: Step-wise post-processing of current measured at sweep 1 (I_1), from patch-clamp experiments of cell in C19 at 310 K and holding potential duration of 10 s. **Panel A**: I_1 with capacitance filtering, along with the linear leak current shown in grey. **Panel B**: I_{n_2} with capacitance filtering, along with the linear leak current shown in grey. **Panel C**: $\hat{I}_1$. **Panel D**: $\hat{I}_{n_2}$. **Panel E**: I_{CaL_1}. **Inset**: Voltage-clamp protocol at each sweep, holding potential held at -90 mV, while its duration between two steps to 0 mV can be: 10 s, 20 s, or 40 s for three different protocols.

where, $\mathrm{I}_{\mathrm{leak}_i}$ occurs due to an imperfect R_{seal} (see Appendix B.2) and is given by:

$$\mathrm{I}_{\mathrm{leak}_i} = g_{leak_i}(V_m - E_{leak_i}). \tag{5.2}$$

Here, g_{leak_i} and E_{leak_i} are the conductance and reversal potential of the leak current at sweep i. The parameters of $\mathrm{I}_{\mathrm{leak}_i}$ were estimated by fitting the linear function in Equation 5.2 to I_i recorded during the voltage-ramp (-120 to -90 mV). A similar procedure was used in Lei et al. [2019]. These parameters were then used to calculate $\mathrm{I}_{\mathrm{leak}_i}$ as a function of time (shown in grey in Figure 5.3A–B), and the resulting trace was subsequently subtracted from I_{i} to obtain $\hat{\mathrm{I}}_i$ (shown in Figure 5.3C–D).

Finally, effects of non-$\mathrm{I}_{\mathrm{CaL}}$ currents [e.g. endogenous current or non-linear leak Lei et al., 2020b] were removed from any sweep i to obtain $\mathrm{I}_{\mathrm{CaL}_i}$, by subtracting the current during n_2:

$$\mathrm{I}_{\mathrm{CaL}_i} = \hat{\mathrm{I}}_i - \hat{\mathrm{I}}_{n_2}. \tag{5.3}$$

The use of this equation can be seen in Figure 5.3, where the plot in Figure 5.3D was subtracted from the plot in Figure 5.3C to obtain the plot in Figure 5.3E.

This process was applied to all sweeps recorded before the application of nifedipine, on all cells to extract $\mathrm{I}_{\mathrm{CaL}}$ from the measured current.

5.2.4 Decomposition of leak current

$\mathrm{I}_{\mathrm{leak}}$ is carried by all the free ions and charged molecules that flow in and out of the cell through a hole caused by an imperfect seal between the well on the chip and the cell's membrane. In this section, an equation is derived to estimate the contribution to $\mathrm{I}_{\mathrm{leak}}$ due to any particular ion X with a special interest in estimating the proportion of $\mathrm{I}_{\mathrm{leak}}$ carried by Ca^{2+}. There are seven different ionic species in the solutions as shown in Table 5.1. Therefore, $\mathrm{I}_{\mathrm{leak}}$ can be re-written as:

$$\mathrm{I}_{\mathrm{leak}} = \mathrm{I}_{\mathrm{leakK}} + \mathrm{I}_{\mathrm{leakNa}} + \mathrm{I}_{\mathrm{leakCl}} + \mathrm{I}_{\mathrm{leakF}} + \mathrm{I}_{\mathrm{leakCa}} + \mathrm{I}_{\mathrm{leakCs}} + \mathrm{I}_{\mathrm{leakMg}}. \tag{5.4}$$

The flux due to each ion is assumed to be independent of the other and each ion diffuses

over a length L. Therefore, the current density (I_X) due to any ion X can be re-written by modifying Equation 2.9 as:

$$I_X = \frac{D_X}{L} V_m \frac{z_X^2 F^2}{RT} \left(\frac{\gamma_i [X]_i - \gamma_o [X]_o \exp\left(-z_X V_m F/RT\right)}{1 - \exp\left(-z_X V_m F/RT\right)} \right). \tag{5.5}$$

Here, γ is calculated using the empirical Equation 5.6 [Davies and Malpass, 1964], where α is the ionic strength, c_X is the concentration of ion X in molar ($10^{-3}[X]$), ϵ is the dielectric constant, and A_0 is a constant representing the Davies equation constant.

$$\begin{aligned} \log_{10} \gamma &= -z_X^2 A \left(\frac{\sqrt{\alpha}}{1 + \sqrt{\alpha}} - 0.3\alpha \right), \\ A &= A_0 \cdot (\epsilon \cdot T)^{-1.5}, \qquad \alpha = 0.5 \sum_X c_X \cdot z_{Xi}^2. \end{aligned} \tag{5.6}$$

Next, D_X is replaced with $\frac{kT}{6\pi\mu a_X}$, where a_X is the radius of the ionic species, k is the Boltzmann constant, and μ is the viscosity of the solvent to get Equation 5.7. This relationship is the Stokes-Einstein equation, which has been proved for spherical solutes that are much larger than the solvent [Keener and Sneyd, 1998, Köddermann et al., 2008].

$$I_X = \frac{F^2 k}{RL6\pi\mu} \underbrace{\left(\frac{z_X^2 V_m}{a_X} \frac{\gamma_i [X]_i - \gamma_o [X]_o \exp\left(-\frac{zFV_m}{RT}\right)}{1 - \exp(-\frac{zFV_m}{RT})} \right)}_{\mathrm{X_{eff}}}. \tag{5.7}$$

As per the above equation, while L and μ remain constant as the experiment progresses, the leak current carried by any ion is proportional to a factor given by $\mathrm{X_{eff}}$. This can be plugged back in Equation 5.4 to estimate the effective $\mathrm{I_{leak}}$ carried by any single ion X as:

$$\mathrm{I_{leakX}} = \frac{\mathrm{X_{eff}}}{\sum \mathrm{X_{eff}}} \mathrm{I_{leak}}. \tag{5.8}$$

The plot of $\mathrm{X_{eff}}$ as a function of voltage is shown in Figure 5.4 for Ca^{2+}, K^+, and Na^+ along with $\sum \mathrm{X_{eff}}$ over all ions present in the solution. While the individual $\mathrm{X_{eff}}$ show non-linear dependence with respect to voltage, $\sum \mathrm{X_{eff}}$ shows almost linear dependence in accordance with the relationship given by Equation 5.2. This confirms that Equation 5.8 can be used to calculate the proportion of $\mathrm{I_{leak}}$ carried by Ca^{2+} and is estimated to be 2.4% and 7.0% at

−90 mV and 0 mV respectively.

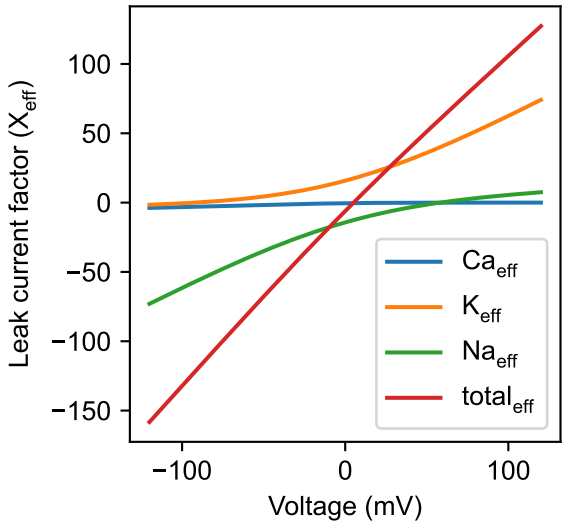

Figure 5.4: Leak current proportionality factor X_{eff} calculated using Equation 5.8 and the values given in Table 5.2.

5.2.5 Quality control

Cells with reliable recordings were identified by applying a series of quality control (QC) criteria to all cells. In this section, the QC criteria that were used to select *good* cells for inclusion in this study are defined. A preliminary QC0 was first applied to exclude recordings from wells in which the seal resistance did not remain intact until the end of the experiment. This resulted in the selection of only 74, 50, 52, 44, 56, and 40 cells out of 384 cells on the chip plate 1, 2, 3, 4, 5, and 6 respectively (Figure 5.2). The cells selected at this stage were then subject to the five quality control criteria mentioned below.

1. QC1, Machine properties: QC1.1 excluded cells in which the R_{seal} was greater than 8 GΩ or less than 0.1 GΩ, QC1.2 excluded cells in which the recorded C_m was less than 1 pF (as this is probably not a CHO cell), and QC1.3 excluded cells in which the R_s was greater than 40 MΩ as this leads to artefacts affecting the shape of the recorded ionic current.

2. QC2, Current contamination: QC2.1 excluded cells in which the magnitude of the peak current recorded during the channel opening step was less than the leak current (estimated using Equation 5.2), while QC2.2 excluded cells in which the magnitude

Name	Definition	Value
$[K^+]_i$	Intracellular potassium concentration	110 mM (Table 5.1)
$[K^+]_o$	Extracellular potassium concentration	3.5 mM (Table 5.1)
$[Na^+]_i$	Intracellular sodium concentration	9.1 mM (Table 5.1)
$[Na^+]_o$	Extracellular sodium concentration	78.75 mM (Table 5.1)
$[Cs^+]_i$	Intracellular caesium concentration	0 mM (Table 5.1)
$[Cs^+]_o$	Extracellular caesium concentration	0.5 mM (Table 5.1)
$[Mg^{2+}]_i$	Intracellular magnesium concentration	0 mM (Table 5.1)
$[Mg^{2+}]_o$	Extracellular magnesium concentration	1 mM (Table 5.1)
$[Cl^-]_i$	Intracellular chloride concentration	15 mM (Table 5.1)
$[Cl^-]_o$	Extracellular chloride concentration	89.05 mM (Table 5.1)
$[F^-]_i$	Intracellular fluoride concentration	100 mM (Table 5.1)
$[F^-]_o$	Extracellular fluoride concentration	0 mM (Table 5.1)
$[Ca^{2+}]_o$	Extracellular calcium concentration	2.15 mM (Table 5.1)
a_K	Effective ionic radius of $[K^+]$	138 pm [Shannon, 1976]
a_{Na}	Effective ionic radius of $[Na^+]$	102 pm [Shannon, 1976]
a_{Cl}	Effective ionic radius of $[Cl^-]$	181 pm [Shannon, 1976]
a_F	Effective ionic radius of $[F^-]$	133 pm [Shannon, 1976]
a_{Ca}	Effective ionic radius of $[Ca^{2+}]$	100 pm [Shannon, 1976]
a_{Mg}	Effective ionic radius of $[Mg^{2+}]$	72 pm [Shannon, 1976]
a_{Cs}	Effective ionic radius of $[Cs^+]$	167 pm [Shannon, 1976]

Table 5.2: Concentration and ionic radii of the chemical species in the intracellular and extracellular solution (Table 5.1). The concentrations are calculated by assuming complete ionisation of the compounds in Table 5.1.

of the endogenous current was more than I_{CaL} (peak current during $\hat{I}_i < \hat{I}_{n_2}$).

3. QC3, Signal-to-noise: QC3 excluded cells in which the signal-to-noise ratio (SNR) was less than 50.

4. QC4, Variation in g_{leak}: QC4 excluded cells in which the standard deviation of the calculated g_{leak} was greater than 2 nS for any sweep recorded up to two sweeps after the application of the LCC blocker (n_2).

5. QC5, I_{CaL} likelihood: QC5 excluded cells that were not likely to be I_{CaL} by checking that there was a net influx of ions rather than outflow for more than 50% of sweeps of post-processed current (no reversal of current is observed for I_{CaL} at 0 mV).

The number of cells selected after each QC criterion and the net number of cells selected after applying all QC criteria are given in Table 5.3.

QC	**310 K** $t_{hold} = 10s$	**310 K** $t_{hold} = 20s$	**310 K** $t_{hold} = 40s$	**298 K** $t_{hold} = 10s$	**298 K** $t_{hold} = 20s$	**298 K** $t_{hold} = 40s$
QC0	74	50	52	44	56	40
QC1.1	63	44	37	43	55	37
QC1.2	74	50	50	44	56	40
QC1.3	74	48	48	44	55	36
QC2.1	65	43	43	39	54	40
QC2.2	46	37	26	31	43	31
QC3	48	34	31	19	40	32
QC4	73	47	50	44	55	38
QC5	74	45	49	42	56	40
	36	24	18	18	35	25

Table 5.3: Number of cells that passed each quality control (QC) criterion, for all experimental conditions. The QC criteria are explained in the main text. The last row shows the total number of cells selected on each chip, after all selection criteria have been applied.

5.2.6 Definition of some terms

In this section, the formulation of rundown and rate of rundown is defined; terms that have been used to present the results of this study. The mathematical expressions used to estimate effective $[Ca^{2+}]$ achieved inside the cell are also defined.

Rundown was quantified by recording the peak I_{CaL} during the step to 0 mV in each sweep, which was subsequently normalised by the peak I_{CaL} at the first sweep (while preserving the direction of the current). Figure 5.1 shows an example of rundown calculation using this method for cell C19 of chip number 1 (Figure 5.2).

The rate of rundown (R_{rate}) was calculated between any two sweeps in ms^{-1}. The R_{rate} between sweeps i and $i+1$ is given by: $(\text{Rundown}_{i+1} - \text{Rundown}_{i+1})/t_{hold}$, where t_{hold} was used in ms. The median R_{rate} across the sweeps was then used.

This chapter investigates if the $[Ca^{2+}]$ local to LCCs induces rundown. While it is difficult to calculate the 'local' $[Ca^{2+}]$, the overall intracellular $[Ca^{2+}]$ can be assumed to be proportional to the local $[Ca^{2+}]$. The intracellular $[Ca^{2+}]$ can be estimated using the number of moles of Ca^{2+} inside the cell and the total volume of the cell.

The total number of moles of incoming Ca^{2+} (N_{Ca}) brought in by any current carried by

Ca^{2+} (I_{Ca}) was calculated using Equation 5.9:

$$N_{Ca} = -\frac{\int_0^{t_{exp}} I_{Ca}\, dt}{2F}, \tag{5.9}$$

where t_{exp} is the total duration of the experiment before the addition of nifedipine.

Next, to correctly estimate the effective concentration, the volume of the cell is needed. However, since information on the size of individual cells is not available, the capacitance recorded for each cell (C_m) was instead used as an indication of the cell's volume.

The specific capacitance (C_s) is often a constant [Gentet et al., 2000] equal to 1 μF/cm^2. This implies that the surface area (A) of the cell can be assumed to be proportional to C_m ($A \propto C_m/C_s$)[4]. Since C_s is a constant, for a cell of approximately spherical shape with radius R_0: $4\pi R_0^2 \propto C_m \implies R_0 \propto C_m^{1/2}$. Therefore, the volume of a sphere which is proportional to R_0^3 can be estimated to vary across cells by a factor $C_m^{3/2}$. The intracellular [Ca^{2+}] can thus be approximated by $N_{Ca}/C_m^{3/2}$ (fmol/pF$^{3/2}$).

5.3 Results

5.3.1 Rundown

The rundown in the selected cells for each of these conditions is shown in Figure 5.5.

In Figure 5.5, regardless of temperature, protocol, and I_{NaCa} blocker presence, a general trend of drop in magnitude of the peak I_{CaL} is shown as the experiment progresses. In extreme cases, this rundown reduces the current to 20% of its initial value. Qualitatively, three different shapes of rundown-versus-time curves are observed. The predominant pattern is a near-linear decrease with time (observed in 36% of cells), the second most common pattern saturates with time (observed in 18% of cells). The remaining cells (46%) have varying irregular shapes, where one such shape has a 'reverse rundown' in which the current magnitude increases for the first few sweeps and decreases thereafter.

The differences across the experimental conditions do not account for the vast variability

[4]In myocytes, the surface area within C_m is twice than the geometrical surface area, with the T-tubular network contributing to the additional recorded surface area [Luo and Rudy, 1994b]. However, in this chapter CHO cell were used which do not have such membrane folding.

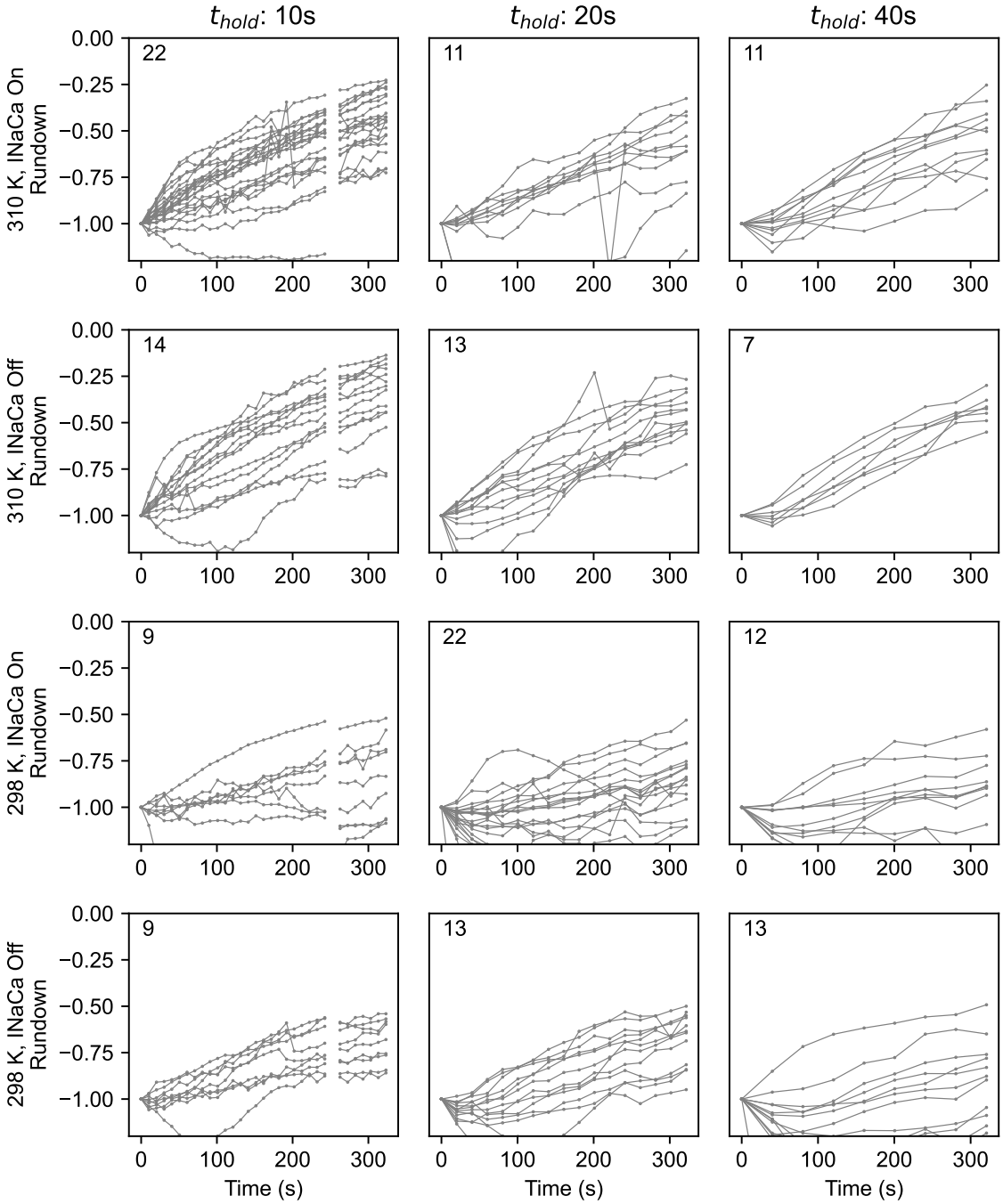

Figure 5.5: The rundown recorded for all cells passing quality control, for each of the twelve experimental conditions. The number of cells in each subplot is given in the upper left corner. Note: The missing data point in the first column at approximately 250 s corresponds to a malfunction in machine recording.

in rundown across different cells. This suggests that there must be some other factors that contribute towards rundown in these experiments.

One of the reasons for the cell-to-cell differences in rundown can be due to differing levels

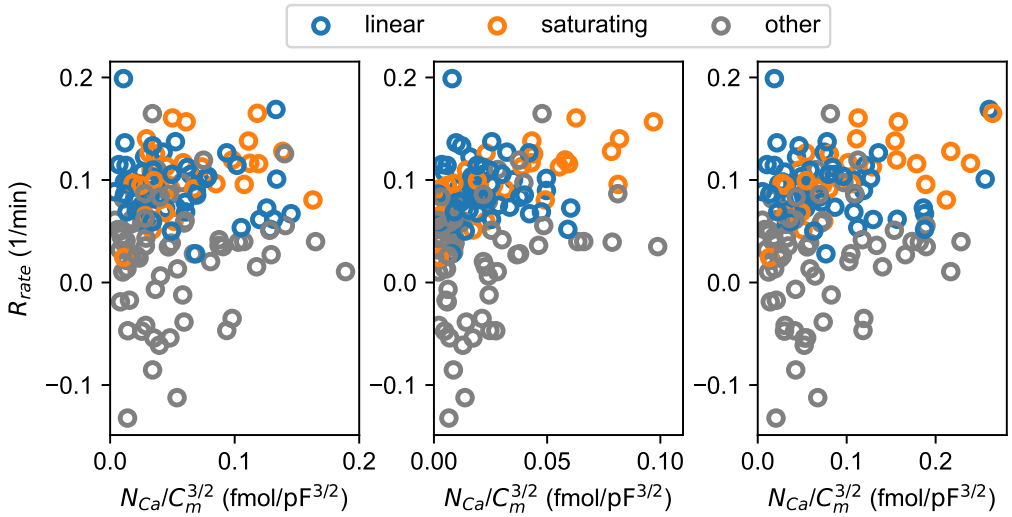

Figure 5.6: The rate of rundown (R_{rate}) for each cell (1/min) is plotted against an estimate of the intracellular [Ca^{2+}] ($N_{Ca}/C_m^{3/2}$) given in fmol/pF$^{3/2}$. The qualitative shape of rundown-versus-time curve associated with each cell is represented by the color scheme. R_{rate} is plotted against $N_{Ca}/C_m^{3/2}$, where N_{Ca} is calculated from different sources using Equation 5.9 which are I_{CaL} (**Left**), leak current (where leak current due to Ca^{2+} is calculated using Equation 5.8) (**Centre**), and both I_{CaL} and leak current due to Ca^{2+} (**Right**).

of $Ca_V1.2$ expression resulting in varying levels of intracellular [Ca^{2+}]. Figure 5.6 (left) shows the plot between R_{rate} and an estimate of the local [Ca^{2+}] given by $N_{Ca}/C_m^{3/2}$, where Ca^{2+} is brought in by I_{CaL}. The R_{rate} was calculated for all cells between each successive sweeps of rundown shown in Figure 5.5. The median R_{rate} for each cell was used to plot this figure. This plot also shows the shape of the rundown-versus-time curve, and it can be seen that the linear and saturating patterns are associated with higher R_{rate} than other patterns. Since the correlation between the quantities on each axis is weak, other sources of Ca^{2+} into the cell besides I_{CaL}, such as that brought in via the leak current were considered.

Next, the amount of calcium brought in by the leak current (I_{leak}) was calculated, which was estimated using the method described in Section 5.2.4. Figure 5.6 (centre) shows the plot of R_{rate} plotted against $N_{Ca}/C_m^{3/2}$, where Ca^{2+} is brought in by I_{leakCa}. This plot also shows weak correlation between R_{rate} and the [Ca^{2+}] accumulated due to leak current. As expected, a plot between the total intracellular [Ca^{2+}] from both sources of Ca^{2+} (I_{CaL} and I_{leakCa}) against R_{rate} (Figure 5.6, right) continues to show a correlation albeit it does not change much from the panel on the left. This is unsurprising given the small fraction of Ca^{2+} coming in from I_{leakCa} compared to I_{CaL} (Appendix B.4).

This section shows that although a small amount of correlation exists between the effective $[Ca^{2+}]$ inside the cell and R_{rate}, it is evident that there also are other factors affecting rundown.

5.3.2 Effect of holding duration on rundown

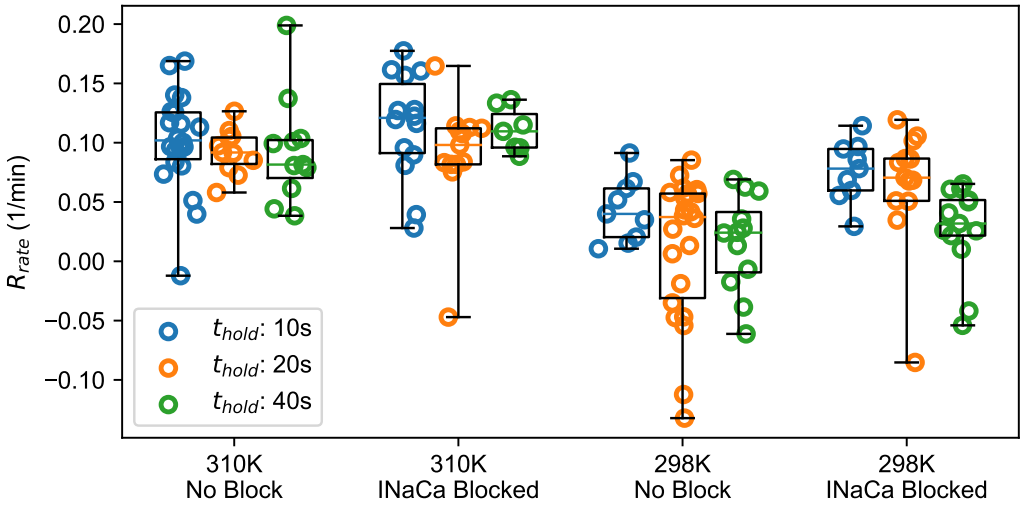

Figure 5.7: Rundown rate (R_{rate}) of cells at different experimental conditions indicated on the x-axis. Within each experimental condition, the R_{rate} can be compared across cells with a t_{hold} of 10 s, 20 s, and 40 s. The box-plot shows the interquartile range along with the median rate at each condition. The whiskers show the range of the data points. ANOVA tests were used to determine the statistical significance of the difference in means of R_{rate} for each group, and none of the groups showed a statistically significant difference (Appendix B.5).

Next, the median R_{rate} is compared across different experimental conditions.

First, the difference in the rundown rate across the varying voltage-clamp protocols (see Section 5.2.2) is compared. The protocol with a smaller inter-pulse duration (t_{hold}) will allow the LCCs to open a larger number of times allowing more Ca^{2+} to be carried into the cell via I_{CaL}. Note that the fraction of Ca^{2+} coming in from I_{leak} increases with increasing t_{hold}, however this remains much smaller than the number of Ca^{2+} brought in by I_{CaL} (Appendix B.4). Therefore, if the intracellular $[Ca^{2+}]$ contributes to rundown then a decrease in the amount of rundown with an increase in t_{hold} would be expected.

Figure 5.7 shows the distribution of R_{rate} at different experimental conditions along with the box plots indicating the median and interquartile range of the distribution. Within each

experimental condition, a slightly higher R_{rate} was observed indicated by the boxplot when t_{hold} is 10 s, which decreases as t_{hold} increases to 20 s, and then further to 40 s. Although this difference is not statistically significant (see Appendix B.5), there exists a weak downward trend and collecting similar data on more number of cells could help in clarifying the trend. Other factors possibly interfering with the trend could be increase of R_{rate} caused by other factors (e.g. loss of phosphorylation agents and LCCs) with increasing t_{hold}. Nevertheless, the small differences seen here indicate that R_{rate} could be proportional to the amount of Ca^{2+} entering the cell.

5.3.3 Effect of sodium-calcium exchanger on rundown

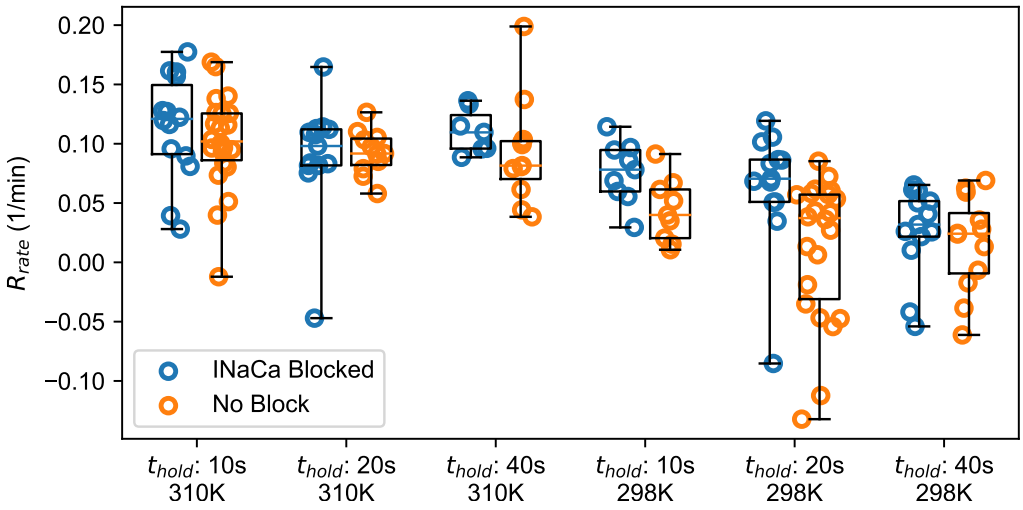

Figure 5.8: R_{rate} of cells at different experimental conditions indicated on the x-axis. Within each experimental condition, R_{rate} can be compared across cells where I_{NaCa} was blocked using ORM-10103 and where it was not. The box-plot shows the interquartile range along with the median rate at each condition. The whiskers show the range of the data points. T-tests were used to determine the statistical significance of the difference in means of R_{rate} for each group, and none of the groups (except fourth and fifth) showed a significant difference (Appendix B.5).

I_{NaCa} exchangers are natively expressed (albeit much less than I_{CaL}) in the CHO cells used for this study. This current removes Ca^{2+} from inside the cells in exchange for Na^{+} [Blaustein and Lederer, 1999, Ottolia et al., 2013] as discussed in Section 2.2.3. If the accumulation of calcium inside the cell contributes to rundown then more rundown would be expected for cells in which I_{NaCa} was blocked.

Figure 5.8 shows the R_{rate} distribution along with the interquartile boxplot for all six combinations of experimental conditions (temperature and t_{hold}) separated such that the I_{NaCa} is blocked on the left, and not blocked on the right.

Across the six experimental conditions, a slightly less R_{rate} was observed when I_{NaCa} is not blocked. Similar to the previous subsection, this difference is not statistically significant (see Appendix B.5). Nevertheless, the small increase in R_{rate} on application of an I_{NaCa}-blocker suggests that the accumulation of Ca^{2+} inside the cell contributes to rundown. It is important to note that while the blocker ORM-10103 is highly selective for I_{NaCa} [Jost et al., 2013], it has also been known to alter the I_{CaL} kinetics at the concentrations used in this study [Jost et al., 2013], thereby possible interfering with the rundown recordings.

5.3.4 Effect of temperature on rundown

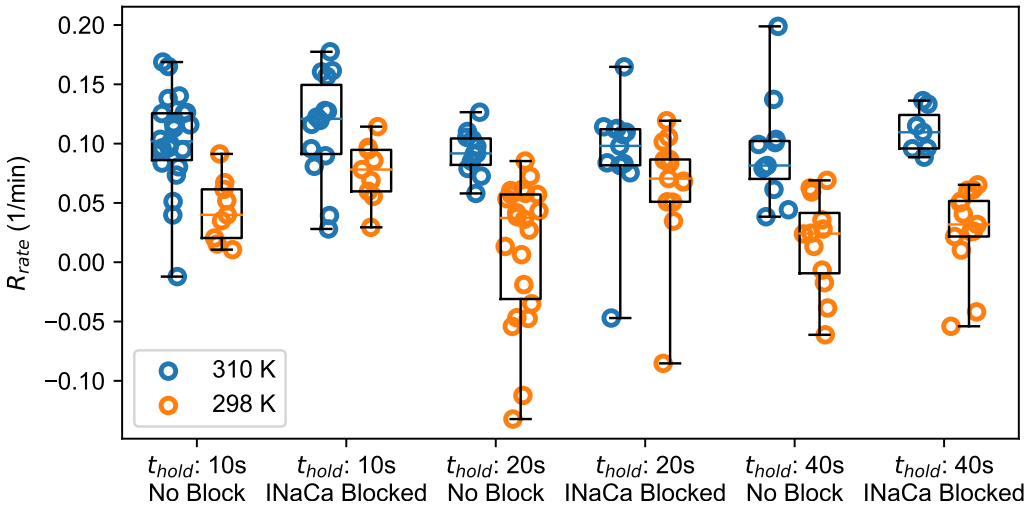

Figure 5.9: Rundown rate of cells at different experimental conditions indicated on the x-axis. Within each experimental condition, the rundown rate can be compared across cells kept at 310 K and 298 K. The box-plot shows the interquartile range along with the median rate at each condition. The whiskers show the range of the data points. T-tests were used to determine the statistical significance of the difference in means of R_{rate} for each group, and all groups showed a statistical significance (Appendix B.5).

In this study, experiments were performed at 310 K and 298 K. The magnitude of I_{CaL} is known to be lower at room temperature as compared to physiological temperature [Wang et al., 1991], and so the Ca^{2+} influx is also lower at room temperature. As a result, more rundown is expected at a higher temperature. It is expected that the increase in tempera-

ture will also accelerate I_{NaCa}, however this effect will be negligible because of the higher expression density of I_{CaL}.

Figure 5.9 shows that for all 6 combinations of experimental conditions (t_{hold} and I_{NaCa} block), R_{rate} is significantly more pronounced at a higher temperature. The difference in R_{rate} because of temperature as a factor is found to be statistically significant using t-tests with a p value of 0.05 (see Appendix B.5).

It is important to note that although CHO cells do not have a endoplasmic reticulum (SR), they are known to have other internal reservoirs of Ca^{2+} (see Section 2.5.1) which may release Ca^{2+} into the cell at higher temperature [Iredale and Hill, 1993, Gamper et al., 2005], further increasing CDI-induced rundown.

5.4 Discussion

In this chapter, patch-clamp experiments at various conditions were used to test if the accumulation of $[Ca^{2+}]$ inside the cell, and the CDI it induces in LCCs is responsible for the perceived rundown of I_{CaL}. While several other processes such as a gradual loss of phosphorylating agents or LCCs themselves have also been reported as causes of rundown, only rundown due to CDI was investigated.

Rundown was defined as the attenuation of peak current *after* the first sweep. While in this study the rundown induced by CDI was considered, there are two ways in which this rundown is different from CDI. Firstly, there might be some amount of CDI that the LCCs have already undergone by the end of the first sweep. However, by the definition of CDI-induced rundown adopted here, only the CDI that the cell experiences *after* the first sweep can be accounted for. Therefore, this sets up a system wherein a cell which experiences the same amount of CDI in each sweep is classified as having less rundown as compared to a cell that experiences increasing amounts of CDI in successive sweeps. However, in such a case the actual amount of CDI experienced by the second cell might be less than the first cell. Rundown therefore refers to the *rate of change* of CDI in this chapter. Secondly, CDI does not just influence the peak I_{CaL}, but also slightly changes the *kinetics* as can be seen in Figure 5.1. However, in this study the CDI-induced changes in the *kinetics* of I_{CaL}

were ignored. While there are nuanced differences between rundown and its implication for CDI in this study, in order to collect data that can be used for calibration of the voltage-dependent part of I_{CaL} models, it is the attenuation of the current that should be avoided, therefore our approach in defining rundown suffices for the purposes of this study.

A weak relationship was shown between the rate of rundown (R_{rate}) observed and the estimate of the intracellular calcium concentration inside the cell. Although this is promising and confirms our hypothesis, there are various other factors that can be affecting its strength. Firstly, a factor of C_m, more specifically $C_m^{3/2}$ was used as a proxy for the volume of the cell. This assumption is valid as long as the relationship between the capacitance and the cell surface area, or the *specific membrane capacitance* (C_s) remains uniform across all cells. While the standing assumption is that this relationship will remain constant across the cells, slight variations in C_s have also been reported [Gentet et al., 2000]. Secondly, it is the local $[Ca^{2+}]$ near the I_{CaL}-channels which are involved in most of the CDI (see Chapter 2), however in this chapter a 'whole-cell' intracellular concentration was used rather than the $[Ca^{2+}]$ 'local' to the LCCs. Finally, this local $[Ca^{2+}]$ is not just determined by the incoming $[Ca^{2+}]$, it is also reduced by its diffusion away from the cell membrane towards the centre of the cell, and chemical reaction with the calcium-chelating buffer (BAPTA) to form a calcium-buffer complex.

In this study, a vast variability was also observed in the amount of rundown recorded at various experimental conditions which cannot be explained by the three varying factors established in this chapter. There must therefore also be other factors that influence intracellular accumulation of Ca^{2+}. Some of these factors might be size of the cell, LCC density, buffering, and diffusing away of Ca^{2+} towards the patch-hole at the centre of the cell.

5.5 Summary

In this chapter, the attenuation of current or rundown of I_{CaL} was investigated qualitatively. The predominant pattern of the rundown-versus-time curve was found to be linear, followed by a saturating pattern where rundown approaches a 'steady state' with time. A full factorial design was performed to test if the intracellular Ca^{2+} contributes towards rundown by varying experimental conditions that affect its accumulation inside the cell.

The results showed an increase in the rate of rundown for experimental conditions at which more intracellular Ca^{2+} accumulation occurs. This was especially evident by the observation of a higher rundown rate at an increased temperature. Interestingly, vast variability was observed in the rundown effect across different cells which could not be explained by the factors considered in this chapter (temperature, holding potential duration between sweeps, and block of I_{NaCa}). In the next chapter, the experimental setup is modelled to see if other factors such as the cell size, LCC density, diffusion, and reaction kinetics can explain, at least in part, the observed variability.

6 | Modelling the effect of calcium accumulation in rundown of L-type calcium current

Part of this chapter has been accepted as a conference paper in the 49th volume of Computing in Cardiology (CINC), available at https://doi.org/10.22489/CinC.2022.051. I received the Bill and Gary Sanders poster award for presenting the associated poster in September, at CINC 2022.

6.1 Introduction

In the previous chapter, patch-clamp experiments were performed where attenuation of I_{CaL} with time (*rundown*), was observed. Although rundown can be attributed to several reasons, it was shown that one of the primary reasons is likely to be the accumulation of intracellular $[Ca^{2+}]$ near LCCs and their subsequent calcium-dependent inactivation (CDI). In this chapter, a mechanistic model of CDI-induced rundown (CIR) of LCCs in a CHO cell is built, in an automated (planar patch)-patch-clamp setting.

In the automated planar patch setup, the cell sits on top of a plate with a punctured hole from where the intracellular solution diffuses into the cell (Figure 6.1, left). This solution also contains a buffer (B) that can react with any free Ca^{2+} to form a Ca^{2+}-B complex (CaB). When the L-type calcium channels (LCCs) open, Ca^{2+} is brought into the cell by I_{CaL}. This initiates a cascade of events, wherein $[Ca^{2+}]$ near the LCCs increases, thus inducing CDI. The Ca^{2+} also reacts with the free buffer present in the cell to form CaB. A concentration gradient is thus created in the cell for the three chemical entities as shown in Figure 6.1 (centre). This causes diffusion of Ca^{2+} and CaB towards the centre of the cell, whereas, the free buffer diffuses towards the LCCs (Figure 6.1, right).

In this chapter, the sequence of events described above are modelled using several components. An I_{CaL} model first simulates Ca^{2+} entering the cell on the application of a voltage-clamp protocol. Next, this is integrated with the chemical reaction of Ca^{2+} with the free buffer followed by diffusion of three chemical species (Ca^{2+}, CaB, and B). Finally, the $[Ca^{2+}]$ near the membrane is fed back to the I_{CaL} model to initiate CDI. The model predicts

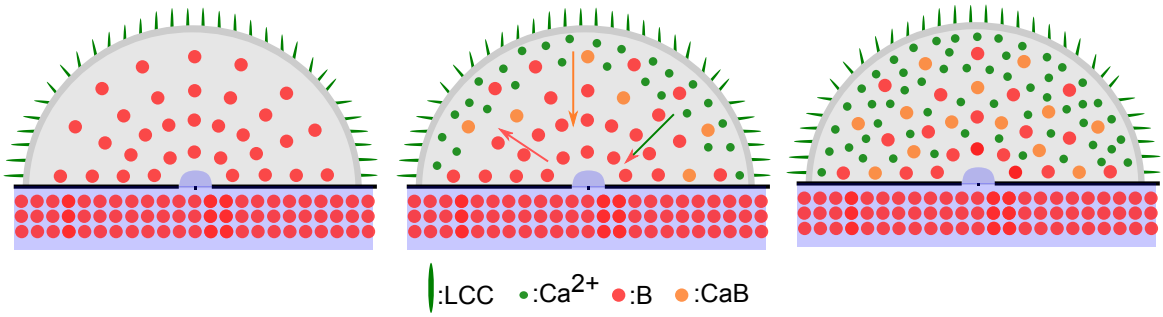

Figure 6.1: Schematic depicting the sequence of events described in text. **Left**: Cell placed on a seal chip before the voltage-clamp is applied and after buffer (B) has equilibrated into the cell. **Centre**: Ca^{2+} enters the cell via the LCCs and reacts with B to form CaB, creating a concentration gradient for all three chemical species. **Right**: Ca^{2+}, B, and CaB diffused into the cell according to their concentration gradient.

the change in spatial concentrations of Ca^{2+}, B, and CaB with time. Primarily, $[Ca^{2+}]$ near the LCCs is of interest because of the CDI it initiates leading to CIR.

First, the simple case of pure diffusion of the free buffer inside a cell is considered, in the absence of any Ca^{2+}. Next, the more complicated case of diffusion and chemical reaction of Ca^{2+}, B, and CaB is modelled followed by CIR of I_{CaL}. Numerical and analytical methods are then adopted to simulate CIR using the model and predict biological and experimental conditions at which the CIR can be minimised. Our model predicts both saturating and inverse shapes of the rundown-versus-time curve observed in data shown in the previous chapter. Further, three time constants are identified in the experiment that show how the relationship between them can be used to predict if CIR will occur in a cell or not. This relationship is then used to conclude that CIR can be avoided by choosing to work with small cells.

6.2 Modelling diffusion of the buffer

This section describes the experimental setup briefly mentioned in Section 6.1 which is used here to model the diffusion of buffer from the patch hole to the entirety of the cell. Since diffusion is not just dependent on time but also space, the axes of symmetry within the cell are also identified. Numerical methods are adopted to simulate diffusion according to cylindrical and spherical axes of symmetry. Finally, an analytical solution of the buffer's diffusion in spherical space is derived.

6.2.1 Shape and symmetry of the cell

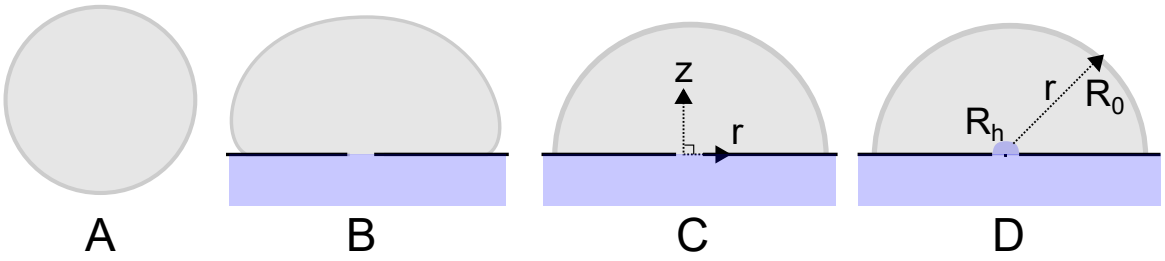

Figure 6.2: A) Schematic of a freely suspended CHO cell, B) CHO cell ruptured and attached to the seal chip plate from which the intracellular solution enters the cell, C) hemispherical shape assumption of the ruptured CHO cell with the cylindrical co-ordinate system, and D) hollow hemispherical model of the ruptured CHO cell showing a spherical co-ordinate system.

Here the shape of the cell is described which is sitting on a chip plate, and its axes of symmetry is established for the automated patch-clamp system used in Chapter 5. To perform patch-clamp experiments, the Chinese hamster ovary (CHO) cells are punctured to allow the intracellular solution to enter the cell. In the automated patch-clamp system used in our experiments, the cell sits on top of the chip plate and the intracellular solution enters the cell from the punctured hole as shown in Figure 6.2B. This results in the 'squashing' of the CHO cell which is otherwise spherical in shape (Figure 6.2A).

In order to model the diffusion of the buffer present in the intracellular solution to the bulk of the cellular cytosol, it is important to consider the shape and the symmetry of the cell. For the purpose of this study, the 'squashed' cell is assumed to be hemispherical in shape. The diffusion of the intracellular solution from the patch hole at $z = 0$ to the entirety of the cell will occur along the axial (z) and radial (r) directions sketched in Figure 6.2C and is therefore cylindrical in symmetry (with a three-dimensional solution that is a function of two co-ordinates r and z). The diffusion of the buffer (BAPTA, denoted by B from hereon), which is a part of the intracellular solution, in these cylindrical coordinates is given by the equation below:

$$\frac{\partial \mathrm{B}}{\partial t} = \frac{D_B}{r}\frac{\partial}{\partial r}\left(r\frac{\partial \mathrm{B}}{\partial r}\right) + D_B\frac{\partial \mathrm{B}}{\partial z^2}, \tag{6.1}$$

here, D_B is the diffusion coefficient of the buffer. The boundary and initial conditions of

the equation are given by:

$$
\begin{aligned}
\mathrm{B}|_{z=0} &= \mathrm{B}_{\max} \quad \text{if} \quad r \leq R_i, \\
\frac{\partial \mathrm{B}}{\partial z}|_{z=0} &= 0 \qquad \text{if} \quad r > R_i, \\
\frac{\partial \mathrm{B}}{\partial r}|_{r=0} &= 0 \qquad \text{and,} \\
\mathrm{B}|_{t=0} &= \begin{cases} \mathrm{B}_{\max} & r \leq R_i \quad \& \quad z = 0, \\ 0 & \text{otherwise.} \end{cases}
\end{aligned}
$$

$\mathrm{B}_{\max}$ is the maximum concentration of the buffer while R_i is the radius of the patch hole. Since it is computationally expensive to run simulations of this set of 2-D equations, I check whether, for this experiment, these 2-D equations might be simplified to a 1-D hemispherically-symmetric solution (with a three-dimensional solution that is a function of just r). To check this, Equation 6.1 was solved for one plane of the cylinder by numerically discretising the boundary and initial conditions using the finite difference method (Appendix D) explicitly [Morton and Mayers, 2005] on a 2-D mesh of size $100 \times 100\,\mu$m with 200 divisions in each direction of the square lattice (and no-flux conditions at maximum r and z).

Figure 6.3 shows the resulting concentration gradient at 1 ms, 10 ms, and 100 ms from the start of the experiment. This figure confirms that the diffusion is approximately radially symmetric for the patch-clamp setup. Therefore, a spherical symmetry was adopted as shown in Figure 6.2D where the surface area of the planar hole in Figure 6.2C was projected onto a hemispherical volume of equivalent curved surface area. The radius of this small hemisphere was thus calculated as $R_h = R_i/\sqrt{2}$.

The diffusion equation of the buffer in spherical coordinates is given by:

$$
\frac{\partial \mathrm{B}}{\partial t} = \frac{D_B}{r^2} \frac{\partial}{\partial r} \left(r^2 \frac{\partial \mathrm{B}}{\partial r} \right). \tag{6.2}
$$

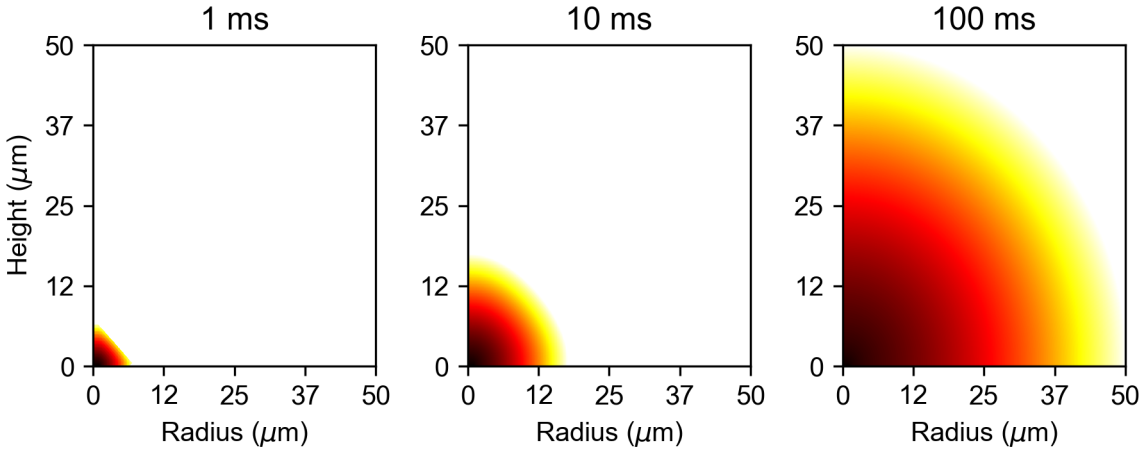

Figure 6.3: Contour map showing the diffusion of the buffer from the patch hole to the whole spherical cell using cylindrical coordinates given in Equation 6.1. The maximum concentration of 10 mM is shown in black while concentration of 0 mM is shown in white. The values of D_B and R_h are given in Table 6.1.

The boundary and initial conditions of the problem in these coordinates is given by:

$$\begin{aligned} \mathrm{B}|_{r=R_h} &= \mathrm{B}_{\max}, \\ \frac{\partial \mathrm{B}}{\partial r}|_{r=R_0} &= 0, \quad \text{and} \\ \mathrm{B}|_{t=0} &= 0; \end{aligned} \tag{6.3}$$

where R_0 is the radius of the cell. To further confirm if the symmetrical approximation of cylindrical symmetry is valid for this experiment, the concentration profile with a 1-D spherical symmetry (adopting a finite difference scheme explicitly [Morton and Mayers, 2005]) is simulated and compared to the cylindrical symmetry simulation at a 45° angle between the cylindrical r and z. Figure 6.4 (top left) shows the resulting concentration gradient. The plots in Figure 6.4 (top right, bottom left, and bottom right) show the time profile of a point 5 μm, 25 μm, and 37.5 μm away from the centre along the 45° angle between the cylindrical r and z. From these simulations, it is concluded that the 2-D cylindrical symmetry of the 'squashed' cell can be simplified to a 1-D spherical symmetry for the purpose of making *qualitative* comparisons as required in this study.

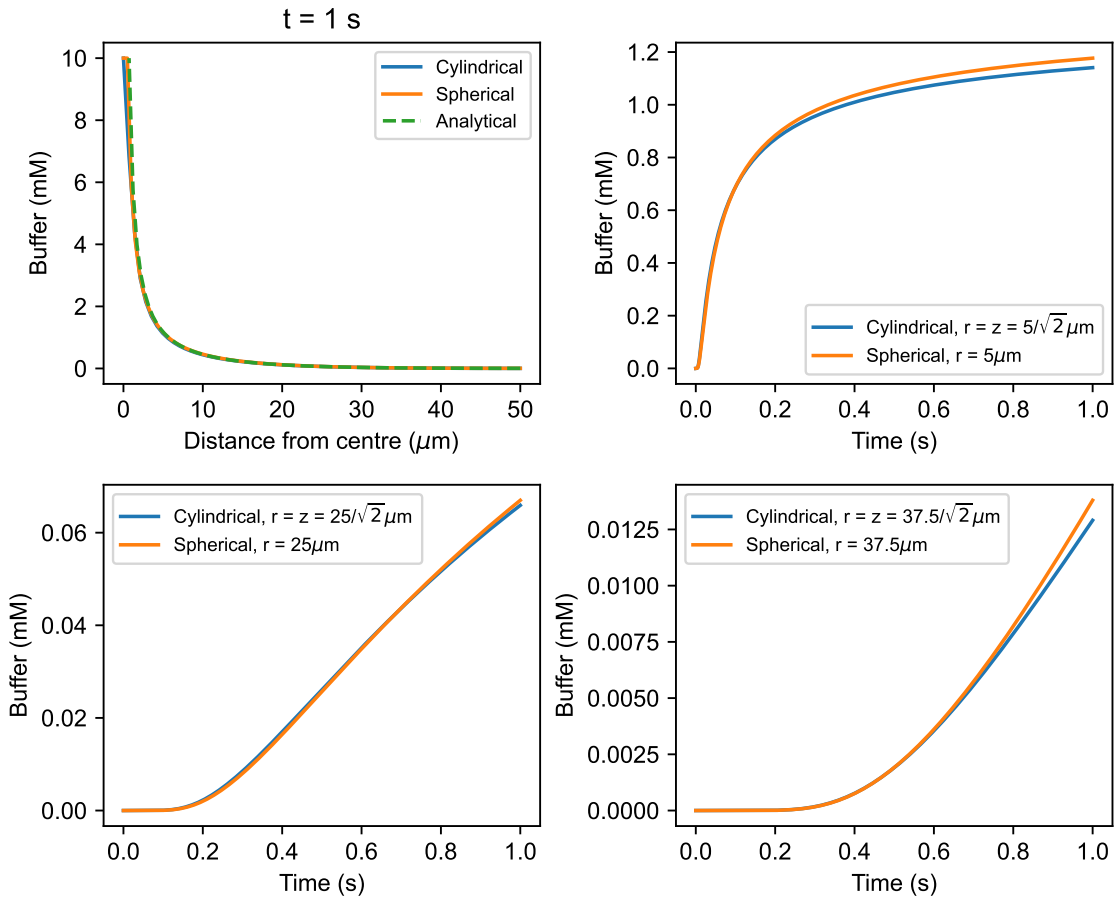

Figure 6.4: Simulation of diffusion of buffer inside a cell while assuming two-dimensional cylindrical and one-dimensional spherical symmetry. All axes of symmetry were discretised to 100 divisions. **Top Left**: The concentration gradient at $t = 1\,\text{s}$ along the 45° angle between the cylindrical r and z for the cylindrical geometry and along the radius r for the spherical geometry. (Also compared against the analytical solution derived in the next section (Equation 6.16)). **Top Right**: The simulation of the concentration with time at the space point 5 μm from the centre of the cell along the 45° angle between the cylindrical r and z for the cylindrical geometry and along the radius r for the spherical geometry. Similarly, **Bottom Left** and **Bottom Right** show the concentration with time at 25 μm and 37.5 μm from the centre of the sphere.

6.2.2 Diffusion of buffer into the cell

Next, the shape and symmetry of the cell are used to derive an analytical equation describing the diffusion of the buffer into the cell. This equation can be used to determine the initial conditions of the buffer concentration with respect to time and space before the application of a voltage-clamp protocol.

From the 1-D spherical approximation, it is known that the concentration of the free buffer

([B]) is a function of the distance from the centre of the hole (r) as well as the time (t) as given in Equation 6.2 along with the boundary and initial condition given by Equation 6.3.

This partial differential equation (PDE) can be non-dimensionalised using $x = \frac{r-R_0}{R_h-R_0}$, $\tau = \frac{D_B t}{(R_h-R_0)^2}$, $u(x,\tau) = \frac{\mathrm{B}_r}{\mathrm{B}_{\max R_h}}$, and solved analytically. These non-dimensionalised entities are now substituted into the PDE and the boundary equations to obtain (simplification shown in Appendix B.6):

$$\begin{aligned} &\frac{\partial u}{\partial \tau} = \frac{\partial^2 u}{\partial x^2}, \\ &u|_{x=1} = 1, \\ &\left[\frac{\partial u}{\partial x} - \frac{hu}{hx-1}\right]_{x=0} = 0, \quad \text{and} \\ &u|_{\tau=0} = 0; \end{aligned} \tag{6.4}$$

where $h = 1 - \frac{R_h}{R_0}$. Equation 6.4 can now be solved using separation of variables similar to the method adopted by Lü and Bülow [2000]. The general solution of Equation 6.4 is given by the trigonometrical series [Lü and Bülow, 2000]:

$$u(x,\tau) = f(x) + \sum_{n=1}^{\infty} [A_n \sin \lambda_n x + B_n \cos \lambda_n x] \exp(-\lambda_n^2 \tau), \tag{6.5}$$

where A_n and B_n are variables to be identified, and λ_n represents the eigenvalue to be determined. $f(x)$ is a linear function determined by the diffusion profile at infinite time [Lü and Bülow, 2000]. Assuming that the buffer will fully equilibrate to the entire cell in infinite time; $u(0,\infty) = \frac{1}{1-h}$, and $u(1,\infty) = 1$. The above equation can then be re-written as:

$$u(x,\tau) = \frac{hx-1}{h-1} + \sum_{n=1}^{\infty} [A_n \sin \lambda_n x + B_n \cos \lambda_n x] \exp(-\lambda_n^2 \tau). \tag{6.6}$$

A_n, B_n, and λ_n can now be determined using the boundary and initial conditions of Equation 6.4.

First applying the boundary condition at $x = 0$ to Equation 6.6::

$$\sum_{n=1}^{\infty} (\lambda_n A_n + h B_n) \exp(-\lambda_n^2 \tau) = 0, \tag{6.7}$$

which is possible only if [Lü and Bülow, 2000]:

$$\lambda_n A_n + hB_n = 0, \quad \text{and} \tag{6.8}$$

$$B_n = -\frac{\lambda_n A_n}{h}. \tag{6.9}$$

Next, applying the boundary condition at $x = 1$ to: Equation 6.6:

$$\sum_{n=1}^{\infty}(A_n \sin \lambda_n + B_n \cos \lambda_n) = 0, \tag{6.10}$$

which is possible only if:

$$A_n \sin \lambda_n + B_n \cos \lambda_n = 0. \tag{6.11}$$

Substituting Equation 6.9 to the above condition:

$$\tan \lambda_n = \frac{\lambda_n}{h}, \tag{6.12}$$

which can be solved to give the eigenvalues of Equation 6.6.

Equation 6.12 has infinitely many roots. Here, the positive roots of this equation are considered to be the particular solution of the PDE (λ_n).

Now that the values of λ_n have been determined, next A_n and B_n were identified by applying the initial condition $u(x, 0) = 0$ to Equation 6.6:

$$-f(x) = \sum_{n=1}^{\infty} A_n F_n(x), \tag{6.13}$$

where $F_n(x) = \sin \lambda_n x - \frac{\lambda_n}{h} \cos \lambda_n x$. A_n can be identified from this relationship by adopting the orthogonality condition derived by Lü and Bülow [2000] using *Sturm-Liouville*

theory [Kreyszig et al., 2008], which gives:

$$\begin{aligned} A_n &= -\frac{\alpha_n}{\beta_n}, \\ \alpha_n &= \frac{1}{h-1}\left[\left(\frac{1}{h}+\frac{h}{\lambda_n^2}-1\right)\sin\lambda_n - \frac{h}{\lambda_n}\cos\lambda_n\right], \\ \beta_n &= \frac{1}{2h^2}\left[\lambda_n^2+h^2+\frac{\lambda_n^2-h^2}{2\lambda_n}\sin 2\lambda_n - 2h\sin^2\lambda_n\right]. \end{aligned} \tag{6.14}$$

B_n can now be determined using Equation 6.9 and Equation 6.14 as:

$$B_n = -\frac{\lambda_n\alpha_n}{h\beta_n}. \tag{6.15}$$

The resultant analytical solution of the diffusion of the buffer is given by Equation 6.16:

$$u(x,\tau) = \frac{hx-1}{h-1} - \sum_{n=1}^{\infty}\frac{\alpha_n}{\beta_n}[\sin\lambda_n x - \frac{\lambda_n}{h}\cos\lambda_n x]\exp(-\lambda_n^2\tau). \tag{6.16}$$

This analytical equation is also compared against the discretised numerical simulation in the previous section (Figure 6.4). Figure 6.5 (left) shows a plot of the analytical solution for different τ.

Figure 6.5 (right) shows the time taken for complete equilibration of the free buffer (t_{diff}) for the range of R_0 values of interest (see Section 6.4.1). This relationship between R_0 and t_{diff} is well-approximated by a cubic function: $0.0077R_0^3 - 0.014R_0^2 + 0.014R_0 - 0.0499$ (later used in Section 6.5.3).

In a real experiment, the time given to the buffer to diffuse into the cell before any Ca^{2+} comes in is often less than t_{diff}, and is given by t_0 (Section 2.5.2).

This section described the simple diffusion of the free buffer (B) in the absence of any Ca^{2+}. The next section explains the integration of Ca^{2+} diffusion, chemical reaction of Ca^{2+} and B, along with the CDI-induced rundown (CIR) of I_{CaL}.

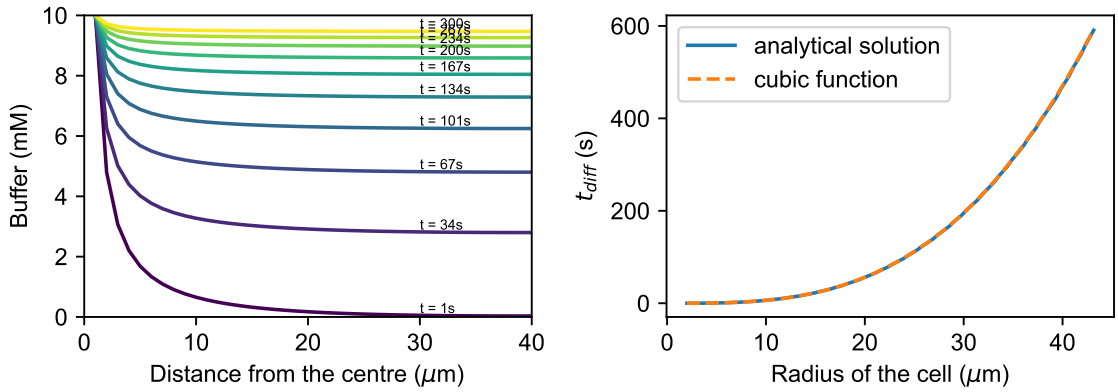

Figure 6.5: The free buffer requires more time to diffuse farther away from the centre and therefore bigger cells require more time to equilibrate. **Left**: Concentration profile of the buffer inside a cell with hemispherical geometry computed at different times using the analytical solution given by Equation 6.16. Here R_0 = 40 μm and the remaining variables are given in Table 6.1. **Right**: Time taken for near complete equilibration (B $\geq$ 0.99B_{max}) at $r = R_0$ for cells of different sizes, calculated using the analytical solution of the diffusion of buffer given by Equation 6.16.

6.3 Modelling diffusion, chemical reaction, and CIR

This section describes the mathematical equations that govern the model of I_{CaL} used in this study and the rationale behind using it. Then the effects of 1) entry of Ca^{2+} via I_{CaL} into the cell, 2) attenuation of I_{CaL} due to CDI, and 3) modification of calcium levels via diffusion along with chemical reaction are combined to simulate CIR.

6.3.1 Model of the L-type calcium current

From Chapters 2 & 3 it is known that I_{CaL} is carried primarily by Ca^{2+}, but also to some extent by Na^+ and K^+. The components can be broken down as:

$$\begin{aligned} I_{CaL} &= I_{CaLCa} + I_{CaLNa} + I_{CaLK}, \\ I_{CaLCa} &= \bar{P}_{Ca} \cdot \delta_{GHK_{Ca}} \cdot O, \\ I_{CaLNa} &= \alpha_{Na} \cdot \bar{P}_{Ca} \cdot \delta_{GHK_{Na}} \cdot O, \\ I_{CaLK} &= \alpha_{K} \cdot \bar{P}_{Ca} \cdot \delta_{GHK_{K}} \cdot O, \end{aligned} \tag{6.17}$$

here, O is the open probability of a single channel, δ_{GHK_X} is the electrochemical force driving the ionic movement of X calculated using the GHK flux equation (see Chapter 2

and Chapter 3), $\bar{P}_{Ca}$ is the maximum permeability which is a function of the total number of channels in a membrane, and α_X is the relative permeability of the ion X with respect to Ca^{2+}.

In this chapter, the I_{CaL} kinetics from the model proposed in Zeng et al. [1995] was adopted because it uses a simple Hill's equation to describe the kinetics for CDI of LCCs. The overall kinetics is given by the simple **type C1** kinetics defined in Chapter 3 [Agrawal et al., 2022]. The gating structure of the model is given by:

$$\frac{\mathrm{d}d}{\mathrm{d}t} = \frac{d_\infty - d}{\tau_d}, \quad \frac{\mathrm{d}f}{\mathrm{d}t} = \frac{f_\infty - f}{\tau_f}, \quad f_{Ca} = 1/(1 + Ca_s/K_{\mathrm{IC50}}), \quad O = d \cdot f \cdot f_{Ca}. \tag{6.18}$$

Here, d_∞, f_∞, τ_d, and τ_f are functions of V_m; Ca_s is the local $[Ca^{2+}]$ near the LCCs and K_{IC50} is the $[Ca^{2+}]$ at which the f_{Ca} becomes half. All the original parameters of the model by Zeng et al. [1995] were used except for the activity coefficients which were changed to be computed using the Davies equation (see Equation 5.6 in Chapter 5).

For the sake of simplicity, I_{CaL} was considered as the only source of Ca^{2+} inside the cell and any contribution by the leak current was ignored. This should not make a difference to the qualitative predictions of CIR as Ca^{2+} from leak anyhow contributes to less than 10% of the total incoming Ca^{2+} (Appendix B.4).

6.3.2 Diffusion and chemical reaction

When the membrane voltage (V_m) is clamped according to the protocols described in the previous chapter (see Section 5.2.2), Ca^{2+} ions are brought into the cell by I_{CaL}, which initiates a cascade of events involving diffusion and chemical reaction shown in Figure 6.1.

The chemical reaction of calcium and the free buffer is considered to be a mass-action reaction given by:

$$[Ca^{2+}] + [B] \underset{k_{off}}{\overset{k_{on}}{\rightleftharpoons}} [CaB],$$

where CaB is the calcium-buffer complex, and k_{on} and k_{off} are the rates of forward and backward reaction respectively. The three chemical species (Ca^{2+}, B, and CaB) simultane-

ously diffuse according to their chemical gradient as well as react as per the reaction above. Considering diffusion in one-dimensional spherical polar coordinates (as in Equation 6.2) along with the mass-action reaction, the rate of change of each species can be written using a PDE as:

$$\frac{\partial[\mathrm{B}]}{\partial t} = \overbrace{\frac{D_B}{r^2}\frac{\partial}{\partial r}\left(r^2\frac{\partial[\mathrm{B}]}{\partial r}\right)}^{\text{diffusion}} - \overbrace{(k_{on}\cdot[\mathrm{Ca}^{2+}][\mathrm{B}] - k_{off}\cdot[\mathrm{CaB}])}^{\text{chemical reaction}}, \tag{6.19}$$

$$\frac{\partial[\mathrm{Ca}^{2+}]}{\partial t} = \frac{D_{Ca}}{r^2}\frac{\partial}{\partial r}\left(r^2\frac{\partial[\mathrm{Ca}^{2+}]}{\partial r}\right) - (k_{on}\cdot[\mathrm{Ca}^{2+}][\mathrm{B}] - k_{off}\cdot[\mathrm{CaB}]), \tag{6.20}$$

$$\frac{\partial[\mathrm{CaB}]}{\partial t} = \frac{D_B}{r^2}\frac{\partial}{\partial r}\left(r^2\frac{\partial[\mathrm{CaB}]}{\partial r}\right) + (k_{on}\cdot[\mathrm{Ca}^{2+}][\mathrm{B}] - k_{off}\cdot[\mathrm{CaB}]). \tag{6.21}$$

Since the molecular weight of the buffer used (in this case BAPTA, which is ∼760 Da) is much higher than that of Ca^{2+} (∼40 Da), the diffusion coefficient of the complex CaB can be assumed to be the same as that of B. Further, the initial and boundary conditions for each of these chemical quantities are given by:

$$\begin{aligned}
&[\mathrm{B}]_{r=R_h} = \mathrm{B}_{\max}; && \left.\frac{\partial[\mathrm{B}]}{\partial r}\right|_{r=R_0} = 0; && [\mathrm{B}]_{t=0} = f(r,t_0);\\
&[\mathrm{Ca}^{2+}]_{r=R_h} = 0; && \left.\frac{\partial[\mathrm{Ca}^{2+}]}{\partial r}\right|_{r=R_0} = \frac{-\mathrm{I}_{\mathrm{CaL}}}{2FAD_{Ca}}; && [\mathrm{Ca}^{2+}]_{t=0} = 0;\\
&[\mathrm{CaB}]_{r=R_h} = 0; && \left.\frac{\partial[\mathrm{CaB}]}{\partial r}\right|_{r=R_0} = 0; && [\mathrm{CaB}]_{t=0} = 0.
\end{aligned} \tag{6.22}$$

Here, A is the surface area of the squished-cell, D_{Ca} is the diffusion coefficient of Ca^{2+}, and F is Faraday's constant. The initial condition for the buffer is a function of both the radial distance from the centre (r) and the time the buffer is allowed to diffuse into the cell before the voltage-clamp experiment begins (t_0). This is given by $f(r,t_0)$ and can be easily calculated for each r given R_0 and t_0 using the analytical solution given by Equation 6.6. The equations governing $\mathrm{I}_{\mathrm{CaL}}$ are given in the previous section and are a function of membrane voltage (V_m), local $[\mathrm{Ca}^{2+}]$ near the LCCs, and time.

Usually, the time-dependent dynamics of [CaB] modelled by Equation 6.21 are not needed if the initial condition of the free buffer is uniform over space and equal to $\mathrm{B}_{\max}$ which happens as $t_0 \to \infty$. In such cases, [CaB] changes as $\mathrm{B}_{\max} - [\mathrm{B}]$ with time. However, this is

not applicable for most cells in this study because t_0 is not large enough to allow complete equilibration of the free buffer; therefore, both [B] and [CaB] (along with [Ca^{2+}]) have been modelled separately.

6.4 Methods

The previous sections established the mathematical model used in this study, this section now describes the methods adopted to simulate CIR using the model defined in Section 6.3, the inputs and parameter values of the model, and a simplified proxy to investigate CIR predicted by the model.

6.4.1 Parameter values

This section describes how the parameter values for the model have been selected. Some values have been established from the experimental conditions while others have been estimated using the capacitance and current recordings of Chapter 5. The remaining variables have been taken from values reported in literature.

First, the variables that were determined from the experimental setup are discussed. The maximum concentration of the free buffer (B_{max}) was determined by [BAPTA] used in the intracellular solution and is given in Table 5.1 of Chapter 5. The radius of the projected hollow-hemisphere (R_h) was determined from the physical setup of the experiment. It was estimated by equating the surface area of the planar patch-hole onto the curved surface area of the hollow-hemisphere. Since the radius of the hole on the seal chip plate in this experiment was 1 μm, by equating the surface areas; R_h can be calculated as: $1/\sqrt{2}\,\mu$m. Additionally, the time between exposure of the cell to the intracellular solution and the application of the voltage-clamp (t_0) varies from one cell to another. Five seconds before the application of the voltage-clamp, a suction was applied to the cells before taking recordings in Chapter 5. Since some cells only rupture after the application of the suction (thus allowing the intracellular solution to enter), the lower bound of t_0 was assumed to 5 seconds. On the other hand, the time between the cell being put on the seal chip plate and the application of the membrane-voltage clamp was 5 minutes. Since some cells can rupture as soon as they are exposed to the chip, the upper bound for t_0 was assumed to be 5 minutes.

Similar to t_0, the radius of the cell R_0 varies from cell-to-cell, however its range was estimated through a combination of capacitative and microscopic recordings. The two techniques used to estimate this range are shown via a flowchart in Figure 6.6. In the first method, the radius of the cell measured under a microscope before the patch-clamp experiment was conducted was used. Within this, the measurement could have corresponded to a hemispherical or a spherical cell. Assuming that the volume of the cell remained conserved, the volume of the cell before and after can be equated in both cases to determine the new range of the cell's radius. Exhaustively, using the microscopic measurements, the possible radius of the cell in the study can vary from 2 μm to 25.14 μm (Figure 6.6). In an alternative method, R_0 was estimated using the C_m measured from the Syncropatch, by assuming that the specific capacitance of all cells was 1 μF/cm^2. Now, there are further two kinds of variations here: one where the surface area only consists of the curved portion of the hemisphere and the other where both the curved hemisphere and flat surface pressed against the chip plate contribute to the surface area. Exhaustively, this results in a variation of the radius from 8.3 to 40.6 μm (using the 6.6–104 pF range of the capacitance estimates from recordings shown in Appendix B.1). Considering the extreme R_0 estimates using both techniques, R_0 can be considered to vary from 2 to 40.6 μm.

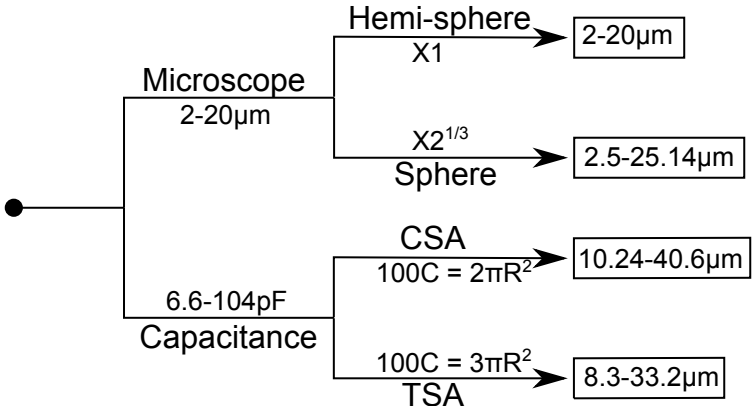

Figure 6.6: Flowchart showing the possible range of the cell's radius. Here CSA — curved surface area and TSA — total surface area.

Next, the range of $\bar{P}_{Ca}$ is considered. From the post-processed current recorded (shown in Figure B.3, left), it is known that the peak current value recorded during a sweep varies from -490.7 pA to -4444.4 pA while the peak value of the quantity $(O \times \delta_{\text{GHK}})$ during the step to 0 mV for the model used in this study is -97458.1 C/m^3 (shown in Figure B.3, right). Therefore, the $\bar{P}_{Ca}$ value ranges from 0.005 nL/s to 0.0457 nL/s $(I/(O \times \delta_{\text{GHK}}))$.

The parameter values mentioned in this section along with that of the diffusion coefficients and equation rates as taken from literature are given in Table 6.1. For parameters that can vary across a range, the default value used in this chapter has been listed in this table in addition to the permissible range in brackets.

The model was used to simulate the step voltage protocol adopted from the one defined in Section 5.2.2. The duration of the voltage step to 0 mV was reduced to 120 ms interspersed with a holding potential at −90 mV.

The three factors varied across experiments in the previous chapter were the holding time between two sweeps (t_{hold}), temperature, and presence/absence of I_{NaCa} blocker. In this chapter, CIR was simulated only in the absence of I_{NaCa} (presence of blocker), at 310 K, and unless mentioned otherwise, at a t_{hold} of 10 s. A physiologically-relevant temperature was chosen for the simulations and it was out of the scope of this study to select and calibrate a model of I_{NaCa} for CHO cells overexpressing $Ca_V1.2$.

Parameter	Value
α_K	5×10^{-4} [Shannon et al., 2004]
α_{Na}	2.78×10^{-5} [Shannon et al., 2004]
K_{IC50}	0.9×10^{-6} mM
D_{Ca}	4×10^{-9} cm^2/ms [Wu et al., 1996, Kits et al., 1999]
D_B	2×10^{-9} cm^2/ms [Nowycky and Pinter, 1993]
k_{off} at 310 [K]	0.298 ms^{-1} [Lattanzio Jr and Bartschat, 1991]
k_{on} at 310 [K]	1700 mM^{-1}ms^{-1} [Lattanzio Jr and Bartschat, 1991]
B_{max}	10 mM
R_h	$\frac{1}{\sqrt{2}}$ μm
R_0	30 μm (2 μm, 40.6 μm)
t_0	180 s (5 s, 300 s)
$\bar{P}_{Ca}$	0.04 nL/s (0.005 nL/s, 0.046 nL/s)

Table 6.1: Parameters used as input for the model to predict CIR. Values taken from the literature are cited here with the appropriate reference while the others are discussed in the text. Parameters for which the exact value may vary across a range, the default value used in this chapter has been listed while the range is shown in brackets.

6.4.2 Simulation methods

Having now established all the elements that comprise the CIR model in Equations 6.17–6.22, this section describes the simulation methods used for these equations.

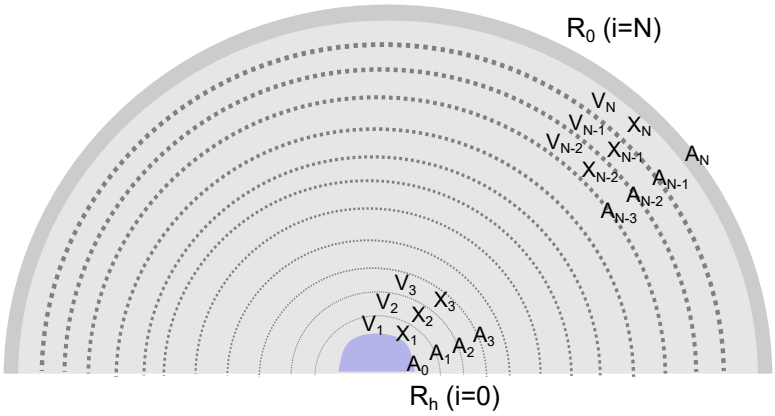

Figure 6.7: Schematic showing discretisation of the hemispherical cell into N shells.

Equations 6.19–6.21 were solved by adopting the finite volume method [Fallah et al., 2000] and dividing the hemispherical cell of radius R_0 into N shells as shown in Figure 6.7. Then the diffusion terms were rewritten as a difference in flux using Fick's first law of diffusion; this reduced the equations from a second order PDE to a set of first order ODEs. The chemical species in each discretised shell was computed from $i = 1$ to $N - 1$ using the equation:

$$\frac{\mathrm{d}[\mathrm{X}]_i}{\mathrm{d}t} = \overbrace{D_X \frac{A_i([\mathrm{X}]_{i+1} - [\mathrm{X}]_i)}{LV_i}}^{\text{flux across outer boundary}} - \overbrace{D_X \frac{A_{i-1}([\mathrm{X}]_i - [\mathrm{X}]_{i-1})}{LV_i}}^{\text{flux across inner boundary}} \pm \overbrace{(k_{on} \cdot [\mathrm{Ca}^{2+}]_i[\mathrm{B}]_i - k_{off} \cdot [\mathrm{CaB}]_i)}^{\text{chemical reaction}}, \quad (6.23)$$

where X represents the chemical species — Ca^{2+}, B, and CaB. Here, $L = (R_0 - R_h)/N$, $V_i = \frac{2}{3}\pi((R_0 - (N - i) \cdot L)^3 - (R_0 - (N - (i - 1)) \cdot L)^3)$, and A_i was calculated at each boundary as $2\pi((R_0 - (N - i) \cdot L)^2$. At $i = N$ boundary (in the outermost shell), there is no flux across the outer boundary for [B] and [CaB], however there is a voltage- and time-dependent flux of $[Ca^{2+}]$ given by $-\mathrm{I}_{\mathrm{CaL}}/(2FV_N)$. The constant values of the species $[\mathrm{X}]_0$ along with the initial conditions are given by the conditions outlined in Equation 6.22 at $r = R_h$ and $t = 0$ respectively. The value of the constants used in this chapter are given in Table 6.1 of Section 6.4.1.

Simulations of the above discretised system of equations was performed using Myokit version 1.33.0 [Clerx et al., 2016], with the CVODE version 5.7.0 (CVODE is described in Appendix D). The solver's absolute and relative tolerances were set to 10^{-7}. The system

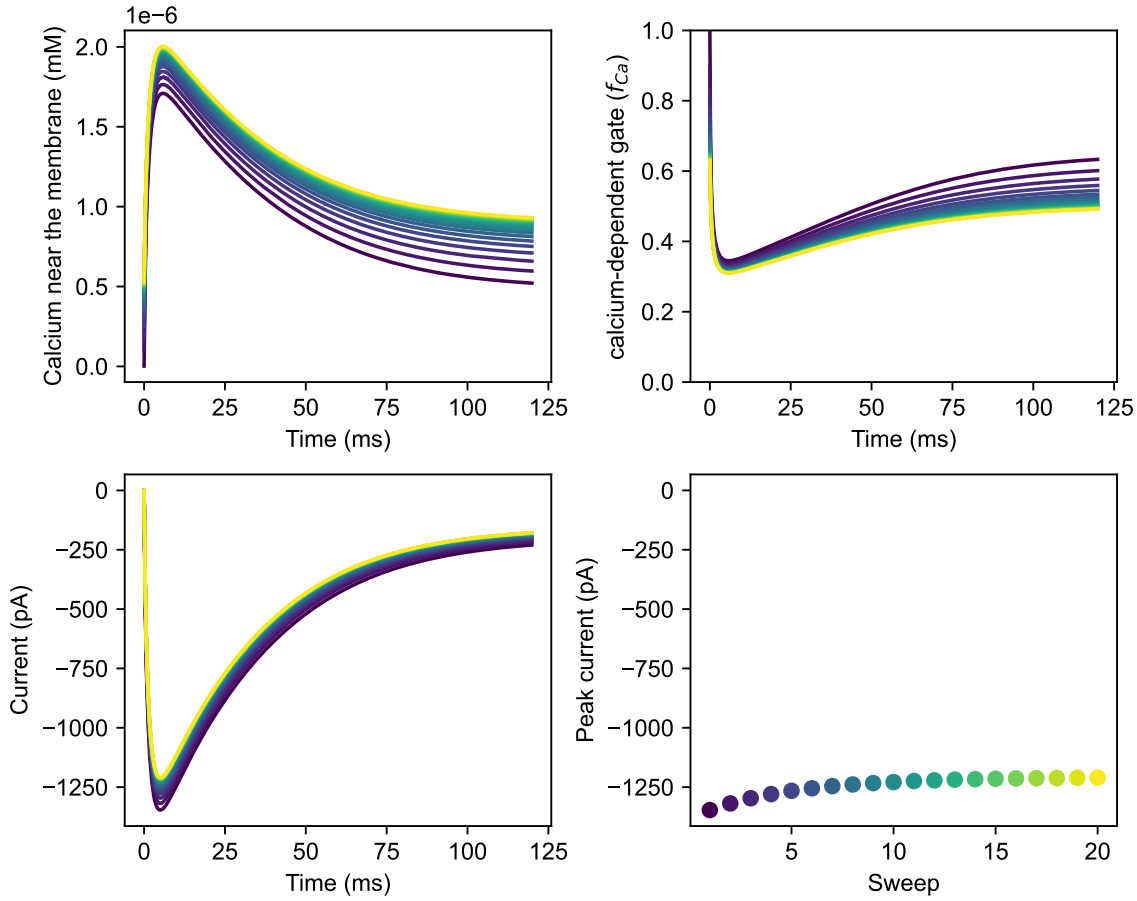

Figure 6.8: **Top Left**: Simulation of the local $[Ca^{2+}]$ near the membrane, **Top Right**: Simulation of the CDI gate (f_{Ca}), and **Bottom Left**: Simulation of I_{CaL} during the V_m step to 0 mV for successive sweeps with indigo and yellow corresponding to the first and last sweep respectively. **Bottom Right**: Peak I_{CaL} simulated at each sweep against the sweep number. CIR was simulated at default values given in Table 6.1.

was discretised such that the shell width (L) was ≈0.05 μm, which was the minimum L required to ensure negligible error as shown in the convergence tests in Appendix B.7 (using the analytical solution for the diffusion of [B] derived in Section 6.2.2 for comparison). For simulations in which the default cell size (30 μm) is used, the convergence condition implies that N should be at least 600.

The CIR shown in Figure 6.8 (bottom right) has been simulated at the default values of Table 6.1. On applying the voltage protocol, Ca^{2+} enters the cell via I_{CaL}. Although this Ca^{2+} is subject to diffusion and buffering as previously explained, some amount of calcium accumulates with time near the cell membrane in subsequent sweeps as shown in Figure 6.8 (top left). The increase in $[Ca^{2+}]$ per sweep is responsible for the decrease in the magnitude

of the CDI gate of I_{CaL}, f_{Ca} in each sweep (Figure 6.8, top right). This in turn attenuates the magnitude of the source of Ca^{2+} itself — I_{CaL} (Figure 6.8, bottom left), thus contributing to CIR of the current. The peak I_{CaL} at each sweep is plotted in Figure 6.8 (bottom right). This shows that a saturating shape of rundown-versus-time curve is predicted at default values of the model and protocol parameters selected in this study.

6.4.3 Relationship of shell width and CDI gate

In the previous section, CIR was simulated at the default parameter of the CDI gate (f_{Ca}), wherein, $K_{IC50} = 0.9\,\text{nM}$. This section shows how (and why) the value of K_{IC50} is embedded within the numerical scheme. This is followed by the suggestion of using $[Ca^{2+}]$ transient as a proxy for I_{CaL} to study rundown. Finally, the translation of the shape of the rundown-versus-time curve onto the shape of (peak $[Ca^{2+}]$)-versus-time curve is shown.

How the numerical scheme affects concentration

To simplify visualisation, a 'cuboidal' cell is considered, wherein Ca^{2+} diffuses in from the side as shown in Figure 6.9. This cell has been discretised using two schemes such that the number of divisions in Scheme 2 is twice that in Scheme 1. This discretisation along with the concentration gradient implies that the concentration on the right-hand side will always be greater than the concentration on the left-hand side. Therefore, the number of moles in the first meshed cell of Scheme 1 (n) will be the average of the number of moles in the first two meshed cells in Scheme 2 (n_A and n_B). To see how the predicted current changes in both schemes, components of I_{CaL}'s equations which can vary depending upon the choice of discretisation (i.e. terms with some concentration or volume component: δ_{GHK} and f_{Ca}) are individually considered. Since the extracellular $[Ca^{2+}]$ is several folds higher than the internal concentration, differences in δ_{GHK} are negligible between the two schemes.

The schematic in Figure 6.9 is used to prove through contradiction that K_{IC50} is embedded in the numerical scheme. Using Equation 6.18 it can be said that for f_{Ca} to be equivalent in both schemes, $[Ca^{2+}]/K_{IC50}$ should be equivalent. If K_{IC50} is equal in both schemes, it implies that [Ca] is also equal, which is only possible if $n_A = n/2$ (see Figure 6.9). However, this is a contradiction since diffusion is happening from the right-hand side, therefore n_A has to be greater than $n/2$. This contradiction implies that the assumption of $[Ca]/K_{IC50}$

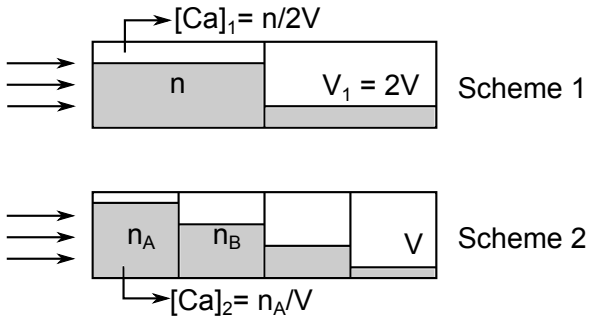

Figure 6.9: Schematic showing the impact of discretisation on the resultant concentration of $[Ca^{2+}]$ near the membrane in a simplified "cuboidal" cell. Schematic 2 has twice the number of divisions of Schematic 1. Here Ca^{2+} enters via I_{CaL} from the left-hand side, V is the volume, and n, n_A, and n_B represent the number of moles in each compartment.

being equal across the two schemes is incorrect, and therefore K_{IC50} is embedded in the numerical scheme.

The logical argument presented above can be extended to say that as N increases, the corresponding K_{IC50} also increases. This relationship was confirmed by generating synthetic I_{CaL} for one sweep at the default parameters like the plot shown in Figure 6.8 (bottom left). A series of models were then created by varying the shell width (L) from 0.043 μm to 0.060 μm, which were then fit to the synthetic data to infer the new K_{IC50} while the remaining parameters were kept constant. Inference of the parameter was performed using the Nelder-Mead global optimisation algorithm (Appendix D), as incorporated into the open source Python package PINTS [Clerx et al., 2019b]. Figure 6.10 shows the inferred K_{IC50} plotted against the corresponding L for each model, showing that the K_{IC50} has an inverse relationship with the shell width.

Calcium-transients used as a proxy to study rundown

To prevent the choice of numerical scheme from influencing the results of this study, the effect of f_{Ca} is blocked completely, and instead trends of peak $[Ca^{2+}]$ were used as a proxy for investigating CIR. This allows the impact of CIR to be studied separately from the source of $[Ca^{2+}]$ (I_{CaL}). Since the model is designed such that CIR is dependent on the local $[Ca^{2+}]$ near the I_{CaL} channels, it is necessarily sufficient to investigate the causes behind the increase in local $[Ca^{2+}]$ from one sweep to the other rather than explicitly studying I_{CaL}. Therefore, results of this chapter show the simulation of transient $[Ca^{2+}]$ during each I_{CaL} channel activation step.

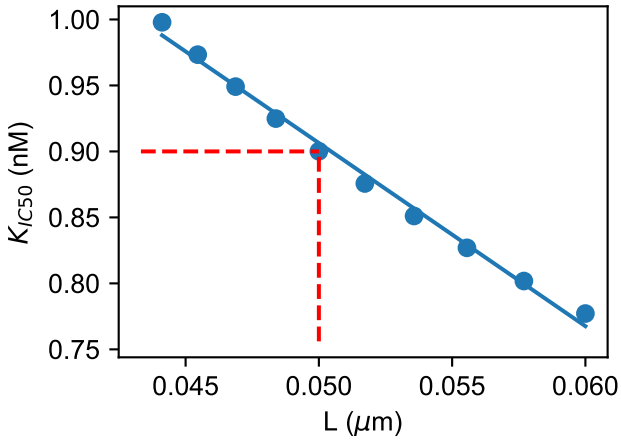

Figure 6.10: Inferred K_{IC50} plotted against L, each combination replicates the first sweep of I_{CaL} simulated at the default parameters (highlighted in red) and shown in Figure 6.8 (bottom left).

Translation of rundown trends to peak calcium trend

Next, the non-linear translation of the shape of the rundown-versus-time curve to the shape of the (peak $[Ca^{2+}]$)-versus-time curve is described. For all three rundown patterns identified in Chapter 5 (linear, saturating, and inverse), the equivalent pattern of the (peak $[Ca^{2+}]$)-versus-time is established, assuming that all of them occur due to CDI. This is done by first investigating the relationship between I_{CaL} and $[Ca^{2+}]$. When comparing the peak I_{CaL} and peak $[Ca^{2+}]$ at successive sweeps, the voltage-dependent kinetics remains the same, and only f_{Ca} changes, therefore the relationship can be written using a positive constant α as:

$$\begin{aligned} I &= -\alpha \cdot f_{Ca}, \\ I &= -\alpha \cdot \frac{1}{1 + [Ca^{2+}]/K_{\text{IC50}}}, \end{aligned} \tag{6.24}$$

where I is the peak I_{CaL} during the activation step. This equation can be re-written as:

$$[Ca^{2+}] = -K_{\text{IC50}} \left(1 + \frac{1}{I_{norm}}\right), \tag{6.25}$$

where, I_{norm} is the normalised current I/α.

Equation 6.25 can now be used to determine the qualitative trend of peak $[Ca^{2+}]$ corresponding to each pattern of rundown. The top row of Figure 6.11 shows different linear,

saturating, and inverse functions which resemble the different patterns of rundown-versus-time plot identified in Chapter 5. These functions are taken as I_{norm} and passed through Equation 6.25 to obtain the corresponding pattern of (peak $[Ca^{2+}]$)-versus time curve.

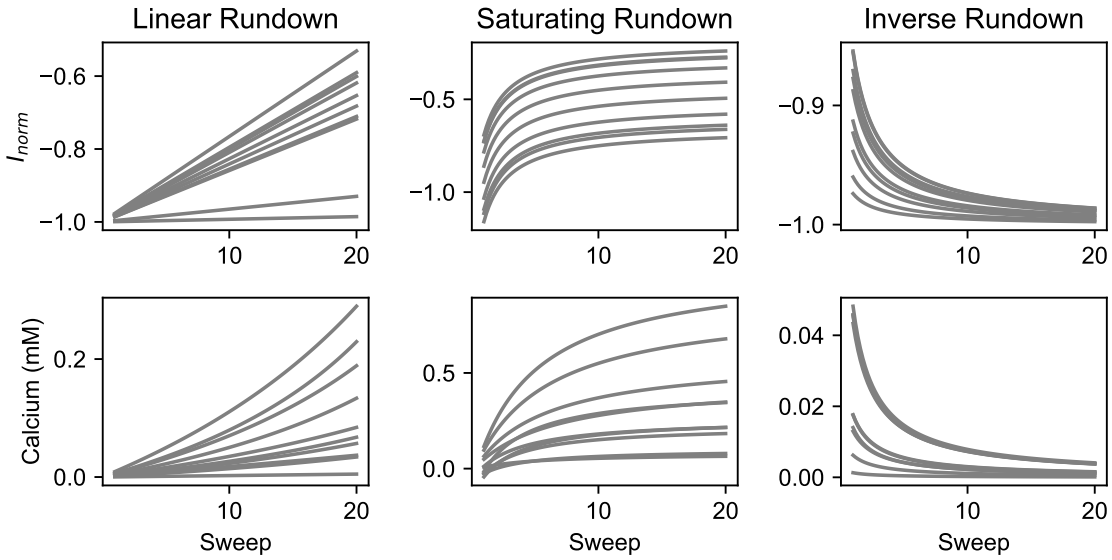

Figure 6.11: **Top Row**: Functions resembling the shapes of rundown-versus time curve observed in patch-clamp experiments. **Bottom Row**: The corresponding shape of (peak $[Ca^{2+}]$)-versus-time curve for each type of rundown pattern obtained using Equation 6.25 by varying K_{IC50}.

This plot of I_{norm} and peak $[Ca^{2+}]$ shows that for a linear pattern of rundown, the corresponding pattern of peak $[Ca^{2+}]$ will be hyperbolic or linear (left column of Figure 6.11). For saturating and inverse patterns of rundown, the corresponding pattern of (peak $[Ca^{2+}]$)-versus-time remains unchanged (centre and right columns in Figure 6.11). Finally, it is self-explanatory that for no rundown, there would correspondingly be no change in peak $[Ca^{2+}]$ across sweeps.

In the results presented in the next section, the shape of the (peak $[Ca^{2+}]$)-versus-time curve at various conditions is studied and translated back to the corresponding pattern of rundown using Figure 6.11.

6.5 Results

6.5.1 CIR at extremes of experimental conditions

In this section, the effect of the range of the experimental variables, that is, radius of the cell (R_0), initial time (t_0), and permeability of the membrane channels ($\bar{P}_{Ca}$), given in Table 6.1 on the peak $[Ca^{2+}]$ pattern is explored. This is done by simulating the voltage-clamp protocol described in Section 6.4.1, while one by one considering the extreme values of the three variables resulting in eight sets of conditions (2^3).

Figure 6.12 shows the simulation of the local calcium and free buffer concentrations near the LCCs for each of the eight conditions. Within each plot, the $[Ca^{2+}]$ transients simulated during the channel opening steps of successive sweeps are plotted next to each other. These transients are useful to see how the $[Ca^{2+}]$ changes within a single sweep, however, CIR is only affected by inter-sweep changes in *peak*-$[Ca^{2+}]$ which is used to determine the shape of the rundown-versus-time curve.

Based on the results of Chapter 5, it is reasonable to expect that there should be more CIR when more Ca^{2+} comes into the cell. Figure 6.12 shows that increasing $\bar{P}_{Ca}$ from left to right in each row (increased incoming Ca^{2+}), increases CDI (which is accompanied by increased depletion of [B]: compare A with B and C with D). However, while the CDI has increased, the corresponding trend of CIR which is defined by the *rate of change* of CDI does not change for the first two rows. This suggests that merely increasing the local intracellular $[Ca^{2+}]$, and the corresponding CDI is not enough to induce CIR if rundown does not occur at a smaller $[Ca^{2+}]$. This seems contradictory to the findings of Chapter 5, where increased rundown rate was observed for conditions that correspond to increasing incoming of Ca^{2+} (smaller t_{hold}) and reduced extrusion of Ca^{2+} (blocked I_{NaCa}). This can be explained by the finding that while increasing $\bar{P}_{Ca}$ is not enough to induce attenuation of I_{CaL} due to CDI where not present, it does lead to a slight increase in CIR where it is present (indicated by faster increase in peak $[Ca^{2+}]$ when comparing G to H).

It is apparent that rundown-like shape of the (peak $[Ca^{2+}]$)-versus-time curve is only observed for large cells (bottom two rows of Figure 6.12). Bigger cells require more time for complete equilibration of buffer into the cell (t_{diff}) than smaller cells.

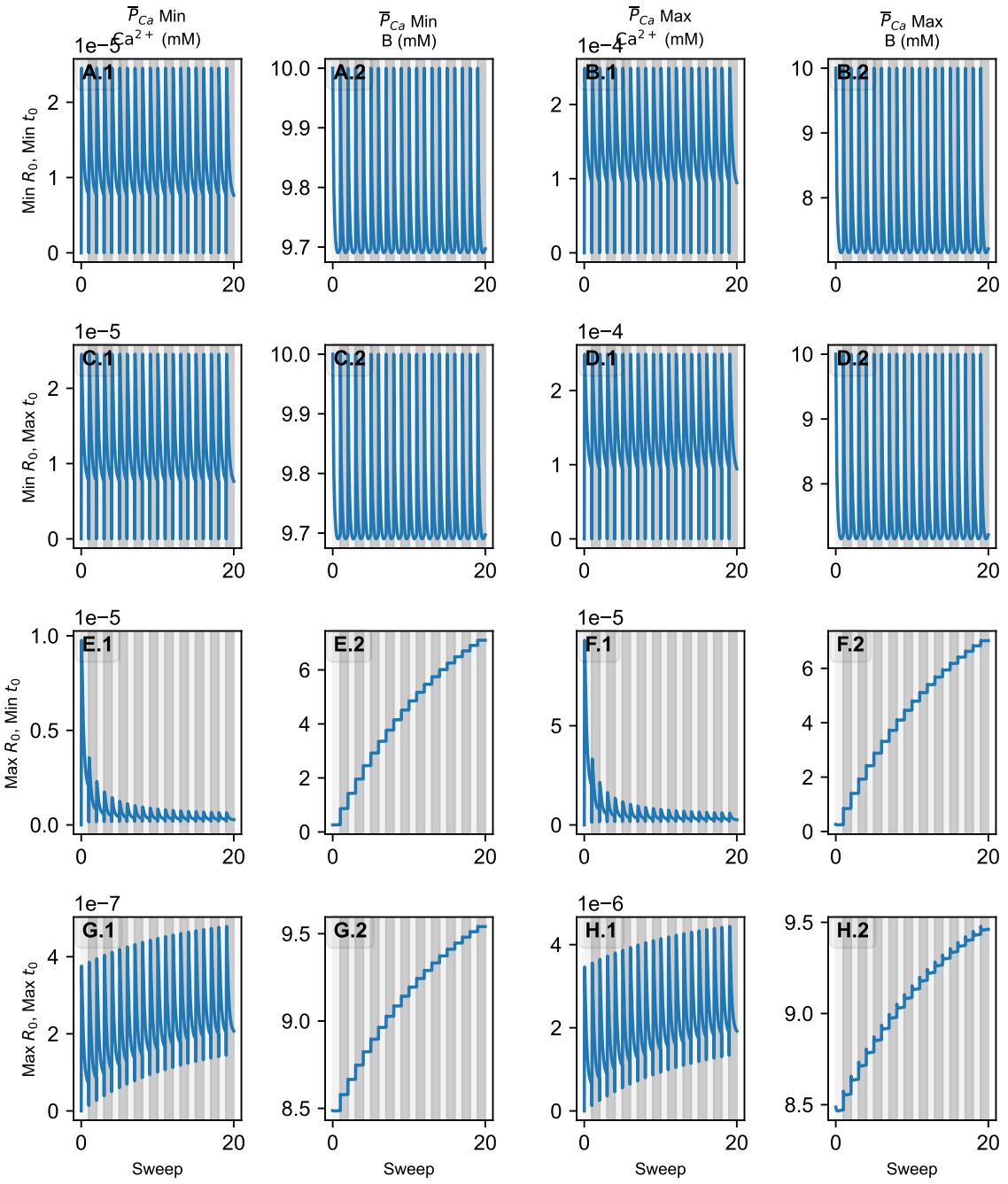

Figure 6.12: Calcium and free buffer concentrations simulated near the I_{CaL} channels during the channel opening steps to 0 mV plotted successively (alternating grey backgrounds represent simulations from different sweeps). These simulations were performed for eight unique conditions spanning over the corner cases of $\bar{P}_{Ca}$, t_0, and R_0 mentioned in Table 6.1, while the remaining model variables and protocol conditions were held at default values.

Next, for large enough cells in which rundown-like patterns are observed, variation in t_0 switches the trend of rundown. A larger t_0 allows buffer to equilibrate into the cell before the voltage-clamp is applied while a smaller t_0 does not, thus affecting the initial conditions of the free buffer state variables ($[B]_i$). If t_0 is small, $[Ca^{2+}]$ decreases per sweep before saturating which is typical of a 'reverse' rundown (E and F), whereas if t_0 is large, $[Ca^{2+}]$ increases per sweep before saturating (saturating rundown) (G and H). While the accumulation of $[B]$ per sweep increases at both the extremes of t_0, it increases substantially more for very small t_0.

This section shows that of the three types of rundown patterns identified in Chapter 5, two of them — saturating and inverse rundown — can be explained by the CIR model developed here at different experimental conditions. Where, t_0 and t_{diff} seem to be important factors that determine both the possibility of CIR and further the shape of the rundown-versus-time curve.

6.5.2 Rundown at default experimental conditions

Next, the model was used at default parameters while changing only one of the experimental variables ($\bar{P}_{Ca}$ or t_0) to simulate the I_{CaL} response to the voltage-clamp protocol.

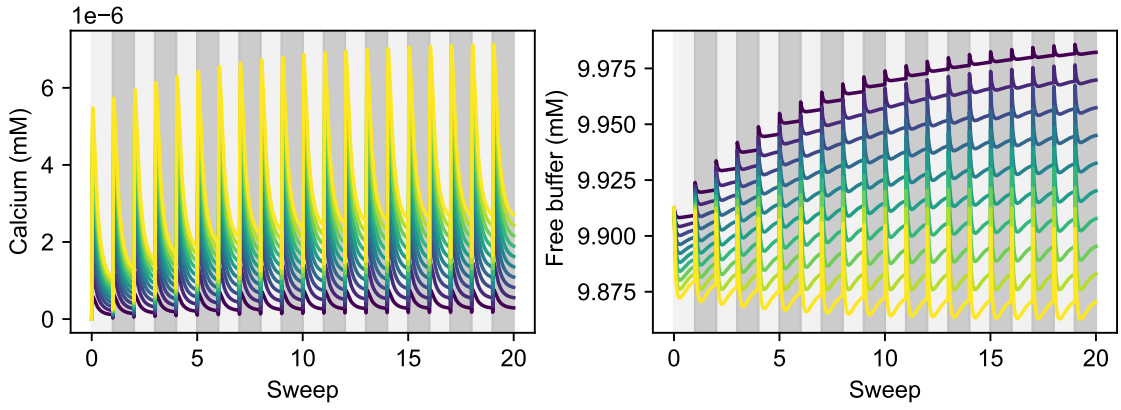

Figure 6.13: Simulation of $[Ca^{2+}]$ (**Left**) and $[B]$ (**Right**) near LCCs plotted successively for each sweep. These simulations were performed at default conditions while $\bar{P}_{Ca}$ was varied from 0.005 nL/s (indigo) to 0.046 nL/s (yellow).

Figure 6.13 shows the simulation of calcium and free buffer concentrations in successive channel opening steps. This simulation is performed at default conditions, however, $\bar{P}_{Ca}$ is varied across the experimentally permissible range. Figure 6.12 shows that changing

$\bar{P}_{Ca}$ (which is biologically reflective of channel density and chemically the amount of Ca^{2+} entering the cell), is not able to affect *whether* CIR happens or not. However, Figure 6.13 confirms that increasing $\bar{P}_{Ca}$ always contributes to an increased CDI, which *can* translate to inducing an increased rate of change of CDI (which is CIR), *if* such a rate change already exists at lower values of $\bar{P}_{Ca}$ (as is also apparent from the last row of Figure 6.12).

Interestingly, changes in [B] show that two different kinds of underlying mechanisms are contributing to CIR. In the first case, even though the $[Ca^{2+}]$ increases per sweep, the corresponding [B] also increases per sweep (small $\bar{P}_{Ca}$ simulations in Figure 6.13 and last row in Figure 6.12). This increase in [B] occurs despite near maximum concentration having already been attained suggesting that more buffer diffuses to the cell periphery between sweeps than the amount used up. One possible explanation of the counter-intuitive increase of both $[Ca^{2+}]$ as well as [B] can be that the reaction kinetics of the two entities try to attain 'quasi'-equilibrium concentrations. In the second case, an increase in $[Ca^{2+}]$ is accompanied by a reduction in the free buffer per sweep (high $\bar{P}_{Ca}$ simulations in Figure 6.13), which is more intuitive and can be simply explained by the slow rate of diffusion of the free buffer to the cell periphery causing it to be depleted faster than it can be replenished.

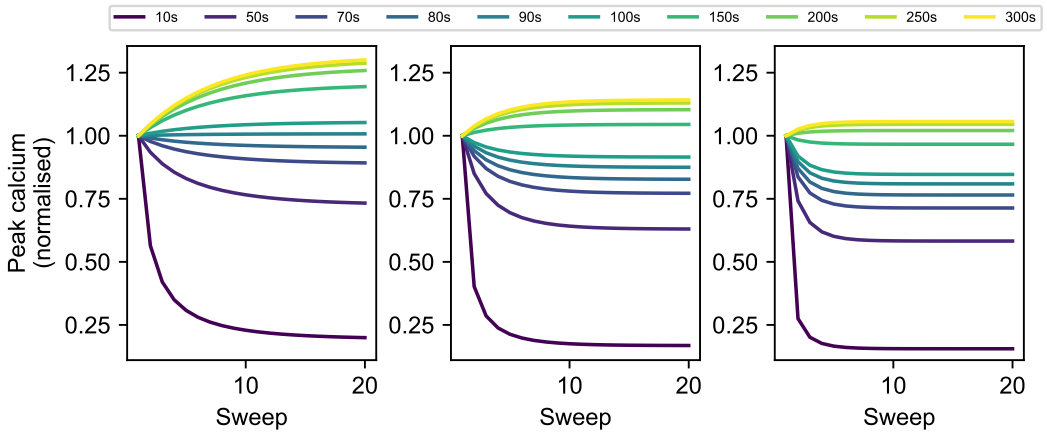

Figure 6.14: Peak $[Ca^{2+}]$ recorded at steps to 0 mV at each sweep normalised by the first peak. These simulations were performed at varying t_0 as shown in the key and otherwise default conditions with the holding potential maintained for a duration (t_{hold}) which varies as 10 s (**Left**), 20 s (**Centre**), and 40 s (**Right**).

The diffusion of free buffer into the cell *between* sweeps also plays an important role in determining the [B] kinetics. Therefore, CIR is simulated at varying times between sweeps (t_{hold}). Figure 6.14 shows the normalised peak $[Ca^{2+}]$ (normalised by the peak $[Ca^{2+}]$ in the

first sweep) simulated for 20 sweeps at $t_{hold} = 10\,s$ (left), 20 s (centre), and 40 s (right) for the CIR model at otherwise default conditions. Each panel shows the model predictions at ten different values of t_0 varying from 10 s to 300 s. Each subplot shows that at very small t_0, the rundown trend is inverse while at bigger t_0, this trend becomes saturating. This is also consistent with the observation of change in pattern of rundown from E to G and F to H in Figure 6.12. There seems to be a critical t_0 that switches the rundown pattern, which, interestingly, changes depending upon t_{hold}. This is evident from the observation that this critical t_0 increases on increasing t_{hold} shown by the higher number of inverse rundown trends in the right panel of Figure 6.12 than the left and centre panel.

6.5.3 Experimental time scales determine rundown and its trend

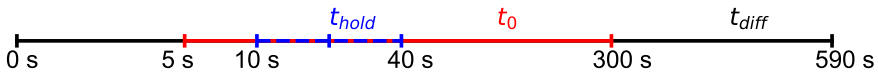

Figure 6.15: The range of values possible for 1) time taken for complete equilibration of the free buffer into the cell (t_{diff}), 2) initial time before experiment begins (t_0), and 3) time between successive voltage pulses (t_{hold}). Solid lines indicate values that can be continuous, t_{hold} is indicated in dashed lines because it can only take the discrete value $\in \{10, 20, 40\}$ s.

The results discussed until now show that *whether* CIR occurs or not depends on the size of the cell (which can be indicated by t_{diff}). Further, *if* CIR does occur, then its trend (saturating or inverse) is determined by a combination of two time constants — t_0 and t_{hold}. Extending the findings from the previous sections, these three different time scales that seem critical to simulating CIR are compared. The permissible range of t_0 is known from Table 6.1 in Section 6.4.1. Three different possible values of t_{hold} (10, 20, and 40 s) are assumed as per the possible variations of the voltage-step protocol in Chapter 5. Finally, t_{diff} is calculated using the analytical solution derived in Section 6.2.2, and for the range of the cell size in this study (see Section 6.4.1) it is found to vary from 0 to 590 s as shown in Figure 6.5, right. The number line in Figure 6.15 shows the range of the three time scales and how they overlap. By randomly drawing each time from its permissible range on the number line, three different conditions for the experimental time scales can be identified — where t_{diff}, t_0, or t_{hold} is the smallest time compared to the other time scales.

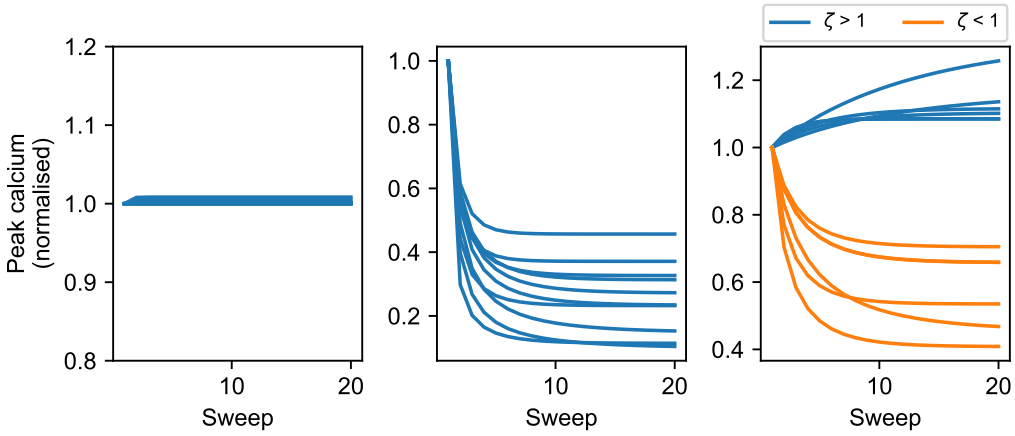

Figure 6.16: Normalised peak $[Ca^{2+}]$ across sweeps predicted by the CIR model when all three time scales are randomly drawn from their permissible range such that the minimum time is t_{diff} (**Left**), t_0 (**Centre**), and t_{hold} (**Right**). The value of ζ is given by Equation 6.26.

Figure 6.16 shows the simulated normalised peak $[Ca^{2+}]$ (normalised by the first peak) across 20 sweeps, where each subplot shows predictions obtained from ten random draws of the time scales from the number line. The size of the cell (R_0) was easily calculated for each t_{diff} using the cubic function approximated in Figure 6.5.

Figure 6.16 (left) shows ten random draws of the time scales such that t_{diff} is always the smallest. No discernible rundown trend is observed in any of these simulations confirming that for very small cells, no CIR will be observed, similar to the first two rows of Figure 6.12. This can be attributed to the fact that in small cells, the free buffer has enough time to diffuse completely to the periphery of the cell, both before the voltage-clamp is applied and also between sweeps. This also explains the results of previous chapter where increasing t_{hold} showed only small decreases in rundown rate (Figure 5.7). For cells small enough to allow complete equilibration at small t_{hold}, increasing t_{hold} will not make any difference.

Figure 6.16 (centre) shows a similar normalised peak $[Ca^{2+}]$ for random draws such that t_0 is always the smallest of all time constants. This always results in an inverse pattern of rundown which can attributed to the very small amount of $[B]$ that equilibrated to the periphery of the cell before Ca^{2+} enters the cell. Subsequently, $[B]$ increases by a large amount between sweeps as the experiment progresses (thus decreasing the $[Ca^{2+}]$). This is also observed in the third row of Figure 6.12.

Finally, Figure 6.16 (right) shows normalised peak $[Ca^{2+}]$ for random draws such that t_{hold} is always the smallest of all time constants. The resulting pattern in this situation depends on a complex interaction of the three time scales given by ζ, which was determined heuristically as:

$$\zeta = \frac{t_0^2}{2t_{diff}t_{hold}}. \tag{6.26}$$

If ζ is greater than one then the resulting rundown pattern is predicted to be saturating while if its less than one, then it is predicted to be inverse. ζ can be rewritten as a function of two entities — t_0/t_{diff} (an estimate of the $[B]$ that actually diffused into the cell versus the $[B]$ that should have diffused into the cell before the application of a voltage-clamp) and t_0/t_{hold} (an estimate of the $[B]$ that actually diffused into the cell before the voltage-clamp versus the $[B]$ that will diffuse into the cell between sweeps after the application of a voltage-clamp).

Interestingly, the findings of prediction of the rundown pattern using the threshold value of ζ is also valid for the conditions in which t_0 or t_{diff} is the smallest. The two possible sub-conditions when t_0 is the smallest can be either $t_0 < t_{diff} < t_{hold}$ or $t_0 < t_{hold} < t_{diff}$. For both of these conditions, the quantities t_0/t_{diff} and t_0/t_{hold} are less than one, making the product ζ less than 0.5, where the predicted rundown pattern should be inverse in nature as is already observed (Figure 6.16, centre). Similarly, the ζ value can also predict the rundown pattern when t_{diff} is the smallest quantity, albeit the change is so small that it classifies as almost no rundown. Nevertheless, see Appendix B.9 for a zoomed in version showing the predictive capabilities of ζ.

In this section, the conditions at which CIR is anticipated were discussed. Further, if such conditions exist, its associated trend was also studied by individually considering cases in which t_{diff}, t_0, or t_{hold} are the smallest compared to the other two time scales. This gives rise to four corner cases, of which the rundown trend can be predicted for three of them without simulations using ζ. When $t_0 = t_{diff} < t_{hold}$, ζ will always be less than one, and similarly when $t_{hold} = t_0 < t_{diff}$ (provided $t_{diff} > 0.5$, which holds for nearly 100% of the cell size range), therefore the predicted rundown trend is inverse in nature for both of these corner cases. When $t_0 = t_{diff} = t_{hold}$, $\zeta = 0.5$, therefore also predicting an inverse rundown trend. On the other hand, when $t_{hold} = t_{diff} < t_0$, ζ can take any value greater than 0.5 and the rundown trend varies between saturating and inverse. Nevertheless, simulations (shown

in Appendix B.9) confirm that whenever t_{diff} is the smallest time constant, there is almost no CIR as the change across peaks is very small (even if other time constants are equally small).

6.6 Discussion

In this chapter, CDI-induced rundown (CIR) was modelled by accounting for the Ca^{2+} brought in by I_{CaL}, its chemical reaction with B to form the complex CaB, and the diffusion of all three chemical entities as per their concentration gradient. This model was used to make qualitative predictions of CIR. Since several factors besides CDI are responsible for rundown, it was difficult to tune the parameters of the model to make *quantitative* predictions about rundown from the data collected in Chapter 5.

The shape of the (peak $[Ca^{2+}]$)-versus-time curve was used as a proxy to determine the pattern of rundown predicted by the CIR model. The rundown pattern was then reverse-engineered from this peak $[Ca^{2+}]$ pattern using an instantaneous gate. Despite the use of this gate, the translation of peak-$[Ca^{2+}]$ trend to a rundown trend using a non-instantaneous gate should be qualitatively similar. This is because CDI is expected to be a fast process [20 ms to 100 ms Kubalova, 2003, Sham et al., 1995, Stotz et al., 2004, compared to tens, or even hundreds of seconds required for diffusion].

In the previous chapter, a high degree of variability was observed in the rundown even when the measurements were made at the same temperature, presence/absence of I_{NaCa} blocker, and holding potential duration (t_{hold}). In this chapter, all of these experimental conditions were kept constant and the prediction of CIR was investigated as other factors varied within each experimental condition. Some of the sources of variability were identified to be different LCC density (indicated by $\bar{P}_{Ca}$), the cell's radius (R_0), and t_0. This is evidenced by non-identical predictions as these factors are varied as shown in Figures 6.12, 6.13, and 6.14.

Changing the channel density (varying the Ca^{2+} entering the cell by varying $\bar{P}_{Ca}$) was shown to not be a sufficient condition that induces or stops rundown trends; however, if t_{diff} is relatively small enough to allow CIR, then LCC density was found to directly affect the

magnitude of CIR. This is perhaps in accordance with the low statistical significance found in Chapter 5 for cases where the amount of $[Ca^{2+}]$ coming into the cell is changed (changing I_{NaCa} and t_{hold}).

In Chapter 5, three types of rundown patterns — linear, saturating, and an 'inverse' trend were identified. The CIR model here was able to predict two of these patterns (i.e. saturating and inverse) However, the model was not able to predict a linear shape of the rundown-versus-time curve. This suggests that some other factors could be responsible for experimentally recorded rundown (e.g. washing away of LCCs or phosphorylation agents) which dominate over CIR when the attenuation of the current is linear with time.

By testing the CIR model under conditions that vary from cell-to-cell, a relationship was established between the three time constants: t_{hold}, t_{diff}, and t_0 which can be used to predict rundown due to CDI. Future work investigating the origins of this relationship can be beneficial.

The time constants were randomly drawn 10 000 times from their permissible range given in the number line in Figure 6.15 (assuming uniform distribution of all three variables). This process was repeated 20 times and the resulting relationships between the time constants were used to predict the rundown trends using Equation 6.26. This process showed that for the experimental setup used in this study, there is a 64.3% probability of observing a saturating pattern of rundown, 31.3% probability of an inverse pattern of rundown, and only a 4.4% probability of observing no CIR. Although these estimates are not in accordance with the observed rundown distribution in Chapter 5, this discrepancy can be because of other sources of rundown in the rundown recording. Nevertheless, this investigation shows that for 95.6% cases, the experimental setup used is not adequate to ensure that recordings are not contaminated with CIR.

6.7 Summary

This chapter showed the extent to which rundown of I_{CaL} presented in Chapter 5 can be explained by accumulation of Ca^{2+} inside the cell. CDI-induced rundown (CIR) was modelled by accounting for I_{CaL} activity, chemical reaction of calcium and the free buffer, and their

diffusion along the concentration gradient. The resulting model of CIR was used to predict experimental conditions at which CIR can be minimised in a patch-clamp setup.

The underlying mechanism of CIR was found to be the buffer kinetics close to the LCCs which is determined by the diffusion rate of the free buffer along with the equilibrium $[\mathrm{B}]$ established by the reaction kinetics of $[\mathrm{B}]$ and $[\mathrm{Ca}^{2+}]$. Three different time constants were found to dominate the trend of rundown. The relationship between t_{hold} (time between two sweeps), t_0 (time given to the buffer to diffuse into the cell before the experiment begins), and t_{diff} (time required by the cell for complete equilibration of the buffer) can be used to determine if rundown will occur in a patch-clamp experiment or not. If rundown does occur as established by this relationship, the value of a dimensionless quantity calculated using these three different time constants will predict the exact trend of rundown (linear, saturating, or inverse).

This study suggests that it is important to work with small cells (or large t_0 and t_{hold}) to avoid CIR of $\mathrm{I_{CaL}}$ recordings. This model of CIR predicts that in the commonly used experimental setup, only 4.4% of cases will not induce CIR. Therefore, it is critical to change the experimental setup so that both t_0 and t_{hold} are large enough in comparison to t_{diff}.

In the next chapter, $\mathrm{I_{CaL}}$ recordings are collected using a high-throughput automated patch-clamp machine and subsequently corrected for rundown. This data is then used to calibrate and validate a preliminary model of the voltage-dependent aspect of the L-type calcium current.

7 | Preliminary model of the L-type calcium current

Due to COVID-19 travel restrictions, the patch-clamp experiments in this chapter were performed in Basel, by collaborators at Roche, but I designed them and performed all the data analysis, drew conclusions, interpretations, and performed the subsequent model-building exercise.

7.1 Introduction

Chapter 3 showed that over 73 I_{CaL} models exist. These models differ in how they account for the driving flux, in their assumptions about the channel's localisation, and most widely in their gating kinetics or open probability — O. Fifteen unique gating structures have been identified that attempt to capture O (see Chapter 3 or Agrawal et al. [2022]), each with varying levels of complexity. Since the underlying biophysical mechanisms of I_{CaL} such as that of inactivation are widely debated (see Section 2.2.4 in Chapter 2), it could be beneficial to use simpler models to characterise I_{CaL}.

Most of the existing I_{CaL} models have been developed by using multiple protocols to determine different aspects of the model, for example, the conventional patch-clamp protocols like the activation, inactivation, and recovery from inactivation protocols used in Chapter 4. These protocols typically run for hundreds of seconds each; therefore, it is often not possible to run all these protocols on a single-cell. Short, information-rich voltage-clamp protocols on the other hand can be run on a single-cell and can contain sufficiently condensed information enough to estimate the parameters of an ion-channel model, as shown by Fink and Noble [2009]. Such protocols have recently been used to characterise I_{Kr} models using manual [Beattie et al., 2018] and automated patch-clamp [Lei et al., 2019]. Here the use of such protocols is extended for rapid characterisation of I_{CaL}.

In this chapter, I_{CaL} was recorded under a novel 14 s information-rich protocol which was adapted from Lei et al. [2019] to maximise the information obtained for I_{CaL}. This voltage-clamp protocol was then performed on an automated patch-clamp machine to calibrate an ion-channel model. This is a simple two-gate model that uses first principles to define the transition rates. The predictions of this model were validated against data collected from

eight other protocols, all run on the same cell. Before being used, the data (both for training and validation) was corrected for rundown by assessing the amount of rundown via steps to 0 mV interspersed over the course of the experiment. This allowed the modelling exercise to focus on the voltage-dependent kinetics of I_{CaL} (assuming calcium-dependent kinetics are independent from voltage-dependent kinetics).

Cell-specific calibrations of the model were obtained by using data from five different cells along with an additional hierarchical calibration where the kinetic parameters describing O were shared across all five cells (while the permeability and residual leak current vary cell-to-cell). The six cell-specific parameter sets (five cell-specific and one hierarchical) of the model are found to be in close proximity, which confirms that there is little cell-to-cell variability in the I_{CaL} kinetics. However, existing models present wide variability in their predictions to the calibration protocol used in this chapter as shown in Figure 7.1. This work shows that it is possible to capture the complex voltage-dependent kinetics of I_{CaL} using a simple model.

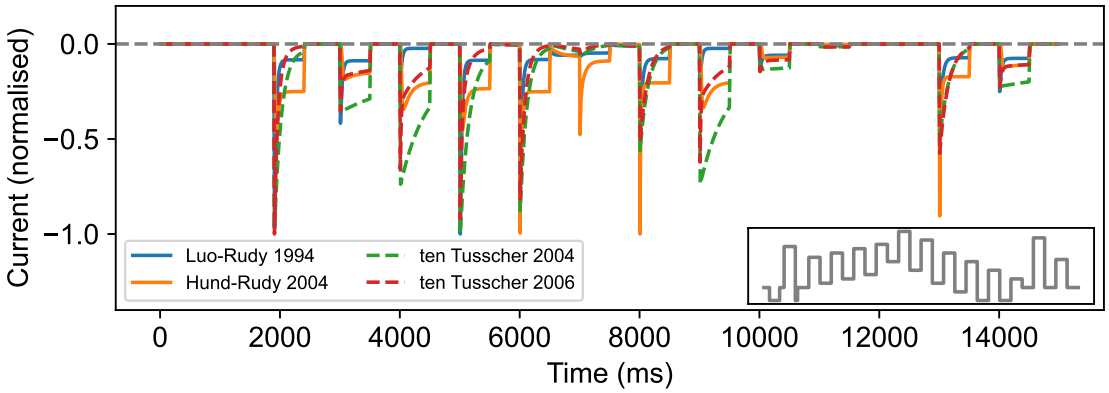

Figure 7.1: Current simulated by four different models using the staircase protocol (inset). A zoomed in version of the protocol can be seen in Figure 7.2C.

7.2 Methods

The methods used in this study are described here in three parts 1) data collection, 2) a mathematical model of I_{CaL}, and 3) simulation and optimisation techniques.

7.2.1 Data collection

Patch-clamp experiments

Whole-cell patch-clamp voltage-clamp experiments were performed on ready-to-use CHO cells stably transfected with $Ca_V1.2$, using the Syncropatch 384PE platform (Nanion Technologies). This machine and the experimental setup has been previously described in Section 5.2.1 and Section 2.5.2. Compositions of bath (extracellular) and intracellular solutions remain unchanged from the previous patch-clamp experiments and are given in Table 5.1. The experiment was performed at physiological temperature (310 K). Having recognised the importance of allowing the buffer (BAPTA) to diffuse into the cell (Chapter 6), the experimental setup was modified so that the minimum value of t_0 (see Section 6.1 for definition) was updated from 5 s to 120 s.

Voltage-clamp protocols

Current was recorded from cells as the membrane voltage (V_m) was clamped according to various voltage protocols. Current recorded under one such protocol was used for training an I_{CaL} model (see Section 7.2.2) to determine its parameters, while eight other protocols were used for validating the predictions of the model using the parameters obtained. Since the current measured was contaminated with leak, endogenous current, and rundown, measurements with additional protocols were made and used to correct the current recordings. Firstly, current was measured under 'leak ramps' similar to those discussed in Section 5.2.3. Secondly, current was measured under 'rundown steps' to correct the recorded current from any rundown effect such as those observed in Chapter 5. Finally, current was measured after the addition of the I_{CaL}-blocker nifedipine, so that endogenous currents could be removed using a subtraction step. The subsequent section 'Post-processing', describes how I_{CaL} is extracted from the recorded current at each protocol.

Figure 7.2C shows a novel 14 second staircase protocol adapted from Lei et al. [2019] for I_{CaL}. The initial step to -120 mV ensures that the channels are fully closed before the application of an opening voltage-step. This protocol consists of several short steps (500 ms each) that force the activation and inactivation gates of the model to explore different values (or exploration of the state-space). The voltage-steps were chosen to vary from -20 to

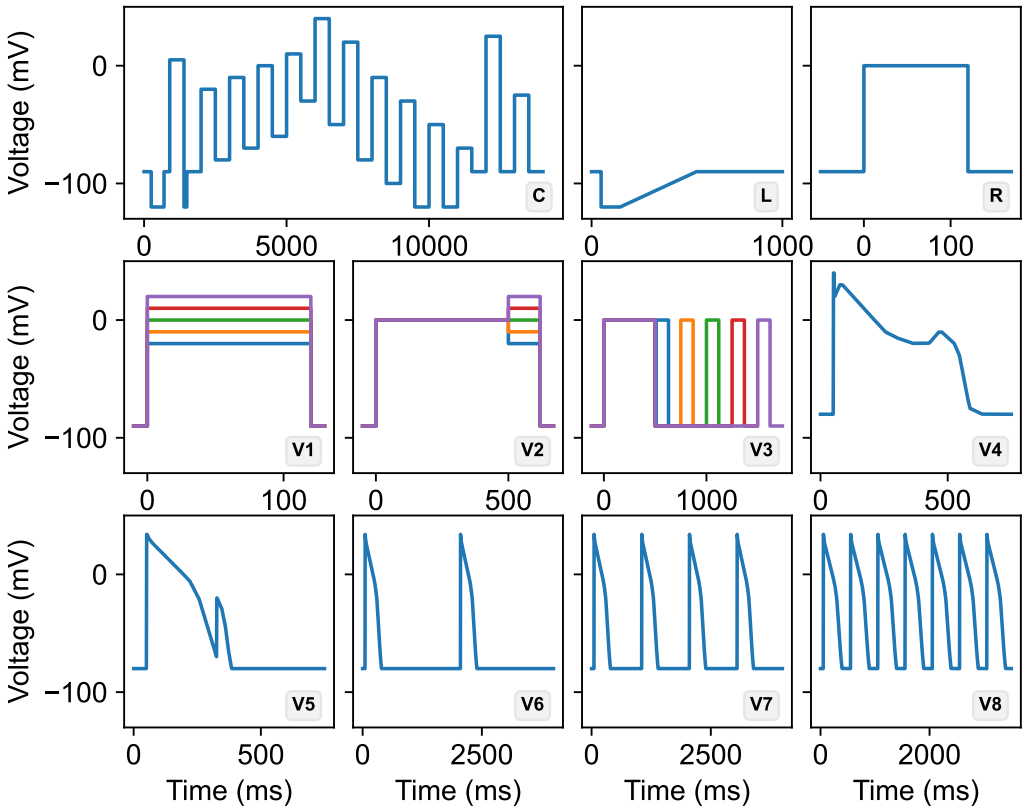

Figure 7.2: All voltage-clamp protocols used in this study. Here C is the calibration protocol and V1–V8 are validation protocols. L and R are short protocols which are used to post-process the current measured under these nine protocols. The duration of each protocol is given in Table 7.1 and all protocols are explained in the text. Please note that the protocols R, V1, V2, and V3 have been modified to clearly show the length of the voltage step. Protocol R used in the study only has the step at 0 mV. Similarly, protocols V1, V2, and V3 do not include any holding potential before the first sweep and after the last sweep. The sweeps in these protocols (shown in different colours) have been overlaid on top of each other and have a holding potential duration of 6 s between them.

40 mV since the LCCs are known to 'open' at these voltage values. The protocol was then used on some existing models to check that it elicited a varying response across different models (see Figure 7.1). The state-space plot generated using this protocol was also found to occupy much more 'space' than conventional voltage-clamp protocols for existing models (an example is shown in Figure C.1). This protocol showed identification of much more 'information' in the recorded current than is possible through much longer, conventional protocols. Subsequently, the current measured under this protocol was used to train the I_{CaL} model.

Eight different validation protocols were used to compare the predictions of the trained model against data that were not used in the training process. These protocols are shown in the subplots V1–V8 of Figure 7.2. V1 was adapted from a typical activation protocol used for I_{CaL} (see Section 4.3.1). Similarly, V2 and V3 were adapted from voltage-dependent inactivation (VDI) and recovery from VDI protocols similar to those used in Section 4.3.2. In all three protocols, the holding potential duration between two sweeps is 6 s. All sweeps have been overlaid on top of each other in the subplots V1–V3 of Figure 7.2. The holding potential duration between the conditioning and test step of V3 (see Section 4.3.2) is 10 ms for the first sweep, and changes to 250, 500, 750, and 1000 ms for consecutive sweeps. V4 and V5 show an early-after-depolarisation (EAD) and a delayed-after-depolarisation (DAD) protocol respectively. V6, V7, and V8 show the protocols with action potential (AP) pacing at 0.5, 1, and 2 Hz pacing respectively.

Current from all nine protocols (one calibration and eight validation) were measured twice — before and after the application of 10 μM nifedipine (which should selectively block I_{CaL} by at least 90% [Shen et al., 2000]). The schematic in Figure 7.3 shows the sequence in which current from each protocol is measured. To account for rundown due to calcium-dependent inactivation (CDI) as well as other factors, a rundown step was included (see Figure 7.2R) before each of the nine protocols. Attenuation of current measured at this step over the course of the experiment was used to measure and 'correct' data from rundown (see "post-processing" in Section 7.2.1). Finally, all voltage-protocols were preceded by a linear-leak ramp (Figure 7.2L, depicted by the pink arrows in Figure 7.3) used to measure and correct the leak current present in the recordings.

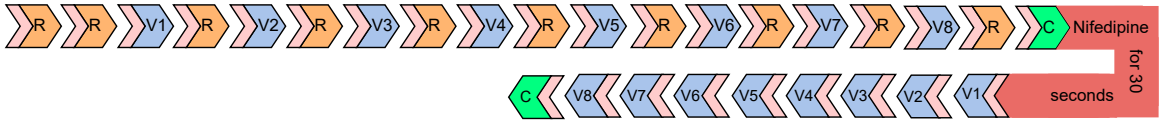

Figure 7.3: The sequence of the voltage-clamp protocols used in the patch-clamp experiments. The boxes labelled V1–V8 represent validation protocols, C represents the calibration protocol, and R represents the rundown protocols. The pink arrow before each protocol represents the leak protocol, L. The voltage-clamp protocols themselves are shown in Figure 7.2. The white gaps represent holding potential at −90 mV for 9 s.

The white space between two arrows in the schematic shown in Figure 7.3 represents a holding potential duration of 9 s at −90 mV and the time duration of each protocol is given

	Protocol	Time (s)
R	Rundown	0.12
L	Leak	1
C	Training	14
V1	Activation	25
V2	Inactivation	28
V3	Recovery	30
V4	EAD	0.75
V5	DAD	0.75
V6	AP (0.5 Hz)	4
V7	AP (1 Hz)	4
V8	AP (2 Hz)	3.5
-	Hold (−90 mV)	9
Nifedipine	-	30

Table 7.1: Total time for each step in the experiment.

in Table 7.1. The total run time of the experiment was 513.2 s, of which 292.2 s took place before the application of nifedipine.

Post-processing

Similar to the process explained in Section 5.2.3, the recorded current was first filtered to remove artefacts due to capacitance by removing recordings for 1 ms after the step-wise V_m changes. Subsequently, it was corrected for leak and endogenous current (see Equations 5.2–5.3 in Chapter 5). It was possible to remove the effects of any endogenous currents because of the current recorded under all of the protocols after the addition of nifedipine. However, no current was recorded under the R protocol after the addition of nifedipine. Nevertheless, the first sweep of V2 (up until 120 ms) was exactly the same as R and was therefore used to extract drug-subtracted current from each recording under R.

Next, the R protocols were used to assess the rundown that occurred in each cell over the course of the experiment. Figure 7.4 (left) shows I_{CaL} during each R step for a representative cell (J20). The peak I_{CaL} at each step was normalised with respect to the peak I_{CaL} in the first sweep and plotted against the time from the beginning of the experiment in Figure 7.4 (right, shown in crosses). Since the voltage protocol (as well as the preceding holding potential duration) is exactly the same for each R, the change in current is expected to be voltage-independent and purely due to rundown (both due to CDI and other factors). From

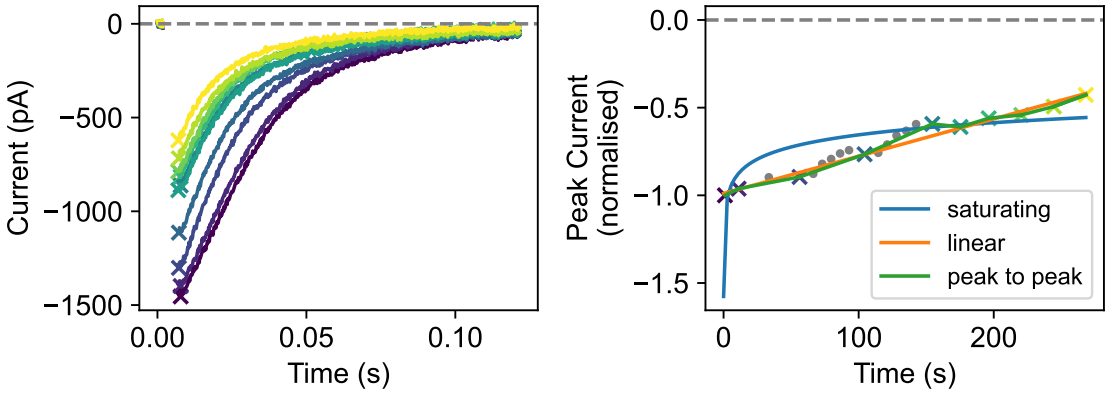

Figure 7.4: **Left**: I_{CaL} under each R protocol (in cell J20) overlaid on top of each other with the first recording in indigo and the last one in yellow. The peak I_{CaL} at each sweep is marked with a cross. **Right**: The normalised peak I_{CaL} at each sweep plotted against the time from the beginning of the experiment (shown in crosses) and fit to linear, saturating, and peak to peak functions. Validation peaks (normalised) are shown by grey dots (see text for details).

Chapter 5 it is known that the rundown-versus-time curve follows a predominantly linear or saturating trend, therefore, the normalised peak I_{CaL} was fit to both linear and saturating functions. In addition to these two functions, normalised peak I_{CaL} measurements were also fit 'peak to peak' (allowing for different rundown rates throughout the experiment).

To select the best method for correcting rundown, the fitted functions were validated using additional data. For this purpose, the peak I_{CaL} at the step to 0 mV of V1 as well as the conditioning pulse of each sweep in V2 and V3 were used as 'validation peaks'; all of these values are shown using grey dots in Figure 7.4 (right). This figure shows that neither linear nor saturating fits seem appropriate and therefore the peak to peak method was used to correct all recorded data for rundown. The rundown between any two R protocols in this figure was estimated using $R_i(t) = m_i t + c_i$, where, $R_i(t)$ is the amount of rundown between two protocols and t is the time in seconds. The parameters m_i and c_i were calculated using the normalised peak I_{CaL} and corresponding time at both R protocols. Current recorded from the protocol that lies between the two R protocols was subsequently corrected for rundown by dividing by $-R_i(t)$.

Quality control

Similar to Chapter 5, cells with reliable recordings were identified by applying a series of quality control (QC) criteria. A preliminary QC0 was first applied to exclude recordings from wells in which the seal resistance did not remain intact until the end of the experiment. This resulted in the selection of only 45 out of the 384 cells on the chip (one cell in each well of the chip that has 16 rows and 24 columns). The cells selected at this stage were then subjected to five quality control criteria (similar to those used in Chapter 5, but more strict).

1. QC1, Machine properties: QC1.1 excluded cells in which the minimum seal resistance (R_{seal}) recorded across all sweeps was less than 0.2 GΩ, or in which the standard deviation (σ) of R_{seal} was greater than 1 GΩ. QC1.2 excluded cells in which the recorded capacitance (C_m) across the sweeps was less than 1 pF, greater than 100 pF, or in which σ was greater than 10 pF. QC1.3 excluded cells in which the series resistance (R_s) was greater than 30 MΩ or σ was greater than 4 MΩ.

2. QC2, Current contamination: QC2.1 excluded cells in which the magnitude of the peak current recorded during the channel opening step of the R protocol was less than the leak current, while QC2.2 excluded cells in which the apparent endogenous current was more than I_{CaL}.

3. QC3, Signal-to-noise: QC3 excluded cells in which the signal-to-noise ratio (SNR) for any R protocol was less than 20 or if the maximum SNR across all R protocols was less than 60.

4. QC4, Variation in leak conductance (g_{leak}): QC4 excluded cells in which the standard deviation of the calculated g_{leak} was greater than 0.3 nS across all sweeps in a single cell.

5. QC5, I_{CaL} likelihood: QC5 excluded cells that were not likely to be I_{CaL} by checking that there was a net influx of ions rather than outflow for all sweeps of post-processed current under the R protocol (no reversal of current is observed for I_{CaL} at 0 mV).

The number of cells selected after each QC criterion is given in Table 7.2. Application of all QC criteria resulted in the selection of just five cells, labelled according to the well they were in: “C22”, “H06”, “I11”, “J20”, and “K05”.

QC	QC0	QC1.1	QC1.2	QC1.3	QC2.1	QC2.2	QC3	QC4	QC5
Cells	45	29	41	32	41	43	17	27	33

Table 7.2: Number of cells that passed each quality control (QC) criterion where each QC is explained in the text. Five cells were selected after the application of all selection criteria.

The post-processed currents across all the selected cells recorded during the calibration and validation protocols are shown in Appendix C.2.

7.2.2 Mathematical model

The most common representation of the I_{CaL} model is given by $\bar{P}_{Ca} \cdot O \cdot \delta_{GHK}$ (see Chapters 2 and 3). For the mathematical model used in this chapter, the permeability ratio of Na^+ and K^+ is kept the same as that used in Chapter 6, and the activity coefficients were defined using the Davies equation (see Equation 5.6 in Chapter 5). The gating (indicated by O) is set to a simple structure of the **type C1** (see Table 3.2 in Chapter 3), so that $O = d \cdot f \cdot f_{Ca}$. Here f_{Ca} is given by a Hill equation and thus acts as a scaling factor to the total I_{CaL}, independent of the voltage effects. Since calcium-dependent effects have already been removed from the recorded current via rundown correction, $[Ca^{2+}]$ can be assumed to be zero near the LCCs which implies that f_{Ca} can be treated as a constant. The voltage-dependent activation (d) and inactivation (f) gates are defined by first-principles of chemical equilibrium of two states:

$$(1-d) \underset{k_2}{\overset{k_1}{\rightleftharpoons}} d \quad \text{and} \quad (1-f) \underset{k_3}{\overset{k_4}{\rightleftharpoons}} f, \tag{7.1}$$

similar to the approach adopted by Beattie et al. [2018] for a hERG model. The gates are modelled using the ODEs:

$$\frac{\mathrm{d}d}{\mathrm{d}t} = k_1(1-d) - k_2 d \quad \text{and} \quad \frac{\mathrm{d}f}{\mathrm{d}t} = k_4(1-f) - k_3 f, \tag{7.2}$$

where, k_i are voltage-dependent rates of the type $p_i \exp(\pm p_j V_m)$. The model therefore contains eight kinetic parameters which are used to compute the rate constants:

$$\begin{aligned} k_1 &= p_1 \exp(p_2 V_m), & k_3 &= p_5 \exp(p_6 V_m), \\ k_2 &= p_3 \exp(-p_4 V_m), & k_4 &= p_7 \exp(-p_8 V_m), \end{aligned} \tag{7.3}$$

and an additional non-kinetic parameter to account for the combined permeability of all LCCs ($p_9 = \bar{P}_{Ca}$). Here, k_1, k_2, k_3, and k_4, are the rate constants representing voltage-dependent activation, deactivation, inactivation, and recovery from inactivation respectively. Parameters of the type p_j determine the voltage-dependence of each rate constant while parameters of type p_i directly influence its magnitude. The boundary and permissible range of each of these parameters is explained in Appendix C.3. To determine the positive parameters p_1–p_9, the model is then fit to the post-processed I_{CaL} data recorded under the staircase protocol, by using optimisation methods described in Section 7.2.4.

The model was used to simulate the calibration protocol along with three validation protocols (V1–V3) using an analytical solver incorporated into Myokit version 1.33.0 [Clerx et al., 2016] that calculates the state variables at each voltage-step. The simulation of the protocols V4–V8 was done using CVODE version 5.7.0 (CVODE is described in Appendix D), also incorporated into Myokit. The solver's absolute and relative tolerances were set to 10^{-7}.

7.2.3 Identifiability analysis

Before attempting to calibrate an I_{CaL} model using the current from patch-clamp experiments, the model's parameters are first shown to be identifiable from the data generated under the calibration protocol using a synthetic study.

Synthetic data were generated by simulating the calibration protocol experiment using the model described in Section 7.2.2. For this purpose, four sets of kinetic parameters (see Figure C.3) were chosen randomly from within the boundaries established in Appendix C.3 (parameters were discarded if they did not stimulate a physiological response). To simulate experimental noise, independent and identically distributed noise $\epsilon \sim \mathcal{N}(0, \sigma^2)$ was added to the model output. Here σ was chosen to be 1% of the maximum value of I_{CaL} simulated (this is slightly higher noise than expected as per the experimental data) for each of the five simulated currents.

The synthetic data thus obtained for the first parameter set is shown in Figure 7.5 (top). These data were subsequently used to calibrate the model and determine its parameters. An initial guess ($\boldsymbol{\theta_0}$) was chosen from within the boundary restrictions and subsequently

the CMA-ES algorithm (see Appendix D) was used to estimate the correct parameters by minimising the mean squared error (MSE):

$$\mathrm{MSE}(\mathbf{v}_1, \mathbf{v}_2) = \frac{1}{N}\sum_{i=1}^{N}(v_{1,i} - v_{2,i})^2, \tag{7.4}$$

where, $\mathbf{v}_1$ and $\mathbf{v}_2$ are two time-varying vectors and N is the number of time points.

The MSE used for this synthetic study is given by:

$$\xi_{syn} = \mathrm{MSE}(I_{CaL}^{data\text{-}syn}, I_{CaL}^{model}(V_m, t, \boldsymbol{\theta})), \tag{7.5}$$

where, $I_{CaL}^{data\text{-}syn}$ is the synthetically generated data, I_{CaL}^{model} is the current simulated by the model, and $\boldsymbol{\theta}$ is the parameter vector to be determined $\{p_1, \ldots, p_9\}$. To check the reproducibility of the optimisation results while slightly varying the experimental conditions (or robustness) of the results, the optimisation was repeated for 50 different initial guesses of $\boldsymbol{\theta_0}$ for each data set.

The resultant best fit (least ξ_{syn}) is shown in Figure 7.5, and it matches the synthetic data well. The error in the recovery of each parameter value was less than 0.4% of the true value for the best fit, and this was matched in 72% of all results. Similar parameter estimation exercises from the other four synthetically generated data led to determination of the parameters within 1%, 0.5%, and 0.3% error with the same best parameter estimate obtained for 56%, 72%, and 28% of initial guesses. The low percentage of best fits for the last parameter set can be explained by the comparatively low amount of data simulated by the model (see lack of current generated beyond 9 s in the last row of Figure C.4 in Appendix C.4).

These results show that true parameters are identifiable from the current generated using the training protocol used in this study (while the assumptions about the model are correct). Moreover, these parameters can be robustly estimated with reasonable accuracy.

7.2.4 Optimisation

This section describes the optimisation method adopted to infer the parameters of the model using real data recorded from CHO cells in an automated patch-clamp and subse-

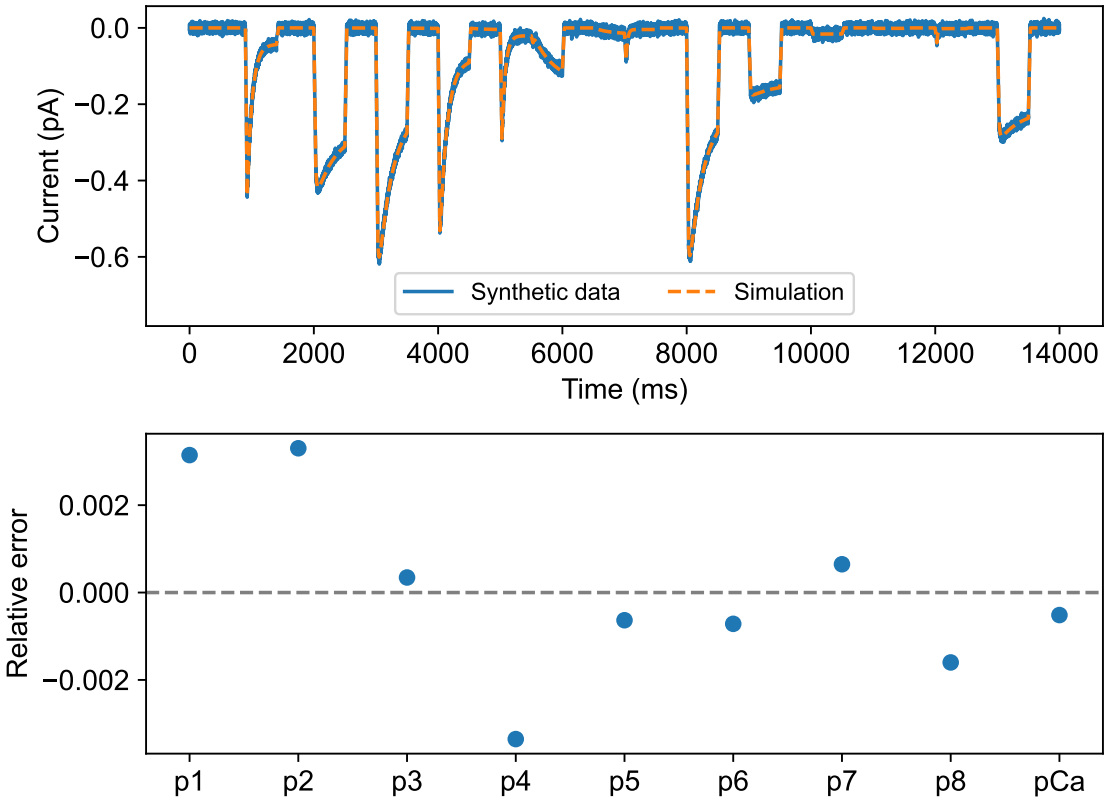

Figure 7.5: **Top**: Synthetically generated data and simulation by the model trained using the data. The voltage-clamp protocol used is given in Figure 7.2C. **Bottom**: Relative error of each estimated parameter with respect to the true parameter, where each parameter is labelled as per the equations described in Section 7.2.2.

quently post-processed for capacitative artefacts, leak and endogenous currents, and run-down. While the data were already corrected for leak current, some amount of residual leak current remained which was accounted in the calculation of the error between the recorded current and that simulated by the model. This was done by performing the optimisation exercise to infer two parameters in addition to the parameters of the model that account for the residual leak current ($I^*_{leak} = g^*_{leak}(V_m - E^*_{leak})$). As before, each optimisation was repeated from 50 randomly chosen initial points ($\boldsymbol{\theta_0}$).

For any given cell, the residual error (ξ_{cell}) between the data and current simulated by the model is defined as:

$$\xi_{cell} = \frac{1}{2\sigma^2}\text{MSE}(I^{cell}_{CaL}, I^{model}_{CaL}(V_m, t, \boldsymbol{\theta}_{model}) + I^*_{leak}(V_m, t, \boldsymbol{\theta}_{leak})), \tag{7.6}$$

where, I^{model}_{CaL} is the current simulated which is a function of voltage (V_m), time (t), and the

model parameters to be optimised ($\boldsymbol{\theta}_{model} = \{p_1, p_2, p_3, p_4, p_5, p_6, p_7, p_8, p_9\}$). The residual leak current, I^*_{leak} is a function of voltage (V_m), time (t), and $\boldsymbol{\theta}_{leak} = \{g^*_{leak}, E^*_{leak}\}$. The total parameter vector to be determined is given by $\boldsymbol{\theta} = \boldsymbol{\theta}_{model} \cup \boldsymbol{\theta}_{leak}$. I^{cell}_{CaL} is the post-processed current recorded from a cell and the total error is normalised with respect to the variance (σ^2_{cell}), which is a measure of the noise in that cell's recording. This normalisation does not affect cell-specific optimisation but is useful for hierarchical optimisations (see below).

Two kinds of optimisations were performed: 1) cell-specific and 2) global across all selected cells. In the cell-specific method, ξ_{cell} was minimised for each cell to estimate eleven parameters (eight kinetic, one permeability, and two for the residual leak current). This was repeated for all of the selected cells so that five sets of unique parameters (one set per cell) were found. In the hierarchical optimisation process, the sum of ξ_{cell} across all cells was minimised: $\sum_{i=1}^{N_T} \xi_{cell_i}$, where, N_T is the total number of selected cells. In this method, the kinetic parameters were shared across all cells, while the permeability and residual leak current parameters varied from one cell to another. Therefore the total number of parameters calibrated in the second method was $8 + 3N_T$.

All optimisations were run using the covariance matrix adaptation evolution strategy (CMA-ES) (see Appendix D) as incorporated into the open source Python package PINTS [Clerx et al., 2019b].

7.3 Results

After initial iterations of model calibration with real data using the optimisation method described in Section 7.2.4, the parameters p_4 and p_6 were repeatedly found to hit the lower boundary of their permissible range. From Appendix C.3, it is known that at very low values of these parameters, the corresponding chemical rate varies less than 0.002% due to changes in voltage. Therefore, k_2 and k_3 were assumed to be voltage-independent and accordingly the parameters p_4 and p_6 of the model were set to zero. Therefore, the parameters to be inferred for the model $\boldsymbol{\theta}_{model}$ were reduced from nine to seven.

An identifiability analysis similar to Section 7.2.3 was repeated for the reduced model. The results of that study were also promising and showed the identification of the true

parameters within 1% error by 66% of the initial guesses within the parameter space.

The following sections present the results obtained by fitting a reduced model to real data recorded from automated patch-clamp experiments. Therefore, the error function in Section 7.2.4 was updated so that $\boldsymbol{\theta}_{model}$ only consists of seven parameters ($\boldsymbol{\theta}_{model} = \{p_1, p_2, p_3, p_5, p_7, p_8, p_9\}$). Subsequently, the cell-specific optimisations infer nine parameters (six kinetic, one permeability, and two leak) and the hierarchical optimisation infers $6 + 3N_T$ parameters, where, N_T is the number of selected cells (five). As before, each optimisation was repeated for 50 randomly chosen initial points.

7.3.1 Model training

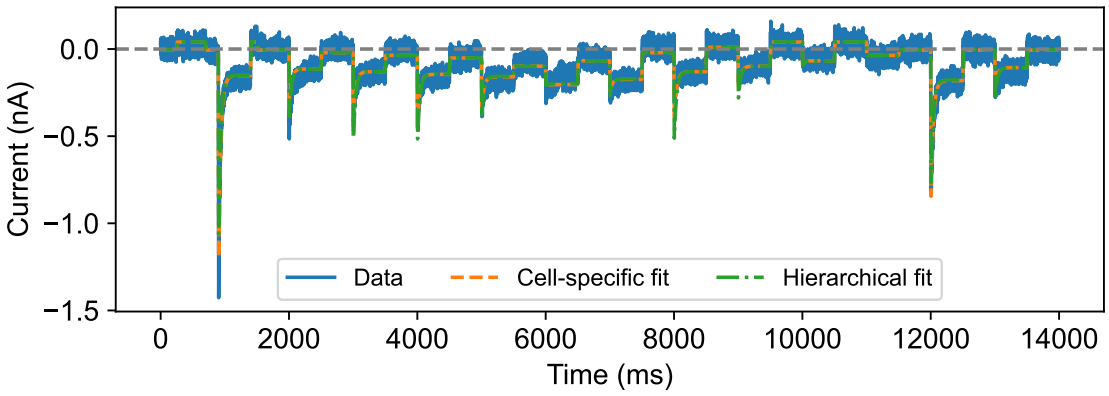

Figure 7.6: Post-processed I_{CaL} measured from CHO cell in well I11 under the calibration protocol given in Figure 7.2C, along with the corresponding current simulated by the calibrated model obtained by fitting to this data via two different optimisation processes.

Figure 7.6 shows the post-processed data along with the best fit obtained from both types of optimisation processes for one of the cells (I11). Results for the remaining cells are given in Appendix C.5. Predictions from cell-specific and hierarchical optimisation match the data from the CHO cell reasonably well. Although the robustness (reproducibility of the optimisation results while slightly varying the experimental conditions) of the estimated parameter decreased from 32–94% observed in the synthetic study to 26–58% across the five cells for cell-specific optimisation, and 22% for hierarchical optimisation, it is still impressive. Root mean square error (RMSE) was used to estimate the goodness of a fit,

wherein the lower the value of RMSE, the better the fit. This quantity is given by:

$$\text{RMSE} = \sqrt{\text{MSE}(I_{CaL}^{cell}, I_{CaL}^{model}(V_m, t, \boldsymbol{\theta}_{model}) + I_{leak}^{*}(V_m, t, \boldsymbol{\theta}_{leak}))}, \tag{7.7}$$

where, $\boldsymbol{\theta}_{model}$ and $\boldsymbol{\theta}_{leak}$ were determined during the optimisation process. The RMSE values for all cells are given in Table C.1 of Appendix C.7. Across all cells, the hierarchical optimisation led to slightly worse fits than the cell-specific optimisations.

The kinetic parameters estimated using cell-specific optimisations are depicted by dots within the boundary plots shown in Figure 7.7. As can be seen, the estimated parameter values for different cells are very similar. The kinetic parameter values estimated using the hierarchical optimisation (depicted by a cross in Figure 7.7) lie at the centre of the dots.

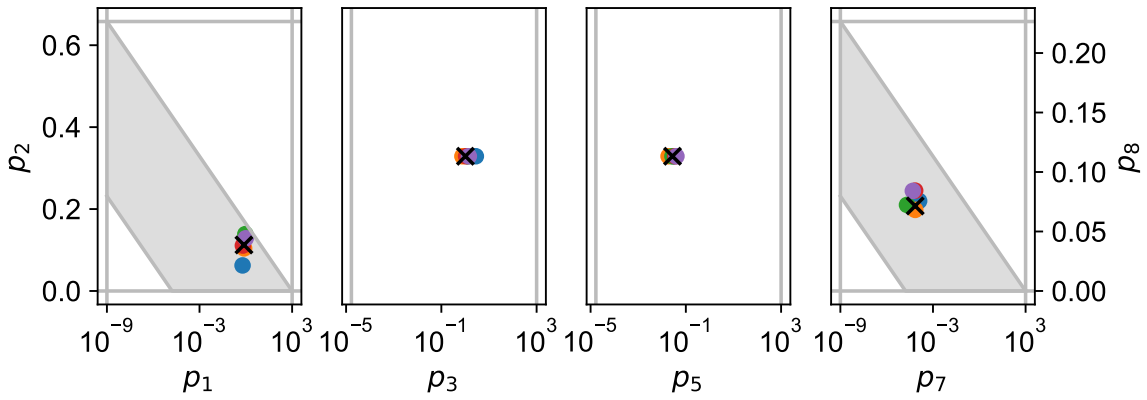

Figure 7.7: The parameter values estimated using the cell-specific and hierarchical optimisation are shown in dots and crosses respectively within the boundary region of the kinetic parameters. The shaded area shows the permissible range of the parameters (see Appendix C.3).

7.3.2 Model predictions

Next, the predictive capabilities of the calibrated model (according to both cell-specific and hierarchical optimisations) were tested against data that were not used in the training process. This is important to assess the reliability as well as limitations of the model.

Experiments with V1–V8 were simulated and compared to post-processed currents by clamping the voltage of the model to the protocols shown in Figures 7.2 V1–V8. Each simulation used the values of the kinetic parameters obtained in training, but $\bar{P}_{Ca}$, g_{leak}^{*}, and

E^*_{leak} were allowed to vary to account for the variations in residual leak current as well as the error in rundown correction. These three parameters were deduced by minimising a cell-specific and protocol-specific error:

$$\xi_{val} = \text{MSE}(I^{cell}_{CaL}, I^{model}_{CaL}(V_m, t, \boldsymbol{\theta}_{model\text{-}val}) + I^*_{leak}(V_m, t, \boldsymbol{\theta}_{leak})), \tag{7.8}$$

where the parameters characterising O have already been identified in the model training process. Here, $\boldsymbol{\theta}_{leak}$ remained the same as before and $\boldsymbol{\theta}_{model\text{-}val} = \{p_9\}$. The total parameters to be determined by the calibration process are given by $\boldsymbol{\theta}_{val} = \boldsymbol{\theta}_{model\text{-}val} \cup \boldsymbol{\theta}_{leak}$. The initial values of $\boldsymbol{\theta}_{val}$ were taken as the values of $\bar{P}_{Ca}$, g^*_{leak}, and E^*_{leak} estimated during the training step. This was repeated for the parameters values obtained via both cell-specific and hierarchical optimisation. As before, the error function was minimised using the CMA-ES algorithm to determine $\boldsymbol{\theta}_{val}$. The permeability is found to be stable over the course of an experiment determined in this manner as shown in Figure 7.8.

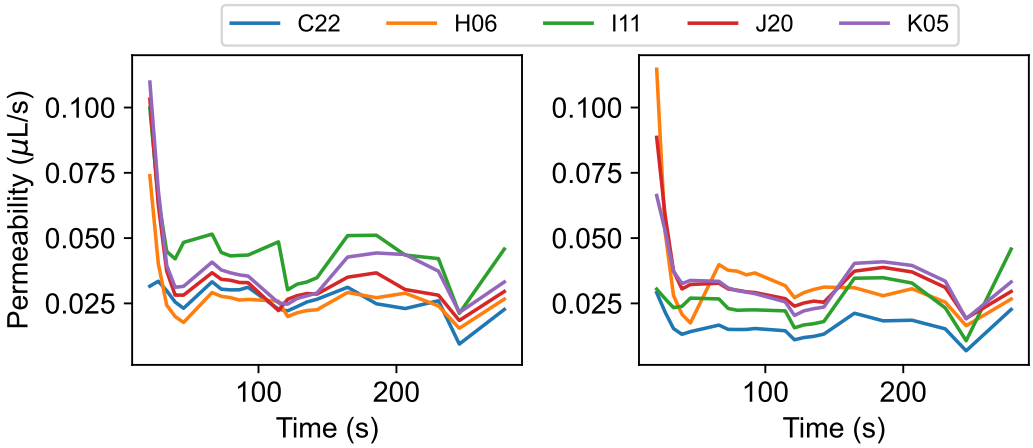

Figure 7.8: Variation in the estimated permeability over the course of the experiment for cell-specific models (**Left**) and hierarchical models (**Right**).

Figure 7.9 shows the post-processed currents for cell — I11, and the corresponding predictions using parameters of the model obtained using cell-specific and hierarchical optimisation. Here the current recorded (or simulated) at each sweep of V1, V2, and V3 is plotted consecutively. Each sweep can be distinguished by the alternating shade of grey background. Such breaks were not required for the remaining protocols (V4–V8). Model calibrations with both types of optimisations provide good predictions of the response to the EAD and DAD protocols (V4 and V5). Similarly, the prediction for the pacing protocol is

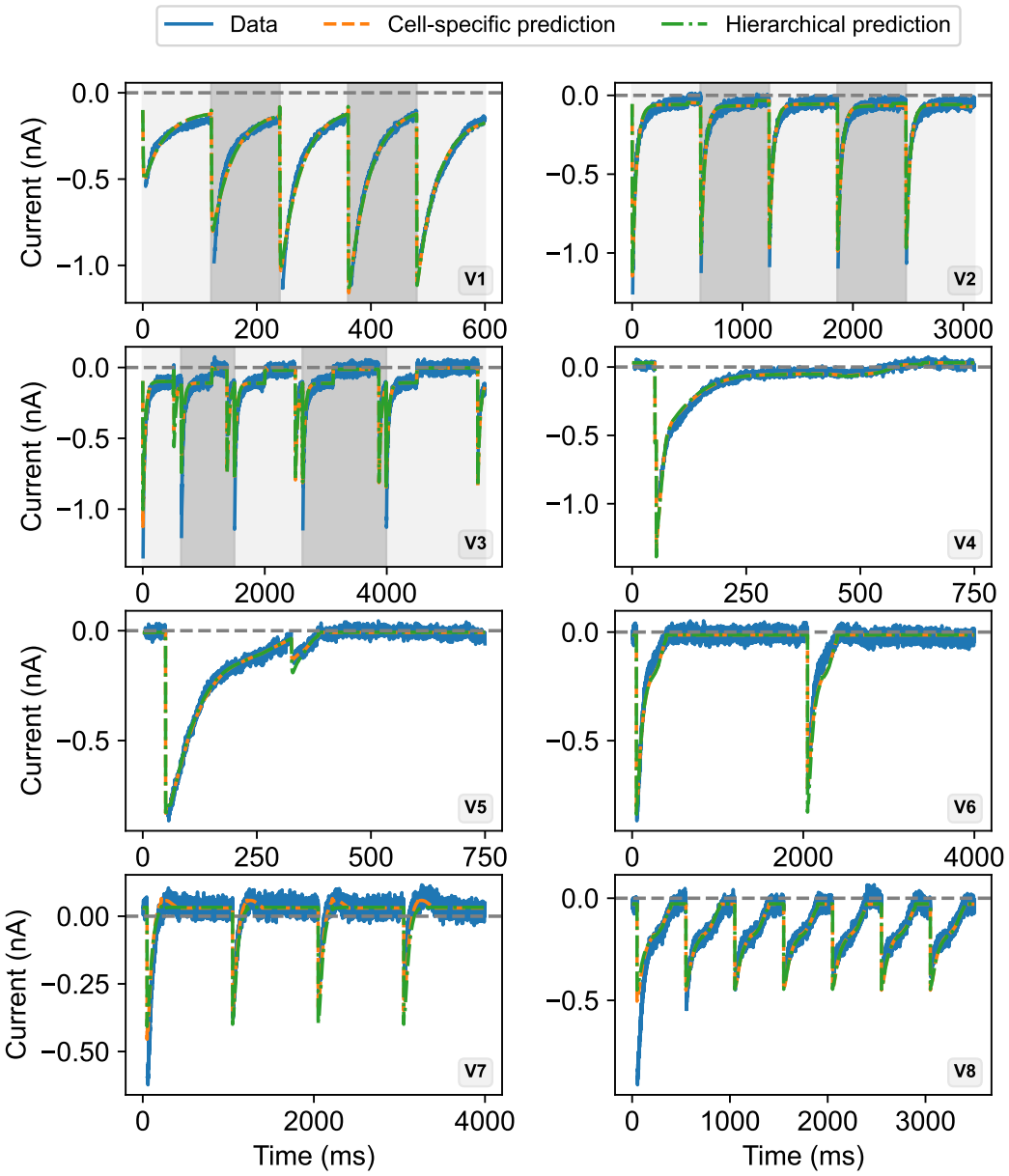

Figure 7.9: Post-processed I_{CaL} measured from CHO cell in well I11 under V1–V8 (Figure 7.2) and the corresponding model prediction for both cell-specific and hierarchical optimisations. Current recorded from each sweep in V1–V3 is plotted consecutively with the grey background alternating between each sweep.

good at 0.5 Hz (V6), but not for the higher frequencies of 1 and 2 Hz (V7 and V8). Finally, while responses to the activation (V1) and inactivation protocols (V2) are predicted well by calibrations obtained from both types of optimisation, the recovery from inactivation protocol is not predicted well by either of them. This is also indicated by the higher root mean square error (RMSE) values for the V3 protocol compared to V1 and V2 (see Table C.1 in

Appendix C.7).

For the remaining four cells, activation and inactivation kinetics are also predicted well by both cell-specific and hierarchical calibrations but the recovery from inactivation kinetics is not (see figures in Appendix C.6). Response to the EAD and DAD protocols is also predicted well across all cells except H06, which has a sharp kink in the current (V4) that neither set of calibrated parameters predict. Finally, while hierarchical calibration predicts the current simulated by the pacing protocols (V6–V8) similar to those observed for I11 across cells, the cell-specific calibration is not able to predict current at the lower frequencies for cells C22, J20, and K05.

7.4 Discussion

In this chapter, current recorded from a novel short, information-rich voltage-clamp protocol was used to determine the parameters of an I_{CaL} model. This allowed the determination of all aspects of the model using data from a single cell, which is in contrast to the models that have been developed using data collected from multiple sources. The model developed was then verified against validation data that were also obtained from the same cell.

7.4.1 Data post-processing and quality control

Current recorded from each cell was post-processed for leak and endogenous current and new methods were adopted to tackle the prominent problem of rundown in I_{CaL} recordings (see Chapter 5). The minimum value of t_0 was updated from 5 s to 120 s, which ensured that no recordings showed the trend of 'inverse' rundown (see Section 6.5.3 in Chapter 6). However, other forms of rundown were still prevalent which were corrected using a peak to peak fit (discussed in detail in the next paragraph). The success of the rundown correction methods adopted in this chapter is confirmed by the observed stability in the $\bar{P}_{Ca}$ estimated over the course of an experiment (see Figure 7.8).

The rundown correction method was validated using peaks that were not used to estimate the rundown. These were current recorded during steps to 0 mV in protocols V1, V2, and V3 (shown by the grey dots in Figure 7.4, right). Interestingly, the validation points taken from V2 and V3 show a mini-saturating pattern (similar to the saturating shape of the

rundown-versus-time curve recorded in Chapter 5 and simulated in Chapter 6). Although the reason for this pattern is unclear, it can be explained by the increase in the amount of $[Ca^{2+}]$ near the LCCs channel after each sweep in V2 and V3. Since this shape of the peak currents-versus-time was found to be a saturating trend, it further confirms the simulated results of Chapter 6; i.e. CDI-induced rundown accounts for the saturating shape of the rundown-versus time curve observed in the experiments of Chapter 5.

After the recorded current was post-processed, only five cells passed the quality control criteria. It was found that several cells gave erratic recordings when the LCCs were pushed to remain open at higher voltages for a longer duration. Accounting for this in the next iteration of the calibration protocol should allow the selection of a higher number of cells.

7.4.2 Inferred parameters and model predictions

After post-processing, the calibration data were used to fit a candidate I_{CaL} model. There exist several candidates for the model's structure as shown in Figure 3.4. The existence of so many models can be attributed to differences in laboratory techniques, underlying voltage-clamp protocols used to obtain calibration data, modelling techniques, and assumptions in different electrophysiological mechanisms of I_{CaL}. Many of these models are overly complex because some of their parameters (or even the structure) are unidentifiable. To circumvent these issues, in this chapter a 2-gate model with simple transition rates was used.

Calibration protocol data from the cells which passed QC were used to determine the parameters of an I_{CaL} model using cell-specific and hierarchical optimisation processes. The cell-specific methods all led to the identification of similar kinetic parameters across different cells. Moreover, these parameters were similar to those identified by the hierarchical optimisation. This lack of cell-to-cell variability is promising as previous studies have suggested that it can be due to experimental artefacts [Lei et al., 2020a]. Chapter 4 on the other hand showed vast variability in the predictions of the I_{CaL} models; the results of this chapter suggest that this is probably due to different model-building processes adopted for different models rather than cell-to-cell variability. Improvements to the calibration protocol so that it contains more information can allow the development of a simple I_{CaL} model that can give

a holistic representation of I_{CaL}.

The trained model was able to predict activation and inactivation kinetics well along with the cellular responses to the EAD and DAD protocols, using both cell-specific and hierarchical optimisations. While the hierarchical model was less accurate for the predictions to the AP pacing at various frequencies, the cell-specific model was found to be unreliable for these protocols especially at lower pacing frequencies. Finally, neither of the models were able to predict the I_{CaL} response to the recovery from inactivation protocol. This suggests that the next iteration in the model building pipeline should especially focus on how to correctly incorporate the time-course of recovery.

As was mentioned in Section 7.3, the parameter p_6 (along with p_4) was set to zero. Therefore, the recovery from inactivation was assumed to be voltage-independent while training the model. While the synthetic-study performed on the full model to check the identifiability and robustness showed promising results, these parameters could not be identified from the data. Future work with longer time duration at each voltage-step in the calibration protocol (Figure 7.2C) may help with this complication.

As discussed in Chapter 5, CDI affects not just the magnitude of the recorded current but also its kinetics (which may explain the small changes between sweeps in Figure 7.4). Despite this limitation, in this chapter a preliminary model of the voltage-dependent I_{CaL} gating with simple rate equations was developed, that was able to predict cellular behaviour in response to simulated EADs, DADs, AP response at different frequencies, and activation and inactivation kinetics. This is a promising starting point for future studies.

7.5 Summary

In this chapter, I_{CaL} recorded from CHO cells under a short information-rich voltage-clamp protocol was used to calibrate a simple two-gate I_{CaL} model. Novel methods were adopted to remove rundown from the recorded data and subsequently the rundown-corrected data were considered to be free from calcium-dependent effects. This allowed the construction of a purely voltage-dependent model of I_{CaL}. The model was calibrated using data from five cells using two types of optimisation methods: cell-specific and hierarchical (kinetic

parameters shared across all five cells) optimisations. All six kinetic parameters sets (one for hierarchical and five for cell-specific) were found to have similar values from cell-to-cell, suggesting little or no extrinsic [or population Whittaker et al., 2020] variability in I_{CaL} kinetics. This further weakens the possibility of the massive variation observed across the models' predictions in Chapter 4 to exist because of population variability.

Models obtained via both types of optimisation processes were able to predict the response to the validation protocols designed to provide information about I_{CaL} activation and inactivation kinetics, and current during DADs or EADs. The hierarchical model was also able to predict the current during AP pacing at different frequencies. This chapter showed that a simple model is able to replicate a lot of the electrophysiological features of I_{CaL}. This suggests that the more complex gating mechanisms discussed in Chapter 4 should be investigated more thoroughly as it may be possible to simplify them which will be advantageous in ensuring the identifiability of the parameters. Future work focused on improving the information that the protocol provides about recovery from inactivation kinetics of I_{CaL} can be beneficial in developing a model that replicates more electrophysiological properties of I_{CaL}.

8 | Discussion and conclusions

This chapter summarises the key findings of this thesis and how the work undertaken in each chapter contributes to the aims of the thesis (highlighted in Chapter 1), and to the wider cardiac electrophysiology community. The limitations and possible extensions of this work are also outlined.

8.1 Summary and main contributions

The research presented in this thesis is centered around the mathematical modelling of the L-type calcium current (I_{CaL}) — an ionic channel that plays a critical role in contraction of cardiomyocytes.

Chapter 1 presented the inspiration behind this work, highlighting the importance of mathematical modelling of the cardiomyocyte in the prediction of arrhythmias, thus motivating their importance in the drug-safety screening process. This chapter introduced the history and advancements in the field of cardiac modelling and drew attention to some practices that can be improved in the model-building process. It then focused on the importance of I_{CaL} in the cardiomyocyte and presented the aims of this thesis. At its core, this thesis focuses on the question: can we identify or develop a model that accurately represents the underlying I_{CaL} electrophysiology and can be used to make predictions within a clearly defined *context of use* [Pathmanathan et al., 2017, Whittaker et al., 2020]? This question is addressed in two ways: 1) by thoroughly reviewing and comparing the existing models of mammalian I_{CaL}; and 2) by setting up a preliminary pipeline to collect data and subsequently use it to calibrate an I_{CaL} model in a cell-specific manner.

Chapter 2 introduced the concepts required to understand this thesis including the underlying physiology, electrophysiology, biology, and mathematics. Although the concepts described in this chapter were tailored to I_{CaL} and its models, they are easily transferable to the wider cardiac (and electrophysiological) modelling initiative.

Chapters 3 and 4 described the work undertaken to address the first aim of this thesis. Chapter 3 presented a compilation of 73 models of mammalian I_{CaL}. Each model was then

dissected and compared according to its individual components, including driving force, assumed region of the channel's localisation, and the gating mechanisms. The GHK equation was found to be the dominant formalism for the flux used to describe the driving force across I_{CaL} models, while a few models (mostly those published pre-2000s) used an Ohmic equation. Similarly, most models published in the past two decades were found to localise the L-type calcium channels (LCCs) in the 'dyadic' space, while the older models localised it in the 'submembrane' space or more commonly in the 'bulk cytosol'. Even more diversity was observed for the open probability (O) with the identification of fifteen major gating mechanisms and a further thirteen subtypes. While in some cases the increase in gating complexity can be explained by the addition of new biophysical detail (e.g. identification of CDI gate from type A to type C in Table 3.2 of Chapter 3), many of the different gating mechanisms often represent the same ideas in different ways. It further complicates matters that although the biology of LCCs has been widely studied, its mechanism of inactivation — more complicated than many other ionic channels because of dual voltage/calcium sensitivity — still remains widely debated. This chapter showed that for each aspect of the I_{CaL} model there exist many choices, with no clear indication on *how* to select the components of an I_{CaL} model for any context of use (e.g. drug modulation, proarrhythmic prediction, genetic mutations).

Sixty of the seventy-three models identified in Chapter 3 were investigated via simulations in Chapter 4 using voltage-clamp protocols covering both conventional step protocols and physiological action potentials. Despite the identical experimental setup across the models, large variability was observed in the predictions of the models that could not be explained by inter-species or inter-cellular differences.

The physiological clamp used in this study was an action potential (AP) from an epicardial human ventricular model. A possible limitation of this approach is that APs can vary across cell-types. This was addressed by repeating the experiment using an endocardial and atrial AP clamp. Inter-species differences were not considered to be as important as the underlying proteins involved for the expression of LCCs in different species are highly conserved [Tyson and Snutch, 2013].

This chapter also highlighted an interesting concept of compensation wherein drawbacks in

one aspect of the I_{CaL} model were compensated by other aspects of the I_{CaL} model (e.g. large sensitivity of the model to local $[Ca^{2+}]$ compensated by a large volume of LCC localisation). While such 'intra-model corrections' of one aspect of the model by another may lead to overall acceptable behaviour, it reduces the physiological relevance of the mechanisms within each of these individual components, and in some cases predictive power for new situations.

Owing to the rich history of cardiac modelling dating back more than 60 years, some forums for model sharing exist, such as the Physiome Model Repository (PMR). Several models downloaded from this repository were corrected (and subsequently updated on PMR) for error in equations, units, and/or parameter values. Chapters 3 and 4 (adapted from the associated publication, Agrawal et al. [2022]) together represent a first-ever compilation and qualitative/quantitative review of the impressive number of notable I_{CaL} models published to date.

The substantial variability in predictions from these models raises the question of whether all of the models represent cell-to-cell variability (implying that each model represents an I_{CaL} that can be found biologically) or if it is simply a result of the different methods adopted in the model-building process. Certainly, the presence of the immense number of choices on how to model I_{CaL}, especially with respect to its gating structure, suggests the latter. This could include differences in the assumptions of the electrophysiological mechanism of I_{CaL}, experimental methods used to collect data, or mathematical modelling techniques. One way to determine which model of I_{CaL} truly represents the biological I_{CaL} is by performing experiments in a manner that the data collected are directly useful in the model-building process. This sets up the motivation for the work presented in Chapters 5–7 which address the second aim of this thesis. Since it is difficult to perform experiments that measure localised $[Ca^{2+}]$ in a cell, these chapters focus on the development of the voltage-dependent kinetics of I_{CaL} by setting up a pipeline from data-collection to model-building.

Data collected from LCCs overexpressed in isolated CHO cells using patch-clamp techniques are often contaminated with 'rundown' of current. While several causes contribute to this phenomenon, Chapter 5 presents results indicating that calcium-sensitivity of LCC inactivation contributes towards rundown. Experiments involving I_{CaL} are typically per-

formed using calcium-chelating buffers in the intracellular solution that can bind to incoming Ca^{2+}. The results presented in this chapter show that despite the use of a 'fast' buffer at high concentration, experimental conditions that allow increased accumulation of intracellular $[Ca^{2+}]$ are associated with more rundown of the current. Of the three predominant shapes of the rundown-versus-time curve identified in this chapter — linear, saturating, and inverse — the latter two shapes were accounted for by the CDI-induced rundown (CIR) model developed in Chapter 6.

In Chapter 6 simplified spatial model of the CHO cell was developed that simulates $[Ca^{2+}]$ near the LCCs by accounting for diffusion and 'buffering away' of the time- (and voltage) dependent incoming $[Ca^{2+}]$ from I_{CaL}. For this purpose, the cell was discretised into N shells. Accurate modelling of diffusion over the cellular space required choosing a large number of shells, making the volume of the outermost shell (where LCCs localise) unusually small. To avoid 'compensation' (previously identified in Chapter 4) of this small volume with calcium-sensitivity of I_{CaL}, the shape of the (peak $[Ca^{2+}]$)-versus-time curve in the shell nearest to the LCCs was used as a proxy to study the shape of rundown-versus time curve. Although calcium- and voltage-dependent kinetics were assumed to be independent of each other in this chapter (which is a limitation of this study), the use of peak $[Ca^{2+}]$ to study rundown allows the qualitative extrapolation of the results of the model beyond this assumption. This model showed that while CIR could not account for the linear pattern of the rundown-versus-time curve identified in Chapter 5, it could explain the saturating and inverse patterns.

Chapter 6 showed that the shape of CIR-versus-time curve depends on two things — 1) the degree to which buffer has reached equilibrium within the cell before Ca^{2+} enters via I_{CaL}, and 2) how fast the buffer is replenished over the course of the experiment. Both of these entities are dictated by the experimental design, set by the person designing the experiment. If the cell is small enough to allow the buffer to diffuse fully (i.e. achieve steady-state both before and during the experiment), CIR can be avoided. Often the experimental setup is 'copy-pasted' from the isolated study of one ion-channel to another and only the voltage-clamp protocols are changed to be specific to the ion-channel. However, the importance of spatial distribution of $[Ca^{2+}]$ for I_{CaL} shown in this chapter requires optimising the experimental settings of high-throughput automated patch-clamps in a cell-specific manner. This

would ideally require the measurement of a cell's radius before subjecting it to electrophysiological experiments. The results of Chapter 6 suggest that to avoid CIR, the experimental settings need to be optimised or alternatively, only recordings from small cells should be used. This changes the way the issue of CIR is currently tackled wherein the use of 'fast binding' buffers is promoted. The use of such buffers can only reduce the amount of CDI and the quantitative extent of CIR it initiates, but not eliminate CIR completely.

While Chapter 6 provided explanations on how to eliminate CIR, it was evident that there are multiple other factors that contribute to the rundown recorded in Chapter 5. This limitation was addressed in Chapter 7.

Firstly, the findings of Chapter 6 were used to optimise the experimental setting so that the buffer can equilibrate completely within the cell before any Ca^{2+} enters. This eliminated the occurrence of 'inverse' rundown in the patch-clamp recordings of Chapter 7. Secondly, rundown due to other factors was removed by introducing 'checkpoints' over the course of the experiment that measured the attenuation of the current with time. This chapter set up a proof-of-principle that allows the removal of rundown from I_{CaL} recordings, so that the resultant data can be considered to be purely voltage-dependent (and free from $[Ca^{2+}]$-effects).

Chapter 7 extended the use of short, information-rich voltage-clamp protocols that have previously shown success in hERG, to I_{CaL}. In this chapter a protocol of only 14 s was used to train the model of I_{CaL}. This allowed all the features of the model to be determined from the same data set, and subsequent building of a cell-specific model. This is in contrast to the use of conventional voltage-clamp protocols which run for hundreds of seconds and can then only be used to determine one feature of the model. Such protocols are too long to all be run on the same cell and therefore the resulting model is often not representative of any one individual cell. The use of short protocols in Chapter 7 not only addresses this problem but also leaves scope for the collection of validation data from the same cell. Additionally, analyses of the data from conventional voltage-clamp protocols often use 'summary curves' to determine the parameters of a model, however, in this chapter all the information recorded was used by solving an inverse problem. Finally, while the complex models identified in Chapter 3 are useful in explaining different biological concepts, the parameters

of such models are often unidentifiable, both because of the models' structure and because of *a-priori* unidentifiability of the parameters (formulation of equations such that infinitely many parameter sets give the same behaviour). Therefore, in Chapter 7 a simple model was used with equations derived from transition-state theory to avoid issues with identifiability. A pilot study was also performed to check that the model's parameters are identifiable using synthetically generated data.

While existing models show wide variability in their predictions to the short protocols used in Chapter 7, the cell-specific calibrations of the model closely replicated the data. Not only this, they were also able to predict a wide range of physiological data not used in the training process. These promising results were obtained despite several simplifications such as an assumption of independence of voltage- and calcium-dependent kinetics and no 'mode-switching' of voltage kinetics. Furthermore, while the data from different cells showed some variability, accounting for residual leak current in the data allowed the determination of cell-specific parameters similar enough to suggest the absence of variability of I_{CaL} from cell-to-cell. This finding supports the idea that the presence of wide variability in the choices and predictions of the existing I_{CaL} models (Chapters 3 and 4), is probably because of the model-development process rather than being representative of cell-to-cell variability.

The results of this thesis contribute towards future modelling efforts (of I_{CaL}) in three ways. Firstly, Chapters 3 and 4 facilitate future modelling of I_{CaL} by providing an overview of the existing models of I_{CaL} which acts as a stepping stone for improvement of the existing state-of-the art. Secondly, Chapters 5 and 6 show how the experimental setup can be optimised to avoid rundown of I_{CaL}, thus improving the quality of data collected for modelling efforts. Similarly, Chapter 7 shows by example how a new model can be calibrated and validated, thus setting up a pipeline for the future from data-collection to model-building. All these three major results will allow the development of an improved model of I_{CaL}. Such models when integrated with the full action potential (AP) model can help to better understand conditions that lead to cardiovascular diseases *in silico*.

8.2 Future work

Possible future work borne out of this thesis is discussed in this section, focusing especially on suggestions on how to build better models and test their predictions.

A natural extension of Chapter 7 is to improve the model built so that it can accurately predict all physiological aspects of I_{CaL}. This can be done by: 1) improving the model structure; 2) using better voltage-clamp protocols; and 3) improving the quality of the collected data.

First focusing on the model structure and using the results of Chapter 7, recovery from inactivation kinetics should be incorporated into the cell-specific models presented in the previous chapter. This task is closely coupled with investigating the identifiability of the p_6 parameter that determines the voltage-dependence of the recovery from inactivation of I_{CaL}. Although the synthetic pilot study showed that all parameters were identifiable, the results of the study are valid only for the assumptions made concerning the noise in the signal and the model structure. Cellular recordings showed higher noise than that assumed synthetically; and although the simplified model used in this chapter showed promising results, it could be beneficial to choose the candidate model structure in a better way. One way in which this choice could be made is by screening all fifteen different types of I_{CaL} gating mechanisms identified in Chapter 3 against data collected from short, information-rich protocols. Ongoing work has showed that many of the different types of model structures give rise to issues with parameter identifiability. Furthermore, several features of the more complex models can also be replicated by calibrating a simple transition-state model. Future work investigating structural identifiability of the existing gating mechanisms may be beneficial in isolating a model whose parameters are identifiable and is capable of producing robust and reliable predictions. Some of the promising gating structure which may have not have issues of unidentifiability include Types A and N shown in Figure 3.4. A systematic review that identifies how each parameter of the complex models contributes to I_{CaL}'s physiological properties such as activation, inactivation, and recovery from inactivation can prove to be instrumental in the model-building process.

Another avenue for improving the model is by designing better voltage-clamp protocols to collect data by maximising the amount of information that can be obtained from the

calibration protocol. Using a reasonable enough guess of the model structure, a voltage-clamp protocol can be optimised by maximising the volume of the phase-space (a space determined by the number of gates in the model wherein the value of each gate varies from 0 to 1) that is visited by the model states under forcing by the protocol. This involves finding the optimal series of voltage-steps along with the duration of each step so that the phase-space gets filled. Although this is a chicken and egg kind of approach where the best protocol can only be developed if the exact model is already known, preliminary work involving phase-filling design has shown that a protocol optimised for a certain parameter set works equally well for other local sets of model parameters.

The pipeline set up in Chapter 7 is a promising way to clean I_{CaL} data of any rundown effects (CDI-induced or otherwise), and obtain voltage-dependent I_{CaL}. Further, the experimental conditions can be optimised to minimise (or eliminate) CIR in accordance with the modelling results of Chapter 6. These results can be verified by performing patch-clamp experiments to study rundown by varying the time given to the buffer to diffuse into the cell both before and after the application of a voltage-clamp in accordance with the cell's radius.

The studies described thus far in this section can be used to improve the model-building process for I_{CaL}. This specifically focuses on building a model corresponding to data recorded from individual cells. The variability in the data recorded from different cells in Chapter 7 was found to be well-explained by the presence of residual leak current in the post-processed data. It could also be beneficial to consider implementing a model describing the experimental artefacts that account for error in patch-clamp recordings [Lei et al., 2020a] to see further removal of variability across the cell-specific models' parameters.

The model-building discussion up to this point (and certainly in the entire thesis) has been focused on the voltage-dependent aspects of I_{CaL}. CDI is perhaps the most challenging characteristic of I_{CaL} to model, both because of the difficulty in experimental measurement of localised $[Ca^{2+}]$ and also because of the computationally heavy numerical simulations required (as adopted in Chapter 6) that consist of more than 1000 state variables (due to discretisation of the cell into smaller units), rendering any parameter optimisation difficult. Further, given the difficulty in separating CDI effects from rundown, CHO cells (or indeed

any other expression system) may not be ideal to identify CDI.

Once a new model of I_{CaL} has been identified, it can be integrated with an AP model (like the Tomek et al. [2019] model) and its effects on the prediction of APs, DADs, EADs, APD restitution, and formation of alternans can be studied. This can be compared to the effects of any existing I_{CaL} model on the same physiological properties. This work would require substantial re-calibration of the volume of localisation and the associated $[Ca^{2+}]$-sensitivity of each model.

8.3 Concluding remarks

To conclude, this thesis shows that more than 70 models of I_{CaL} exist. The large number of models display both differences in their structures as well as wide variability in their predictions in response to identical experiments. This raises the question: which I_{CaL} model is most representative of the underlying biology for a given context of use? A pipeline was developed from data-collection to model-building that facilitates the answer to this question. First focusing on data-collection, it was identified that I_{CaL}'s sensitivity to local $[Ca^{2+}]$ contributes to its attenuation with time (rundown) in patch-clamp measurements of cells overexpressing LCCs. Then, a mechanistic model was used to show that rundown due to CDI can be avoided by optimising the experimental setup in a cell-specific manner. Secondly, an example of correcting I_{CaL} recordings for rundown was shown by introducing checkpoints in the experimental design. A short, information-rich voltage-clamp protocol was then implemented to rapidly characterise a preliminary transition-state I_{CaL} model. Calibration of the model to data recorded from several cells showed that there is very little variability in the underlying *biology* of I_{CaL} from cell-to-cell. This indicates that the wide variability observed in the predictions of existing I_{CaL} models can be designated to differences in the model-construction process.

I hope that this thesis has drawn attention to fact that there exist a vast array of models that are all meant to represent the same ionic current, but each model predicts that current in a slightly different way than any other. While minor physiological explanations exist for these differences, it is unlikely that the underlying biology has completely differently mechanisms in different individuals or cells. Usually, several features of the more complex

models are also well explained by simpler models suggesting it might be possible to reduce the number of candidate models.

The plethora of ionic models developed would not have been possible without the discovery and advancement of patch-clamp technique that allows the measurement of an isolated current. Nevertheless, recent studies have found that they introduce some artefacts in the recorded data (e.g. cells may 'experience' different voltage than planned). Rundown is another such artefact where the recorded current is contaminated such that the identification of the 'pure' current is not straightforward. Not only this, rundown is also a source of variability that differs from one cell to the other, especially when recording I_{CaL}. Artefacts such as rundown should be carefully accounted for before the data can be used to draw insight on or develop a model of, an ionic current.

In this thesis, the unique challenges posed by I_{CaL}'s electrophysiology were highlighted and a pipeline was setup that can be used to arrive at a more robust, reliable, and ubiquitous model of I_{CaL}.

A | Comparison of the models of L-type calcium current

This appendix provides some additional information referred to in Chapters 3 and 4.

Description	URL
Compilation of data sources	https://bit.ly/3DhmUM9
Animation showing voltage-dependent activation	https://bit.ly/3W9o7O8
Animation showing voltage-dependent inactivation	https://bit.ly/3DDu3HQ
Animation showing recovery from voltage-dependent inactivation	https://bit.ly/3DdR9DF
Compilation of CellML code of the models used in Chapter 4	https://bit.ly/3SHuPbb
Interactive story of the results presented in Chapter 4	https://bit.ly/3FmUMdc
Interactive story showing response of models to different AP clamps	https://bit.ly/3Fml0fy

Table A.1: Some useful links with additional information referred to in Chapters 3 and 4

A.1 Example equations of L-type calcium current models

In this section example equations of a Hodgkin-Huxley model (HHM) and a Markov model (MM) are presented. An example of an HHM is the model by McAllister et al. [1975], given by the equations:

$$
\begin{aligned}
I_{si} &= g_{si} \cdot d \cdot f \cdot (V_m - E_{si}) + g_{si_n} \cdot d_1 \cdot (V_m - E_{si}), \\
d_1 &= \frac{1}{1 + \exp(-0.15 \cdot (V_m + 40))}, \\
\alpha_d &= \frac{0.002 \cdot (V_m + 40)}{1 - \exp(-0.1 \cdot (V_m + 40))}, \\
\beta_d &= 0.02 \cdot \exp(-0.0888 \cdot (V_m + 40)), \\
\frac{\mathrm{d}d}{\mathrm{d}t} &= \alpha_d \cdot (1 - d) - \beta_d \cdot d, \\
\alpha_f &= 0.000987 \cdot \exp(-0.04 \cdot (V_m + 60)), \\
\beta_f &= \frac{0.02}{\exp(-0.087 \cdot (V_m + 26)) + 1}, \\
\frac{\mathrm{d}f}{\mathrm{d}t} &= \alpha_f \cdot (1 - f) - \beta_f \cdot f,
\end{aligned}
\tag{A.1}
$$

where, I_{si} is the 'secondary inward' current (see Section 2.2.4), g_{si} is the maximal conductance, E_{si} is the reversal potential, d is the voltage-dependent activation gate, f is the

voltage-dependent inactivation gate, g_{si_n} is the maximal conductance of channels that do not inactivate, and d_1, α_d, β_d, α_f and β_f are voltage-dependent chemical transition rates.

An example of an MM is the model by Faber et al. [2007], given by the equations:

$$
\begin{aligned}
\frac{\mathrm{d}C_0}{\mathrm{d}t} &= \beta_0 \cdot C_1 + \theta \cdot C_{0Ca} - (\alpha_0 + \delta) \cdot C_0,\\
\frac{\mathrm{d}C_{0Ca}}{\mathrm{d}t} &= \beta_0 \cdot C_{1Ca} + \delta \cdot C_0 - (\alpha_0 + \theta) \cdot C_{0Ca},\\
\frac{\mathrm{d}C_1}{\mathrm{d}t} &= \alpha_0 \cdot C_0 + \beta_1 \cdot C_2 + \theta \cdot C_{1Ca} - (\beta_0 + \alpha_1 + \delta) \cdot C_1,\\
\frac{\mathrm{d}C_{1Ca}}{\mathrm{d}t} &= \alpha_0 \cdot C_{0Ca} + \beta_1 \cdot C_{2Ca} + \delta \cdot C_1 - (\beta_0 + \alpha_1 + \theta) \cdot C_{1Ca},\\
\frac{\mathrm{d}C_2}{\mathrm{d}t} &= \alpha_1 \cdot C_1 + \beta_2 \cdot C_3 + \theta \cdot C_{2Ca} - (\beta_1 + \alpha_2 + \delta) \cdot C_2,\\
\frac{\mathrm{d}C_{2Ca}}{\mathrm{d}t} &= \alpha_1 \cdot C_{1Ca} + \beta_2 \cdot C_{3Ca} + \delta \cdot C_2 - (\beta_1 + \alpha_2 + \theta) \cdot C_{2Ca},\\
\frac{\mathrm{d}C_3}{\mathrm{d}t} &= \alpha_2 \cdot C_2 + \beta_3 \cdot O + I_{vf} \cdot \omega_f + I_{vs} \cdot \omega_s + C_{3Ca} \cdot \theta - (\beta_2 + \alpha_3 + \gamma_f + \gamma_s + \delta) \cdot C_3,\\
\frac{\mathrm{d}C_{3Ca}}{\mathrm{d}t} &= \alpha_2 \cdot C_{2Ca} + \beta_3 \cdot I_{Ca} + I_{vfCa} \cdot \omega_f + I_{vsCa} \cdot \omega_s + C_3 \cdot \delta - (\beta_2 + \alpha_3 + \gamma_f + \gamma_s + \theta) \cdot C_{3Ca},\\
\frac{\mathrm{d}I_{Ca}}{\mathrm{d}t} &= \alpha_3 \cdot C_{3Ca} + I_{vfCa} \cdot \lambda_f + \lambda_s \cdot I_{vsCa} + O \cdot \delta - (\beta_3 + \phi_f + \phi_s + \theta) \cdot I_{Ca},\\
\frac{\mathrm{d}I_{vf}}{\mathrm{d}t} &= \gamma_f \cdot C_3 + \phi_f \cdot O + \omega_{sf} \cdot I_{vs} + I_{vfCa} \cdot \theta - (\omega_f + \lambda_f + \omega_{fs} + \delta) \cdot I_{vf},\\
\frac{\mathrm{d}I_{vfCa}}{\mathrm{d}t} &= \gamma_f \cdot C_{3Ca} + \phi_f \cdot I_{Ca} + \omega_{sf} \cdot I_{vsCa} + I_{vf} \cdot \delta - (\omega_f + \lambda_f + \omega_{fs} + \theta) \cdot I_{vfCa},\\
\frac{\mathrm{d}I_{vs}}{\mathrm{d}t} &= \gamma_s \cdot C_3 + O \cdot \phi_s + \omega_{fs} \cdot I_{vf} + I_{vsCa} \cdot \theta - (\omega_s + \lambda_s + \omega_{sf} + \delta) \cdot I_{vs},\\
\frac{\mathrm{d}I_{vsCa}}{\mathrm{dt}} &= \gamma_s \cdot C_{3Ca} + I_{Ca} \cdot \phi_s + \omega_{fs} \cdot I_{vfCa} + I_{vs} \cdot \delta - (\omega_s + \lambda_s + \omega_{sf} + \theta) \cdot I_{vsCa},\\
\frac{\mathrm{d}O}{\mathrm{d}t} &= \alpha_3 \cdot C_3 + \lambda_f \cdot I_{vf} + \lambda_s \cdot I_{vs} + I_{Ca} \cdot \theta - (\beta_3 + \phi_f + \phi_s + \delta) \cdot O,\\
I_{maxCa} &= \frac{4V_m F^2 \bar{P}_{Ca}}{RT} \left(\frac{\gamma_{Cai} Ca_{ss} \exp\left(\frac{2V_m F}{RT}\right) - \gamma_{Cao} Ca_o}{\exp\left(\frac{2V_m F}{RT}\right) - 1} \right),\\
I_{maxK} &= \frac{V_m F^2 \bar{P}_K}{RT} \left(\frac{\gamma_{Ki} K_{ss} \exp\left(\frac{V_m F}{RT}\right) - \gamma_{Ko} K_o}{\exp\left(\frac{V_m F}{RT}\right) - 1} \right),\\
I_{maxNa} &= \frac{V_m F^2 \bar{P}_{Na}}{RT} \left(\frac{\gamma_{Nai} Na_{ss} \exp\left(\frac{V_m F}{RT}\right) - \gamma_{Nao} Na_o}{\exp\left(\frac{V_m F}{RT}\right) - 1} \right),\\
I_{Ca} &= I_{maxCa} \cdot O, \quad I_{Ca,Na} = I_{maxNa} \cdot O, \quad I_{Ca,K} = I_{maxK} \cdot O,
\end{aligned}
\tag{A.2}
$$

where, C_i, C_{iCa}, I_{Ca}, I_{vf}, I_{vfCa}, I_{vs}, I_{vsCa}, and O are state variables of the MM, θ is an independent parameter and δ is a calcium-dependent transition rate. α_i, β_i, γ_i, ϕ_i, λ_i, and

ω_i are voltage-dependent transition rates.

A.2 Predictions using AP-CaT clamp

In Chapter 4, simulations were run on 60 models using an AP-CaT clamp and the resulting predictions showed lots of variability (see Section 4.3.4). The predicted gating or O of these models was then grouped using factors including year of publication (Figure 4.9) and localisation of the LCCs (Figure 4.10). Here the models' predictions are grouped using three other factors: species, cell, and gating kinetics.

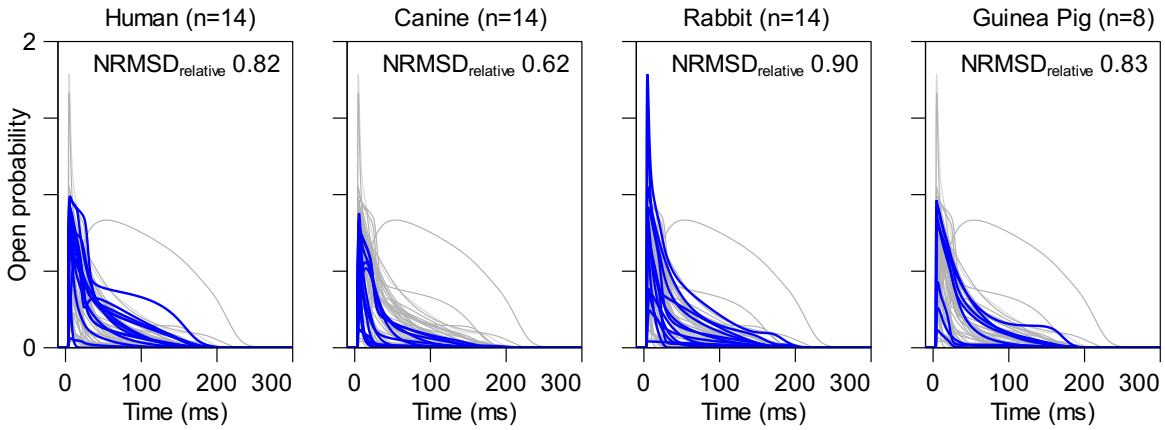

Figure A.1: Open probability in response to AP clamp 3 (Figure 4.8), grouped according to species. Blue curves in each panel correspond to I_{CaL} predictions of models representing the particular species, while the remaining predictions are shown in grey. (Note how some models allow O to be greater than 1, so that it is not strictly a probability in these models.)

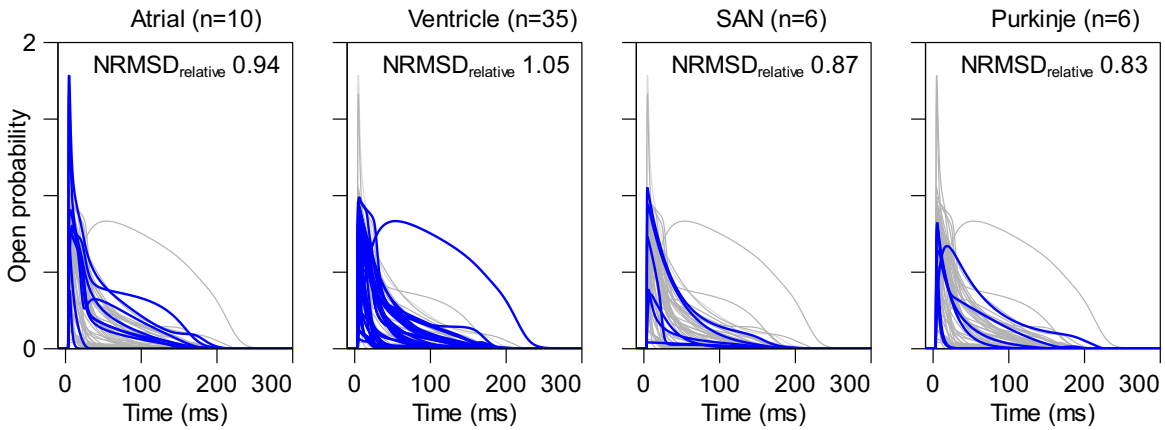

Figure A.2: Open probability in response to AP clamp 3 (Figure 4.8), grouped according to cell type. Blue curves in each panel correspond to I_{CaL} predictions of models representing the particular cell, while the remaining predictions are shown in grey.

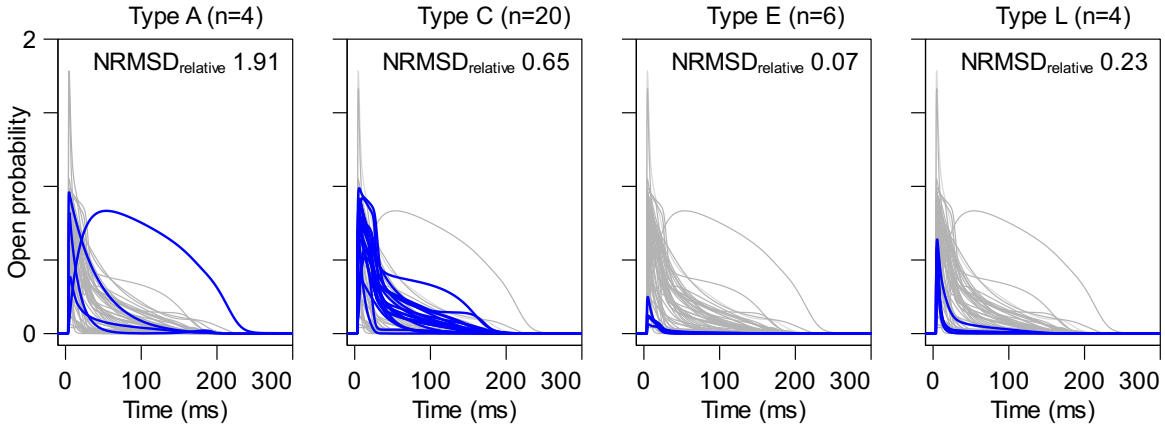

Figure A.3: Open probability in response to AP clamp 3 (Figure 4.8), grouped according to gating type (Figure 3.4). Blue curves in each panel correspond to I_{CaL} predictions of models representing the particular gating, while the remaining predictions are shown in grey.

B | Calcium-dependent inactivation induced run-down

This appendix provides supporting material that has been referred to in Chapters 5 and 6.

B.1 Machine properties

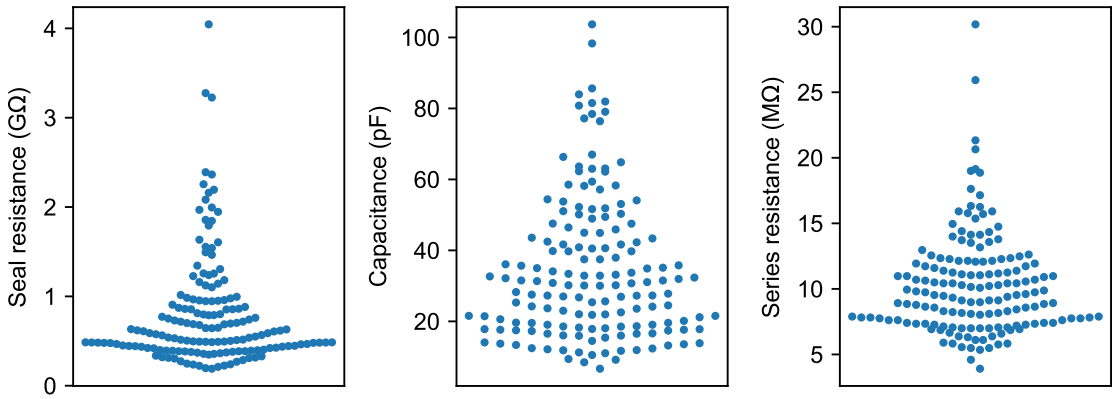

Figure B.1: Distribution of properties recorded during the patch-clamp for the selected cells- **Left**: seal resistance, **Centre**: capacitance, and **Right**: series resistance.

In the automated patch-clamp setup used in this thesis, the seal resistance (R_{seal}), membrane capacitance (C_m), and series resistance (R_s) are measured for each sweep. The median of these properties across all sweeps for each cell that passed the quality control criteria established in Section 5.2.5 is shown in Figure B.1.

B.2 Leak in an automated patch-clamp

The leak current in a cardiomyocyte is caused by the presence of leak channels in the sarcolemma. However, the leak current in a patch-clamp occurs due to imperfect seal resistance, R_{seal} [Lei et al., 2020b], rather than because of ionic channels. Therefore, the weaker the R_{seal}, the stronger the *conductance* of the leak current would be. This argument is confirmed by the inverse relationship shown in Figure B.2 (left). Note, that there may be deviation in this relationship if E_{leak} is large (see Figure B.2, right, for the probability distribution of E_{leak}).

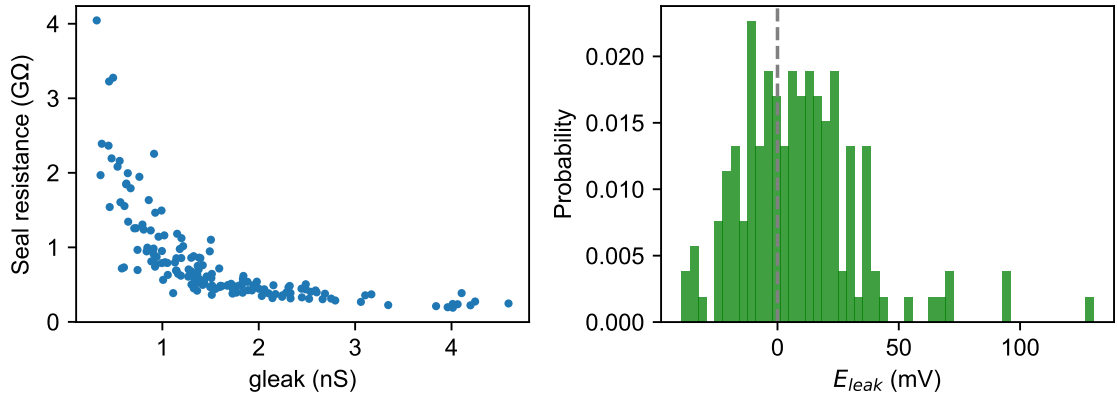

Figure B.2: **Left**: Scatter plot showing the inverse relationship between the machine recorded seal resistance and the calculated leak conductance using the linear-leak ramp (see Section 5.2.3). **Right**: Distribution of the calculated E_{leak}.

B.3 Range of LCC permeability

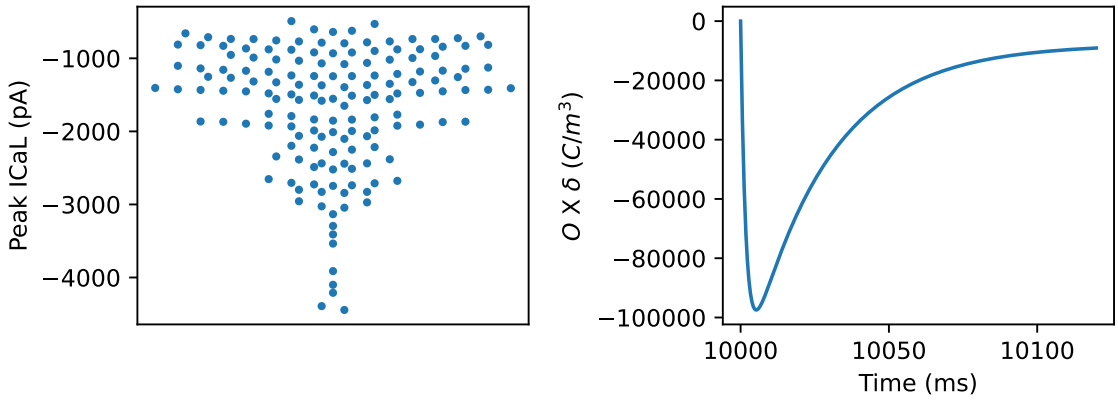

Figure B.3: **Left**: Distribution of the peak I_{CaL} recorded at the step to 0 mV from all the selected cells in Section 5.2.5. **Right**: Simulation of $I_{CaL}/\bar{P}_{Ca}$ from the model by Zeng et al. [1995] used in Chapter 6.3.1.

The possible range of the permeability of the LCCs was calculated based on the data collected in Chapter 5 and the I_{CaL} model by Zeng et al. [1995] used in Chapter 6.3.1. The peak I_{CaL} was found to vary from -490.7 pA to -4444.4 pA for all the cells selected after the quality control criteria in Section 5.2.5 as shown in Figure B.3 (left). The maximum value of the quantity given by $O \times \delta$ at a step to 0 mV (same as the voltage-clamp protocol applied to cells in Chapter 5) was found to be -97458.12 C/m^3 (Figure B.3, right). The possible range of $\bar{P}_{Ca}$ was estimated by dividing the two quantities and was found to vary

from 0.005 nL/s to 0.046 nL/s.

B.4 Fraction of calcium from leak current

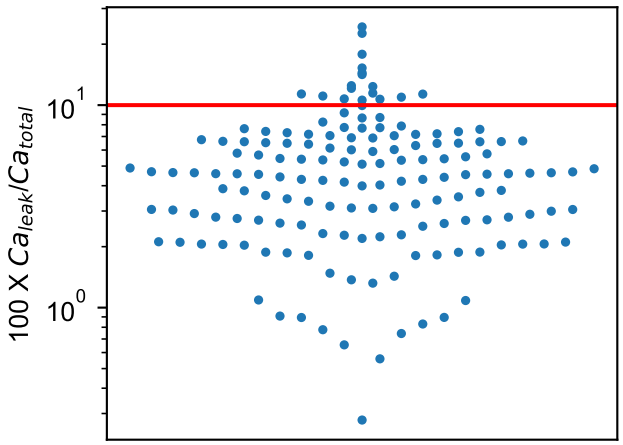

Figure B.4: Distribution of the percentage of total calcium brought into the cell by leak current. Each point represents the percentage from a quality control selected cell (Section 5.2.5). The 10% threshold is marked by a red line.

While there exist two sources of Ca^{2+} into the cell used in Chapter 5 (I_{CaL} and I_{leak}), the fraction of calcium brought in by the leak current is less than 10% of the total Ca^{2+} brought into the cell (Figure B.4). Therefore, for simplification, when simulating rundown due to $[Ca^{2+}]$, only I_{CaL} was considered as the major source of Ca^{2+}.

B.5 Statistical tests to determine significance of results

Figures 5.7, 5.8, and 5.9 showed that within each subgroup, a higher rundown rate is observed at conditions in which more Ca^{2+} enters the cell/less Ca^{2+} is removed from the cell. Here, the results from statistical tests are used to determine if the difference in the means across the groups is significant using one-way ANOVA [Ostertagová and Ostertag, 2013] and t-tests [Kim, 2015]. One assumption of both these methods is that the samples should be drawn from a normal distribution. Figure B.5 (shows) shows that the rundown rates form part of an almost normal distribution.

Although the other assumption for these tests is not valid here (independence of samples), the tests show a significant difference in means for all subgroups in Figure 5.9 and two

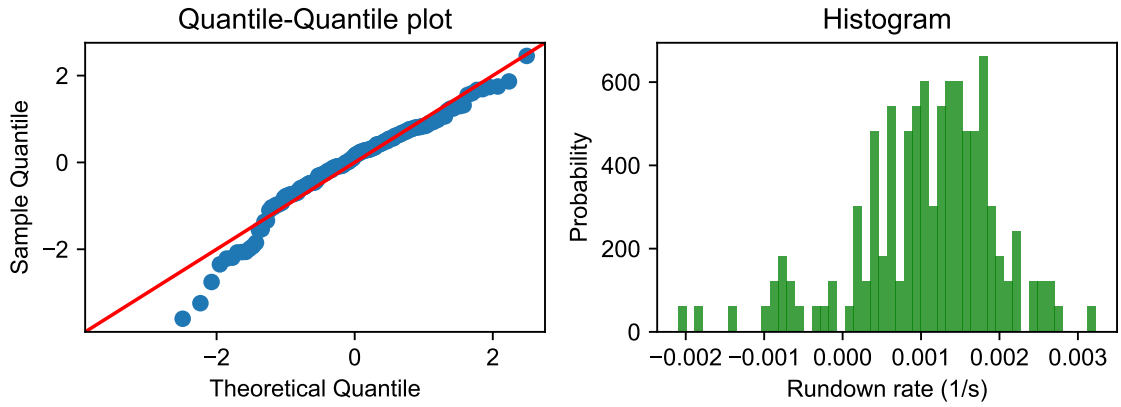

Figure B.5: **Left**: Quantile-quantile plot and **Right**: histogram showing the distribution of the rundown rate calculated from the selected cells in Chapter 5.

subgroups in Figure 5.8. A more complex statistical model that accounts for the interdependence of these groups may be able to show significant difference (and more importantly the effect size) for all the factors simultaneously — temperature, block of I_{NaCa}, and holding potential duration.

B.6 Non-dimensionalisation of PDE

This section provides a step-by-step account of how Equation 6.2 along with the boundary and initial conditions given in Equation 6.3 are non-dimensionalised. First, Equation 6.2 is re-written as:

$$\frac{1}{D_B}\frac{\partial \mathrm{B}}{\partial t} = \frac{\partial^2 \mathrm{B}}{\partial r^2} + \frac{2}{r}\frac{\partial \mathrm{B}}{\partial r}. \tag{B.1}$$

Then the non-dimensionalised variable u is considered, which is defined as: $\frac{\mathrm{B}r}{B_{max}R_h}$. u is then differentiated twice with respect to r to obtain:

$$\begin{aligned}
\frac{\partial u}{\partial r} &= \frac{1}{B_{max}R_h}\left(r\frac{\partial \mathrm{B}}{\partial r} + \mathrm{B}\right), \\
\frac{\partial^2 u}{\partial r^2} &= \frac{r}{B_{max}R_h}\left(\frac{\partial^2 \mathrm{B}}{\partial r^2} + \frac{2}{r}\frac{\partial \mathrm{B}}{\partial r}\right), \\
\frac{B_{max}R_h}{r}\frac{\partial^2 u}{\partial r^2} &= \frac{\partial^2 \mathrm{B}}{\partial r^2} + \frac{2}{r}\frac{\partial \mathrm{B}}{\partial r}.
\end{aligned} \tag{B.2}$$

The left hand side (LHS) of Equations B.1 and B.2 are equated to get:

$$\frac{1}{D_B}\frac{\partial \mathrm{B}}{\partial t} = \frac{B_{max}R_h}{r}\frac{\partial^2 u}{\partial r^2}. \tag{B.3}$$

Rearranging the above equation and substituting $\mathrm{B} = \frac{uB_{max}R_h}{r}$:

$$\frac{\partial u}{\partial t} = D_B\frac{\partial^2 u}{\partial r^2}. \tag{B.4}$$

Next, the above equation is rearranged and multiplied on both sides by the quantity $(R_h - R_0)^2$ to get:

$$\frac{(R_h - R_0)^2}{D_B}\frac{\partial u}{\partial t} = (R_h - R_0)^2\frac{\partial^2 u}{\partial r^2}. \tag{B.5}$$

Here, the non-dimensional quantity $\frac{D_B t}{(R_h - R_0)^2}$ can be re-written as τ to get:

$$\frac{\partial u}{\partial \tau} = (R_h - R_0)^2\frac{\partial^2 u}{\partial r^2}. \tag{B.6}$$

Now, introducing a non-dimensional radius x, and using the chain rule, the above equation can be re-written as:

$$\frac{\partial u}{\partial \tau} = (R_h - R_0)^2\frac{\partial^2 u}{\partial x^2}\left(\frac{\partial x}{\partial r}\right)^2. \tag{B.7}$$

By substituting the quantity $x = \frac{r - R_0}{R_h - R_0}$, the above equation reduces to:

$$\frac{\partial u}{\partial \tau} = \frac{\partial^2 u}{\partial x^2}. \tag{B.8}$$

Next, the boundary conditions given in Equation 6.3 are non-dimensionalised. At $r = R_h$ and $r = R_0$, $x = 1$ and $x = 0$ respectively. The first boundary condition simplifies to

$ul|_{x=1} = 1$. The second boundary condition can be derived from Equation B.2.

$$\begin{aligned}
\left.\frac{\partial u}{\partial r}\right|_{r=R_0} &= \frac{1}{B_{max}R_h}\left[r\frac{\partial \mathrm{B}}{\partial r} + \mathrm{B}\right]_{r=R_0}, \\
\left.\frac{\partial u}{\partial r}\right|_{r=R_0} &= \left.\frac{\mathrm{B}}{B_{max}R_h}\right|_{r=R_0} = \left.\frac{u}{r}\right|_{r=R_0}, \\
\left.\frac{\partial u}{\partial x(R_h - R_0)}\right|_{x=0} &= \left.\frac{u}{R_0 + x(R_h - R_0)}\right|_{x=0}, \\
\left.\frac{\partial u}{\partial x}\right|_{x=0} &= \left.\frac{hu}{hx - 1}\right|_{x=0}.
\end{aligned} \tag{B.9}$$

The initial condition simplifies to $u|_{\tau=0} = 0$.

B.7 Convergence

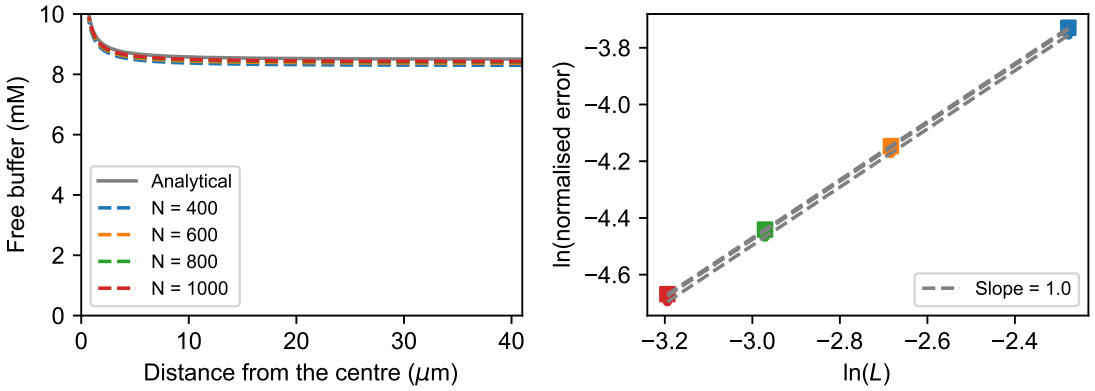

Figure B.6: **Left**: Concentration profile showing diffusion of the buffer at $t = 300\,s$ using the analytical solution (Equation 6.16) and simulations using equations described in Section 6.4.2 for different N. **Right**: Plot of log of the normalised error at each N plotted against the log of the corresponding shell width (L), showing the expected first order convergence for a centred finite volume scheme (at three different radial distances from the centre).

In Section 6.4.2, the cell was discretised into N shells as given by Equation 6.23. Here a convergence test is conducted to determine the minimum number of shells that a cell should be discretised into so that the resulting simulation has a very low error when compared to the true solution.

To ignore the effects of time-varying boundary conditions, the convergence test was performed on the free diffusion of the buffer prior to applying a voltage clamp (i.e. LCCs are

closed or no Ca^{2+} ion side the cell). For this test, a cell of the maximum possible radius — 40.6 μm (see Table 6.1) and the maximum time of interest (300 s) was used to determine the convergence conditions for the 'most difficult configuration'.

Figure B.6 (left) shows the concentration profile of the free buffer at $t = 300\,s$ using both the derived analytical solution given by Equation 6.16, and discretisation of the equations described in Section 6.4.2 at varying values of N. The concentration profile plotted using the analytical solution was considered to be the 'true' solution. The error in the prediction of [B] by each discretisation scheme was calculated at three different radial distances from the centre of the sphere (10 μm, 20 μm, and 30 μm). The error at each radial distance was calculated by normalising the absolute difference of the predicted [B] with respect to the corresponding concentration at that distance using the analytical solution. The width of the shell (L) rather than N was chosen here because the radius of the cell varies from cell-to-cell and L allows the evaluation of a discretisation scheme independent of the cell's size. Figure B.6 (right) shows the convergence of error at smaller L (larger N). Simulations at all N shown in this figure show negligible error. A shell width of ≈0.05 μm (40.6 μm/800) was chosen as the minimum shell width that all numerical discretisations should have. This ensures that the error in [B] at any point is less than 1.5% ($\ln 0.015 = -4.2$, see Figure B.6, right).

B.8 Effect of (not) blocking CDI gate

For the results shown in Chapter 6, the CDI gate (f_{Ca}) was blocked as discussed in Section 6.4.3. Here, Figure 6.13 was recreated by not blocking f_{Ca} as shown in Figure B.7. This shows figure that, while the actual amount of CDI predicted in both cases is different, the *rate of change of CDI* (or rundown) is qualitatively similar. Therefore, blocking f_{Ca} did not affect the results of this study.

B.9 Rundown prediction

Section 6.5.3 of Chapter 6 showed that when ζ (given by Equation 6.26) is greater than one, the model predicts a saturating shape of CDI-induced rundown (CIR), otherwise, it predicts

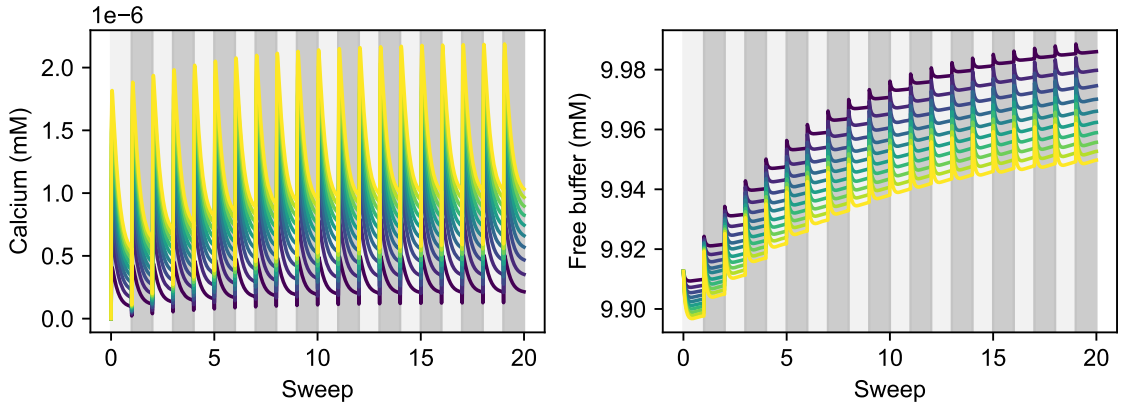

Figure B.7: Simulation of $[Ca^{2+}]$ (**Left**) and [B] (**Right**) near LCCs plotted successively for each sweep. These simulations were performed at default conditions while $\bar{P}_{Ca}$ was varied from 0.005 nL/s (indigo) to 0.046 nL/s (yellow).

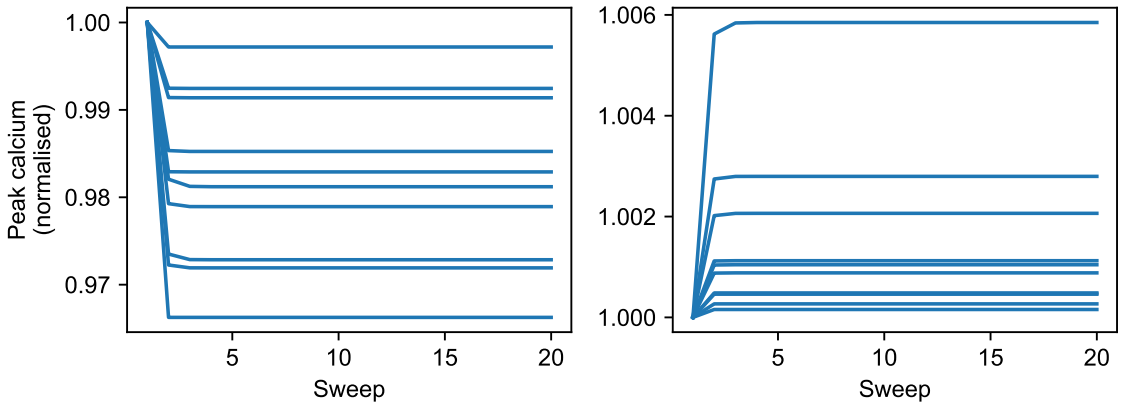

Figure B.8: Normalised peak $[Ca^{2+}]$ predicted when the number line is randomly sampled so that t_{diff} is the smallest time constant. **Left**: ζ is less than one. **Right**: ζ is greater than one.

an inverse rundown. Here this concept is shown to hold true not only when t_{hold} and t_0 are the smallest time scales but also when t_{diff} is the smallest.

When the cell is much smaller than the other time scales (t_{hold} and t_0), the model does not predict CIR as shown in Figure 6.16 (left) of Chapter 6. Here the left panel of Figure 6.16 is zoomed in to show that while the amount of CIR simulated by the model is negligible, the shape of the rundown-versus-time curve still follows from that predicted by ζ as shown in Figure B.8.

Similar observations are made for the corner cases where the predictions made by ζ are upheld. Even when two or more time constants are equal, the shape of the rundown-versus-time curve follows the predictions by ζ, but the amount of rundown is negligible if t_{diff} is one of the smallest time constants. The three corner cases are shown in Figure B.9.

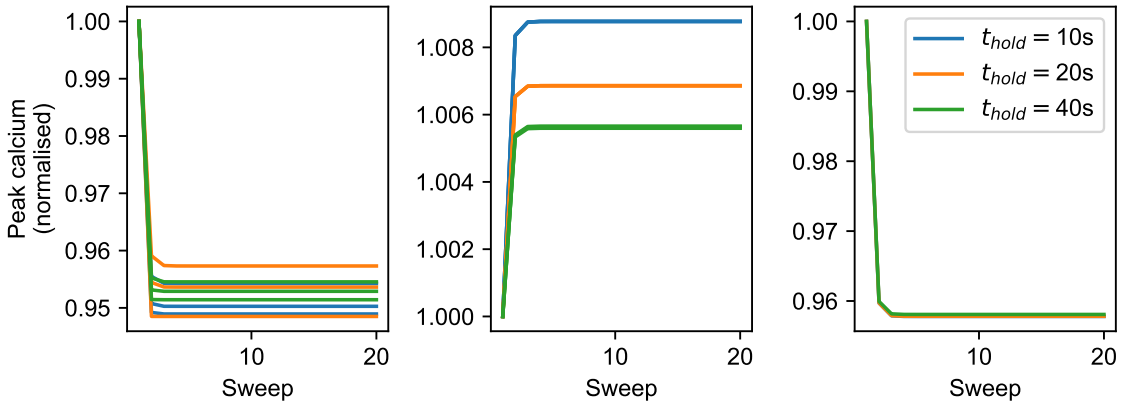

Figure B.9: Normalised peak $[Ca^{2+}]$ predicted by the rundown model at corner cases where t_{diff} is one of the smallest time constant. **Left**: $t_{diff} = t_0 < t_{hold}$, **Centre**: $t_{diff} = t_{hold} < t_0$, and **Right**: $t_{diff} = t_{hold} = t_0$,

C | Preliminary model of the L-type calcium current

This appendix provides supporting material that has been referred to in Chapter 7.

C.1 State-space plot

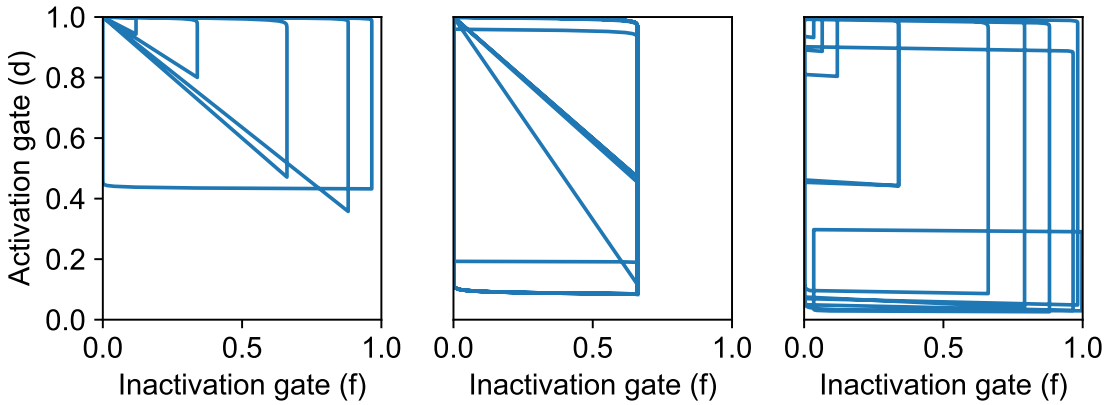

Figure C.1: State-space plot of the model by Ten Tusscher and Panfilov [2006] using activation (left), recovery from inactivation (right), and staircase (right) protocols used in Chapter 7 given by V1, V3, and C respectively in Figure 7.2.

C.2 Post-processed current

Post-processed data under each protocol of the experimental design (see Figure 7.3) are shown in Figure C.2. To allow easy comparison of the data across cells, current at each protocol has been normalised by the maximum magnitude of current recorded, while conserving the direction of current. This plot shows that while the data recorded under some protocols is consistent across cells, it varies quite a lot for others.

C.3 Feasible parameter region

The feasible parameter region (or prior) assumptions for the values of each parameter in the model were adapted from the method used by Beattie et al. [2018]. $\bar{P}_{Ca}$ was taken

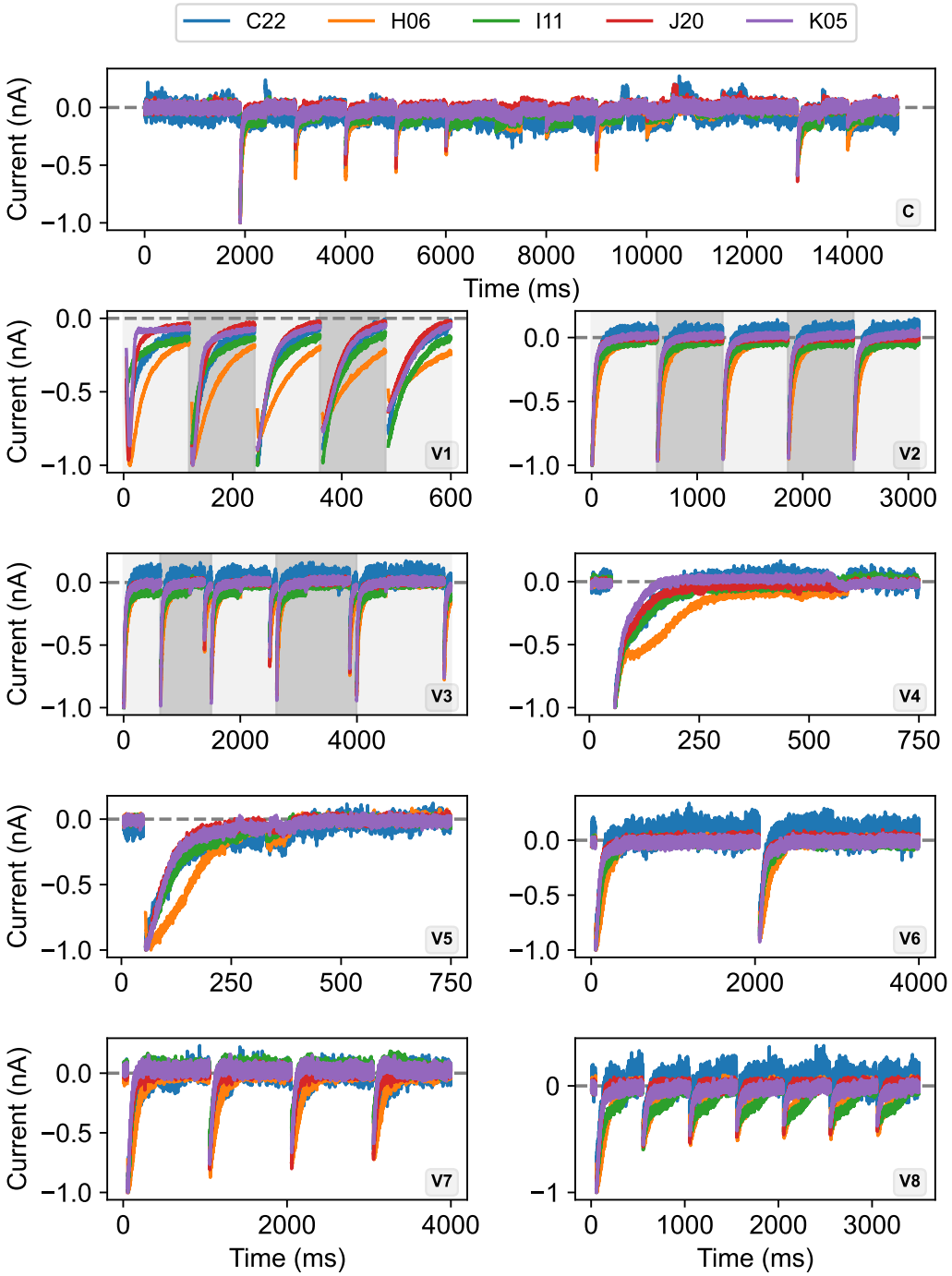

Figure C.2: Post-processed data (normalised) for all the selected cells recorded under each protocol given in Figure 7.2.

to be uniformly distributed between 10^{-4} to 10 nL/s. These values were determined from the magnitude of the experimental data. The range of residual leak conductance (g^*_{leak}) and

reversal potential (E^*_{leak}) was similarly determined from the recorded data to lie between -100 nS to 100 nS and -200 mV to 200 mV respectively.

The remaining parameters follow the transition rate given by $k = p_i \exp(\pm p_j V)$ where k was constrained to lie between 1.67×10^{-5} and 1000 ms^{-1}.

Physiological arguments were used to determine the permissible range of the p_i type parameters. The time constants associated with the activation and inactivation gates are given by $1/(k_1 + k_2)$ and $1/(k_3 + k_4)$, respectively. Assuming that the order of magnitude of parameters of type p_i will be similar to that of the rate constants, the time constants can be approximated as $1/(p_1 + p_2)$ and $1/(p_3 + p_4)$. Furthermore, assuming that the two rates would be approximately equal to each other, the time constants can be approximated as $1/(2p_i)$. From the literature it is known that the inactivation time constant can vary from 50 to 700 ms [Li et al., 1999, Kim et al., 2016]. Time constants for activation can be even faster [McDonough et al., 2005]. By assuming that the time constants vary from 0.1 ms to 1000 ms, the corresponding value of p_i would vary from 5×10^{-4} ms^{-1} to 5 ms^{-1}. In this study, a broader range of the p_i type parameters was assumed and allowed to vary between 10^{-9} ms^{-1} and 10^{3} ms^{-1}.

The permissible range of parameter type p_j was chosen to vary according to the quantity given by $\exp(\pm p_j V_m)$. The membrane voltage (V_m) in the calibration protocol varies from -120 mV to 40 mV (see Figure 7.2C). For this voltage range, at very low values of p_j (i.e. 10^{-7}), the quantity $\exp(bV_m)$ varies by $\sim$0.0016%. Since the reaction rate k should be voltage-dependent, it is implausible that p_j would be lower than 10^{-7}, so this was selected as the lower bound of p_j. On the other hand, at high values of p_j (i.e. 0.9), the quantity $\exp(p_j V_m)$ varies by $\sim3.4\times10^{64}$% across the voltage range used in the protocol. Since it is implausible that k would be more voltage-dependent than this, the upper bound of p_j was chosen to be lower than 0.9. The maximum value of p_j is also restricted by the limits in the allowed range of k, which is lower than 0.9 as shown in Figure 7.7. The upper bound of p_j was adjusted accordingly.

The resulting boundaries of the kinetic parameters are shown in Figure 7.7. Please note that for the results presented in Chapter 7, the parameters p_4 and p_6 were set to zero (see Section 7.2.3).

C.4 Synthetic data

The parameters chosen to create the synthetic data for the identifiability analysis are shown in Figure C.3.

Examples of synthetic data generated using the method described in Section 7.2.3 using the priors shown in Figure C.3 are shown in Figure C.4. This figure also shows the simulations by the calibrated model obtained using this exercise, which replicates the underlying 'synthetic' data well.

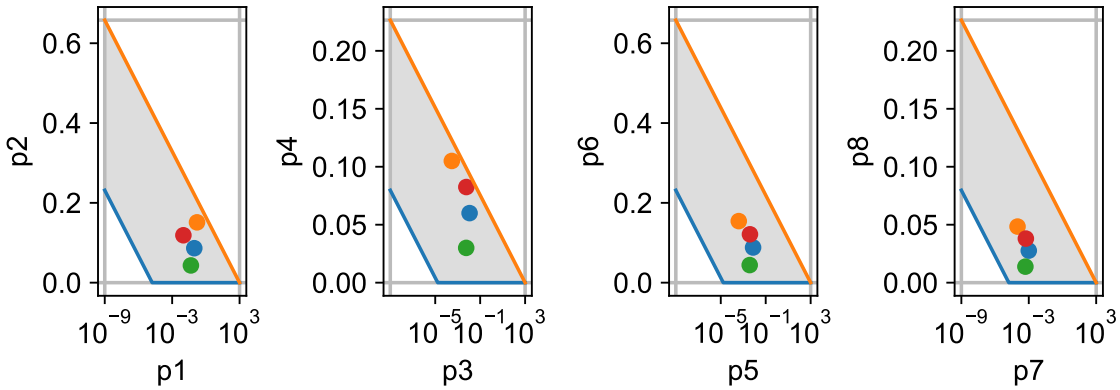

Figure C.3: The parameter values used to generate data for the synthetic study. The shaded area shows the permissible range of the parameters (see Appendix C.3).

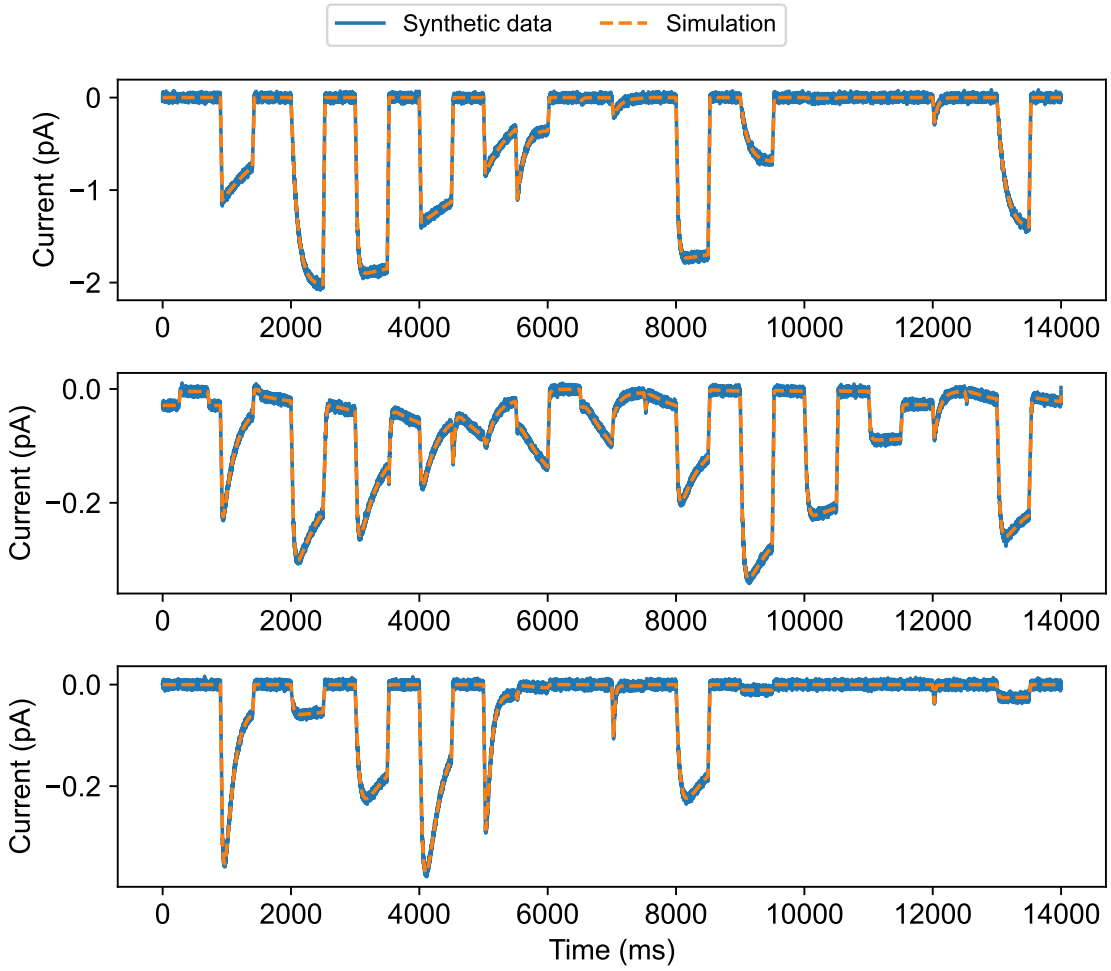

Figure C.4: Synthetic data generated using the calibration protocol in Figure 7.2C and simulation by the corresponding model trained using this data for three different parameters sets.

C.5 Calibration

The post-processed calibration data along with the best fit obtained from two types of optimisation processes (cell-specific and hierarchical) for cells not shown in Chapter 7 are shown in Figure C.5.

C.6 Validation

The post-processed validation data (protocols shown in Figure 7.2V1–V8) along with the best fit obtained from two types of optimisation processes (cell-specific and hierarchical)

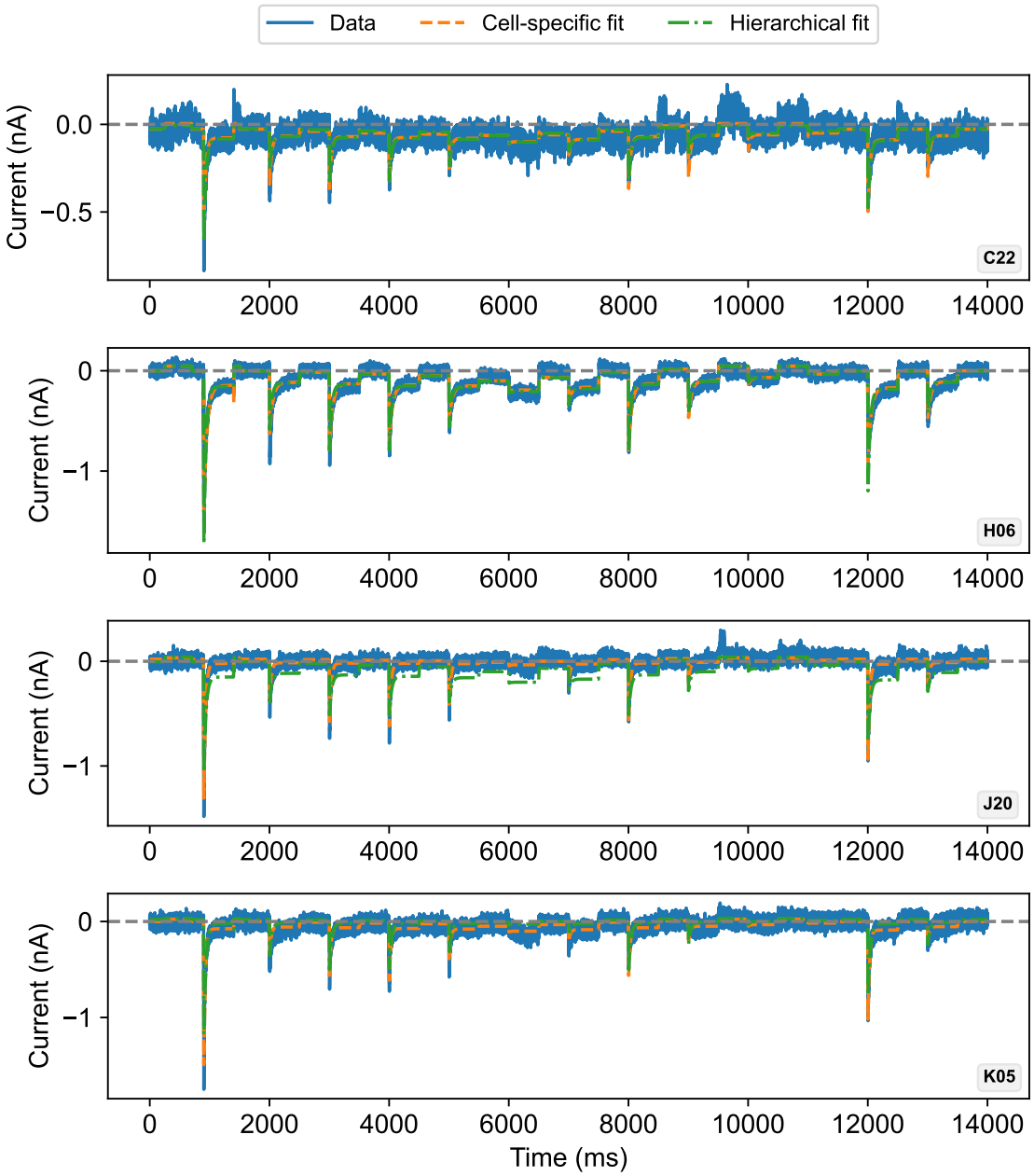

Figure C.5: Post-processed I_{CaL} measured from CHO cell in wells C22, H06, J20, and K05 under the calibration protocol given in Figure 7.2C, along with the corresponding simulation of the models fit using this data via two different optimisation processes.

for the cells not shown in Chapter 7 are shown in Figures C.6–C.9. The current recorded from each sweep in V1–V3 is plotted consecutively with alternating grey background to highlight a change in sweep.

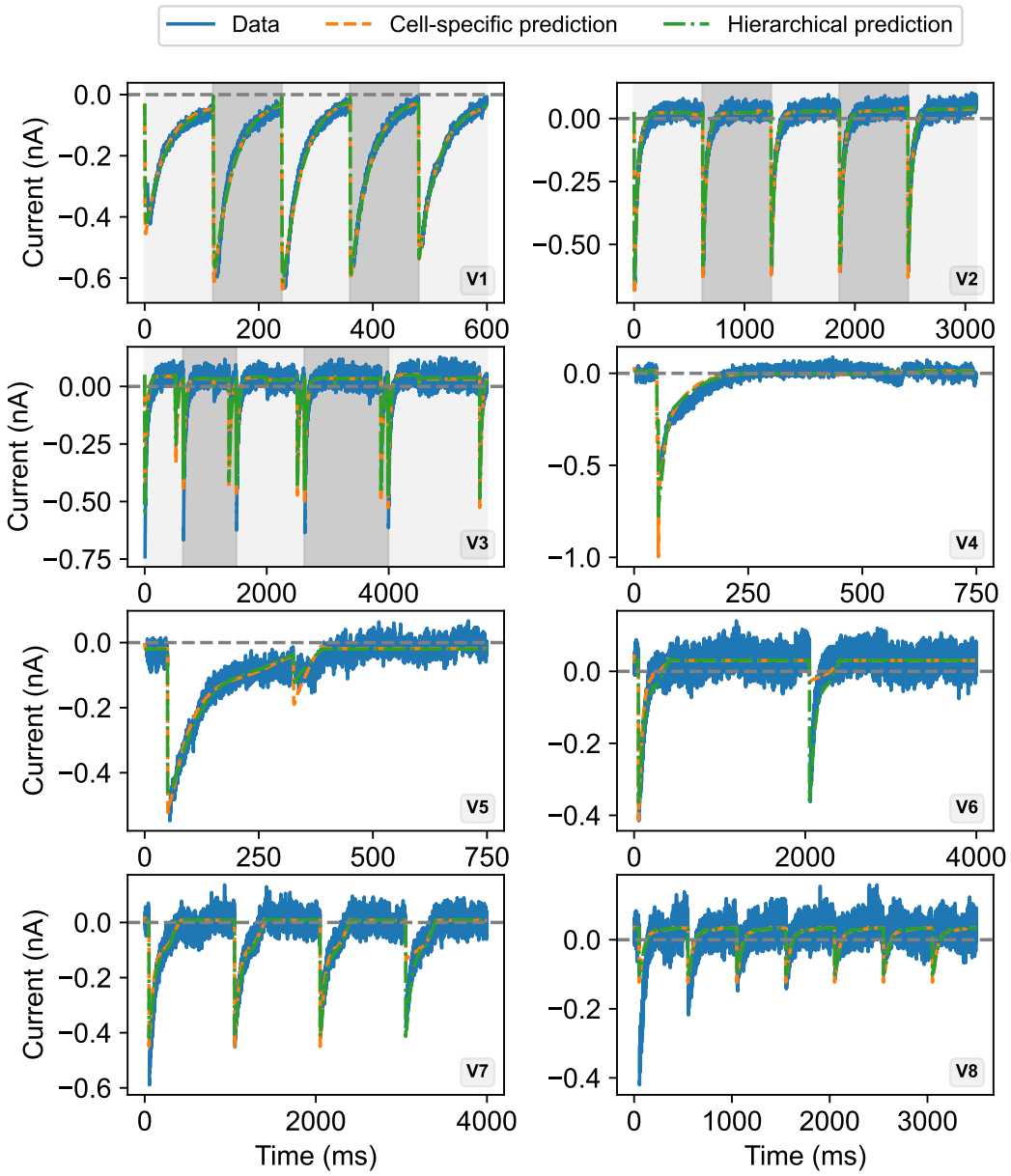

Figure C.6: Post-processed current from the cell C22 and the corresponding predictions by the two models.

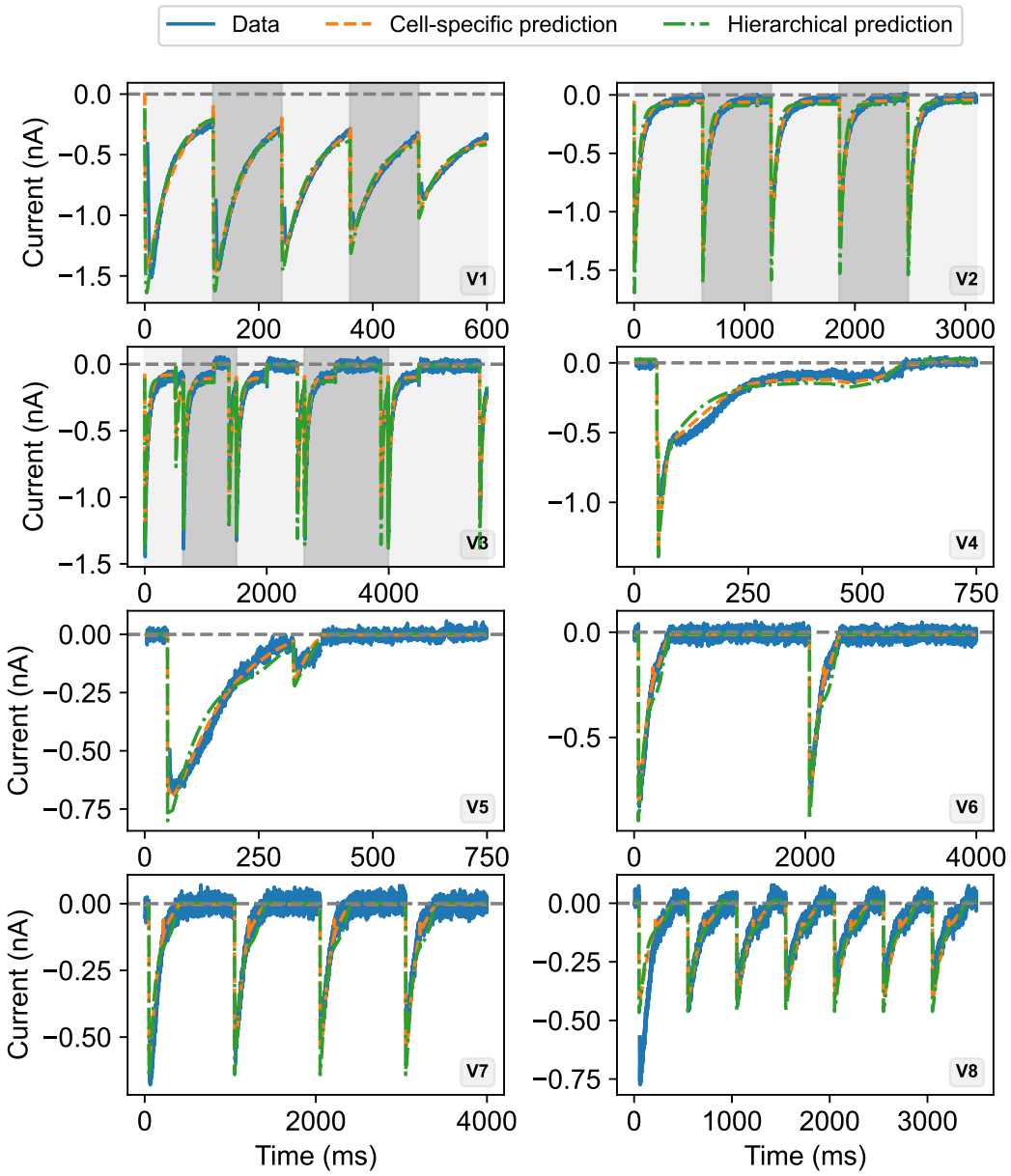

Figure C.7: Post-processed current from the cell H06 and the corresponding predictions by the two models.

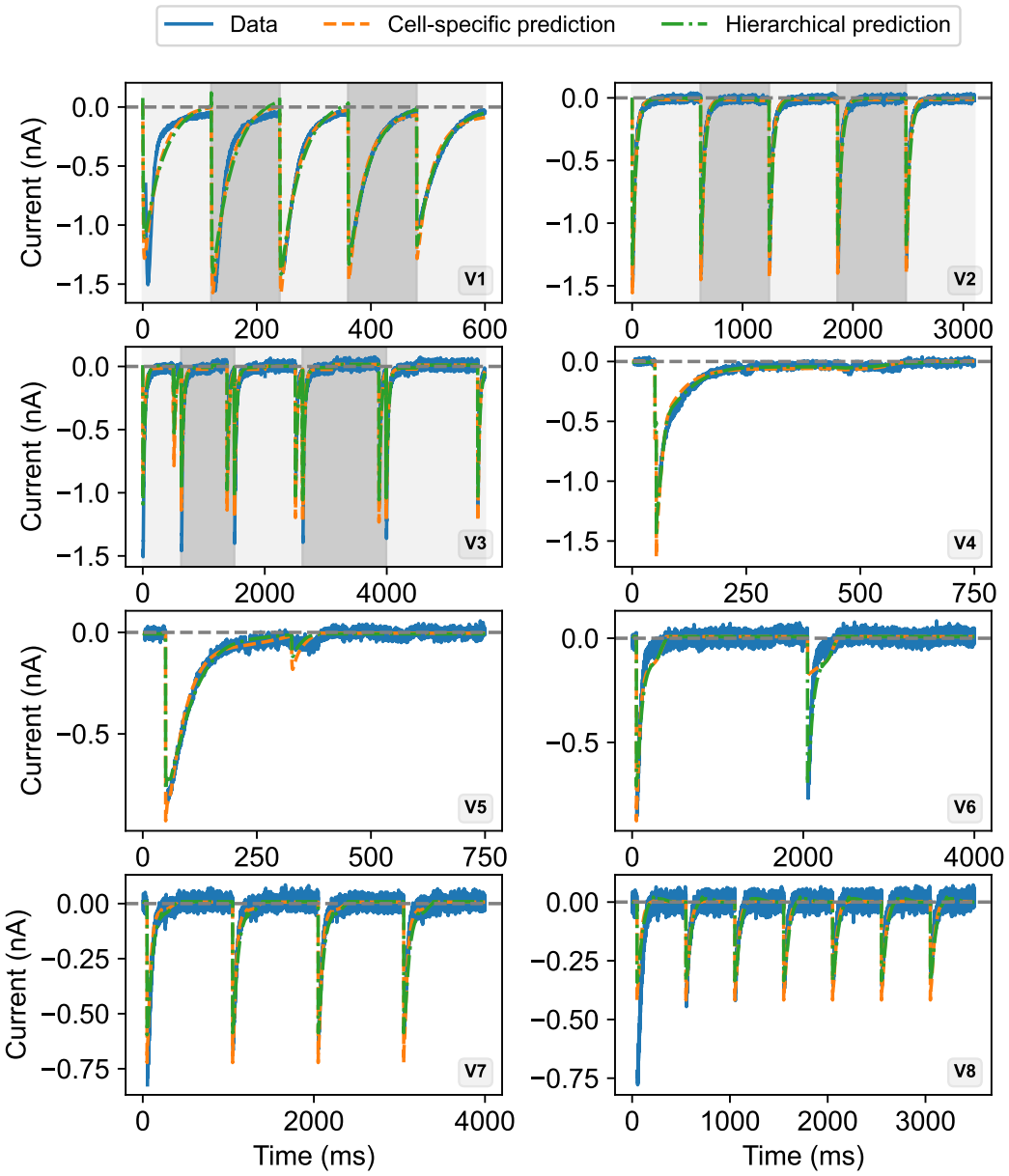

Figure C.8: Post-processed current from the cell J20 and the corresponding predictions by the two models.

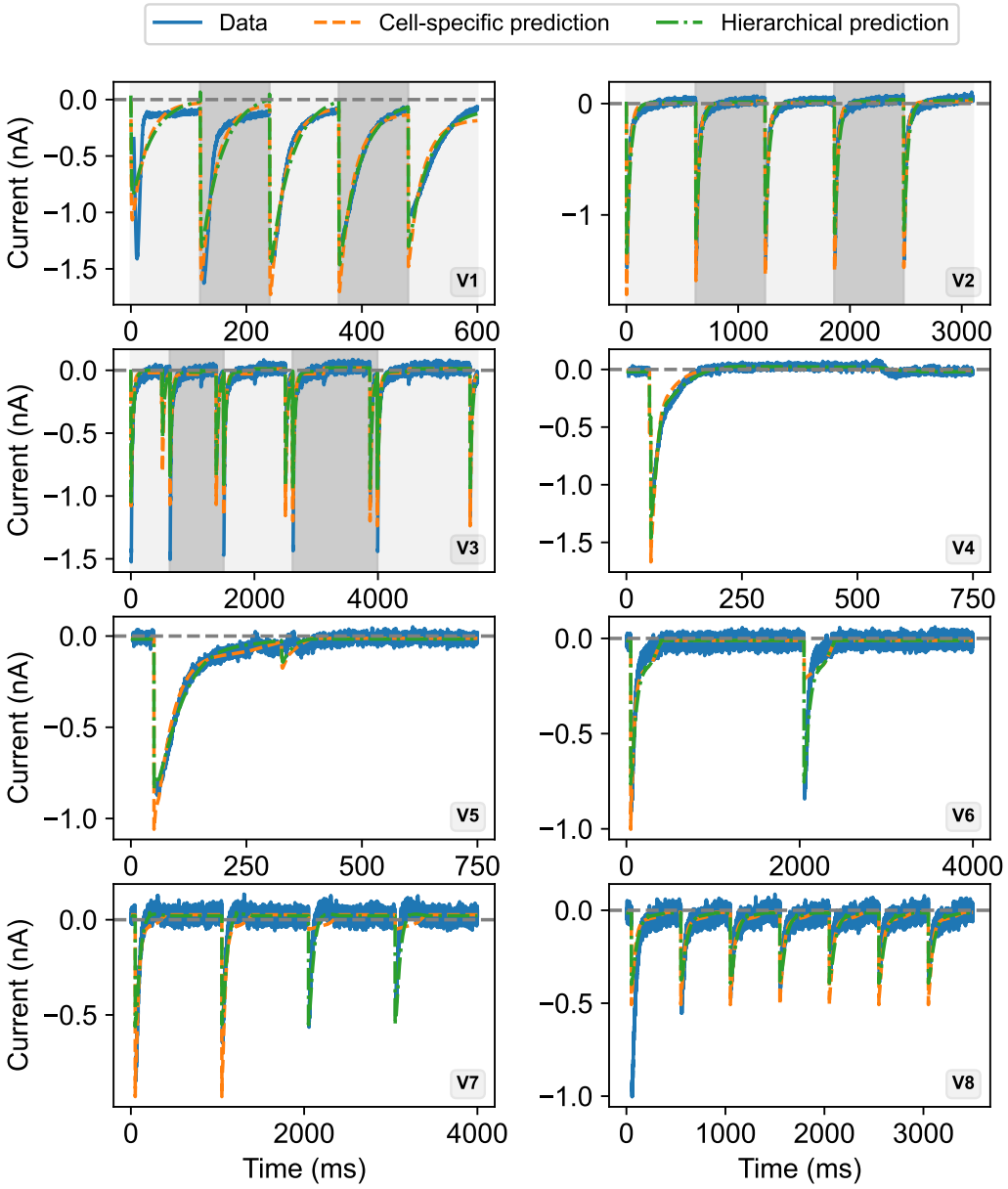

Figure C.9: Post-processed current from the cell K05 and the corresponding predictions by the two models.

C.7 RMSE

The values of the root mean square error (RMSE) (defined in Equation 7.7) for cell-specific and hierarchical calibrations of the model at various protocols is given in Table C.1.

	C22		H06		I11		J20		K05	
Pro	Opt A	Opt B	Opt A	Opt B	Opt A	Opt B	Opt A	Opt B	Opt A	Opt B
C	41.0	41.6	38.5	42.4	32.3	33.7	36.0	37.0	41.4	42.9
V1	15.4	14.5	36.4	45.3	20.6	20.5	41.7	51.3	58.3	65.7
V2	20.4	19.7	21.9	45.8	23.3	23.3	19.5	31.1	27.6	38.8
V3	37.4	34.3	50.1	58.6	45.3	48.4	53.5	51.3	57.1	58.5
V4	30.9	29.2	39.7	64.1	24.5	25.8	33.6	23.1	35.6	22.0
V5	26.5	25.5	23.2	41.3	16.4	16.8	22.0	22.7	28.2	26.6
V6	35	28	18.4	35.7	28.6	28.6	49.8	33.9	53.7	36.6
V7	33.7	30.2	26.7	37.9	29.2	37.3	24.3	31.0	58.1	40.3
V8	38.9	39.0	55.9	58.5	45.6	49.2	43.1	44.4	58.1	60.2

Table C.1: Comparison of RMSE values of model calibrated via cell-specific (opt A) and hierarchical (opt B) optimisation for each protocol (Figure 7.2) across all selected cells. These values can be compared across different cells, protocols, and type of optimisation to determine the better simulation/prediction, where the better fit is determined by the lower RMSE value.

D | Numerical and Statistical methods

This appendix describes some numerical and statistical methods that have been used in this thesis.

D.1 Numerical methods

D.1.1 Discretisation

Finite difference methods are used to solve ordinary and partial differential equations (ODEs and PDEs) numerically [Morton and Mayers, 2005]. The space (and time, if applicable) interval is divided into subintervals such that the dependent value of the ODE/PDE is stored at each node on the grid. The *derivative* for each point is evaluated as a linear interpolation using the nearby points. For example, for an ODE given by:

$$\frac{\mathrm{d}y}{\mathrm{d}t} = f(y,t), \tag{D.1}$$

the derivative at t_n can be written as:

$$\frac{y_{n+1} - y_n}{h} = y' = f(y_n, t), \tag{D.2}$$

where $h = t_{n+1} - t_n$. The above equation can be rearranged and written as:

$$y_{n+1} = y_n + hf(y_n, t) \tag{D.3}$$

In this way, the solution for y can be computed at any time point using the previous time point. The example illustrated here shows a forward Euler scheme which can be solved if y is known at $t = 0$. Other schemes such as central or backward of the required order can be applied as needed for a problem, each with its own conditions of stability and computational complexity.

Finite volume methods are similar to finite differences; the key aspect in which they differ

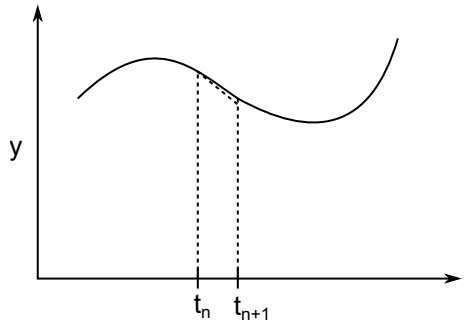

Figure D.1: Illustration of numerical integration using the forward Euler method.

is that here the dependent value is stored at the centre (or centroid) of the finite volume.

D.1.2 Numerical solver

The system of ODEs used to represent ion channels (Chapters 2 and 3) are stiff due to different time scale orders of various kinetic processes. Such ODEs can be solved using variable-order, variable-step multistep methods used by CVODE incorporated into the sundials library [Hindmarsh et al., 2005, Gardner et al., 2022]. CVODE uses the backward differential formulae [Gear, 1967] (implicit methods) to solve the non-linear system at each integration step. The CVODE solver as incorporated into Myokit [Clerx et al., 2016] was used for the work presented in this thesis (unless mentioned otherwise).

D.2 Optimisation algorithms

D.2.1 CMA-ES

Covariance matrix adaptation evolution strategy (CMA-ES) is a class of methods (stochastic, derivative-free) that adopts the principles of 'survival-of-the-fittest' to find the optimum solution ($\boldsymbol{\theta}$) to a non-linear, non-convex, black-box optimisation within a search-space ($\mathbb{R}^n$) [Hansen, 2006, Akimoto et al., 2010]. Broadly, the strategy involves generation and evaluation of a population of candidate solutions, selection of a fixed number of fittest individuals as parents for the next generation, and subsequent reproduction of offspring using recombination and mutation [Beyer and Schwefel, 2002]. This process is repeated until a termination criterion is met. Reproduction of each new generation depends on the n-dimensional mean vector ($\boldsymbol{\mu}$) and $n \times n$ covariance matrix ($\boldsymbol{C}$) of the fittest candidates from the pre-

vious generation. A new generation is sampled from a multivariate Gaussian distribution $\mathcal{N}(\boldsymbol{\mu}, \eta^2\boldsymbol{C})$, where η is the learning rate that controls the convergence of $\boldsymbol{C}$, forcing the algorithm to cast a wider or smaller net of the next generation's candidates depending upon the closeness of the best solutions of the current generation [Dang et al., 2019].

D.2.2 Nelder-Mead

Nelder-mead is a heuristic search method that can be applied to non-linear optimisation problems [Nelder and Mead, 1965]. Unlike CMA-ES, it is a deterministic approach that uses a geometrical 'simplex' of $n + 1$ points in an n-dimensional space to find the optimal solution ($\boldsymbol{\theta}$). It assigns a score to each point on the simplex according to their ability to fit the function to be solved. The n best points are used to calculate the centroid of the simplex. Broadly, it then follows a process of reflection (sometimes including an extra step of expansion/contraction) of the worst-ranked point to update the simplex. Although rare (never for convex functions [Conn et al., 2009]), sometimes the simplex might shrink if the points in the direction of exploration give worse scores than the existing points of the simplex. Nelder-mead performs exceptionally well for convex functions, but may get stuck in a local minima when dealing with non-convex functions, therefore a good initial guess of the solution is often critical for optimisation of such problems.

E | Abbreviations

AP . . . . . Action potential

APD . . . . . Action potential duration

AVN . . . . . Atrioventricular node

CaMKII . . . . . Calcium/calmodulin-dependent protein kinase II

cAMP . . . . . Cyclic adenosine monophosphate

CaT . . . . . Calcium transient

CDI . . . . . Calcium-dependent inactivation

CDF . . . . . Calcium-dependent facilitation

CHO . . . . . Chinese hamster ovary

CICR . . . . . Calcium-induced-calcium-release

CiPA . . . . . Comprehensive *in vitro* proarrhythmic assay

CIR . . . . . (Calcium-dependent inactivation)-induced rundown

CMA-ES . . . . . Covariance matrix adaptation evolution strategy

DAD . . . . . Delayed-after-depolarisation

EAD . . . . . Early-after-depolarisation

ECG . . . . . Electrocardiogram

FDA . . . . . United Stated food and drug administration

GHK . . . . . Goldman-Hodgkin-Katz

hERG . . . . . Human ether-a-go-go-related gene

HH . . . . . Hodgkin-Huxley

HHM . . . . . Hodgkin-Huxley model

JSR . . . . . Junctional sarcoplasmic reticulum

LA . . . . . Left atrium

LCC . . . . . L-type calcium channel

LV . . . . . Left ventricle

MM . . . . . Markov model

MSE . . . . . Mean squared error

NRMSD . . . . . Normalised root mean square difference

NSR . . . . . Network sarcoplasmic reticulum

ODE . . . . . Ordinary differential equation

PDE . . . . . Partial differential equation

PKA . . . . . Protein kinase A

PMR . . . . . Physiome model repository

QC . . . . . Quality control

RA . . . . . Right atrium

RMSD . . . . . Root mean square difference

RMSE . . . . . Root mean square error

RV . . . . . Right ventricle

RyR . . . . . Ryanodine receptor

SAN . . . . . Sinoatrial node

SNR . . . . . Signal-to-noise

SR . . . . . Sarcoplasmic reticulum

TdP . . . . . Torsade de Pointes

VDI . . . . . Voltage-dependent inactivation

Bibliography

K. Acsai, G. Antoons, L. Livshitz, Y. Rudy, and K. R. Sipido. Microdomain Ca^{2+} near ryanodine receptors as reported by L-type Ca^{2+} and Na^{+}/Ca^{2+} exchange currents. *The Journal of Physiology*, 589(10):2569–2583, 2011.

R. Aggarwal and P. A. Boyden. Diminished Ca^{2+} and Ba^{2+} currents in myocytes surviving in the epicardial border zone of the 5-day infarcted canine heart. *Circulation Research*, 77(6):1180–1191, 1995.

R. Aggarwal and P. A. Boyden. Altered pharmacologic responsiveness of reduced L-type calcium currents in myocytes surviving in the infarcted heart. *Journal of Cardiovascular Electrophysiology*, 7(1):20–35, 1996.

A. Agrawal, K. Wang, L. Polonchuk, J. Cooper, M. Hendrix, D. J. Gavaghan, G. R. Mirams, and M. Clerx. Models of the cardiac L-type calcium current: a quantitative review. *WIREs Mechanisms of Disease*, 2022.

C. A. Ahern, J. Payandeh, F. Bosmans, and B. Chanda. The hitchhiker's guide to the voltage-gated sodium channel galaxy. *Journal of General Physiology*, 147(1):1–24, 2016.

R. E. Ahmed, T. Tokuyama, T. Anzai, N. Chanthra, and H. Uosaki. Sarcomere maturation: function acquisition, molecular mechanism, and interplay with other organelles. *Philosophical Transactions of the Royal Society B: Biological Sciences*, 377(1864):20210325, 2022.

Y. Akimoto, Y. Nagata, I. Ono, and S. Kobayashi. Bidirectional relation between CMA Evolution Strategies and Natural Evolution Strategies. In R. Schaefer, C. Cotta, J. Kołodziej, and G. Rudolph, editors, *Parallel Problem Solving from Nature, PPSN XI*, pages 154–163, Berlin, Heidelberg, 2010. Springer Berlin Heidelberg.

B. Alberts, A. Johnson, J. Lewis, M. Raff, K. Roberts, and P. Walter. Isolating, cloning, and sequencing DNA. In *Molecular Biology of the Cell. 4th edition*. Garland Science, 2002.

J. B. Ames. L-type Ca^{2+} channel regulation by calmodulin and CaBP1. *Biomolecules*, 11 (12):1811, 2021.

A. Amin, A. Verkerk, Z. Bhuiyan, A. Wilde, and H. Tan. Novel Brugada syndrome-causing mutation in ion-conducting pore of cardiac Na^+ channel does not affect ion selectivity properties. *Acta Physiologica Scandinavica*, 185(4):291–301, 2005.

C. Antzelevitch and A. Burashnikov. Overview of basic mechanisms of cardiac arrhythmia. *Cardiac Electrophysiology Clinics*, 3(1):23–45, 2011.

C. M. Armstrong and F. Bezanilla. Charge movement associated with the opening and closing of the activation gates of the Na channels. *The Journal of General Physiology*, 63(5):533–552, 1974.

K. Asakura, C. Y. Cha, H. Yamaoka, Y. Horikawa, H. Memida, T. Powell, A. Amano, and A. Noma. EAD and DAD mechanisms analyzed by developing a new human ventricular cell model. *Progress in Biophysics and Molecular Biology*, 116(1):11–24, 2014.

O. V. Aslanidi, M. R. Boyett, H. Dobrzynski, J. Li, and H. Zhang. Mechanisms of transition from normal to reentrant electrical activity in a model of rabbit atrial tissue: interaction of tissue heterogeneity and anisotropy. *Biophysical Journal*, 96(3):798–817, 2009a.

O. V. Aslanidi, P. Stewart, M. R. Boyett, and H. Zhang. Optimal velocity and safety of discontinuous conduction through the heterogeneous Purkinje-ventricular junction. *Biophysical Journal*, 97(1):20–39, 2009b.

H. Asmara, E. Minobe, Z. A. Saud, and M. Kameyama. Interactions of calmodulin with the multiple binding sites of $Ca_v1.2$ Ca^{2+} channels. *Journal of Pharmacological Sciences*, 112(4):397–404, 2010.

V. A. Baronas and H. T. Kurata. Inward rectifiers and their regulation by endogenous polyamines. *Frontiers in Physiology*, 5:325, 2014.

C. Bartolucci, E. Passini, J. Hyttinen, M. Paci, and S. Severi. Simulation of the effects of extracellular calcium changes leads to a novel computational model of human ventricular action potential with a revised calcium handling. *Frontiers in Physiology*, 11:314, 2020.

D. C. Bartos, E. Grandi, and C. M. Ripplinger. Ion channels in the heart. *Comprehensive Physiology*, 5(3):1423, 2015.

J. B. Bassingthwaighte and H. Reuter. Calcium movements and excitation-contraction cou-

pling in cardiac cells. In W. C. De Mello, editor, *Electrical Phenomena in the Heart*, chapter 13, pages 266–290. Academic Press, 1972.

K. A. Beattie, A. P. Hill, R. Bardenet, Y. Cui, J. I. Vandenberg, D. J. Gavaghan, T. P. de Boer, and G. R. Mirams. Sinusoidal voltage protocols for rapid characterisation of ion channel kinetics. *The Journal of Physiology*, 596(10):1813–1828, 2018.

G. W. Beeler and H. Reuter. Membrane calcium current in ventricular myocardial fibres. *The Journal of Physiology*, 207(1):191–209, 1970.

G. W. Beeler and H. Reuter. Reconstruction of the action potential of ventricular myocardial fibres. *The Journal of Physiology*, 268(1):177–210, 1977.

B. Belles, C. Malecot, J. Hescheler, and W. Trautwein. "Run-down" of the Ca current during long whole-cell recordings in guinea pig heart cells: role of phosphorylation and intracellular calcium. *Pflügers Archiv — European Journal of Physiology*, 411(4):353–360, 1988.

M. Bellin, M. C. Marchetto, F. H. Gage, and C. L. Mummery. Induced pluripotent stem cells: the new patient? *Nature Reviews Molecular Cell Biology*, 13(11):713–726, 2012.

M. Ben-Johny, I. E Dick, L. Sang, W. B Limpitikul, P. Wei Kang, J. Niu, R. Banerjee, W. Yang, J. S Babich, J. B Issa, et al. Towards a unified theory of calmodulin regulation (calmodulation) of voltage-gated calcium and sodium channels. *Current Molecular Pharmacology*, 8(2):188–205, 2015.

J. P. Bénitah, P. Bailly, M. C. D'Agrosa, J. P. Da Ponte, C. Delgado, and P. Lorente. Slow inward current in single cells isolated from adult human ventricles. *Pflügers Archiv — European Journal of Physiology*, 421(2-3):176–187, 1992.

D. M. Bers. Calcium cycling and signaling in cardiac myocytes. *Annual Review of Physiology*, 70:23–49, 2008.

D. M. Bers and S. Morotti. Ca^{2+} current facilitation is CaMKII-dependent and has arrhythmogenic consequences. *Frontiers in Pharmacology*, 5:144, 2014.

D. J. Beuckelmann, M. Näbauer, and E. Erdmann. Characteristics of calcium-current in

isolated human ventricular myocytes from patients with terminal heart failure. *Journal of Molecular and Cellular Cardiology*, 23(8):929–937, 1991.

D. J. Beuckelmann, M. Näbauer, and E. Erdmann. Intracellular calcium handling in isolated ventricular myocytes from patients with terminal heart failure. *Circulation*, 85(3):1046–1055, 1992.

H. G. Beyer and H. P. Schwefel. Evolution strategies — A comprehensive introduction. *Natural Computing*, 1(1):3–52, 2002.

M. P. Blaustein and W. J. Lederer. Sodium/calcium exchange: its physiological implications. *Physiological Reviews*, 79(3):763–854, 1999.

V. E. Bondarenko, G. P. Szigeti, G. C. Bett, S.-J. Kim, and R. L. Rasmusson. Computer model of action potential of mouse ventricular myocytes. *American Journal of Physiology — Heart and Circulatory Physiology*, 287(3):H1378–H1403, 2004.

M. R. Boyett, H. Honjo, S. M. Harrison, W. J. Zang, and M. S. Kirby. Ultra-slow voltage-dependent inactivation of the calcium current in guinea-pig and ferret ventricular myocytes. *Pflügers Archiv — European Journal of Physiology*, 428(1):39–50, 1994.

Z. Buraei and J. Yang. The β subunit of voltage-gated Ca^{2+} channels. *Physiological Reviews*, 90(4):1461–1506, 2010.

A. Burashnikov and C. Antzelevitch. Late-phase 3 EAD. A unique mechanism contributing to initiation of atrial fibrillation. *Pacing and Clinical Electrophysiology*, 29(3):290–295, 2006.

C. Cabo and P. A. Boyden. Electrical remodeling of the epicardial border zone in the canine infarcted heart: a computational analysis. *American Journal of Physiology — Heart and Circulatory Physiology*, 284(1):H372–H384, 2003.

D. L. Campbell, W. R. Giles, J. R. Hume, D. Noble, and E. F. Shibata. Reversal potential of the calcium current in bull-frog atrial myocytes. *The Journal of Physiology*, 403(1): 267–286, 1988.

A. Cavalié, D. Pelzer, and W. Trautwein. Fast and slow gating behaviour of single calcium

channels in cardiac cells. *Pflügers Archiv — European Journal of Physiology*, 406(3): 241–258, 1986.

T. Cens, M. Rousset, J.-P. Leyris, P. Fesquet, and P. Charnet. Voltage-and calcium-dependent inactivation in high voltage-gated Ca^{2+} channels. *Progress in Biophysics and Molecular Biology*, 90(1-3):104–117, 2006.

F. Charpentier, E. Drouin, C. Gauthier, and H. L. Marec. Early after/depolarizations and triggered activity: mechanisms and autonomic regulation. *Fundamental & Clinical Pharmacology*, 7(1):39–49, 1993.

L. Chen, K. J. Sampson, and R. S. Kass. Cardiac delayed rectifier potassium channels in health and disease. *Cardiac Electrophysiology Clinics*, 8(2):307–322, 2016.

M. Clerx, P. Collins, E. de Lange, and P. G. A. Volders. Myokit: a simple interface to cardiac cellular electrophysiology. *Progress in Biophysics and Molecular Biology*, 120 (1-3):100–114, 2016.

M. Clerx, K. A. Beattie, D. J. Gavaghan, and G. R. Mirams. Four ways to fit an ion channel model. *Biophysical Journal*, 117(12):2420–2437, 2019a.

M. Clerx, M. Robinson, B. Lambert, C. L. Lei, S. Ghosh, G. R. Mirams, and D. J. Gavaghan. Probabilistic Inference on Noisy Time Series (PINTS). *Journal of Open Research Software*, 7(1):23, 2019b. 10.5334/jors.252.

M. A. Colman, E. Alvarez-Lacalle, B. Echebarria, D. Sato, H. Sutanto, and J. Heijman. Multi-scale computational modeling of spatial calcium handling from nanodomain to whole-heart: Overview and perspectives. *Frontiers in Physiology*, page 278, 2022.

A. R. Conn, K. Scheinberg, and L. N. Vicente. *Introduction to derivative-free optimization*. SIAM, 2009.

J. Cooper, G. R. Mirams, and S. A. Niederer. High-throughput functional curation of cellular electrophysiology models. *Progress in Biophysics and Molecular Biology*, 107(1): 11–20, 2011.

J. Cooper, M. Scharm, and G. R. Mirams. The cardiac electrophysiology web lab. *Biophysical Journal*, 110(2):292–300, 2016.

A. Corrias, W. Giles, and B. Rodriguez. Ionic mechanisms of electrophysiological properties and repolarization abnormalities in rabbit Purkinje fibers. *American Journal of Physiology — Heart and Circulatory Physiology*, 300(5):H1806–H1813, 2011.

S. Cortassa, M. A. Aon, B. O'Rourke, R. Jacques, H. J. Tseng, E. Marbán, and R. L. Winslow. A computational model integrating electrophysiology, contraction, and mitochondrial bioenergetics in the ventricular myocyte. *Biophysical Journal*, 91(4):1564–1589, 2006.

M. Courtemanche, R. J. Ramirez, and S. Nattel. Ionic mechanisms underlying human atrial action potential properties: insights from a mathematical model. *American Journal of Physiology — Heart and Circulatory Physiology*, 275(1):H301–H321, 1998.

A. C. Daly, M. Clerx, K. A. Beattie, J. Cooper, D. J. Gavaghan, and G. R. Mirams. Reproducible model development in the cardiac electrophysiology Web Lab. *Progress in Biophysics and Molecular Biology*, 139:3–14, 2018.

V. H. Dang, N. A. Vien, and T. Chung. A covariance matrix adaptation evolution strategy in reproducing kernel Hilbert space. *Genetic Programming and Evolvable Machines*, 20 (4):479–501, 2019.

C. W. Davies and V. E. Malpass. Ion association and the viscosity of dilute electrolyte solutions. *Transactions of the Faraday Society*, 60:2075–2084, 1964.

K. F. Decker, J. Heijman, J. R. Silva, T. J. Hund, and Y. Rudy. Properties and ionic mechanisms of action potential adaptation, restitution, and accommodation in canine epicardium. *American Journal of Physiology — Heart and Circulatory Physiology*, 296 (4):H1017–H1026, 2009.

S. S. Demir, J. W. Clark, C. R. Murphey, and W. R. Giles. A mathematical model of a rabbit sinoatrial node cell. *American Journal of Physiology — Cell Physiology*, 266(3): C832–C852, 1994.

S. S. Demir, J. W. Clark, and W. R. Giles. Parasympathetic modulation of sinoatrial node pacemaker activity in rabbit heart: a unifying model. *American Journal of Physiology — Heart and Circulatory Physiology*, 276(6):H2221–H2244, 1999.

D. DiFrancesco and D. Noble. A model of cardiac electrical activity incorporating ionic pumps and concentration changes. *Philosophical Transactions of the Royal Society of London. B, Biological Sciences*, 307(1133):353–398, 1985.

R. E. Dixon, E. P. Cheng, J. L. Mercado, and L. F. Santana. L-type Ca^{2+} channel function during Timothy syndrome. *Trends in Cardiovascular Medicine*, 22(3):72–76, 2012.

S. Dokos, B. Celler, and N. Lovell. Ion currents underlying sinoatrial node pacemaker activity: a new single cell mathematical model. *Journal of Theoretical Biology*, 181(3): 245–272, 1996.

A. C. Dolphin. A short history of voltage-gated calcium channels. *British Journal of Pharmacology*, 147(S1):S56, 2006.

A. C. Dolphin. Voltage-gated calcium channel $\alpha_2\delta$ subunits: an assessment of proposed novel roles. *F1000Research*, 7, 2018.

K. A. Dufendach, K. Timothy, M. J. Ackerman, B. Blevins, A. Pflaumer, S. Etheridge, J. Perry, N. A. Blom, J. Temple, D. Chowdhury, et al. Clinical outcomes and modes of death in Timothy syndrome: a multicenter international study of a rare disorder. *JACC: Clinical Electrophysiology*, 4(4):459–466, 2018.

T. M. Egan, D. Noble, S. J. Noble, T. Powell, A. J. Spindler, and V. W. Twist. Sodium-calcium exchange during the action potential in guinea-pig ventricular cells. *The Journal of Physiology*, 411(1):639–661, 1989.

J. R. Ehrlich, T. J. Cha, L. Zhang, D. Chartier, P. Melnyk, S. H. Hohnloser, and S. Nattel. Cellular electrophysiology of canine pulmonary vein cardiomyocytes: action potential and ionic current properties. *The Journal of Physiology*, 551(3):801–813, 2003.

E. A. Ertel, K. P. Campbell, M. M. Harpold, F. Hofmann, Y. Mori, E. Perez-Reyes, A. Schwartz, T. P. Snutch, T. Tanabe, L. Birnbaumer, et al. Nomenclature of voltage-gated calcium channels. *Neuron*, 25(3):533–535, 2000.

D. Escande, A. Coulombe, J. F. Faivre, and E. Coraboeuf. Characteristics of the time-dependent slow inward current in adult human atrial single myocytes. *Journal of Molecular and Cellular Cardiology*, 18(5):547–551, 1986.

G. M. Faber and Y. Rudy. Action potential and contractility changes in $[Na^+]_i$ overloaded cardiac myocytes: a simulation study. *Biophysical Journal*, 78(5):2392–2404, 2000.

G. M. Faber, J. Silva, L. Livshitz, and Y. Rudy. Kinetic properties of the cardiac L-type Ca^{2+} channel and its role in myocyte electrophysiology: a theoretical investigation. *Biophysical Journal*, 92(5):1522–1543, 2007.

N. Fallah, C. Bailey, M. Cross, and G. Taylor. Comparison of finite element and finite volume methods application in geometrically nonlinear stress analysis. *Applied Mathematical Modelling*, 24(7):439–455, 2000.

C. J. Fearnley, H. L. Roderick, and M. D. Bootman. Calcium signaling in cardiac myocytes. *Cold Spring Harbor Perspectives in Biology*, 3(11):a004242, 2011.

B. Fermini and R. D. Nathan. Removal of sialic acid alters both T-and L-type calcium currents in cardiac myocytes. *American Journal of Physiology — Heart and Circulatory Physiology*, 260(3):H735–H743, 1991.

G. Ferreira, J. Yi, E. Ríos, and R. Shirokov. Ion-dependent inactivation of barium current through L-type calcium channels. *The Journal of General Physiology*, 109(4):449–461, 1997.

G. Ferreira, E. Ríos, and N. Reyes. Two components of voltage-dependent inactivation in $Ca_V1.2$ channels revealed by its gating currents. *Biophysical Journal*, 84(6):3662–3678, 2003.

F. Findeisen and D. L. Minor Jr. Disruption of the IS6-AID linker affects voltage-gated calcium channel inactivation and facilitation. *Journal of General Physiology*, 133(3): 327–343, 2009.

I. Findlay. Voltage-and cation-dependent inactivation of L-type Ca^{2+} channel currents in guinea-pig ventricular myocytes. *The Journal of Physiology*, 541(3):731–740, 2002.

I. Findlay. Physiological modulation of inactivation in L-type Ca^{2+} channels: one switch. *The Journal of Physiology*, 554(2):275–283, 2004.

M. Fink and D. Noble. Markov models for ion channels: versatility versus identifiability

and speed. *Philosophical Transactions of the Royal Society A: Mathematical, Physical and Engineering Sciences*, 367(1896):2161–2179, 2009.

M. Fink, D. Noble, L. Virag, A. Varro, and W. R. Giles. Contributions of HERG K^+ current to repolarization of the human ventricular action potential. *Progress in Biophysics and Molecular Biology*, 96(1-3):357–376, 2008.

B. E. Flucher. Specific contributions of the four voltage-sensing domains in L-type calcium channels to gating and modulation. *Journal of General Physiology*, 148(2):91–95, 2016.

J. J. Fox, J. L. McHarg, and R. F. Gilmour Jr. Ionic mechanism of electrical alternans. *American Journal of Physiology — Heart and Circulatory Physiology*, 282(2):H516–H530, 2002.

H. A. Fozzard. Cardiac sodium and calcium channels: a history of excitatory currents. *Cardiovascular Research*, 55(1):1–8, 2002.

B. Frankenhaeuser. Sodium permeability in toad nerve and in squid nerve. *The Journal of Physiology*, 152(1):159–166, 1960.

N. Friedman, A. Vinet, and F. Roberge. A study of a new model of the cardiac ventricular cell incorporating myoplasmic calcium regulation. In *22^{nd} Canadian Medical and Biological Engineering Society Conference*, pages 92–93, 1996.

W. Fuller, L. B. Tulloch, M. J. Shattock, S. C. Calaghan, J. Howie, and K. J. Wypijewski. Regulation of the cardiac sodium pump. *Cellular and Molecular Life Sciences*, 70(8): 1357–1380, 2013.

L. Fülöp, T. Bányász, J. Magyar, N. Szentandrássy, A. Varró, and P. P. Nánási. Reopening of L-type calcium channels in human ventricular myocytes during applied epicardial action potentials. *Acta Physiologica Scandinavica*, 180(1):39–47, 2004.

T. Furukawa, R. J. Myerburg, N. Furukawa, A. L. Bassett, and S. Kimura. Differences in transient outward currents of feline endocardial and epicardial myocytes. *Circulation Research*, 67(5):1287–1291, 1990.

A. Fus-Kujawa, P. Prus, K. Bajdak-Rusinek, P. Teper, K. Gawron, A. Kowalczuk, and A. L.

Sieron. An overview of methods and tools for transfection of eukaryotic cells in vitro. *Frontiers in Bioengineering and Biotechnology*, page 634, 2021.

N. Gaborit, S. Le Bouter, V. Szuts, A. Varro, D. Escande, S. Nattel, and S. Demolombe. Regional and tissue specific transcript signatures of ion channel genes in the non-diseased human heart. *The Journal of Physiology*, 582(2):675–693, 2007.

N. Gamper, J. D. Stockand, and M. S. Shapiro. The use of Chinese hamster ovary (CHO) cells in the study of ion channels. *Journal of Pharmacological and Toxicological Methods*, 51(3):177–185, 2005.

T. Gao, A. Yatani, M. L. Dell'Acqua, H. Sako, S. A. Green, N. Dascal, J. D. Scott, and M. M. Hosey. cAMP-dependent regulation of cardiac L-type Ca^{2+} channels requires membrane targeting of PKA and phosphorylation of channel subunits. *Neuron*, 19(1): 185–196, 1997.

D. J. Gardner, D. R. Reynolds, C. S. Woodward, and C. J. Balos. Enabling new flexibility in the SUNDIALS suite of nonlinear and differential/algebraic equation solvers. *ACM Transactions on Mathematical Software (TOMS)*, 2022. 10.1145/3539801.

H. Gazzano-Santoro, L. G. Chan, M. S. Ballard, and J. C. Young. Ready-to-use cryopreserved primary cells: a novel solution for QC lot release potency assays. *BioProcess International*, 12:28–39, 2014.

C. W. Gear. The numerical integration of ordinary differential equations. *Mathematics of Computation*, 21(98):146–156, 1967.

L. J. Gentet, G. J. Stuart, and J. D. Clements. Direct measurement of specific membrane capacitance in neurons. *Biophysical Journal*, 79(1):314–320, 2000.

L. S. Gettes and H. Reuter. Slow recovery from inactivation of inward currents in mammalian myocardial fibres. *The Journal of Physiology*, 240(3):703–724, 1974.

D. E. Goldman. Potential, impedance, and rectification in membranes. *The Journal of General Physiology*, 27(1):37–60, 1943.

J. Golowasch, M. S. Goldman, L. Abbott, and E. Marder. Failure of averaging in the

construction of a conductance-based neuron model. *Journal of Neurophysiology*, 87(2): 1129–1131, 2002.

S. Goutelle, M. Maurin, F. Rougier, X. Barbaut, L. Bourguignon, M. Ducher, and P. Maire. The Hill equation: a review of its capabilities in pharmacological modelling. *Fundamental & Clinical Pharmacology*, 22(6):633–648, 2008.

A. Gradogna, J. Scholz-Starke, P. V. K. Gutla, and A. Carpaneto. Fluorescence combined with excised patch: measuring calcium currents in plant cation channels. *The Plant Journal*, 58(1):175–182, 2009.

E. Grandi, F. S. Pasqualini, and D. M. Bers. A novel computational model of the human ventricular action potential and Ca transient. *Journal of Molecular and Cellular Cardiology*, 48(1):112–121, 2010.

E. Grandi, S. V. Pandit, N. Voigt, A. J. Workman, D. Dobrev, J. Jalife, and D. M. Bers. Human atrial action potential and Ca^{2+} model: sinus rhythm and chronic atrial fibrillation. *Circulation Research*, 109(9):1055–1066, 2011.

A. O. Grant. Cardiac ion channels. *Circulation: Arrhythmia and Electrophysiology*, 2(2): 185–194, 2009.

J. L. Greenstein and R. L. Winslow. An integrative model of the cardiac ventricular myocyte incorporating local control of Ca^{2+} release. *Biophysical Journal*, 83(6):2918–2945, 2002.

J. L. Greenstein, R. Hinch, and R. L. Winslow. Mechanisms of excitation-contraction coupling in an integrative model of the cardiac ventricular myocyte. *Biophysical Journal*, 90 (1):77–91, 2006.

Y. Habuchi, T. Noda, M. Nishimura, and Y. Watanabe. Recovery of the slow inward current from Ca^{2+}-mediated and voltage-dependent inactivation in the rabbit sinoatrial node. *Journal of Molecular and Cellular Cardiology*, 22(4):469–482, 1990.

R. W. Hadley and W. J. Lederer. Ca^{2+} and voltage inactivate Ca^{2+} channels in guinea-pig ventricular myocytes through independent mechanisms. *The Journal of Physiology*, 444 (1):257–268, 1991.

N. Hagiwara, H. Irisawa, and M. Kameyama. Contribution of two types of calcium currents

to the pacemaker potentials of rabbit sino-atrial node cells. *The Journal of Physiology*, 395(1):233–253, 1988.

W. Han, D. Chartier, D. Li, and S. Nattel. Ionic remodeling of cardiac Purkinje cells by congestive heart failure. *Circulation*, 104(17):2095–2100, 2001.

Y. Han, X.-M. Liu, H. Liu, S.-C. Li, B.-C. Wu, L.-L. Ye, Q.-W. Wang, and Z.-L. Chen. Cultivation of recombinant Chinese hamster ovary cells grown as suspended aggregates in stirred vessels. *Journal of Bioscience and Bioengineering*, 102(5):430–435, 2006.

N. Hansen. *The CMA Evolution Strategy: A Comparing Review*, pages 75–102. Springer Berlin Heidelberg, Berlin, Heidelberg, 2006. ISBN 978-3-540-32494-2.

T. H. Hansen, Y. Yan, G. Ahlberg, O. B. Vad, L. Refsgaard, J. L. Dos Santos, N. Mutsaers, J. H. Svendsen, M. S. Olesen, B. H. Bentzen, et al. A novel loss-of-function variant in the chloride ion channel gene CLCN2 associates with atrial fibrillation. *Scientific Reports*, 10(1):1453, 2020.

M. E. L. Hardy, E. Pervolaraki, O. Bernus, and E. White. Dynamic action potential restitution contributes to mechanical restitution in right ventricular myocytes from pulmonary hypertensive rats. *Frontiers in Physiology*, 9:205, 2018.

Y. L. Hashambhoy, R. L. Winslow, and J. L. Greenstein. CaMKII-induced shift in modal gating explains L-type Ca^{2+} current facilitation: a modeling study. *Biophysical Journal*, 96(5):1770–1785, 2009.

W. J. Hedley, M. R. Nelson, D. P. Bellivant, and P. F. Nielsen. A short introduction to CellML. *Philosophical Transactions of the Royal Society of London A: Mathematical, Physical and Engineering Sciences*, 359(1783):1073–1089, 2001.

J. Heijman. *Computational analysis of β-adrenergic stimulation and its effects on cardiac ventricular electrophysiology*. PhD thesis, Maastricht University, 2012.

J. Heijman, P. G. A. Volders, R. L. Westra, and Y. Rudy. Local control of β-adrenergic stimulation: effects on ventricular myocyte electrophysiology and Ca^{2+}-transient. *Journal of Molecular and Cellular Cardiology*, 50(5):863–871, 2011.

H. F. Hemond and E. J. Fechner. *Chemical fate and transport in the environment*. Elsevier, 2014.

S. Hering, E. M. Zangerl-Plessl, S. Beyl, A. Hohaus, S. Andranovits, and E. Timin. Calcium channel gating. *Pflügers Archiv — European Journal of Physiology*, 470(9):1291–1309, 2018.

T. J. Herron, P. Lee, and J. Jalife. Optical imaging of voltage and calcium in cardiac cells & tissues. *Circulation Research*, 110(4):609–623, 2012.

P. Hess and R. W. Tsien. Mechanism of ion permeation through calcium channels. *Nature*, 309(5967):453–456, 1984.

P. Hess, J. B. Lansman, and R. W. Tsien. Calcium channel selectivity for divalent and monovalent cations. voltage and concentration dependence of single channel current in ventricular heart cells. *The Journal of General Physiology*, 88(3):293–319, 1986.

D. W. Hilgemann and D. Noble. Excitation-contraction coupling and extracellular calcium transients in rabbit atrium: reconstruction of basic cellular mechanisms. *Proceedings of the Royal Society of London B: Biological Sciences*, 230(1259):163–205, 1987.

B. Hille. *Ion Channels of Excitable Membranes*. Sinauer Associates, Inc., Sunderland, Massachusetts, 2001.

Y. Himeno, K. Asakura, C. Y. Cha, H. Memida, T. Powell, A. Amano, and A. Noma. A human ventricular myocyte model with a refined representation of excitation-contraction coupling. *Biophysical Journal*, 109(2):415–427, 2015.

R. Hinch, J. L. Greenstein, A. J. Tanskanen, L. Xu, and R. L. Winslow. A simplified local control model of calcium-induced calcium release in cardiac ventricular myocytes. *Biophysical Journal*, 87(6):3723–3736, 2004.

A. C. Hindmarsh, P. N. Brown, K. E. Grant, S. L. Lee, R. Serban, D. E. Shumaker, and C. S. Woodward. SUNDIALS: Suite of nonlinear and differential/algebraic equation solvers. *ACM Transactions on Mathematical Software (TOMS)*, 31(3):363–396, 2005. 10.1145/1089014.1089020.

Y. Hirano and M. Hiraoka. Ca^{2+} entry-dependent inactivation of L-type Ca current: a novel

formulation for cardiac action potential models. *Biophysical Journal*, 84(1):696–708, 2003.

Y. Hirano, H. A. Fozzard, and C. T. January. Characteristics of L-and T-type Ca^{2+} currents in canine cardiac Purkinje cells. *American Journal of Physiology — Heart and Circulatory Physiology*, 256(5):H1478–H1492, 1989.

Y. Hirano, A. Moscucci, and C. T. January. Direct measurement of L-type Ca^{2+} window current in heart cells. *Circulation Research*, 70(3):445–455, 1992.

A. L. Hodgkin and A. F. Huxley. A quantitative description of membrane current and its application to conduction and excitation in nerve. *The Journal of Physiology*, 117(4): 500–544, 1952.

A. L. Hodgkin and B. Katz. The effect of sodium ions on the electrical activity of the giant axon of the squid. *The Journal of Physiology*, 108(1):37–77, 1949.

R. Hoefen, M. Reumann, I. Goldenberg, A. J. Moss, O. Jin, Y. Gu, S. McNitt, W. Zareba, C. Jons, J. K. Kanters, et al. In silico cardiac risk assessment in patients with long QT syndrome: type 1: clinical predictability of cardiac models. *Journal of the American College of Cardiology*, 60(21):2182–2191, 2012.

G. F. Höfer, K. Hohenthanner, W. Baumgartner, K. Groschner, N. Klugbauer, F. Hofmann, and C. Romanin. Intracellular Ca^{2+} inactivates L-type Ca^{2+} channels with a Hill coefficient of $\sim$1 and an inhibition constant of $\sim$4 μM by reducing channel's open probability. *Biophysical Journal*, 73(4):1857–1865, 1997.

F. Hofmann, V. Flockerzi, S. Kahl, and J. W. Wegener. L-type $Ca_V1.2$ calcium channels: from in vitro findings to in vivo function. *Physiological Reviews*, 94(1):303–326, 2014.

T. Hong and R. M. Shaw. Cardiac T-tubule microanatomy and function. *Physiological Reviews*, 97(1):227–252, 2017.

H. Honjo, M. R. Boyett, I. Kodama, and J. Toyama. Correlation between electrical activity and the size of rabbit sino-atrial node cells. *The Journal of Physiology*, 496(3):795–808, 1996.

T. J. Hund and Y. Rudy. Rate dependence and regulation of action potential and calcium

transient in a canine cardiac ventricular cell model. *Circulation*, 110(20):3168–3174, 2004.

T. J. Hund, K. F. Decker, E. Kanter, P. J. Mohler, P. A. Boyden, R. B. Schuessler, K. A. Yamada, and Y. Rudy. Role of activated CaMKII in abnormal calcium homeostasis and I_{Na} remodeling after myocardial infarction: Insights from mathematical modeling. *Journal of Molecular and Cellular Cardiology*, 45(3):420–428, 2008.

P. J. Hunter and N. P. Smith. The Cardiac Physiome Project. *The Journal of Physiology*, 594(23):6815, 2016.

J. P. Imredy and D. T. Yue. Mechanism of Ca^{2+}-sensitive inactivation of L-type Ca^{2+} channels. *Neuron*, 12(6):1301–1318, 1994.

S. Inada, J. C. Hancox, H. Zhang, and M. R. Boyett. One-dimensional mathematical model of the atrioventricular node including atrio-nodal, nodal, and nodal-his cells. *Biophysical Journal*, 97(8):2117–2127, 2009.

P. A. Iredale and S. J. Hill. Increases in intracellular calcium via activation of an endogenous P2-purinoceptor in cultured CHO-K1 cells. *British Journal of Pharmacology*, 110(4): 1305, 1993.

V. Iyer, R. Mazhari, and R. L. Winslow. A computational model of the human left-ventricular epicardial myocyte. *Biophysical Journal*, 87(3):1507–1525, 2004.

M. S. Jafri, J. J. Rice, and R. L. Winslow. Cardiac Ca^{2+} dynamics: the roles of ryanodine receptor adaptation and sarcoplasmic reticulum load. *Biophysical Journal*, 74(3):1149–1168, 1998.

T. N. James. Fine structure of the His bundle. *Circulation*, 44(2):304–305, 1971.

N. Jost, N. Nagy, C. Corici, Z. Kohajda, A. Horváth, K. Acsai, P. Biliczki, J. Levijoki, P. Pollesello, T. Koskelainen, et al. ORM-10103, a novel specific inhibitor of the Na^+/Ca^{2+} exchanger, decreases early and delayed afterdepolarizations in the canine heart. *British Journal of Pharmacology*, 170(4):768–778, 2013.

S. Kääb, H. B. Nuss, N. Chiamvimonvat, B. O'Rourke, P. H. Pak, D. A. Kass, E. Marban, and G. F. Tomaselli. Ionic mechanism of action potential prolongation in ventricular

myocytes from dogs with pacing-induced heart failure. *Circulation Research*, 78(2): 262–273, 1996.

M. Kameyama, A. Kameyama, M. Kaibara, T. Nakayama, and H. Irisawa. Intracellular mechanisms involved in "run-down" of calcium channels. In *Calcium Protein Signaling*, pages 111–117. Springer, 1989.

T. J. Kamp, H. Hu, and E. Marban. Voltage-dependent facilitation of cardiac L-type Ca channels expressed in HEK-293 cells requires β-subunit. *American Journal of Physiology — Heart and Circulatory Physiology*, 278(1):H126–H136, 2000.

R. S. Kass and M. C. Sanguinetti. Inactivation of calcium channel current in the calf cardiac Purkinje fiber. Evidence for voltage-and calcium-mediated mechanisms. *The Journal of General Physiology*, 84(5):705–726, 1984.

Y. Katsube, H. Yokoshiki, L. Nguyen, M. Yamamoto, and N. Sperelakis. L-type Ca^{2+} currents in ventricular myocytes from neonatal and adult rats. *Canadian Journal of Physiology and Pharmacology*, 76(9):873–881, 1998.

S. Kawano and M. Hiraoka. Transient outward currents and action potential alterations in rabbit ventricular myocytes. *Journal of Molecular and Cellular Cardiology*, 23(6): 681–693, 1991.

J. P. Keener and J. Sneyd. *Mathematical Physiology I: Cellular Physiology*, volume 1. Springer, 1998.

D. C. Kernik, S. Morotti, H. Wu, P. Garg, H. J. Duff, J. Kurokawa, J. Jalife, J. C. Wu, E. Grandi, and C. E. Clancy. A computational model of induced pluripotent stem-cell derived cardiomyocytes incorporating experimental variability from multiple data sources. *The Journal of Physiology*, 597(17):4533–4564, 2019.

S. Kettlewell, P. Saxena, J. Dempster, M. A. Colman, R. C. Myles, G. L. Smith, and A. J. Workman. Dynamic clamping human and rabbit atrial calcium current: narrowing I_{CaL} window abolishes early afterdepolarizations. *The Journal of Physiology*, 597(14):3619–3638, 2019.

J. Kim, S. Ghosh, D. A. Nunziato, and G. S. Pitt. Identification of the components controlling inactivation of voltage-gated Ca^{2+} channels. *Neuron*, 41(5):745–754, 2004.

J. G. Kim, D. J. Sung, H. Kim, S. W. Park, K. J. Won, B. Kim, H. C. Shin, K. S. Kim, C. H. Leem, Y. H. Zhang, et al. Impaired inactivation of L-Type Ca^{2+} current as a potential mechanism for variable arrhythmogenic liability of HERG K^+ channel blocking drugs. *PloS One*, 11(3), 2016.

T. K. Kim. T test as a parametric statistic. *Korean Journal of Anesthesiology*, 68(6):540–546, 2015.

K. S. Kits, T. A. de Vlieger, B. W. Kooi, and H. D. Mansvelder. Diffusion barriers limit the effect of mobile calcium buffers on exocytosis of large dense cored vesicles. *Biophysical Journal*, 76(3):1693–1705, 1999.

N. Klugbauer, E. Marais, and F. Hofmann. Calcium channel $\alpha_2\delta$ subunits: differential expression, function, and drug binding. *Journal of Bioenergetics and Biomembranes*, 35 (6):639–647, 2003.

J. H. Ko, W. S. Park, S. J. Kim, and Y. E. Earm. Slowing of the inactivation of voltage-dependent sodium channels by staurosporine, the protein kinase C inhibitor, in rabbit atrial myocytes. *European Journal of Pharmacology*, 534(1-3):48–54, 2006.

I. Kodama, M. R. Boyett, M. R. Nikmaram, M. Yamamoto, H. Honjo, and R. Niwa. Regional differences in effects of E-4031 within the sinoatrial node. *American Journal of Physiology — Heart and Circulatory Physiology*, 276(3):H793–H802, 1999.

T. Köddermann, R. Ludwig, and D. Paschek. On the validity of Stokes-Einstein and Stokes-Einstein-Debye relations in ionic liquids and ionic-liquid mixtures. *ChemPhysChem*, 9 (13):1851–1858, 2008.

J. T. Koivumäki, T. Korhonen, and P. Tavi. Impact of sarcoplasmic reticulum calcium release on calcium dynamics and action potential morphology in human atrial myocytes: a computational study. *PLoS Computational Biology*, 7(1):e1001067, 2011.

E. Kreyszig, K. Stroud, and G. Stephenson. Advanced engineering mathematics. *Integration*, 9:4, 2008.

Z. Kubalova. Inactivation of L-type calcium channels in cardiomyocytes. Experimental and theoretical approaches. *Gen Physiol Biophys*, 22(4):441–454, 2003.

Y. Kurata, I. Hisatome, S. Imanishi, and T. Shibamoto. Dynamical description of sinoatrial node pacemaking: improved mathematical model for primary pacemaker cell. *American Journal of Physiology — Heart and Circulatory Physiology*, 283(5):H2074–H2101, 2002.

L. Lacinová. Voltage-dependent calcium channels. *General Physiology and Biophysics*, 24:1–78, 2005.

F. A. Lattanzio Jr and D. Bartschat. The effect of pH on rate constants, ion selectivity and thermodynamic properties of fluorescent calcium and magnesium indicators. *Biochemical and Biophysical Research Communications*, 177(1):184–191, 1991.

B. L. Le Grand, S. Hatem, E. Deroubaix, J. P. Couétil, and E. Coraboeuf. Calcium current depression in isolated human atrial myocytes after cessation of chronic treatment with calcium antagonists. *Circulation Research*, 69(2):292–300, 1991.

B. L. Le Grand, S. Hatem, E. Deroubaix, J. P. Couétil, and E. Coraboeuf. Depressed transient outward and calcium currents in dilated human atria. *Cardiovascular Research*, 28(4):548–556, 1994.

C. Lei, M. Clerx, D. J. Gavaghan, L. Polonchuk, G. R. Mirams, and K. Wang. Rapid characterization of hERG channel kinetics I: using an automated high-throughput system. *Biophysical Journal*, 117(12):2438–2454, 2019.

C. Lei, M. Clerx, D. G. Whittaker, D. J. Gavaghan, T. P. de Boer, and G. R. Mirams. Accounting for variability in ion current recordings using a mathematical model of artefacts in voltage-clamp experiments. *Philosophical Transactions of the Royal Society A: Mathematical, Physical and Engineering Sciences*, 378(2173):20190348, 2020a.

C. Lei, A. Fabbri, D. G. Whittaker, M. Clerx, M. J. Windley, A. P. Hill, G. R. Mirams, and T. P. de Boer. A nonlinear and time-dependent leak current in the presence of calcium fluoride patch-clamp seal enhancer. *Wellcome Open Research*, 5, 2020b.

G. R. Li and S. Nattel. Properties of human atrial I_{Ca} at physiological temperatures and

relevance to action potential. *American Journal of Physiology — Heart and Circulatory Physiology*, 272(1):H227–H235, 1997.

G. R. Li, B. Yang, J. Feng, R. F. Bosch, M. Carrier, and S. Nattel. Transmembrane I_{Ca} contributes to rate-dependent changes of action potentials in human ventricular myocytes. *American Journal of Physiology — Heart and Circulatory Physiology*, 276(1): H98–H106, 1999.

L. Li, S. A. Niederer, W. Idigo, Y. H. Zhang, P. Swietach, B. Casadei, and N. P. Smith. A mathematical model of the murine ventricular myocyte: a data-driven biophysically based approach applied to mice overexpressing the canine NCX isoform. *American Journal of Physiology — Heart and Circulatory Physiology*, 299(4):H1045–H1063, 2010.

M. Li, Y. Kanda, T. Ashihara, T. Sasano, Y. Nakai, M. Kodama, E. Hayashi, Y. Sekino, T. Furukawa, and J. Kurokawa. Overexpression of KCNJ2 in induced pluripotent stem cell-derived cardiomyocytes for the assessment of QT-prolonging drugs. *Journal of Pharmacological Sciences*, 134(2):75–85, 2017.

P. Li and Y. Rudy. A model of canine Purkinje cell electrophysiology and Ca^{2+} cycling: rate dependence, triggered activity, and comparison to ventricular myocytes. *Circulation Research*, 109(1):71–79, 2011.

Z. Li, B. J. Ridder, X. Han, W. W. Wu, J. Sheng, P. N. Tran, M. Wu, A. Randolph, R. H. Johnstone, G. R. Mirams, et al. Assessment of an *in silico* mechanistic model for proarrhythmia risk prediction under the CiPA initiative. *Clinical Pharmacology & Therapeutics*, 105(2):466–475, 2019.

D. S. Lindblad, C. R. Murphey, J. W. Clark, and W. R. Giles. A model of the action potential and underlying membrane currents in a rabbit atrial cell. *American Journal of Physiology — Heart and Circulatory Physiology*, 271(4):H1666–H1696, 1996.

K. W. Linz and R. Meyer. Modulation of L-type calcium current by internal potassium in guinea pig ventricular myocytes. *Cardiovascular Research*, 33(1):110–122, 1997.

K. W. Linz and R. Meyer. Control of L-type calcium current during the action potential of guinea-pig ventricular myocytes. *The Journal of Physiology*, 513(2):425–442, 1998.

Y. Liu, W. Zeng, M. Delmar, and J. Jalife. Ionic mechanisms of electronic inhibition and concealed conduction in rabbit atrioventricular nodal myocytes. *Circulation*, 88(4): 1634–1646, 1993.

L. M. Livshitz and Y. Rudy. Regulation of Ca^{2+} and electrical alternans in cardiac myocytes: role of CAMKII and repolarizing currents. *American Journal of Physiology — Heart and Circulatory Physiology*, 292(6):H2854–H2866, 2007.

N. H. Lovell, S. L. Cloherty, B. G. Celler, and S. Dokos. A gradient model of cardiac pacemaker myocytes. *Progress in Biophysics and Molecular Biology*, 85(2-3):301–323, 2004.

F. Lu and W. T. Pu. The architecture and function of cardiac dyads. *Biophysical Reviews*, 12(4):1007–1017, 2020.

Y. Lü and M. Bülow. Analysis of diffusion in hollow geometries. *Adsorption*, 6(2):125–136, 2000.

C. H. Luo and Y. Rudy. A dynamic model of the cardiac ventricular action potential II. Afterdepolarizations, triggered activity, and potentiation. *Circulation Research*, 74(6): 1097–1113, 1994a.

C.-h. Luo and Y. Rudy. A dynamic model of the cardiac ventricular action potential I. Simulations of ionic currents and concentration changes. *Circulation Research*, 74(6): 1071–1096, 1994b.

J. Ma, L. Guo, S. J. Fiene, B. D. Anson, J. A. Thomson, T. J. Kamp, K. L. Kolaja, B. J. Swanson, and C. T. January. High purity human-induced pluripotent stem cell-derived cardiomyocytes: electrophysiological properties of action potentials and ionic currents. *American Journal of Physiology — Heart and Circulatory Physiology*, 301(5):H2006–H2017, 2011.

R. V. Madhvani, M. Angelini, Y. Xie, A. Pantazis, S. Suriany, N. P. Borgstrom, A. Garfinkel, Z. Qu, J. N. Weiss, and R. Olcese. Targeting the late component of the cardiac L-type Ca^{2+} current to suppress early afterdepolarizations. *Journal of General Physiology*, 145 (5):395–404, 2015.

P. Madona, R. I. Basti, and M. M. Zain. PQRST wave detection on ECG signals. *Gaceta Sanitaria*, 35:S364–S369, 2021.

R. Maex. *Nernst-Planck Equation*, pages 1–7. Springer New York, New York, NY, 2013. ISBN 978-1-4614-7320-6.

J. Magyar, N. Iost, Á. Körtvély, T. Bányász, L. Virág, P. Szigligeti, A. Varró, M. Opincariu, J. Szécsi, J. G. Papp, et al. Effects of endothelin-1 on calcium and potassium currents in undiseased human ventricular myocytes. *Pflügers Archiv — European Journal of Physiology*, 441(1):144–149, 2000.

J. Magyar, N. Szentandrássy, T. Bányász, L. Fülöp, A. Varró, and P. P. Nánási. Effects of Thymol on calcium and potassium currents in canine and human ventricular cardiomyocytes. *British Journal of Pharmacology*, 136(2):330–338, 2002.

A. Mahajan, Y. Shiferaw, D. Sato, A. Baher, R. Olcese, L.-H. Xie, M.-J. Yang, P.-S. Chen, J. G. Restrepo, A. Karma, et al. A rabbit ventricular action potential model replicating cardiac dynamics at rapid heart rates. *Biophysical Journal*, 94(2):392–410, 2008.

L. S. Maier and D. M. Bers. Role of Ca^{2+}/calmodulin-dependent protein kinase (CaMK) in excitation-contraction coupling in the heart. *Cardiovascular Research*, 73(4):631–640, 2007.

J. P. Mather and P. E. Roberts. *Introduction to cell and tissue culture: theory and technique*. Springer Science & Business Media, 1998.

S. Matsuoka, N. Sarai, S. Kuratomi, K. Ono, and A. Noma. Role of individual ionic current systems in ventricular cells hypothesized by a model study. *The Japanese Journal of Physiology*, 53(2):105–123, 2003.

R. E. McAllister, D. Noble, and R. W. Tsien. Reconstruction of the electrical activity of cardiac Purkinje fibres. *The Journal of Physiology*, 251(1):1–59, 1975.

T. F. McDonald, A. Cavalié, W. Trautwein, and D. J. Pelzer. Voltage-dependent properties of macroscopic and elementary calcium channel currents in guinea pig ventricular myocytes. *Pflügers Archiv — European Journal of Physiology*, 406(5):437–448, 1986.

T. F. McDonald, S. Pelzer, W. Trautwein, and D. J. Pelzer. Regulation and modulation of

calcium channels in cardiac, skeletal, and smooth muscle cells. *Physiological Reviews*, 74(2):365–507, 1994.

S. I. McDonough, Y. Mori, and B. P. Bean. FPL 64176 modification of $Ca_V1.2$ L-type calcium channels: dissociation of effects on ionic current and gating current. *Biophysical Journal*, 88(1):211–223, 2005.

N. McNaughton, D. Bleakman, and A. Randall. Electrophysiological characterisation of the human N-type Ca^{2+} channel II: activation and inactivation by physiological patterns of activity. *Neuropharmacology*, 37(1):67–81, 1998.

P. Mesirca, A. G. Torrente, and M. E. Mangoni. T-type channels in the sino-atrial and atrioventricular pacemaker mechanism. *Pflügers Archiv — European Journal of Physiology*, 466(4):791–799, 2014.

T. Mewes and U. Ravens. L-type calcium currents of human myocytes from ventricle of non-failing and failing hearts and from atrium. *Journal of Molecular and Cellular Cardiology*, 26(10):1307–1320, 1994.

A. Michailova, J. Saucerman, M. E. Belik, and A. D. McCulloch. Modeling regulation of cardiac K_{ATP} and L-type Ca^{2+} currents by ATP, ADP, and Mg^{2+}. *Biophysical Journal*, 88 (3):2234–2249, 2005.

G. R. Mirams, M. R. Davies, Y. Cui, P. Kohl, and D. Noble. Application of cardiac electrophysiology simulations to pro-arrhythmic safety testing. *British Journal of Pharmacology*, 167(5):932–945, 2012.

S. Miyoshi, H. Mitamura, K. Fujikura, Y. Fukuda, K. Tanimoto, Y. Hagiwara, M. Ita, and S. Ogawa. A mathematical model of phase 2 reentry: role of L-type Ca current. *American Journal of Physiology — Heart and Circulatory Physiology*, 284(4):H1285–H1294, 2003.

A. Molleman. *Patch clamping: an introductory guide to patch clamp electrophysiology*. John Wiley & Sons, 2003.

K. W. Morton and D. F. Mayers. *Numerical solution of partial differential equations: an introduction*. Cambridge University Press, 2 edition, 2005.

T. Nakayama, Y. Kurachi, A. Noma, and H. Irisawa. Action potential and membrane currents of single pacemaker cells of the rabbit heart. *Pflügers Archiv — European Journal of Physiology*, 402(3):248–257, 1984.

J. A. Nelder and R. Mead. A simplex method for function minimization. *The Computer Journal*, 7(4):308–313, 1965.

S. A. Niederer, M. Fink, D. Noble, and N. P. Smith. A meta-analysis of cardiac electrophysiology computational models. *Experimental Physiology*, 94(5):486–495, 2009.

B. Nilius. Possible functional significance of a novel type of cardiac Ca channel. *Biomedica Biochimica Acta*, 45(8):K37–45, 1986.

B. Nilius, P. Hess, J. B. Lansman, and R. W. Tsien. A novel type of cardiac calcium channel in ventricular cells. *Nature*, 316(6027):443–446, 1985.

M. Nivala, E. de Lange, R. Rovetti, and Z. Qu. Computational modeling and numerical methods for spatiotemporal calcium cycling in ventricular myocytes. *Frontiers in Physiology*, 3:114, 2012.

D. Noble. Cardiac action and pacemaker potentials based on the Hodgkin-Huxley equations. *Nature*, 188(4749):495–497, 1960.

D. Noble and Y. Rudy. Models of cardiac ventricular action potentials: iterative interaction between experiment and simulation. *Philosophical Transactions of the Royal Society of London A: Mathematical, Physical and Engineering Sciences*, 359(1783):1127–1142, June 2001.

D. Noble, S. J. Noble, G. C. Bett, Y. E. Earm, W. K. Ho, and I. K. So. The role of sodium-calcium exchange during the cardiac action potential. *Annals of the New York Academy of Sciences*, 639(1):334–353, 1991.

D. Noble, A. Varghese, P. Kohl, and P. J. Noble. Improved guinea-pig ventricular cell model incorporating a diadic space, I_{Kr} and I_{Ks}, and length-and tension-dependent processes. *The Canadian Journal of Cardiology*, 14(1):123–134, 1998.

D. Noble, A. Garny, and P. J. Noble. How the Hodgkin–Huxley equations inspired the Cardiac Physiome Project. *The Journal of Physiology*, 590(11):2613–2628, 2012.

A. Noma and T. Shibasaki. Membrane current through adenosine-triphosphate-regulated potassium channels in guinea-pig ventricular cells. *The Journal of Physiology*, 363(1): 463–480, 1985.

C. Nordin. Computer model of membrane current and intracellular Ca^{2+} flux in the isolated guinea pig ventricular myocyte. *American Journal of Physiology — Heart and Circulatory Physiology*, 265(6):H2117–H2136, 1993.

C. Nordin, F. Siri, and R. S. Aronson. Electrophysiologic characteristics of single myocytes isolated from hypertrophied guinea-pig hearts. *Journal of Molecular and Cellular Cardiology*, 21(7):729–739, 1989.

M. Novotová, A. Zahradníková, Z. Nichtová, R. Kováč, E. Král'ová, T. Stankovičová, and I. Zahradník. Structural variability of dyads relates to calcium release in rat ventricular myocytes. *Scientific Reports*, 10(1):1–14, 2020.

M. C. Nowycky and M. J. Pinter. Time courses of calcium and calcium-bound buffers following calcium influx in a model cell. *Biophysical Journal*, 64(1):77–91, 1993.

A. Nygren, C. Fiset, L. Firek, J. W. Clark, D. S. Lindblad, R. B. Clark, and W. R. Giles. Mathematical model of an adult human atrial cell: the role of K^+ currents in repolarization. *Circulation Research*, 82(1):63–81, 1998.

T. O'Hara, L. Virág, A. Varró, and Y. Rudy. Simulation of the undiseased human cardiac ventricular action potential: model formulation and experimental validation. *PLoS Computational Biology*, 7(5):e1002061, 2011.

G. Olivetti, G. Giordano, D. Corradi, M. Melissari, C. Lagrasta, S. R. Gambert, and P. Anversa. Gender differences and aging: effects on the human heart. *Journal of the American College of Cardiology*, 26(4):1068–1079, 1995.

B. O'Rourke, P. H. Backx, and E. Marban. Phosphorylation-independent modulation of L-type calcium channels by magnesium-nucleotide complexes. *Science*, 257(5067):245–248, 1992.

E. Ostertagová and O. Ostertag. Methodology and application of oneway ANOVA. *American Journal of Mechanical Engineering*, 1(7):256–261, 2013.

M. Ottolia, N. Torres, J. H. Bridge, K. D. Philipson, and J. I. Goldhaber. Na/Ca exchange and contraction of the heart. *Journal of Molecular and Cellular Cardiology*, 61:28–33, 2013.

M. Paci, J. Hyttinen, K. Aalto-Setälä, and S. Severi. Computational models of ventricular- and atrial-like human induced pluripotent stem cell derived cardiomyocytes. *Annals of Biomedical Engineering*, 41(11):2334–2348, 2013.

S. V. Pandit, R. B. Clark, W. R. Giles, and S. S. Demir. A mathematical model of action potential heterogeneity in adult rat left ventricular myocytes. *Biophysical Journal*, 81(6): 3029–3051, 2001.

A. J. Pappano and W. Gil Wier. Automaticity: Natural excitation of the heart. In A. J. Pappano and W. Gil Wier, editors, *Cardiovascular Physiology (Tenth Edition)*, pages 31–53. Elsevier, Philadelphia, tenth edition edition, 2013. ISBN 978-0-323-08697-4.

M. Pásek, J. Šimurda, and G. Christé. The functional role of cardiac T-tubules explored in a model of rat ventricular myocytes. *Philosophical Transactions of the Royal Society A: Mathematical, Physical and Engineering Sciences*, 364(1842):1187–1206, 2006.

P. Pathmanathan, R. A. Gray, V. J. Romero, and T. M. Morrison. Applicability analysis of validation evidence for biomedical computational models. *Journal of Verification, Validation and Uncertainty Quantification*, 2(2), 2017.

B. Pelzmann, P. Schaffer, E. Bernhart, P. Lang, H. Mächler, B. Rigler, and B. Koidl. L-type calcium current in human ventricular myocytes at a physiological temperature from children with tetralogy of Fallot. *Cardiovascular Research*, 38(2):424–432, 1998.

B. Z. Peterson, C. D. DeMaria, and D. T. Yue. Calmodulin is the Ca^{2+} sensor for Ca^{2+}–dependent inactivation of L-type calcium channels. *Neuron*, 22(3):549–558, 1999.

J. Pinnell, S. Turner, and S. Howell. Cardiac muscle physiology. *Continuing Education in Anaesthesia, Critical Care and Pain*, 7(3):85–88, 2007.

G. S. Pitt, R. D. Zühlke, A. Hudmon, H. Schulman, H. Reuter, and R. W. Tsien. Molecular basis of calmodulin tethering and Ca^{2+}-dependent inactivation of L-type Ca^{2+} channels. *Journal of Biological Chemistry*, 276(33):30794–30802, 2001.

K. S. Pitzer and G. Mayorga. Thermodynamics of electrolytes. II. Activity and osmotic coefficients for strong electrolytes with one or both ions univalent. *The Journal of Physical Chemistry*, 77(19):2300–2308, 1973.

A. Pohl, A. Wachter, N. Hatam, and S. Leonhardt. A computational model of a human single sinoatrial node cell. *Biomedical Physics & Engineering Express*, 2(3):035006, 2016.

M. Pourrier and D. Fedida. The emergence of human induced pluripotent stem cell-derived cardiomyocytes (hiPSC-CMs) as a platform to model arrhythmogenic diseases. *International Journal of Molecular Sciences*, 21(2):657, 2020.

L. Priebe and D. J. Beuckelmann. Simulation study of cellular electric properties in heart failure. *Circulation Research*, 82(11):1206–1223, 1998.

A. Priel, Z. Gil, V. T. Moy, K. L. Magleby, and S. D. Silberberg. Ionic requirements for membrane-glass adhesion and giga seal formation in patch-clamp recording. *Biophysical Journal*, 92(11):3893–3900, 2007.

J. L. Puglisi, W. Yuan, J. W. M. Bassani, and D. M. Bers. Ca^{2+} influx through Ca^{2+} channels in rabbit ventricular myocytes during action potential clamp: influence of temperature. *Circulation Research*, 85(6):e7–e16, 1999.

S. Ramasubramanian and Y. Rudy. The structural basis of IKs ion-channel activation: Mechanistic insights from molecular simulations. *Biophysical Journal*, 114(11):2584–2594, 2018.

R. J. Ramirez, S. Nattel, and M. Courtemanche. Mathematical analysis of canine atrial action potentials: rate, regional factors, and electrical remodeling. *American Journal of Physiology — Heart and Circulatory Physiology*, 279(4):H1767–H1785, 2000.

R. L. Rasmusson, J. W. Clark, W. R. Giles, K. Robinson, R. B. Clark, E. F. Shibata, and D. L. Campbell. A mathematical model of electrophysiological activity in a bullfrog atrial cell. *American Journal of Physiology — Heart and Circulatory Physiology*, 259 (2):H370–H389, 1990.

J. G. Restrepo, J. N. Weiss, and A. Karma. Calsequestrin-mediated mechanism for cellular calcium transient alternans. *Biophysical Journal*, 95(8):3767–3789, 2008.

H. Reuter. Slow inactivation of currents in cardiac Purkinje fibres. *The Journal of Physiology*, 197(1):233–253, 1968.

H. Reuter. Divalent cations as charge carriers in excitable membranes. *Progress in Biophysics and Molecular Biology*, 26:1–43, 1973.

H. Reuter. Localization of *beta* adrenergic receptors, and effects of noradrenaline and cyclic nucleotides on action potentials, ionic currents and tension in mammalian cardiac muscle. *The Journal of Physiology*, 242(2):429–451, 1974.

J. J. Rice, M. S. Jafri, and R. L. Winslow. Modeling gain and gradedness of Ca^{2+} release in the functional unit of the cardiac diadic space. *Biophysical Journal*, 77(4):1871–1884, 1999.

S. Rohr. Role of gap junctions in the propagation of the cardiac action potential. *Cardiovascular Research*, 62(2):309–322, 2004.

W. C. Rose, C. W. Balke, W. G. Wier, and E. Marban. Macroscopic and unitary properties of physiological ion flux through L-type Ca^{2+} channels in guinea-pig heart cells. *The Journal of Physiology*, 456(1):267–284, 1992.

B. Roux, T. Allen, S. Berneche, and W. Im. Theoretical and computational models of biological ion channels. *Quarterly Reviews of Biophysics*, 37(01):15–103, 2004.

R. Rovetti, X. Cui, A. Garfinkel, J. N. Weiss, and Z. Qu. Spark-induced sparks as a mechanism of intracellular calcium alternans in cardiac myocytes. *Circulation Research*, 106 (10):1582, 2010.

M. Rubart, J. C. Lopshire, N. S. Fineberg, and D. P. Zipes. Changes in left ventricular repolarization and ion channel currents following a transient rate increase superimposed on bradycardia in anesthetized dogs. *Journal of Cardiovascular Electrophysiology*, 11 (6):652–664, 2000.

Y. Rudy and J. R. Silva. Computational biology in the study of cardiac ion channels and cell electrophysiology. *Quarterly Reviews of Biophysics*, 39(1):57–116, 2006.

P. T. Sager, G. Gintant, J. R. Turner, S. Pettit, and N. Stockbridge. Rechanneling the cardiac proarrhythmia safety paradigm: a meeting report from the Cardiac Safety Research Consortium. *American Heart Journal*, 167(3):292–300, 2014.

B. Sakmann and E. Neher. Patch clamp techniques for studying ionic channels in excitable membranes. *Annual Review of Physiology*, 46:455–472, 1984.

M. C. Sanguinetti, C. Jiang, M. E. Curran, and M. T. Keating. A mechanistic link between an inherited and an acquired cardiac arrthytmia: HERG encodes the I_{Kr} potassium channel. *Cell*, 81(2):299–307, 1995.

C. Sarantopoulos, J. B. McCallum, W.-M. Kwok, and Q. Hogan. β-escin diminishes voltage-gated calcium current rundown in perforated patch-clamp recordings from rat primary afferent neurons. *Journal of Neuroscience Methods*, 139(1):61–68, 2004.

D. Sato, Y. Shiferaw, A. Garfinkel, J. N. Weiss, Z. Qu, and A. Karma. Spatially discordant alternans in cardiac tissue: role of calcium cycling. *Circulation Research*, 99(5):520–527, 2006.

H. Satoh. Elevation of intracellular Ca^{2+} concentration by protein kinase C stimulation in isolated single rabbit sino-atrial node cells. *General Pharmacology: The Vascular System*, 25(2):325–332, 1994.

N. Savalli, A. Pantazis, D. Sigg, J. N. Weiss, A. Neely, and R. Olcese. The $\alpha_2\delta$-1 subunit remodels $Ca_V1.2$ voltage sensors and allows Ca^{2+} influx at physiological membrane potentials. *Journal of General Physiology*, 148(2):147–159, 2016.

D. J. Schulz, J.-M. Goaillard, and E. Marder. Variable channel expression in identified single and electrically coupled neurons in different animals. *Nature Neuroscience*, 9(3): 356–362, 2006.

J. S. Sham, L. Cleemann, and M. Morad. Functional coupling of Ca^{2+} channels and ryanodine receptors in cardiac myocytes. *Proceedings of the National Academy of Sciences*, 92(1):121–125, 1995.

R. D. Shannon. Revised effective ionic radii and systematic studies of interatomic distances

in halides and chalcogenides. *Acta Crystallographica Section A*, 32(5):751–767, Sep 1976.

T. R. Shannon, F. Wang, J. Puglisi, C. Weber, and D. M. Bers. A mathematical treatment of integrated Ca dynamics within the ventricular myocyte. *Biophysical Journal*, 87(5): 3351–3371, 2004.

T. R. Shannon, F. Wang, and D. M. Bers. Regulation of cardiac sarcoplasmic reticulum Ca release by luminal [Ca] and altered gating assessed with a mathematical model. *Biophysical Journal*, 89(6):4096–4110, 2005.

S. M. Sharker and A. Rahman. A review on the current methods of Chinese hamster ovary (CHO) cells cultivation for the production of therapeutic protein. *Current Drug Discovery Technologies*, 18(3):354–364, 2021.

M. J. Shattock, K. C. Park, H.-Y. Yang, A. W. C. Lee, S. Niederer, K. T. MacLeod, and J. Winter. Restitution slope is principally determined by steady-state action potential duration. *Cardiovascular Research*, 113(7):817–828, 2017.

J. B. Shen, B. Jiang, and A. J. Pappano. Comparison of L-type calcium channel blockade by nifedipine and/or cadmium in guinea pig ventricular myocytes. *Journal of Pharmacology and Experimental Therapeutics*, 294(2):562–570, 2000.

R. Shirokov, R. Levis, N. Shirokova, and E. Ríos. Ca^{2+}-dependent inactivation of cardiac L-type Ca^{2+} channels does not affect their voltage sensor. *The Journal of General Physiology*, 102(6):1005–1030, 1993.

S. R. Shorofsky and C. W. Balke. Calcium currents and arrhythmias: insights from molecular biology. *The American Journal of Medicine*, 110(2):127–140, 2001.

S. Sicouri and C. Antzelevitch. A subpopulation of cells with unique electrophysiological properties in the deep subepicardium of the canine ventricle. the M cell. *Circulation Research*, 68(6):1729–1741, 1991.

J. Sieira, G. Dendramis, and P. Brugada. Pathogenesis and management of Brugada syndrome. *Nature Reviews Cardiology*, 13(12):744–756, 2016.

J. R. Silva. How to connect cardiac excitation to the atomic interactions of ion channels. *Biophysical Journal*, 114(2):259–266, 2018.

G. D. Smith. Analytical steady-state solution to the rapid buffering approximation near an open Ca^{2+} channel. *Biophysical Journal*, 71(6):3064–3072, 1996.

N. M. Soldatov. Ca^{2+} channel moving tail: link between Ca^{2+}-induced inactivation and Ca^{2+} signal transduction. *TRENDS in pharmacological Sciences*, 24(4):167–171, 2003.

A. R. Soltis and J. J. Saucerman. Synergy between CaMKII substrates and β-adrenergic signaling in regulation of cardiac myocyte Ca^{2+} handling. *Biophysical Journal*, 99(7): 2038–2047, 2010.

S. C. Stotz, S. E. Jarvis, and G. W. Zamponi. Functional roles of cytoplasmic loops and pore lining transmembrane helices in the voltage-dependent inactivation of HVA calcium channels. *The Journal of Physiology*, 554(2):263–273, 2004.

D. G. Strauss, G. Gintant, Z. Li, W. Wu, K. Blinova, J. Vicente, J. R. Turner, and P. T. Sager. Comprehensive in vitro proarrhythmia assay (CiPA) update from a cardiac safety research consortium/health and environmental sciences institute/FDA meeting. *Therapeutic Innovation & Regulatory Science*, 53(4):519–525, 2019.

D. G. Strauss, W. Wu, Z. Li, J. Koerner, and C. Garnett. Translational models and tools to reduce clinical trials and improve regulatory decision making for QTc and proarrhythmia risk (ICH E14/S7b updates). *Clinical Pharmacology & Therapeutics*, 109(2):319–333, 2021.

J. Striessnig, A. Pinggera, G. Kaur, G. Bock, and P. Tuluc. L-type Ca^{2+} channels in heart and brain. *Wiley Interdisciplinary Reviews: Membrane Transport and Signaling*, 3(2): 15–38, 2014.

H. Sun, N. Leblanc, and S. Nattel. Mechanisms of inactivation of L-type calcium channels in human atrial myocytes. *American Journal of Physiology — Heart and Circulatory Physiology*, 272(4):H1625–H1635, 1997.

L. Sun, J.-S. Fan, J. W. Clark, and P. T. Palade. A model of the L-type Ca^{2+} channel in

rat ventricular myocytes: ion selectivity and inactivation mechanisms. *The Journal of Physiology*, 529(1):139–158, 2000.

G. Szabó, N. Szentandrássy, T. Bíró, B. I. Tóth, G. Czifra, J. Magyar, T. Bányász, A. Varró, L. Kovács, and P. P. Nánási. Asymmetrical distribution of ion channels in canine and human left-ventricular wall: epicardium versus midmyocardium. *Pflügers Archiv — European Journal of Physiology*, 450(5):307–316, 2005.

M. R. Tadross, I. E. Dick, and D. T. Yue. Mechanism of local and global Ca^{2+} sensing by calmodulin in complex with a Ca^{2+} channel. *Cell*, 133(7):1228–1240, 2008.

P. Taggart, P. M. I. Sutton, T. Opthof, R. Coronel, R. Trimlett, W. Pugsley, and P. Kallis. Transmural repolarisation in the left ventricle in humans during normoxia and ischaemia. *Cardiovascular Research*, 50(3):454–462, 2001.

S. Takagi, Y. Kihara, S. Sasayama, and T. Mitsuiye. Slow inactivation of cardiac L-type Ca^{2+} channel induced by cold acclimation of guinea pig. *American Journal of Physiology — Regulatory, Integrative and Comparative Physiology*, 274(2):R348–R356, 1998.

K. Takahashi, K. Tanabe, M. Ohnuki, M. Narita, T. Ichisaka, K. Tomoda, and S. Yamanaka. Induction of pluripotent stem cells from adult human fibroblasts by defined factors. *Cell*, 131(5):861–872, 2007.

J. Taniguchi, A. Noma, and H. Irisawa. Modification of the cardiac action potential by intracellular injection of adenosine triphosphate and related substances in guinea pig single ventricular cells. *Circulation Research*, 53(2):131–139, 1983.

K. H. W. J. Ten Tusscher and A. V. Panfilov. Alternans and spiral breakup in a human ventricular tissue model. *American Journal of Physiology — Heart and Circulatory Physiology*, 291(3):H1088–H1100, 2006.

K. H. W. J. Ten Tusscher, D. Noble, P. J. Noble, and A. V. Panfilov. A model for human ventricular tissue. *American Journal of Physiology — Heart and Circulatory Physiology*, 286(4):H1573–H1589, 2004.

J. Tomek, A. Bueno-Orovio, E. Passini, X. Zhou, A. Minchole, O. Britton, C. Bartolucci,

S. Severi, A. Shrier, L. Virag, et al. Development, calibration, and validation of a novel human ventricular myocyte model in health, disease, and drug block. *eLife*, 8, 2019.

C. Trovato, E. Passini, N. Nagy, A. Varró, N. Abi-Gerges, S. Severi, and B. Rodriguez. Human Purkinje in silico model enables mechanistic investigations into automaticity and pro-arrhythmic abnormalities. *Journal of Molecular and Cellular Cardiology*, 2020.

G. N. Tseng. Calcium current restitution in mammalian ventricular myocytes is modulated by intracellular calcium. *Circulation Research*, 63(2):468–482, 1988.

G. N. Tseng, R. B. Robinson, and B. F. Hoffman. Passive properties and membrane currents of canine ventricular myocytes. *The Journal of General Physiology*, 90(5):671–701, 1987.

J. R. Tyson and T. P. Snutch. Molecular nature of voltage-gated calcium channels: structure and species comparison. *Wiley Interdisciplinary Reviews: Membrane Transport and Signaling*, 2(5):181–206, 2013.

M. A. van der Heyden, T. J. Wijnhoven, and T. Opthof. Molecular aspects of adrenergic modulation of cardiac L-type Ca^{2+} channels. *Cardiovascular Research*, 65(1):28–39, 2005.

D. R. Van Wagoner, A. L. Pond, M. Lamorgese, S. S. Rossie, P. M. McCarthy, and J. M. Nerbonne. Atrial L-type Ca^{2+} currents and human atrial fibrillation. *Circulation Research*, 85(5):428–436, 1999.

M. Varela, M. A. Colman, J. C. Hancox, and O. V. Aslanidi. Atrial heterogeneity generates re-entrant substrate during atrial fibrillation and anti-arrhythmic drug action: mechanistic insights from canine atrial models. *PLoS Computational Biology*, 12(12):e1005245, 2016.

C. C. Veerman, I. Mengarelli, K. Guan, M. Stauske, J. Barc, H. L. Tan, A. A. M. Wilde, A. O. Verkerk, and C. R. Bezzina. hiPSC-derived cardiomyocytes from Brugada Syndrome patients without identified mutations do not exhibit clear cellular electrophysiological abnormalities. *Scientific Reports*, 6(1):1–10, 2016.

J. Vicente, R. Zusterzeel, L. Johannesen, J. Mason, P. Sager, V. Patel, M. K. Matta, Z. Li,

J. Liu, C. Garnett, et al. Mechanistic model-informed proarrhythmic risk assessment of drugs: review of the "CiPA" initiative and design of a prospective clinical validation study. *Clinical Pharmacology & Therapeutics*, 103(1):54–66, 2018.

M. Vitek and W. Trautwein. Slow inward current and action potential in cardiac Purkinje fibres. *Pflügers Archiv — European Journal of Physiology*, 323(3):204–218, 1971.

M. Vornanen and N. Shepherd. Restitution of contractility in single ventricular myocytes of guinea pig heart. *Cardiovascular Research*, 33(3):611–622, 1997.

T. D. Vu and T. Kofidis. Biomaterials and cells for cardiac tissue engineering. In *Cardiac Regeneration and Repair*, pages 127–179. Elsevier, 2014.

C. A. Walker and F. G. Spinale. The structure and function of the cardiac myocyte: a review of fundamental concepts. *The Journal of Thoracic and Cardiovascular Surgery*, 118(2): 375–382, 1999.

E. Wan and S. Marx. Diagnosis, treatment, and mechanisms of Long QT Syndrome. In G. S. Pitt, editor, *Ion Channels in Health and Disease*, Perspectives in Translational Cell Biology, pages 113–130. Academic Press, Boston, 2016. ISBN 978-0-12-802002-9.

R. Wang, E. Karpinski, and P. K. Pang. Temperature dependence of L-type calcium channel currents in isolated smooth muscle cells from the rat tail artery. *Journal of Thermal Biology*, 16(2):83–87, 1991.

J. N. Weiss, A. Garfinkel, H. S. Karagueuzian, T. P. Nguyen, R. Olcese, P.-S. Chen, and Z. Qu. Perspective: a dynamics-based classification of ventricular arrhythmias. *Journal of Molecular and Cellular Cardiology*, 82:136–152, 2015.

D. G. Whittaker, M. Clerx, C. Lei, D. J. Christini, and G. R. Mirams. Calibration of ionic and cellular cardiac electrophysiology models. *Wiley Interdisciplinary Reviews: Systems Biology and Medicine*, 12(4):e1482, 2020.

R. Wilders, H. J. Jongsma, and A. C. G. Van Ginneken. Pacemaker activity of the rabbit sinoatrial node: A comparison of mathematical models. *Biophysical Journal*, 60(5): 1202–1216, 1991.

R. L. Winslow, J. Rice, S. Jafri, E. Marban, and B. O'Rourke. Mechanisms of altered

excitation-contraction coupling in canine tachycardia-induced heart failure, II: model studies. *Circulation Research*, 84(5):571–586, 1999.

R. L. Winslow, M. A. Walker, and J. L. Greenstein. Modeling calcium regulation of contraction, energetics, signaling, and transcription in the cardiac myocyte. *Wiley Interdisciplinary Reviews: Systems Biology and Medicine*, 8(1):37–67, 2016.

Y. C. Wu, T. Tucker, and R. Fettiplace. A theoretical study of calcium microdomains in turtle hair cells. *Biophysical Journal*, 71(5):2256–2275, 1996.

S. Yechikov, R. Copaciu, J. M. Gluck, W. Deng, N. Chiamvimonvat, J. W. Chan, and D. K. Lieu. Same-single-cell analysis of pacemaker-specific markers in human induced pluripotent stem cell-derived cardiomyocyte subtypes classified by electrophysiology. *Stem Cells*, 34(11):2670–2680, 2016.

Y. You, D. J. Pelzer, and S. Pelzer. Trypsin and forskolin decrease the sensitivity of L-type calcium current to inhibition by cytoplasmic free calcium in guinea pig heart muscle cells. *Biophysical Journal*, 69(5):1838–1846, 1995.

Y. You, D. J. Pelzer, and S. Pelzer. Modulation of L-type Ca^{2+} current by fast and slow Ca^{2+} buffering in guinea pig ventricular cardiomyocytes. *Biophysical Journal*, 72(1):175–187, 1997.

T. Yu, C. M. Lloyd, D. P. Nickerson, M. T. Cooling, A. K. Miller, A. Garny, J. R. Terkildsen, J. Lawson, R. D. Britten, P. J. Hunter, et al. The Physiome model repository 2. *Bioinformatics*, 27(5):743–744, 2011.

L. Yue, J. Feng, R. Gaspo, G.-R. Li, Z. Wang, and S. Nattel. Ionic remodeling underlying action potential changes in a canine model of atrial fibrillation. *Circulation Research*, 81 (4):512–525, 1997.

A. Zahradníková, Z. Kubalová, J. Pavelková, S. Gyorke, and I. Zahradník. Activation of calcium release assessed by calcium release-induced inactivation of calcium current in rat cardiac myocytes. *American Journal of Physiology — Cell Physiology*, 286(2):C330–C341, 2004.

J. Zeng, K. R. Laurita, D. S. Rosenbaum, and Y. Rudy. Two components of the delayed rec-

tifier K^+ current in ventricular myocytes of the guinea pig type: Theoretical formulation and their role in repolarization. *Circulation Research*, 77(1):140–152, 1995.

H. Zhang, A. V. Holden, I. Kodama, H. Honjo, M. Lei, T. Varghese, and M. R. Boyett. Mathematical models of action potentials in the periphery and center of the rabbit sinoatrial node. *American Journal of Physiology — Heart and Circulatory Physiology*, 279 (1):H397–H421, 2000.

Z. Zhou and D. M. Bers. Ca^{2+} influx via the L-type Ca^{2+} channel during tail current and above current reversal potential in ferret ventricular myocytes. *The Journal of Physiology*, 523(1):57–66, 2000.